Computational investigation of diffusion, flow, and multi-scale mass transport in disordered and ordered materials using high-performance computing

Dissertation zur Erlangung des Doktorgrades
der Naturwissenschaften (Dr. rer. nat.)
dem Fachbereich Chemie
der Philipps-Universität Marburg

vorgelegt von

Dipl.-Phys. Anton Daneyko

aus Minsk, Belarus

Marburg an der Lahn 2015

Vom Fachbereich Chemie
der Philipps-Universität Marburg (Hochschulkennziffer: 1180)
als Dissertation am 11. Mai 2015 angenommen

Erstgutachter: Prof. Dr. Ulrich Tallarek
Zweitgutachter: Prof. Dr. Andreas Seubert

Tag der mündlichen Prüfung: 16. Juni 2015

Abstract

Flow and mass transport processes through porous materials are ubiquitous in nature and industry. In order to study these phenomena, we developed a computational framework for massively parallel supercomputers based on lattice-Boltzmann and random-walk particle tracking methods. Using this framework, we simulated the flow and mass transport (advection-diffusion problem) in several types of ordered and disordered porous materials. The pore network of the materials was either generated algorithmically (using Jodrey-Tory method) or reconstructed using confocal laser scanning microscopy or scanning electron microscopy. The simulated flow velocity field and dynamics of the random-walk tracer ensemble were used to study the transient and asymptotic behavior of macroscopic transport parameters: permeability, effective diffusion, and hydrodynamic dispersion coefficients.

This work has three distinct topics developed and analyzed in four chapters. Each chapter has been published as a separate study. The date of publication and corresponding journal name are denoted at the beginning of each chapter. The first part of this work (Chapter 1) is addressing a timely question of high-performance liquid chromatography on whether particle size distribution of the modern packing materials gives any advantage in terms of separation efficiency. The second part (Chapters 2 and 3) is focused on the effects of dimensionality and geometry of the channels on the transport inside different types of chromatographic supports (particulate packings, monoliths, and pillar arrays). In order to analyze these effects, we recorded transient values of the longitudinal and transverse hydrodynamic dispersion coefficients in unconfined, partially, and fully confined structures and analyzed the time and length scales of the transport phenomena within. In the last part of this work (Chapter 4) we investigated the influence of the shell thickness and diffusivity on separation efficiency of the core–shell packings. Based on the simulation results, we extended the Giddings theory of coupled eddy dispersion and confirmed the validity of the Kaczmarski-Guiochon model of interparticle mass-transfer.

Overall, this study extends the understanding of the connection of geometry and morphology of the porous materials with their macroscopic transport parameters.

Zusammenfassung

Fluss- und Transportprozesse durch poröse Materialien sind in der Natur und Industrie allgegenwärtig. Um diese Phänomene im Detail zu untersuchen, haben wir ein computerbasiertes Framework auf der Basis von Lattice-Boltzmann- und dem Random-Walk-Tracking-Methoden für parallelisierte Rechnungen auf Supercomputern entwickelt. Dieses Framework wurde für die Simulation von Fluss und Massentransport (Advektions-Diffusions-Problem) in verschiedenen geordneten und ungeordneten porösen Systemen eingesetzt. Die Porennetzwerke der Materialien wurden entweder durch den Einsatz von Algorithmen (Nutzung der Jodrey-Tory Methode) generiert oder mit Hilfe von konfokaler Lasermikroskopie bzw. Rasterelektronenmikroskopie rekonstruiert. Die simulierten Fließgeschwindigkeitsfelder und die Dynamik des Random-Walk Tracer Ensembles wurden für die Untersuchung des übergangsverhalten und asymptotischen Verhaltens der folgenden makroskopischen Transportparameter genutzt: Effektive Diffusion, Permeabilität und hydrodynamischer Diffusionskoeffizient.

In dieser Arbeit haben sich drei spezifische Themen herauskristallisiert, die in insgesamt vier Kapiteln untersucht wurden. Jedes Kapitel wurde als eine Studie separat publiziert, wobei das Veröffentlichungsdatum und das entsprechende Journal jeweils zu Beginn des Kapitels angegeben sind. Der erste Abschnitt dieser Arbeit (Kapitel 1) beschäftigt sich mit der aktuellen Frage, ob die enge Partikelgrößenverteilung der modernen Core-Shell Partikel einen Vorteil im Hinblick auf die Trennungseffizienz in der High-Performance Liquid Chromatography liefert. Der zweite Abschnitt (Kapitel 2 und 3) thematisiert die Auswirkung von Dimensionalität und Kanalgeometrie auf die Transporteigenschaften in verschiedenen chromatographischen Supportmaterialien (partikuläre Betten, Monolithen und Pillar-Arrays). Um diese Effekte zu analysieren, wurden die zeitabhängigen Werte der longitudinalen und transversalen hydrodynamischen Dispersionskoeffizienten in gänzlich unendlichen, partiell begrenzten und komplett begrenzten Strukturen aufgenommen und im Hinblick auf die Zeit- und Längenskala der darin ablaufenden Transportphänomene untersucht. Der letzte Abschnitt (Kapitel 4) beschäftigt sich mit dem Einfluss der Dicke der porösen Hülle sowie der Diffusion in dieser Hülle auf die Trenneffizienz von Core-Shell Packungen. Die Ergebnisse dieser Simulationen wurde genutzt, um die Giddings-Theorie der gekoppelten Eddy-Dispersion zu erweitern und die Gültigkeit des Kaczmarski-Guiochon Models von dem interpartikulären Massentransfer zu bestätigen.

Zusammengefasst erweitert diese Arbeit das Verständnis vom Zusammenspiel von Geometrie und Morphologie der porösen Säulenmaterialien mit den makroskopischen Transportparametern.

Acknowledgments

This thesis would never have been possible without the support of numerous people. I would like to thank my supervisor Prof. Dr. Ulrich Tallarek for countless hours of fruitful discussions. I appreciate the valuable input of my coauthors Dr. Siarhei Khirevich, Vasili Baranau, Dr. Dzmitry Hlushkou, and Dr. Alexandra Höltzel. I am grateful to my colleagues who helped me to adapt in a new country and created a pleasant working environment: Dr. Steffen Ehlert, Dr. Stephanie Jung, Dr. Stefan Bruns, Dr. Daniela Stoeckel, Tibor Müllner, Kristof Hormann, Arved Reising, and Julia Rybka.

Most of all I am thankful to my family and friends who supported me throughout the years of this endeavor. My mom and dad, Elena and Pavel Daneyko. My grandma and grandpa, Eleanora Salzmann and Prof. Dr. Roman Aizberg. My uncle Dr. Oleg Aizberg and my cousin Dmitry Kulakovsky. I thank my dear friends Dimitrij Zadorin, Elena Kashirskaya, Veronika Kesova, Babett Richter, Nadia Bulynia, and Taras Paschenko. A special thanks goes to my girlfriend Dr. Maria Billini and my friend Dr. Valentin Markounikau for proofreading this thesis.

List of publications

First author

1. A. DANEYKO, A. HÖLTZEL, S. KHIREVICH and U. TALLAREK. Influence of the particle size distribution on hydraulic permeability and eddy dispersion in bulk packings. *Analytical Chemistry*, 83.10: 3903–3910, 2011. DOI: 10.1021/ac200424p
2. A. DANEYKO, S. KHIREVICH, A. HÖLTZEL, A. SEIDEL-MORGENSTERN and U. TALLAREK. From random sphere packings to regular pillar arrays: effect of the macroscopic confinement on hydrodynamic dispersion. *Journal of Chromatography A*, 1218.45: 8231–48, 2011. DOI: 10.1016/j.chroma.2011.09.039
3. A. DANEYKO, D. HLUSHKOU, S. KHIREVICH, and U. TALLAREK. From random sphere packings to regular pillar arrays: analysis of transverse dispersion. *Journal of Chromatography A*, 1257: 98–115, 2012. DOI: 10.1016/j.chroma.2012.08.024
4. A. DANEYKO, D. HLUSHKOU, V. BARANAU, S. KHIREVICH, A. SEIDEL-MORGENSTERN and U. TALLAREK. Computational investigation of longitudinal diffusion, eddy dispersion, and trans-particle mass transfer in bulk, random packings of core–shell particles with varied shell thickness and shell diffusion coefficient. Submitted *to Journal of Chromatography A*

Coauthor of the following articles

1. S. KHIREVICH, A. DANEYKO, A. HÖLTZEL, A. SEIDEL-MORGENSTERN, and U. TALLAREK. Statistical analysis of packed beds, the origin of short-range disorder, and its impact on eddy dispersion. *Journal of Chromatography A*, 1217.28: 4713–4722, 2010.
   DOI: 10.1016/j.chroma.2010.05.019
2. S. KHIREVICH, A. DANEYKO, and U. TALLAREK. Simulation of fluid flow and mass transport at extreme scale. In *Jülich Blue Gene/P Extreme Scaling Workshop 2010* edited by B. MOHR and W. FRINGS Forschungszentrum Jülich, Jülich Supercomputing Centre, 2010
3. S. KHIREVICH, A. HÖLTZEL, A. DANEYKO, A. SEIDEL-MORGENSTERN, and U. TALLAREK. Structure–transport correlation for the diffusive tortuosity of bulk, monodisperse, random sphere packings. *Journal of Chromatography A*, 1218.37: 6489–6497, 2011.
   DOI: 10.1016/j.chroma.2011.07.066
4. D. HLUSHKOU, F. GRITTI, A. DANEYKO, G. GUIOCHON, and U. TALLAREK. How microscopic characteristics of the adsorption kinetics impact macroscale transport in chromatographic beds. *The Journal of Physical Chemistry C*, 117.44: 22974–22985, 2013.
   DOI: 10.1021/jp408362u
5. U. M. SCHEVEN, S. KHIREVICH, A. DANEYKO, and U. TALLAREK. Longitudinal and transverse dispersion in flow through random packings of spheres: A quantitative comparison of experiments, simulations, and models. *Physical Review E*, 89: 053023, 2014.
   DOI: 10.1103/PhysRevE.89.053023
6. D. HLUSHKOU, U. TALLAREK, A. DANEYKO, G. GUIOCHON, and F. GRITTI. How characteristics of the adsorption kinetics impact macroscale transport in porous media: a microscopic stochastic approach. *Chemie Ingenieur Technik*, 86.9: 1630, 2014.
   DOI: 10.1002/cite.201450547

Erklärung

Ich versichere, dass ich die vorliegende Dissertation mit dem Titel

“Computational investigation of diffusion, flow, and multi-scale mass transport in disordered and ordered materials using high-performance computing”

selbständig, ohne unerlaubte Hilfe angefertigt und mich dabei keiner anderen als der von mir ausdrücklich bezeichneten Quellen und Hilfen bedient habe. Die Dissertation wurde in der jetzigen oder einer ähnlichen Form noch bei keiner anderen Hochschule oder Fachhochschule eingereicht und hat noch keinem sonstigen Prüfungszweck gedient.

Ort, Datum, Unterschrift _____

Contribution of authors

This work is a product of collective effort of many authors, whose contribution is explained below.

- Chapter 1
  All simulations and corresponding data processing were performed by me. The methods section of the manuscript was developed by me. The manuscript was developed in joint effort by Dr. Alexandra Höltzel and me, and subsequently edited by Prof. Dr. Ulrich Tallarek. Dr. Siarhei Khirevich contributed to the planning of the simulations. The manuscript was submitted by Prof. Dr. Ulrich Tallarek.
- Chapter 2
  The simulations and corresponding data processing for the ordered structures were performed by me. The simulations and corresponding data processing for the disordered structures were performed by Dr. Siarhei Khirevich. The manuscript was developed in close collaboration with Prof. Dr. Tallarek and Dr. Siarhei Khirevich. The text was subsequently edited by Dr. Alexandra Höltzel. The manuscript was submitted by Prof. Dr. Ulrich Tallarek.
- Chapter 3
  The simulations and corresponding data processing for the ordered structures and bulk packings of spheres were performed by me. The simulations in monolithic structures were performed by Dr. Dzmitry Hlushkou. Dr. Siarhei Khirevich contributed to the planning of the simulations. The manuscript was prepared together with Prof. Dr. Ulrich Tallarek. The submission was carried out by Prof. Dr. Ulrich Tallarek.
- Chapter 4
  All simulations and corresponding data processing were performed by me. The extension of the random-walk particle tracking (RWPT) method was performed by me. The manuscript was developed by me in close collaboration with Vasili Baranau and Dr. Dzmitry Hlushkou. The extension of the coupled theory of eddy dispersion was performed by me and Vasili Baranau. Dr. Siarhei Khirevich helped with the implementation of the simulation framework. Prof. Dr. Andreas Seidel-Morgenstern contributed to the discussion of the results. The manuscript was edited and submitted by Prof. Dr. Ulrich Tallarek.

Place, Date, Signature of Author _____

Place, Date, Signature of First Supervisor _____

Contents

Introduction

The transport of matter and heat can be found in virtually any physical system and object that surrounds us, ranging from planetary to cell scale. For example, the currents in oceans drive nutrient-rich water from the bottom up into the oceanic mixed layer,[1] where the nutrients become accessible to plankton[2,3] – the base of the marine food chain. Given that any human is a descendant of a universal aquatic ancestor,[4–6] we may speculate that without the matter and heat transport phenomena there would be no human being to appreciate this thesis. In addition, these transport processes play a key role in the most important challenges of the modern civilization: preservation of fresh water aquifers, climate change, and recovery of natural resources. Astonishing number of industrial applications are based on mixing and heat transport: filtration and separation systems, plastics and textile processing, chemicals manufacturing, food production, and many more.

Mathematically, the transport problem for incompressible fluids can be described with the system of the Navier-Stokes[7] and the advection–diffusion[8] equations

$$\begin{cases} \dfrac{\partial \vec{v}}{\partial t} + (\vec{v}\cdot\nabla)\vec{v} = \mu\Delta\vec{v} - \dfrac{1}{\rho}\nabla p + \vec{F} \\ \dfrac{\partial c}{\partial t} = \nabla\cdot(D\nabla c) - \nabla\cdot(\vec{v}c), \end{cases} \tag{1}$$

where $\vec{v}$ is the fluid velocity, μ is the kinematic viscosity, ρ is the fluid density, p is the pressure, $\vec{F}$ is the body force, c is concentration of migrating species, and D is the diffusion coefficient. The Eqs. (1) were solved only for a limited number of simple boundary conditions. Even the basic properties of the solution of the three-dimensional Navier–Stokes equation, namely the existence and smoothness, are still an unsolved problem. In the year 2000 this problem has been included into the list of the seven Millennium Prize Problems stated by the Clay Mathematics Institute.

[1] A. B. Kara, P. A. Rochford, and H. E. Hurlburt. *J. Geophys. Res.*, 105, p. 16803, 2000.
[2] M. J. R. Fasham, H. W. Ducklow, and S. M. McKelvie. *J. Geophys. Res.*, 48, pp. 591–639, 1990.
[3] W. Munk and C. Wunsch. *Deep Sea Res. Pt. I*, 45, pp. 1977–2010, 1998.
[4] C. Woese. *P. Nat. Acad. Sci. USA*, 95, pp. 6854–6859, 1998.
[5] N. Galtier, N. Tourasse, and M. Gouy. *Science*, 283, pp. 220–221, 1999.
[6] D. L. Theobald. *Nature*, 465, pp. 219–22, 2010.
[7] L. D. Landau and E. M. Lifschitz *Fluid mechanics* 2nd ed. Butterworth–Heinemann, 2007
[8] J. Bear *Dynamics of fluids in porous media* Dover Publications, 1988

In this thesis we deal with the transport problems in porous materials. Such materials can be of natural or man-made origin, e.g., a mineral or, as is the case of this work, a chromatographic column. The distinctive feature of porous materials is the complicated geometry of their pore space. Even though, the pore space of some materials has an ordered or close to ordered structure,[9,10] in most of the cases pores have irregular shape and are connected with each other by tortuous channels. Moreover, the sizes of the pores may vary greatly[11] and several scales of pore size often coexist in a single material. For example, in a particulate chromatographic column the mesopores of the packing material are on the order of nanometers, while the size of the pores between the particles is on the order of micrometers. Another example is concrete, where pore size ranges from angstroms to millimeters, spanning seven orders of magnitude. In terms of transport problem, this complex multiscale geometry of the pore space directly corresponds to a complicated boundary condition for the Eqs. (1). However, the good news is that due to the small scale of the material features and typically low fluid velocities (creeping or laminar flow regime), the Reynolds number is much smaller than unity,[12] which means that the Navier-Stokes equation in system (1) is reduced to a more simple Stokes equation

$$\frac{\partial \vec{v}}{\partial t} = \mu \Delta \vec{v} - \frac{1}{\rho} \nabla p + \vec{F}. \tag{2}$$

In the previous years multiple attempts have been undertaken to model porous materials in a way that simplifies the solution of Eqs. (1). One of the methods substitutes the complex geometry of a pore space with a network of interconnected capillaries[13–15] for which the precise solutions of flow and transport equations exist (Poiseuille flow and Taylor-Aris dispersion[16,17]). More precisely, using the graph theory, the flow and tranport can be subsequently calculated[18,19] as a combination of the known weighted solutions for Poiseuille flow and Taylor-Aris dispersion. In this way one does not deal with the partial differential equations (1). Even though some trends and experimental results could be matched with the adjustment of the model,[20] the bottleneck of this approach is the transition from a real porous medium sample to a capillary network representation – the prediction capabilities of these models are sensitive to the reconstruction procedure.[21]

Another class of methods to simplify the transport equations can be grouped under the name

[9] H. He et al. *Adv. Funct. Mater.*, 23, pp. 4720–4728, 2013.
[10] P. Yang et al. *Adv. Mater.*, 13, pp. 427–431, 2001.
[11] J. H. Cushman *The Physics of Fluids in Hierarchical Porous Media: Angstroms to Miles* Springer Netherlands, 1997
[12] D. Hlushkou and U. Tallarek. *J. Chromatogr. A*, 1126, pp. 70–85, 2006.
[13] I. Fatt. *Trans. Am. Inst. Min. Met. Eng.*, 207, 144–159, 1956.
[14] I. Fatt. *Trans. Am. Inst. Min. Met. Eng.*, 207, 160–163, 1956.
[15] I. Fatt. *Trans. Am. Inst. Min. Met. Eng.*, 207, 164–181, 1956.
[16] G. Taylor. *Philos. Trans. R. Soc. A*, 219, pp. 186–203, 1953.
[17] R. Aris. *P. Roy. Soc. A-Math. Phy.*, 235, pp. 67–77, 1956.
[18] P. M. Adler and H. Brenner. *Physicochem. Hydrodyn.*, 5, pp. 245–268, 1984.
[19] P. M. Adler and H. Brenner. *Physicochem. Hydrodyn.*, 5, pp. 269–285, 1984.
[20] M. J. Blunt. *Curr. Opin. Colloid Interface Sci.*, 6, pp. 197–207, 2001.
[21] H. Dong and M. Blunt. *Phys. Rev. E*, 80, p. 036307, 2009.

of upscaling methods.[22] Many authors used variations of this approach,[23–25] but the common idea is to transform Eqs. (1) from their local form into a macroscopic representation. Upscaling methods treat a domain with a pore network as a continuum described by the effective macroscopic (with respect to its own scale) transport coefficients. For example, such upscaling of the Stokes equation (2) leads to a solution, which is known as the Darcy law[26]:

$$\vec{v} = -\frac{1}{\varepsilon\mu}\mathbf{K}\nabla p, \tag{3}$$

where ε is the porosity of the medium and $\mathbf{K}$ is the permeability tensor. The goal of upscaling methods is the derivation of the macroscopic (often tensor) quantities from the microscopic geometry of the porous medium. Using these macroscopic quantities one can solve the transport problems of a larger scale. For example, using the three-dimensional data of the seismic tomography, the transport through the strata of different rock types can be calculated if we know the dispersion tensors of each rock type. The dispersion tensors of each rock type can be obtained by solving the transport equations (1) in their representative elementary volume (REV). However, so far the analytical solutions even for the ideal case of spheres located in the nodes of crystal structures (simple-cubic, face-centered cubic, etc.) have not been obtained. Consequently, the solution of Eqs. (1) in the REV are usually computed numerically[27–29] as is the case of the current work.

Modern numerical analysis boosted during the years of World War II. At that time the word computer referred to a human for whom calculation was a day job and whose major tools were a slide rule and the tables of mathematical functions.[30] Gradually, the human computers were replaced by mechanical and later electronic devices. The first paper to study the influence of rounding error on the computational algorithm was published in 1947 by von Neuman and Goldstine in the Bulletin of the American Mathematical Society.[31] In the following decade an academic discipline was formed with its own community and publication venues. In the meantime, Von Neuman predicted that the "automatic computing machine" would replace the analytic solution of flow equations and that this approach would make experimental fluid dynamics obsolete. More than a half century later these predictions have not fully come true: the crucial properties of the computational fluid dynamics – stability and convergence – are still in need of mathematical study. Despite the ongoing research, some simulation techniques have become widespread and are now recognized among the engineering and scientific community. In 2013 the Nobel Prize in

[22] J. H. Cushman, L. S. Bennethum, and B. X. Hu. *Adv. Water Resour.*, 25, pp. 1043–1067, 2002.
[23] H. Brenner. *Philos. Trans. R. Soc. A*, 297, pp. 81–133, 1980.
[24] M. Quintard and S. Whitaker. *Chem. Eng. Sci.*, 48, pp. 2537–2564, 1993.
[25] L. W. Gelhar and C. L. Axness. *Water Resour. Res.*, 19, pp. 161–180, 1983.
[26] P. M. Adler *Porous Media: Geometry and Transports* Butterworth-Heinemann Series in Chemical Engineering, 1992
[27] D. A. Edwards et al. *Transp. Porous Media*, 6, pp. 337–358, 1991.
[28] J. Salles et al. *Phys. Fluids A*, 5, pp. 2348–2376, 1993.
[29] V. Mourzenko et al. *Phys. Rev. E*, 77, p. 066306, 2008.
[30] Grier D. A. *When Computers Were Human* 2nd ed. Princeton University Press, 2007
[31] J. Von Neumann and H. H. Goldstine. *B. Am. Math. Soc.*, 53, pp. 1021–1099, 1947.

chemistry was awarded for the development of multiscale simulation methods that have allowed to model complex chemical systems and reactions.

In this work we use numerical methods to simulate the flow and mass transport in the pore space of several structures employed in chromatography. Despite the enormous progress of the computing industry in our lifetime, the performance and memory capacity of a modern desktop PC is not sufficient to perform simulations in big domains on the scale of individual pores. Yet, the simulations of that scale are possible on the supercomputers – machines with thousands of processors and terabytes of memory. The methods that we used to compute velocity fields and mass transport are not based on the solution of Eqs. (1), but rather on an alternative mathematical representation of the same problems. A brief description of this mathematical approach is presented below.

The Navier-Stokes (NS) and advection-diffusion (AD) equations are derived under the assumption that the fluid is an infinitely divisible continuum. The NS equation follows from the Newton's second law applied to fluid motion, while AD equation follows from continuity equation, and Fick's first law. An alternative to the continuum representation of fluid is to consider fluid behavior on the molecular level. This can be done in the framework of statistical mechanics by the Boltzmann equation

$$\left(\vec{v}\cdot\frac{\partial}{\partial\vec{r}}+\vec{a}\cdot\frac{\partial}{\partial\vec{v}}+\frac{\partial}{\partial t}\right)f(\vec{r},\vec{v},t)=\left(\frac{\partial f}{\partial t}\right)_{\mathrm{c}}, \tag{4}$$

where $f(\vec{r},\vec{v},t)$ is the probability density distribution of a single particle with coordinate $\vec{r}$. The right-hand side of Eq. (4) is called the collision term and it is responsible for the change of the distribution function when particles collide. In order to solve Eq. (4), a collision term describing the behavior of the particular system should be specified. If we assume that the substance under consideration is an ideal gas at thermodynamic equilibrium, then the velocity probability distribution of the gas particles obeys the Maxwell-Boltzmann statistics $f^{\mathrm{eq}}(\vec{v})$ and the collision term can be represented in the Bhatnagar-Gross-Krook form[32]

$$\left(\frac{\partial f}{\partial t}\right)_{\mathrm{c}}=\frac{f^{\mathrm{eq}}(\vec{v})-f(\vec{r},\vec{v},t)}{\tau}, \tag{5}$$

where τ is the collision time. The density ρ and velocity $\vec{v}$ at a specific space-time point are obtained as the zeroth and first moments of $f(\vec{r},\vec{u},t)$. It has been shown that when the mass and momentum are conserved during the particle collision, the Boltzmann equation is equivalent to the Navier-Stokes equation.[33,34] One of the positive side effects of the microscopic treatment of fluid is that continuum assumption is alleviated and thus the flows with high Knudsen number can be treated using this approach. In a similar way that the Boltzmann equation is equivalent

[32] P. L. Bhatnagar, E. P. Gross, and M. Krook. *Phys. Rev.*, 94, pp. 511–525, 1954.
[33] C. Bardos, F. Golse, and D. Levermore. *J. Stat. Phys.*, 63, pp. 323–344, 1991.
[34] F. Golse and L. Saint-Raymond. *J. Math. Pures Appl.*, 91, pp. 508–552, 2009.

to the Navier-Stokes equation, the stochastic differential equation[35]

$$\mathrm{d}\vec{r}(t) = \vec{v}(\vec{r}(t))\mathrm{d}t + \sqrt{2D}\mathrm{d}\vec{B}(t), \tag{6}$$

where $\vec{B}$ denotes standard Brownian motion, is equivalent to the advection–diffusion equation.[36,37]

Popular Eulerian approaches of solving partial differential equations numerically (finite difference, element, and volume methods) are based on the different types of discretization of the simulation domain and approximation of the differential operators. These methods can be applied to the solution of the Navier-Stokes equation. However, the drawbacks of these methods are the artificial oscillations and numerical dispersion,[38–40] which are especially pronounced for the advection dominated regime. In order to avoid these problems, we simulate flow and mass transport employing Lagrangian approach, namely the lattice-Boltzmann (LBM) and random walk-particle tracking methods (RWPT). These numerical methods are relatively new in the family of computational fluid dynamics algorithms.

The LBM numerically solves a version of the Boltzmann equation with discrete space, time, and a finite set of *velocities*. In general, LBM methods are classified by the number of dimensions in which they operate and the size of the finite set of velocities used. In this work a D3Q19 LBM model is used, i.e., a three-dimensional model, where velocity vector at each point of the discrete space can posses one of the 19 values. The RWPT method is a straightforward implementation of Eq. (6) that employs one step Euler approximation.[41] Due to their locality, both LBM and RWPT are suitable for massive parallelization. Additionally, the typical elongated geometry of the simulated structures allowed us to use one-dimensional decomposition of the simulation domain, which greatly simplifies the parallelization routines. Exploiting these peculiarities, we have developed a highly scalable simulation framework capable of operating on hundreds of thousands processor cores.[42] Another practical advantage of our LBM implementation is due to its Cartesian discretization grid: one can use three-dimensional confocal laser scanning microscopy images of the real porous materials as a direct input to the algorithm (Chapter 3). I would like to point the reader interested in the general ideas of LBM, RWPT, and the details of their implementation to the thesis of my former colleague Dr. Khirevich,[43] which can be easily found online.

[35] C. W. Gardiner *Handbook of stochastic methods: for physics, chemistry and the natural sciences* 2nd ed. Springer-Verlag, 1996

[36] P. Salamon, D. Fernàndez-Garcia, and J. J. Gómez-Hernández. *J. Contam. Hydrol.*, 87, pp. 277–305, 2006.

[37] F. Delay, P. Ackerer, and C. Danquigny. *Vadose Zone J.*, 4, pp. 360–379, 2005.

[38] A.D. Daus, E.O. Frind, and E.A. Sudicky. *Adv. Water Resour.*, 8, pp. 86–95, 1985.

[39] G. Liu, C. Zheng, and S. M. Gorelick. *Water Resour. Res.*, 40, W08308, 2004.

[40] M. N. Guddati and B. Yue. *Comput. Methods Appl. Mech. Eng.*, 193, pp. 275–287, 2004.

[41] P. E. Kloeden and E. Platen *Numerical solution of stochastic differential equations* Springer-Verlag, 1995

[42] S. Khirevich, A. Daneyko, and U. Tallarek "Simulation of fluid flow and mass transport at extreme scale" in: *Jülich Blue Gene/P Extreme Scaling Workshop 2010* ed. by B. Mohr and W. Frings Forschungszentrum Jülich, Jülich Supercomputing Centre, 2010

[43] S. Khirevich "High-Performance Computing of Flow, Diffusion, and Hydrodynamic Dispersion in Random Sphere Packings" PhD thesis Germany: Philipps-Universität Marburg, 2010

The simulation code used in this work originates from the works of Kandhai et al.[44–47] During the last decade, the codes were maintained and extended by my colleagues Dr. Hlushkou and Dr. Khirevich in the group of Prof. Tallarek. The last chapter of this thesis was made possible by the extension of the RWPT code for the case of porous particles (cf. Chapter 4).

Each chapter of this thesis has its own introduction section (pages 8, 28, 69, and 111) and conclusion section (pages 21, 65, 107, and 148) that present the motivation and implications of the individual studies. The concise description of the work done can be found in the conclusion part of this thesis (page 151).

[44] B. D. Kandhai "Large scale lattice-Boltzmann simulations: computational methods and applications" PhD thesis The Netherlands: University of Amsterdam, 1999
[45] D. Kandhai et al. *J. Comput. Phys.*, 150, pp. 482–501, 1999.
[46] D. Kandhai et al. *Int. J. Numer. Methods Fluids*, 31, pp. 1019–1033, 1999.
[47] D. Kandhai et al. *Phys. Rev. Lett.*, 88, p. 234501, 2002.

Chapter 1

Intrinsic Influence of the Particle Size Distribution on Hydraulic Permeability and Eddy Dispersion in Bulk Packings

Authors:

Anton Daneyko, Alexandra Höltzel, Siarhei Khirevich, and Ulrich Tallarek

State of publication:

Published April 22, 2011 in Analytical Chemistry, Vol. 83.10, pp 3903–3910
DOI: 10.1021/ac200424p

Abstract

The narrow particle size distribution (PSD) of certain packing materials has been linked to a reduced eddy dispersion contribution to band broadening in chromatographic columns. It is unclear if the influence of the PSD acts mostly on the stage of the packing process or if a narrow PSD provides an additional, intrinsic advantage to the column performance. To investigate the latter proposition, we created narrow-PSD and wide-PSD random packings based on the experimental PSDs of sub-3 μm core-shell and sub-2 μm fully porous particles, respectively, as determined by scanning electron microscopy. Unconfined packings were computer-generated with a fixed packing protocol at bed porosities from random-close to random-loose packing to simulate fluid flow and advective-diffusive mass transport in the packings' interparticle void space. The comparison of wide-PSD, narrow-PSD, and monodisperse packings revealed no systematic differences in hydraulic permeability and only small differences in hydrodynamic dispersion, which originate from a slightly increased short-range interchannel contribution to eddy dispersion in wide-PSD packings. The demonstrated intrinsic influence of the PSD on dispersion in bulk packings is negligible compared with the influence of the bed porosity. Thus, the reduced eddy dispersion observed for experimental core-shell packings cannot be attributed to a narrow PSD *per se*.

1.1 Introduction

The use of sub-2 µm[48,49] and of solid core-porous shell particles[50,51] as packing materials for high-performance liquid chromatography (HPLC) columns are two of the newer developments in separation science. Both particle types deliver higher separation efficiencies than traditional packing materials, i.e., fully porous particles of $3-5$ µm nominal diameter.

The basic idea of sub-2 µm particles is to increase the separation efficiency by reducing the particle size, albeit at the expense of increased pressure requirements, necessitating specialized equipment. The concept of core-shell particles is to improve the mass transfer kinetics (and thus the separation efficiency) by restricting intraparticle diffusion to the thin porous shell,[52,53] while maintaining the hydraulic permeability associated with the total particle diameter. Core-shell particles differ not only in their architecture from fully porous particles, but also in their particle size distributions (PSDs): Fully porous sub-2 µm particles come in broad size distributions (relative standard deviation: $20-25\%$), because traditional particle sizing methods are ineffective for these particles;[54] core-shell particles come in narrow size distributions (relative standard deviation: $5-6\%$), because the size of the solid cores as well as the thickness of the porous shell can be strictly controlled.[51] Although not part of the original concept, the narrow PSD of core-shell particles is now considered as one of their key properties and claimed to be the major cause for the outstanding separation efficiency of core-shell particle columns. The notion is that a packing material with a narrow PSD allows for a more homogeneous packing, which reduces the eddy dispersion contribution to band broadening and thus improves the separation efficiency of the column. Observations that highly efficient core-shell particle columns exhibit a significantly reduced eddy dispersion contribution to band broadening have indeed been frequently made.[50,51,55,56] Corroborating evidence for a link between the width of the PSD and column performance came from capillary columns packed with submicrometer, fully porous particles: a reduction of the relative standard deviation of the PSD from 33% to 15% effected a substantial increase in hydraulic permeability and separation efficiency of the packed capillaries.[54] But exactly *how* a narrow PSD works to achieve a more homogeneous packing and thus higher column efficiency is unclear. The effect may depend on the slurry-packing process, in which case other particle properties, such as shape, density, and surface roughness,[57,58] but also column

[48] J. R. Mazzeo et al. *Anal. Chem.*, 77, 460 A–467 A, 2005.
[49] K. D. Patel et al. *Anal. Chem.*, 76, pp. 5777–5786, 2004.
[50] J. J. Kirkland, T. J. Langlois, and J. J. DeStefano. *Am. Lab.*, 39, pp. 18–21, 2007.
[51] G. Guiochon and F. Gritti. *J. Chromatogr. A*, 1218, pp. 1915–38, 2011.
[52] A. Cavazzini et al. *Anal. Chem.*, 79, pp. 5972–9, 2007.
[53] J. O. Omamogho et al. *J. Chromatogr. A*, 1218, pp. 1942–53, 2011.
[54] J. Will Thompson, R. A. Lieberman, and J. W Jorgenson. *J. Chromatogr. A*, 1216, pp. 7732–8, 2009.
[55] J. S. Baker et al. *J. Sep. Sci.*, 33, pp. 2547–57, 2010.
[56] D. Cabooter et al. *J. Chromatogr. A*, 1217, pp. 7074–81, 2010.
[57] F. Gritti et al. *J. Chromatogr. A*, 1217, pp. 3819–43, 2010.
[58] J. O. Omamogho and J. D Glennon. *Anal. Chem.*, 83, pp. 1547–56, 2011.

dimensions,[59,60] properties of the slurry liquid, and process control parameters such as the packing pressure play a role.

Apart from the specific properties of the particles and packing process at hand, the question remains if a narrow PSD provides an *intrinsic* advantage to the column performance. A general answer to this question can only be given with the help of computer-generated packings, because this approach enables to study a certain parameter, in our case the PSD, independent from all other parameters, such as the packing process and individual particle properties. Moreover, packings can be computer-generated with high reproducibility over the full range of bed (external) porosities. This feature is indispensable to elucidate the relationship between the studied parameter and its effect on the column performance, as the bed porosity is *the* parameter on which hydraulic permeability[61] and hydrodynamic dispersion,[62,63] and thus column performance, depend first and foremost. The bed porosity of experimental packings is the result of a certain combination of packing material, column dimensions, and packing conditions.[64] Slurry-packed columns of different packing materials, e.g., core-shell and fully porous particles, are therefore necessarily compared at different bed porosities.[56,57]

We investigate if a narrow PSD provides an intrinsic advantage to the column performance by numerical simulations of hydraulic permeability and hydrodynamic dispersion in computer-generated, random packings of monodisperse, narrow polydisperse, or wide polydisperse spheres. The packings are unconfined bulk packings that mimic infinitely wide packings without walls, and the spheres are hard and impermeable (nonporous). The size distributions of the spheres in the narrow-PSD and the wide-PSD packings were modeled after the experimentally determined PSDs of sub-3 μm core-shell and sub-2 μm fully porous particles, respectively. All packings were generated over a range of bed porosities between $\varepsilon = 0.366$ and $\varepsilon = 0.46$, i.e., at densities representing the range from random-close to random-loose packing for monosized spheres.[65] The same packing protocol was followed with all packing types. This approach eliminates the influence of the slurry-packing process as well as of all particle properties other than the size distribution, and enables the comparison of monodisperse, narrow-PSD, and wide-PSD packings at equal bed porosity. The porosity-dependence of the calculated permeabilities is discussed in terms of the Kozeny-Carman model, and the dispersion behavior of the three packing types as reflected in their plate-height curves is analyzed with the comprehensive Giddings equation.[66,67]

[59] F. Gritti and G. Guiochon. *J. Chromatogr. A*, 1217, pp. 5069–5083, 2010.
[60] E. Oláh et al. *J. Chromatogr. A*, 1217, pp. 3642–53, 2010.
[61] X. Garcia et al. *Phys. Rev. E*, 80, p. 021304, 2009.
[62] R. S. Maier et al. *Water Resour. Res.*, 44, W06S03, 2008.
[63] S. Khirevich et al. *J. Chromatogr. A*, 1217, pp. 4713–4722, 2010.
[64] B. G. Yew et al. *AIChE J.*, 49, pp. 642–664, 2003.
[65] C. Song, P. Wang, and H. A. Makse. *Nature*, 453, pp. 629–632, 2008.
[66] J. C. Giddings *Dynamics of Chromatography: principles and theory* Marcel Dekker, 1965
[67] S. Khirevich et al. *Anal. Chem.*, 81, pp. 7057–7066, 2009.

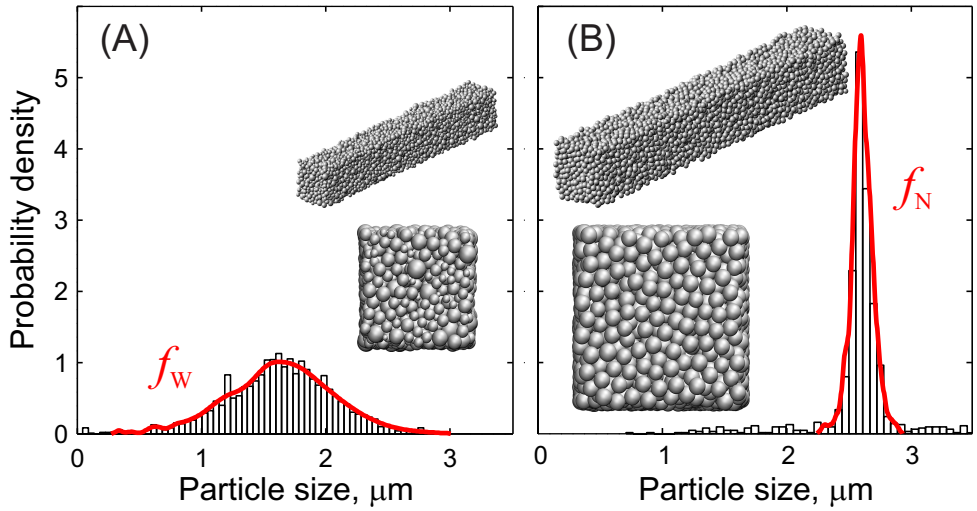

Figure 1.1: Particle size distributions (PSDs) of (A) sub-2 μm fully porous particles (wide PSD) and (B) sub-3 μm core-shell particles (narrow PSD) as experimentally determined by scanning electron microscopy. The histograms were converted into probability density functions (red curves) for the computer-generation of polydisperse random sphere packings. Computer-generated wide-PSD and narrow-PSD packings of ca. $10\,d_A \times 10\,d_A \times 70\,d_A$ (where d_A is the number-mean diameter of the PSD) at a bed porosity of $\varepsilon = 0.366$ are shown as insets.

1.2 Experimental and numerical methods

1.2.1 Particle size distributions

The particle size distributions (PSDs) of porous-shell 2.6 μm Kinetex particles (Phenomenex, Torrance, CA) and of fully porous 1.7 μm Acquity particles (Waters, Milford, MA) were determined with a JSM-7500F scanning electron microscope (JEOL, Eching, Germany). Of Kinetex particles (C_{18}, endcapped, carbon load: 12%; core: 1.9 μm, shell: 0.35 μm, pore size: 100 Å) 44 images were acquired, from which 976 particle diameters were measured. Of Acquity particles (BEH 300 C_{18}, endcapped, carbon load: 18%; pore size: 300 Å) 93 images were acquired, from which 2608 particle diameters were measured. The experimental data (histograms) were converted into smooth, continuous probability density functions f_N (narrow PSD) and f_W (wide PSD) using the kernel density estimation method with Gaussian kernel and restriction to positive values.[68] Experimental PSDs and resulting probability density functions are shown in Figure 1.1. Sets of random numbers to represent the sphere diameters in the computer-generated polydisperse packings were generated from the probability density functions f_N and f_W with an acceptance-rejection method.[69]

[68] A. W. Bowman and A. Azzalini *Applied Smoothing Techniques for Data Analysis: The Kernel Approach with S-Plus Illustrations* Oxford University Press, 1997

[69] J. E. Gentle *Random Number Generation and Monte Carlo Methods* 2nd ed. Springer, 2003

1.2.2 Computer-generation of sphere packings

Unconfined, isotropic, random packings of hard, impermeable spheres at six bed porosities ($\varepsilon = 0.366, 0.38, 0.40, 0.42, 0.44, 0.46$) were generated with a modified Jodrey-Tory algorithm as described previously.[70,71] Packing dimensions of ca. $10\ d_\mathrm{A} \times 10\ d_\mathrm{A} \times 70\ d_\mathrm{A}$, where d_A is the number-mean diameter of the PSD, were chosen to avoid recorrelation artifacts that are observed when the representative domain is too small.[72] The longest packing dimension is along the superficial flow direction (Figure 1.1). For each packing type and porosity, ten individual packings were generated. The results shown in the figures represent the average from ten packings of the same type and porosity, while confidence intervals (95%) reflect the differences between these packings.

1.2.3 Simulation of fluid flow

Low-Reynolds-number flow of an incompressible fluid in the interstitial void space of the generated packings was simulated by the lattice-Boltzmann method using the BGK-collision operator and the D3Q19 lattice as described earlier.[73] The uniform pressure gradient driving the flow was substituted by an equivalent body-force gradient.[74] The generated packings were spatially discretized to obtain a cubic grid at a resolution of 60 nodes/d_A. At the solid-liquid interface (i.e., the spheres' surfaces), a halfway bounce-back rule was applied to implement the no-slip flow-velocity boundary condition.[75] Because the bounce-back rule may introduce a significant error to pore-scale simulations, if the value of the lattice-viscosity differs from $1/6$,[76] we used this value in the simulations. The flow velocity field inside a packing was first calculated at a low Reynolds number ($\mathrm{Re} = 0.005$) and then linearly rescaled[77] to cover the whole velocity range used in the simulations of hydrodynamic dispersion.

1.2.4 Simulation of advection-diffusion

Mass transport was simulated using a random-walk particle-tracking technique,[78] where a large number of inert, point-like tracers is distributed randomly and uniformly throughout the packing void space, and then the time evolution of the tracer coordinates due to fluid flow and molecular (Brownian) motion is monitored. The transient dispersion coefficient $D_\alpha(t)$ along a direction α

[70] S. Khirevich et al. *Anal. Chem.*, 79, pp. 9340–9349, 2007.
[71] S. Khirevich et al. *Anal. Chem.*, 81, pp. 4937–4945, 2009.
[72] R. S. Maier et al. *Phys. Fluids*, 12, pp. 2065–2079, 2000.
[73] S. Khirevich, A. Höltzel, and U. Tallarek. *Philos. Trans. R. Soc. A*, 369, pp. 2485–93, 2011.
[74] P. M. Adler, M. Zuzovsky, and H. Brenner. *Int. J. Multiphase Flow*, 11, pp. 387–417, 1985.
[75] M. A. Gallivan et al. *Int. J. Numer. Methods Fluids*, 25, pp. 249–263, 1997.
[76] C. Pan, L.-S. Luo, and C. T. Miller. *Comput. Fluids*, 35, pp. 898–909, 2006.
[77] M. R. Schure et al. *Anal. Chem.*, 74, pp. 6006–6016, 2002.
[78] J. A. Rudnick and G. D. Gaspari *Elements of the random walk: an introduction for advanced students and researchers* Cambridge University Press, 2004

is determined from

$$D_\alpha(t) = \frac{1}{2N}\frac{\mathrm{d}}{\mathrm{d}t}\sum_{i=1}^{N}\left(\Delta r_{\alpha,i}(t) - \langle \Delta r_\alpha(t)\rangle\right)^2; \tag{1.1}$$

where $\Delta r_{\alpha,i}(t) \stackrel{\text{def}}{=} r_{\alpha,i}(t) - r_{\alpha,i}(0)$, $r_{\alpha,i}(t)$ is the α-coordinate of a given tracer i, N is the number of tracers ($N = 5 \times 10^5$), and $\langle \Delta r_\alpha(t)\rangle$ is the displacement along the direction α averaged over the whole tracer ensemble. Advective displacement of a tracer was calculated using the velocity vector from the nearest lattice node, assuming constant fluid velocity over a lattice voxel. A multiple rejection scheme was implemented to restrict tracer movement to the interparticle void (fluid) space of the packings.[79] Diffusive displacement of a tracer follows a Gaussian distribution in each spatial coordinate with zero mean and a variance of $(2\,D_\mathrm{m}\delta t)^{1/2}$, where D_m is the tracer diffusion coefficient in bulk solution and δt is the simulation time step.

Longitudinal and transverse dispersion coefficients, $D_\mathrm{L}(t)$ and $D_\mathrm{T}(t)$, were calculated with equation (1.1) along and transverse to the flow direction, respectively. In unconfined random sphere packings, the longitudinal dispersion coefficient attains its long-time (asymptotic) limit after a time span of $2-2.5\,\tau_\mathrm{D}$, where τ_D is the transverse dispersive time defined as $\tau_\mathrm{D} = 2\,d_\mathrm{T}t/d_\mathrm{A}$ (with D_T as the asymptotic transverse dispersion coefficient).[67] The transverse dispersive time unit corresponds to the time span after which tracer particles are dispersed laterally by one sphere diameter. Asymptotic values of the longitudinal dispersion coefficient D_L were calculated as the average value over the time span $2 - 2.5\,\tau_\mathrm{D}$ (Figure 1.6, Supporting Information, Section 1.5).

The programs for simulations of fluid flow and mass transport were implemented in C/C++ languages using the MPI standard.[80] Simulations took 250 hours on 1024 processor cores of a BlueGene/P system (JUGENE at Forschungszentrum Jülich, Germany).

1.3 Results and discussion

1.3.1 Generation of polydisperse sphere packings

Figure 1.1 shows the PSDs that were determined by scanning electron microscopy for 1.7 µm fully porous particles (wide PSD) and for 2.6 µm core-shell particles (narrow PSD). Of the various statistical moments that can be calculated for PSDs, we will refer to the number-mean diameter $d_\mathrm{A} = \Sigma\, n_i\, d_{\mathrm{p},i}/\Sigma\, n_i$ and the surface-mean or Sauter diameter $d_\mathrm{S} = \Sigma\, n_i\, d_{\mathrm{p},i}^3/\Sigma\, n_i\, d_{\mathrm{p},i}^2$. The narrow PSD of the core-shell particles contains particle diameters between 2.3 and 2.9 µm, has a relative standard deviation of 3.4%, and closely spaced number-mean and surface-mean diameters of $d_\mathrm{A} = 2.60$ µm and $d_\mathrm{S} = 2.61$ µm, respectively (Table 1.1). We took great care to establish the experimental PSD for the 1.7 µm particles: To cover the relatively wide size range

[79] P. Szymczak and A. J. C. Ladd. *Phys. Rev. E*, 68, p. 036704, 2003.

[80] W. Gropp and A. Lusk E. Skjellum *Using MPI: Portable Parallel Programming with the Message-Passing Interface* 2nd ed. MIT Press, 1999

with a representative number of particles, 2608 particle diameters were measured. The wide PSD covers particle diameters from 0.30 to 2.79 µm and has a relative standard deviation of 25.3%; its number-mean diameter ($d_\mathrm{A} = 1.64$ µm) is smaller than its surface-mean diameter ($d_\mathrm{S} = 1.83$ µm).

For computer-generation of random sphere packings, we converted the histograms into continuous probability density functions f_W and f_N (red curves in Figure 1.1) such that the relevant statistical properties of the experimental PSDs were conserved (Table 1.1). Based on the two probability density functions, f_W and f_N, two types of polydisperse packings, a wide-PSD and a narrow-PSD type, respectively, were generated with the Jodrey-Tory algorithm at bed porosities of $\varepsilon = 0.366 - 0.46$. Examples of the two generated packing types (at $\varepsilon = 0.366$) are shown in Figure 1.1 as front view onto the packing cross-section of ca. $10\ d_\mathrm{A} \times 10\ d_\mathrm{A}$ and as side view onto the longest packing dimension of ca. $70\ d_\mathrm{A}$, which is the macroscopic flow direction in our simulations. The respective width of the two PSDs is well reflected in the appearance of the generated packing types.

1.3.2 Grid resolution

For simulations of fluid flow in the interstitial void space of the packings with the lattice-Boltzmann method, packings are discretized with a simulation grid. The accuracy of the simulation results depends on the grid resolution, which in turn affects the required amount of computational resources. For monodisperse packings, a grid resolution of 30 nodes/d_A is sufficient.[81] For polydisperse packings, the appropriate grid resolution depends on the number and diameter of the smallest spheres in the PSD.[72] We evaluated the effect of the grid resolution on the numerical simulation results by calculating the flow velocity field at grid resolutions between 10 and 90 nodes/d_A. For evaluation we chose the densest of the wide-PSD packings ($\varepsilon = 0.366$), because it contains the smallest sphere diameters and also the smallest voids and should therefore be the most sensitive packing towards grid resolution. The Darcy permeability K_D was calculated from the pressure drop over packing length ($\Delta P/L$) *via* $K_\mathrm{D} = \eta u_\mathrm{sf}/(\Delta P/L)$, where η is the dynamic viscosity of the fluid and u_sf is the superficial flow velocity. The Darcy permeability was then equated with the Kozeny-Carman permeability K_KC, defined as

$$K_\mathrm{KC} = \frac{\varepsilon^3}{(1-\varepsilon)^2}\frac{d_\mathrm{S}^2}{f_\mathrm{KC}} \quad , \tag{1.2}$$

to calculate the Kozeny-Carman constant f_KC, assumed as $f_\mathrm{KC} \approx 180$ for packed beds.[82,83] With increasing grid resolution, the calculated Kozeny-Carman constants approach an asymptotic value close to $f_\mathrm{KC} = 180$ (Figure 1.2). The calculated value does not increase discernibly beyond a grid resolution of 60 nodes/d_A, which is why we judged this resolution as best compromise between accuracy and required computational resources.

[81] D. Kandhai et al. *Philos. Trans. R. Soc. A*, 360, pp. 521–534, 2002.
[82] F. A. L. Dullien *Porous media: fluid transport and pore structure* 2nd ed. Academic Press, 1992
[83] P. C. Carman *Flow of Gases Through Porous Media* Academic Press, 1956

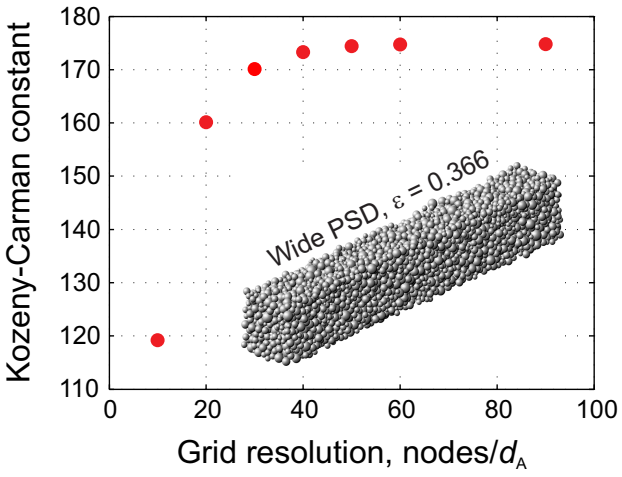

Figure 1.2: Kozeny-Carman constant f_{KC} as a function of the simulation grid resolution (nodes per d_{A}, the number-mean diameter of the PSD) for the densest wide-PSD packing ($\varepsilon = 0.366$). Each point is averaged over 10 different packings, error bars are comparable with the symbol size.

1.3.3 Hydraulic permeability

For comparison between the packing types, the calculated Darcy permeabilities K_{D} were normalized by the square of the surface-mean diameter.[82,83] Figure 1.3A displays the reduced permeabilities $K_{\mathrm{D}}/d_{\mathrm{S}}^2$ of the two polydisperse packing types along with those of a monodisperse packing that was generated with the same generation algorithm and parameters as the polydisperse packings, but from monosized spheres. The reduced hydraulic permeabilities of all three packing types are presented in Figure 1.3A as neatly collapsed data over the whole porosity range. The average value from all packing types at each porosity was taken to fit the data to the Kozeny-Carman equation (1.2), by equating Darcy with Kozeny-Carman permeability ($K_{\mathrm{D}} = K_{\mathrm{KC}}$) and using f_{KC} as a fitting parameter. The fit gave a value of $f_{\mathrm{KC}} = 172.2$ with a correlation coefficient of $R^2 = 0.9995$.

Because the hydraulic permeability of packed beds depends first and foremost on the bed porosity, the large span of $K_{\mathrm{D}}/d_{\mathrm{S}}^2$-values in Figure 1.3A obliterates small differences between the packing types. To decide if a systematic influence of the PSD exists, we calculated f_{KC} separately for each packing type and porosity (Figure 1.3B). The differences in f_{KC} displayed by the packing types in Figure 1.3B are random and in average smaller than the differences between individual packings of the same type and porosity as reflected by the wide, overlapping confidence intervals. The data in Figure 1.3A and Figure 1.3B demonstrate that the hydraulic permeability of bulk random sphere packings depends on the surface-mean diameter (d_{S}), but not on the width of the PSD.

With increasing bed porosity, the calculated Kozeny-Carman constants in Figure 1.3B deviate more from the targeted value of $f_{\mathrm{KC}} = 180$. In the Kozeny-Carman model, the porous medium is a one-dimensional version of a bundle of twisted, nonintersecting capillaries with constant diameter, and f_{KC} is proportional to the hydraulic tortuosity factor.[82,83] But a fixed f_{KC}-value neglects

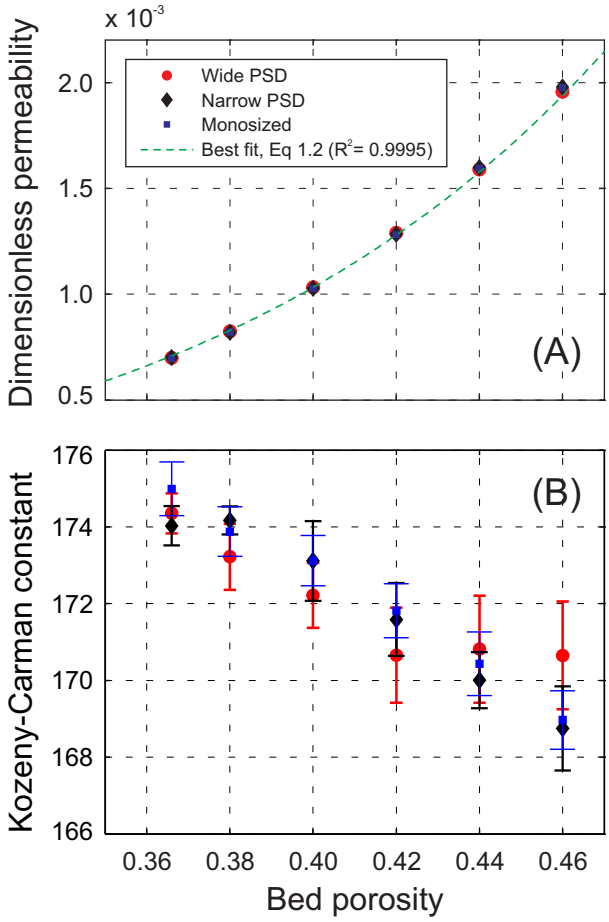

Figure 1.3: (A) Hydraulic permeabilities normalized by the square of the surface-mean diameter, $K_{\mathrm{D}}/d_{\mathrm{S}}^2$, as a function of bed porosity ε for wide-PSD, narrow-PSD, and monodisperse packings. The dashed green line represents the best fit of the data averaged over the three packing types to the Kozeny-Carman equation (eq. (1.2)). (B) Kozeny-Carman constant f_{KC} as a function of ε calculated with eq. (1.2).

that the tortuosity of a real, three-dimensional porous medium depends on its porosity.[84–86] Thus, the decrease of f_{KC} observed in Figure 1.3B may reflect that for the three investigated packing types the hydraulic tortuosity is a decreasing function of bed porosity. If hydraulic tortuosity is imagined as the average crookedness of the flow paths in a packing, a decrease of the hydraulic tortuosity in looser packings, where more void space is available so that the average flow path is less crooked than in dense packings, appears reasonable. The porosity-dependence of the calculated obstruction factors, which are the inverse of the diffusive tortuosity, for the three packing types also support this assumption (Figure 1.7).

1.3.4 Hydrodynamic dispersion

Longitudinal asymptotic dispersion coefficients D_{L} were calculated for a range of reduced velocities $\nu = u_{\mathrm{av}} d_{\mathrm{S}}/D_{\mathrm{m}}$ of $\nu = 0.5 - 750$ and converted into plate heights H *via* $D_{\mathrm{L}} = H u_{\mathrm{av}}/2$,[66] where u_{av} is the average flow velocity and $D_{\mathrm{m}} = 1.56 \times 10^{-9} m^2/s$, as estimated for anthracene in acetonitrile at 295 K.[87] For normalization of fluid velocity ($\nu = u_{\mathrm{av}} d_{\mathrm{S}}/D_{\mathrm{m}}$) and plate height data ($h = H/d_{\mathrm{S}}$), we chose the surface-mean diameter (d_{S}) rather than the number-mean diameter (d_{A}). Whereas the use of d_{S} in connection with the permeability is unquestioned, because in laminar flow the viscous drag on a spherical particle is proportional to the surface area orthogonal to the flow direction,[88] normalization of plate-height curves by d_{S} requires explanation. The pore-scale velocity non-uniformity of the flow field in the interparticle void space of a packing is caused by the no-slip (zero velocity; liquid stick) boundary condition at the spheres' surfaces. Therefore, the surface area has an impact on the flow field and on the eddy dispersion contribution that originates from the non-uniformity of the flow field. Normalization by d_{S} ensures that the packings are compared under the condition of equal total surface area. In fact, the dispersion regime for a bed of *nonporous* spheres in the velocity range of ca. $5 < \nu < 300$ is referred to as the "boundary-layer dispersion regime" in recognition of the presence and importance of the viscous boundary layer at the spheres' surfaces, in which mass transport normal to the surface is diffusion-limited.[89–91] We note for clarity that for *porous* particles the volume-mean diameter could be better suited for normalization of plate height data, due to the dominating contribution of the intraparticle mass transfer resistance to the overall plate height at higher reduced flow velocities.[47]

The use of the surface-mean diameter caused a grouping of the plate-height curves of all

[84] H. L. Weissberg. *J. Appl. Phys.*, 34, pp. 2636–2639, 1963.
[85] E. Mauret and M. Renaud. *Chem. Eng. Sci.*, 52, pp. 1807–1817, 1997.
[86] M. Barrande, R. Bouchet, and R. Denoyel. *Anal. Chem.*, 79, pp. 9115–9121, 2007.
[87] F. Gritti et al. *J. Chromatogr. A*, 1217, pp. 1589–603, 2010.
[88] R. F. Probstein *Physicochemical hydrodynamics* Wiley, 1994
[89] D. L. Koch and J. F. Brady. *J. Fluid Mech.*, 154, pp. 399–427, 1985.
[90] S. G. Weber and P. W. Carr "High Performance Liquid Chromatography" in: ed. by P. R. Brown and R. A. Hartwick John Wiley & Sons, 1989 chap. 1
[91] M. Sahimi *Flow and transport in porous media and fractured rock: From classical methods to modern approaches* Wiley-VCH, 1995
[47] D. Kandhai et al. *Phys. Rev. Lett.*, 88, p. 234501, 2002.

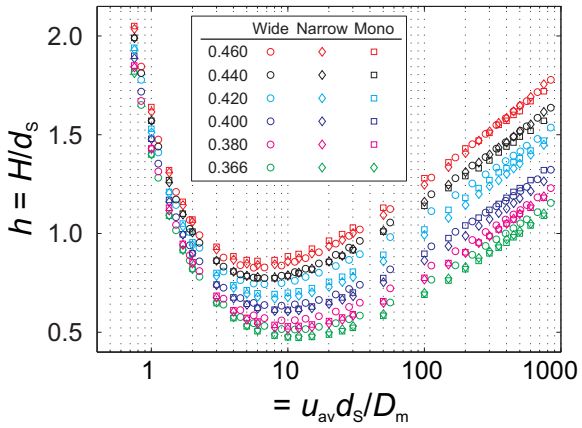

Figure 1.4: Comparison of reduced plate-height curves for wide-PSD, narrow-PSD, and monodisperse packings at bed porosities of $\varepsilon = 0.366 - 0.46$ (ε as indicated) . Plate heights and velocities are normalized by the surface-mean diameter, and $D_\mathrm{m} = 1.56 \times 10^{-9} m^2/s$.

three packing types according to porosity (Figure 1.4), whereas normalization by the number-mean diameter d_A did not yield unified plate-height curves (Figure 1.8). This is an important point, because d_S and d_A of the narrow PSD are nearly equal, but d_S of the wide PSD is larger than d_A (Table 1.1). Thus, comparing wide-PSD and narrow-PSD packings by plate height data normalized by d_A puts wide-PSD packings at a disadvantage. The minima of the plate height curves for the two polydisperse packing types range from $h_\mathrm{min} = 0.5$ and $\nu_\mathrm{min} = 10$ (wide PSD) or 11 (narrow PSD) at $\varepsilon = 0.366$ to $h_\mathrm{min} = 0.9$ and $\nu_\mathrm{min} = 5$ (wide PSD) or 6 (narrow PSD) at $\varepsilon = 0.46$. The small h_min-values result from our model of unconfined (bulk) packings of nonporous particles and the use of nonadsorbing tracers, where the wall effects, intraparticle mass transport, and retention contributions of experimental packings[92,93] are absent, to allow the investigation of eddy dispersion in the interparticle void space with the best possible selectivity and precision.

Closer inspection of Figure 1.4 reveals that the plate-height curves of the wide-PSD packings may show an upward deviation from the well-united plate-height curves of the narrow-PSD and monodisperse packings. But the observed differences in plate heights are small. At a bed porosity of $\varepsilon = 0.38$ – a conservative estimate for well-packed HPLC columns – the difference at the plate height minimum is only 8%, which leaves the advantage of a narrow over a wide PSD too small to be noticed in chromatographic practice. Furthermore, columns packed with sub-2 µm particles typically have bed porosities of $\varepsilon \leq 0.38$, sometimes even as low as $\varepsilon = 0.35 - 0.36$,[94] whereas columns packed with core-shell particles more often have bed porosities of $\varepsilon = 0.40 - 0.43$.[51] If we compare a wide-PSD packing at $\varepsilon = 0.38$ with a narrow-PSD packing at $\varepsilon = 0.40$ in Figure 1.4, the advantage of the lower bed porosity already outweighs that of the narrow PSD.

[92] U. D. Neue *HPLC columns: theory, technology, and practice* Wiley-VCH, 1997
[93] G. Guiochon et al. *Fundamentals of Preparative and Nonlinear Chromatography* Elsevier, 2006
[94] D. Cabooter et al. *J. Chromatogr. A*, 1178, pp. 108–117, 2008.

1.3.5 Eddy dispersion contribution to band broadening

To investigate the origin of the small differences between wide-PSD and narrow-PSD packings observed in Figure 1.4, we analyzed the individual contributions to band broadening by fitting the reduced plate-height data to a condensed form of the comprehensive Giddings equation,[66] which considers only those contributions to band broadening that are experienced by the nonadsorbing tracer in our computer-generated bulk packings of nonporous particles.[63,67]

$$h = \frac{2\gamma}{\nu} + \frac{2\lambda_1}{1+\left(\frac{2\lambda_1}{\omega_1}\right)\nu^{-1}} + \frac{2\lambda_2}{1+\left(\frac{2\lambda_2}{\omega_2}\right)\nu^{-1}}. \tag{1.3}$$

The first term in equation (1.3) is the contribution from longitudinal diffusion in the packing and contains the obstruction factor $\gamma = D_{\mathrm{eff}}/D_{\mathrm{m}}$, which relates the effective (asymptotic) diffusion coefficient of a tracer in the packing (D_{eff}) to the diffusion coefficient of this tracer in bulk solution (D_{m}). The second and third term in equation (1.3) consider the eddy dispersion contributions to band broadening that originate from inhomogeneities of the flow field (Figure 1.9): the second term (*index* 1) refers to a velocity inhomogeneity across the individual flow channels between adjacent particles (transchannel contribution), whereas the third term (*index* 2) covers the flow maldistribution on a lateral length scale of $1-2$ particle diameters (short-range interchannel contribution). Whereas transchannel equilibration is required in any packed bed, ordered or random, the short-range interchannel contribution is associated with the disorder of a random compared with an ordered sphere packing, but also reflects individual degrees of disorder between different random packings.[63,67] Additional flow heterogeneities on a larger lateral length scale as present in confined packings (transcolumn contribution) are absent from our bulk packings. Please note that the use of nonporous particles and nonadsorbing tracers in our packings also eliminates the classical velocity-proportional mass transfer contribution to band broadening.

The obstruction factor γ was calculated for each packing type and porosity from the respective effective diffusion coefficients observed in the long-time limit in simulations of mass transport without flow ($\nu = 0$) (Figure 1.7). For fitting the reduced plate height data to equation (1.3), γ was held fixed at the calculated value. The complete set of reduced plate-height curves for wide-PSD, narrow-PSD, and monodisperse packings as well as the best fits of these curves to equation (1.3) are available in Figure 1.10.

The values for the universal structural parameters λ_1, λ_2, ω_1, and ω_2 that we received from these fits are shown in Figure 1.5. Systematic differences between the three packing types only emerge for λ_2, where the wide-PSD packings deviate from the narrow-PSD and monodisperse packings. All other variations between the packing types with respect to the four structural parameters are random, and therefore due to statistical variations in the arrangement of the individual particles in a packing, not to differences in their PSDs. The λ_1-values are scattered around $\lambda_1 \approx 0.45$, close to the value of $\lambda_1 \approx 0.5$ predicted by Giddings.[66] This parameter reflects the longitudinal length scale on which the flow velocity inequality between center and edge of

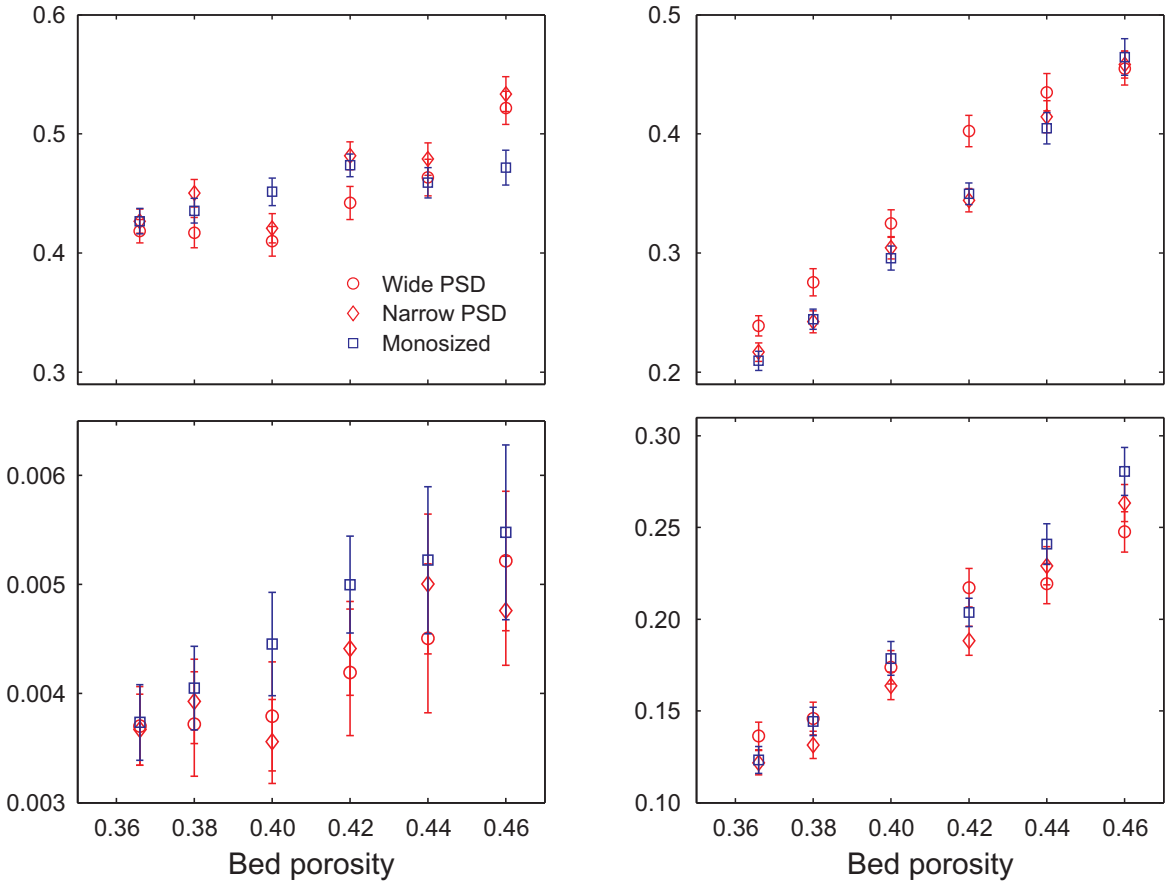

Figure 1.5: Structural parameters characterizing the eddy dispersion contribution to band broadening originating from flow inhomogeneities at the transchannel scale (λ_1 and ω_1) and at the short-range interchannel scale (λ_2 and ω_2). Data were received from fits of the reduced plate-height curves normalized by the surface-mean diameter (Figure 1.4) to equation (1.3) (see also Figure 1.10). The confidence intervals (95%) represent the quality of these fits.

a single pore persists before the flow stream splits up into several subsequent pores down the packing. λ_1 was shown to be insensitive towards variations of packing generation parameters that affect packing microstructure.[63] As λ_1 is neither influenced by the PSD nor the packing microstructure, a value of $\lambda_1 \approx 0.45$ appears to be a general property of random sphere packings in the investigated porosity range. ω_1 depends on the lateral pore dimensions and thus increases with the bed porosity. However, the overall impact of ω_1 is negligible due to its very small values ($0.003 < \omega_1 < 0.006$). The velocity range in which a certain eddy dispersion term reaches half of its maximum value and thereafter begins to flatten noticeably is indicated by the reduced transition velocity $\nu_{1/2,i} = 2\lambda_i/\omega_i$.[66] The reduced transition velocity for the transchannel contribution is estimated at ca. $\nu_{1/2,1} = 2 \times 0.45/0.0045 = 200$, i.e., it raises slowly over most of the velocity range shown in Figure 1.4 and reaches its full potential only at high velocities, which are outside the operational range in chromatography ($5 < \nu < 20$) and even beyond realization with experimental packings and equipment.

The parameters characterizing the short-range interchannel contribution to eddy dispersion, λ_2 and ω_2, both increase monotonously with the bed porosity, which reflects the fact that a looser random packing is more disordered on a short-range scale than a denser one, where the restricted available space narrows the possibilities for sphere placement.[63] The ω_2-values for all three packing types are neatly collapsed in a range of $0.1 < \omega_2 < 0.3$, whereas the λ_2-values show a small, but systematic upward deviation of the wide-PSD packings, immediately reminiscent of their plate-height curves in Figure 1.4. λ_2 characterizes the longitudinal length scale, on which flow inequalities that exist over a lateral length scale of $1-2$ particle diameters persist in a packing, before being leveled out in (and by) the flow field.[66] According to Figure 1.5, the packing microstructure over the short-range scale is less homogeneous in wide-PSD than in narrow-PSD or monodisperse packings, which explains the slightly elevated plate-height curves for the wide-PSD packings in Figure 1.4. Experimental values for λ_2 provided by Gritti et al.[57] and Gritti and Guiochon[95] for core-shell particle columns all fall within our simulated range of $0.2 < \lambda_2 < 0.5$: they determined $\lambda_2 = 0.20$ and $\lambda_2 = 0.35$ for columns packed with 2.6 µm Kinetex-C_{18} particles (100×4.6 mm) and with 2.7 µm Halo-C_{18} particles (150×4.6 mm), respectively;[57] and later $\lambda_2 = 0.30$ and $\lambda_2 = 0.40$ for 150×4.6 mm columns packed with 2.6 µm Kinetex-C_{18} particles and with 2.7 µm Halo-C_{18} particles, respectively.[95] All columns had external (bed) porosities around $\varepsilon = 0.40$. For a narrow-PSD packing at this bed porosity, our simulations predict $\lambda_2 = 0.32$. Experimental λ_2-values for columns packed with Acquity particles are not yet documented in the literature.

Apart from revealing the cause for the slightly raised plate height data of the wide-PSD packings, Figure 1.5 also shows that the three packing types have essentially the same porosity-dependence of their structural parameters (λ_i, ω_i). When we previously studied hydrodynamic dispersion in monodisperse random sphere packings created to possess different degrees of microstructural heterogeneity through systematic variation of packing generation parameters, we found that a packing's degree of microstructural heterogeneity has a large impact on its

[95] F. Gritti and G. Guiochon. *Chem. Eng. Sci.*, 65, pp. 6327–6340, 2010.

hydrodynamic dispersion behavior.[63] The dispersion coefficient of more disordered packings is not only larger than that of less disordered (i.e., more homogeneous) packings at equal bed porosity, but also increases more strongly with the bed porosity. We may therefore infer from the collapsed curves in Figure 1.5 that the generated wide-PSD, narrow-PSD, and monodisperse packing types possess highly similar packing-scale disorder, as was intended through using identical packing generation parameters for all three packing types. When we previously analyzed the individual eddy dispersion contributions for monodisperse packings of different packing-scale disorder,[63] we found larger deviations in the structural parameters than observed between polydisperse and monodisperse packings in Figure 1.5 as well as an individual porosity-dependence of the structural parameters for each packing type. Thus, compared with packing generation parameters that determine the packing-scale disorder of the bulk sphere packings, the width of the PSD exerts only a small influence on the eddy dispersion contribution to band broadening.

1.4 Conclusions

Through numerical simulations in computer-generated monodisperse, narrow-PSD, and wide-PSD bulk random packings of hard, impermeable spheres we have investigated the intrinsic influence of the PSD on hydraulic permeability and hydrodynamic dispersion. The mass transport properties of a packing are determined by its microstructure, which for computer-generated packings depends on the algorithm and parameters used for their generation, not on the underlying PSD. Contrariwise, the microstructure or morphology of experimental packings cannot be reproduced from different PSDs. This underlines the importance of computational methods to investigate an individual parameter, in this case the PSD, independent from other relevant parameters, whose influences are inseparable in experimental packings.

Our simulation results reflect independence from the underlying PSD for the hydraulic permeability of the bulk packings, but a small influence of the PSD on hydrodynamic dispersion. Wide-PSD packings can exhibit slightly raised plate heights compared with narrow-PSD and monodisperse packings. Analysis of the individual eddy dispersion contributions to band broadening according to Giddings revealed an increased short-range interchannel contribution as the cause, suggesting that the microstructure in wide-PSD packings on a scale of $1-2$ particle diameters is less homogeneous than in narrow-PSD or monodisperse packings. In principle, this observation reflects a slight intrinsic advantage of a narrow PSD with respect to hydrodynamic dispersion in bulk packings. The effect of the PSD width on the plate height curves, however, is negligible compared with the influence of the bed porosity and also too small to be noticed in chromatographic practice.

Our simulations have shown that the reduced eddy dispersion reported for columns packed with core-shell particles cannot result from the intrinsic (i.e., unrelated to the packing process) advantage of a narrow PSD. This is all the more intriguing, because these columns often combine low eddy dispersion with a rather high bed porosity. According to our results, the homogeneity of core-shell columns must be clearly superior to those of densely packed columns of fully porous

particles to overcome the disadvantages of high bed porosity. The answer to why core-shell particle columns have low eddy dispersion lies probably in the unraveling of the experimental column packing process.[64] For this challenge the physical reconstruction of column packings and the derivation of appropriate statistical parameters that describe the packing morphology appears promising,[96] because a direct link between the experimental parameters of the slurry-packing process and the properties of the final packing microstructure might thus be established.

Acknowledgement

This work was supported by the Deutsche Forschungsgemeinschaft DFG (Bonn, Germany) under grant TA 268/5. We thank Stefan Bruns (Department of Chemistry, Philipps-Universität Marburg) for the experimental particle size distributions, and the DEISA Consortium (www.deisa.eu), co-funded through the EU FP6 project RI-031513 and the FP7 project RI-222919, for support within the DEISA Extreme Computing Initiative.

1.5 Supporting Information

Table 1.1: Statistical properties of the experimentally determined particle size distributions (PSDs) for sub-2 µm fully porous particles (wide PSD) and for sub-3 µm core-shell particles (narrow PSD) and of the corresponding probability density functions f_W and f_N derived from the experimental PSDs.

	Wide PSD 1.7µm fully porous particles	f_W	Narrow PSD 2.6µm core-shell particles	f_N
Number of measured particle diameters	2608	–	976	–
Number-mean diameter (d_A)	1.64	1.64	2.60	2.60
Surface-mean diameter (d_S)	1.83	1.84	2.61	2.61
Relative standard deviation	25.3%	25.9%	3.4%	3.4%
Minimum diameter	0.30	0.27	2.27	2.24
Maximum diameter	2.79	3.01	2.90	2.93
Quantiles $d_{10}/d_{50}/d_{90}$	1.10/1.64/2.16	1.09/1.65/2.17	2.50/2.60/2.71	2.50/2.60/2.71

[96] S. Bruns and U. Tallarek. *J. Chromatogr. A*, 1218, pp. 1849–60, 2011.

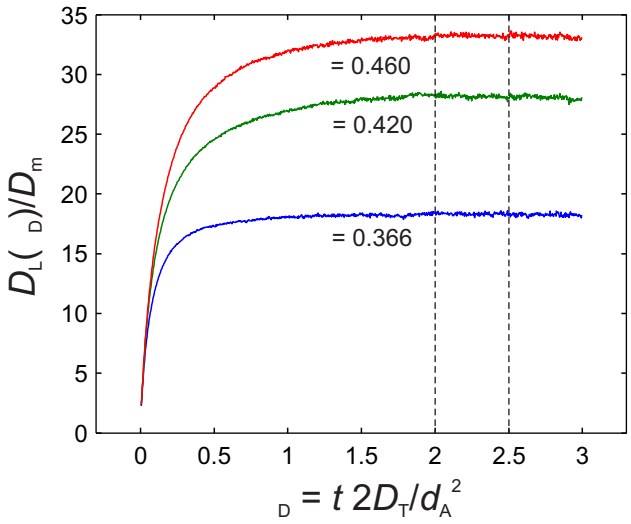

Figure 1.6: Transient behavior of the normalized longitudinal dispersion coefficient $D_{\mathrm{L}}(\tau_{\mathrm{D}})/D_{\mathrm{m}}$ monitored at a reduced flow velocity of $\nu = 50$ as a function of transverse dispersive time $\tau_{\mathrm{D}} = tD_{\mathrm{T}}/d_{\mathrm{A}}^2$ (with D_{T}, the asymptotic transverse dispersion coefficient and d_{A}, the number-mean diameter of the PSD) for the wide-PSD packings at selected bed porosities ε. Dashed lines indicate the interval from which the asymptotic value D_{L} was calculated. Each curve represents the average of ten individual packings of the same type and porosity.

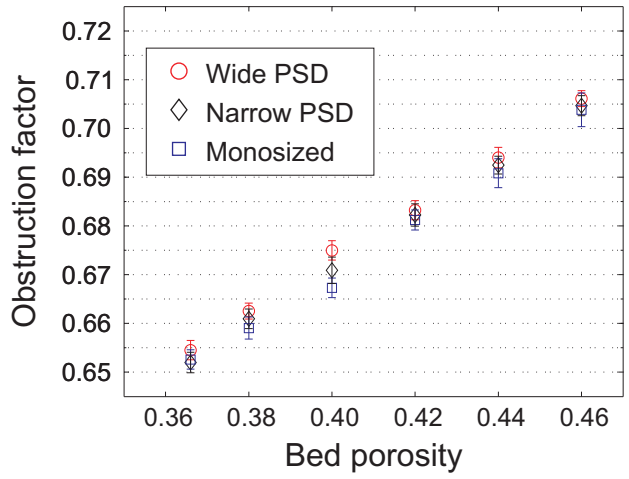

Figure 1.7: Obstruction factor $\gamma = D_{\mathrm{eff}}/D_{\mathrm{m}}$ as a function of bed porosity ε for wide-PSD, narrow-PSD, and monodisperse packings. D_{eff} is calculated from the asymptotic limit of the transient diffusion coefficient at simulations of mass transport without flow, and $D_{\mathrm{m}} = 1.56 \times 10^{-9} m^2/s$.

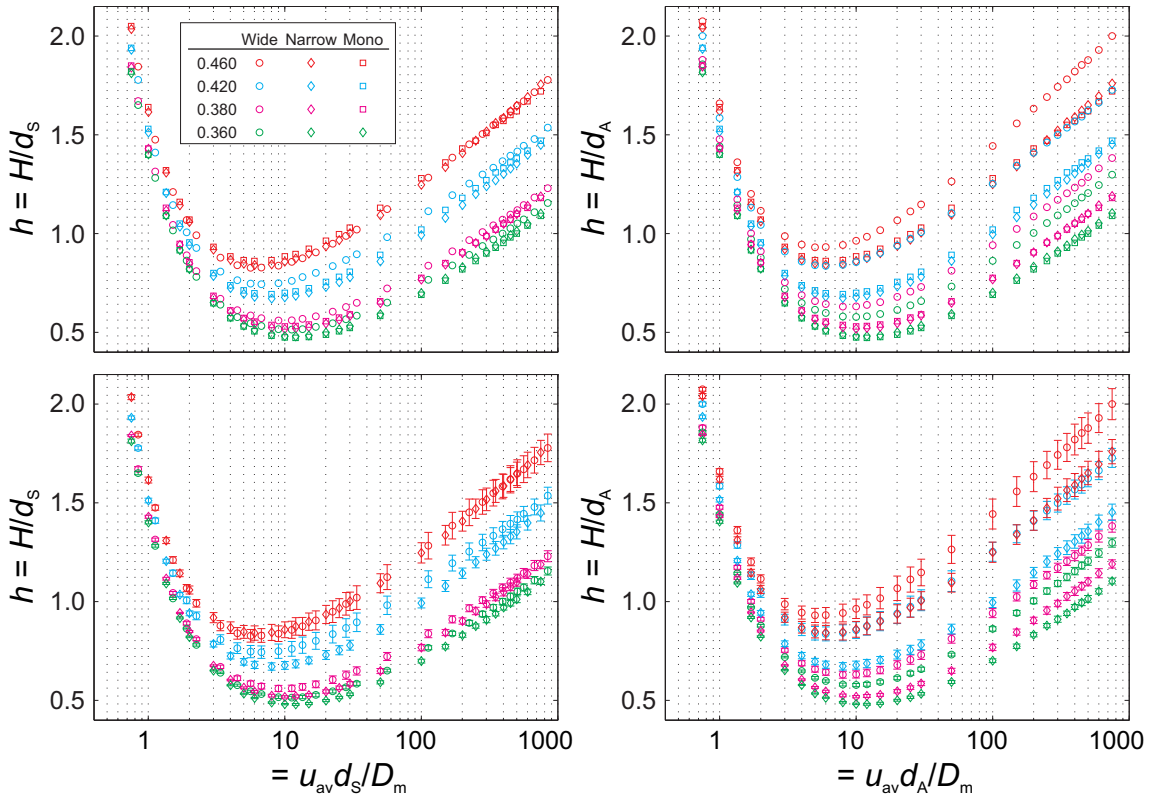

Figure 1.8: Comparison of reduced plate-height curves of the wide-PSD, narrow-PSD, and monodisperse packings at selected bed porosities (ε as indicated). Plate heights and velocities are normalized by the surface-mean diameter d_{S}(left) or the number-mean diameter d_{A} (right), and $D_{\mathrm{m}} = 1.56 \times 10^{-9} m^2/s$. The bottom row repeats the data from the top row, but with the confidence intervals added.

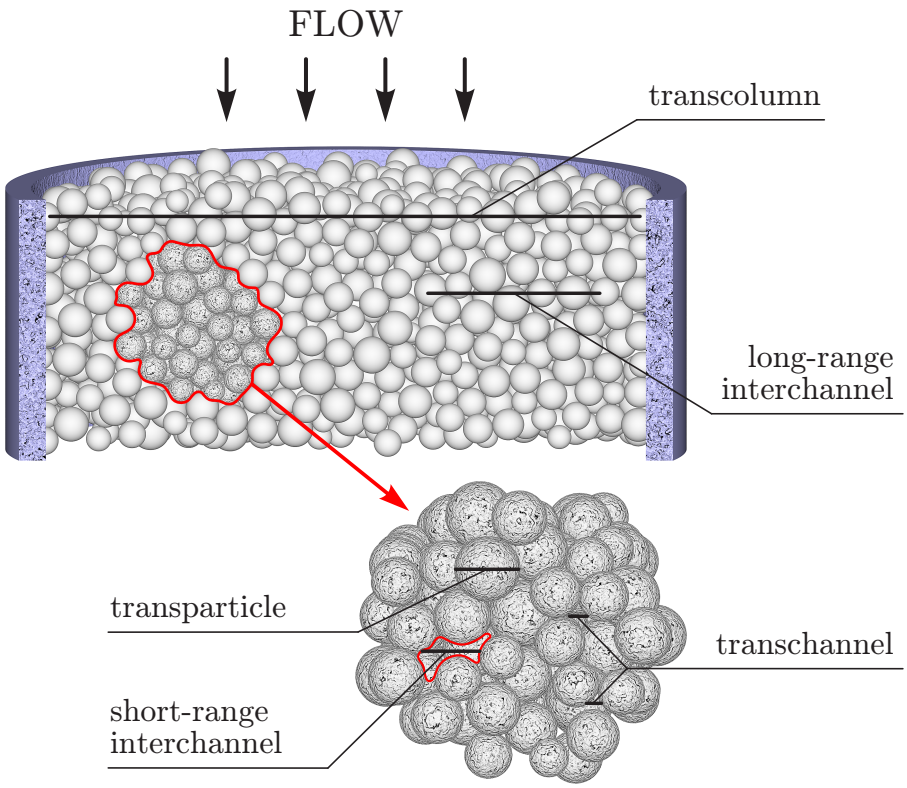

Figure 1.9: Velocity inhomogeneities that contribute to eddy dispersion in confined particle-packed beds according to Giddings. The *transchannel* contribution arises from the transverse distribution of velocities inside each individual channel between particles. The *short-range interchannel* contribution is due to the existence of small groups of tightly packed particles between which more loosely packed regions are found. Fluctuations of local packing density cause this pattern of tightly packed groups of particles interspersed by loosely packed regions to be erratic, which results in the *long-range interchannel* contribution. The existence of systematic variations of the mobile phase velocity between different regions of the column, i.e., in the core and the wall regions, is responsible for the *transcolumn* contribution. A fifth contribution mentioned by Giddings as a source of velocity bias is the *transparticle* contribution, which exists in beds of porous particles. This effect should not be taken into account as an eddy dispersion term, however, as it is actually the strict equivalent of the intraparticle pore diffusion mechanism (the flowing mobile phase does not affect pore diffusion inside the particles). The figure is reproduced with permission of Dr. Khirevich.[43]

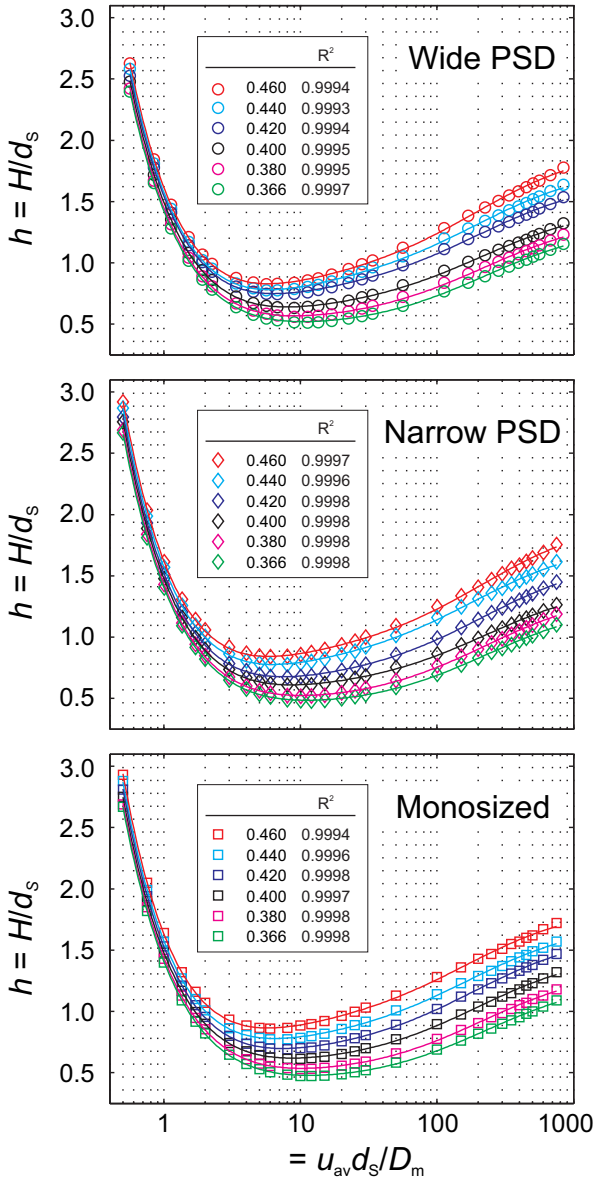

Figure 1.10: Best fits of the reduced plate-height curves of the wide-PSD (top), narrow-PSD (middle), and monodisperse (bottom) packings at bed porosities of $\varepsilon = 0.366 - 0.46$ to equation (1.3).

Chapter 2

From random sphere packings to regular pillar arrays: Effect of the macroscopic confinement on hydrodynamic dispersion

Authors:

Anton Daneyko, Siarhei Khirevich, Alexandra Höltzel, Andreas Seidel-Morgenstern, and Ulrich Tallarek

State of publication:

Published September 21, 2011 in Journal of Chromatography A, Vol. 1218.45, pp 8231–48
DOI: 10.1016/j.chroma.2011.09.039

Abstract

Flow and mass transport in bulk and confined chromatographic supports comprising random packings of solid, spherical particles and hexagonal arrays of solid cylinders (regular pillar arrays) are studied over a wide flow velocity range by a numerical analysis scheme, which includes packing generation by a modified Jodrey-Tory algorithm, three-dimensional flow field calculations by the lattice-Boltzmann method, and modeling of advective-diffusive mass transport by a random-walk particle-tracking technique. We demonstrate the impact of the confinement and its cross-sectional geometry (circular, quadratic, semicircular) on transient and asymptotic transverse and longitudinal dispersion in random sphere packings, and also address the influence of protocol-dependent packing disorder and the particle-aspect ratio. Plate height curves are analyzed with the Giddings equation to quantify the transcolumn contribution to eddy dispersion. Confined packings are compared with confined arrays under the condition of identical bed porosity, conduit cross-sectional area, and laterally fully equilibrated geometrical wall and corner effects on dispersion. Fluid dispersion in a regular pillar array is stronger affected by the macroscopic confinement and does not resemble eddy dispersion in random sphere packings, because

the regular microstructure cannot function as a mechanical mixer like the random morphology. Giddings' coupling theory fails to preserve the nature of transverse dispersion behind the arrays' plate height curves, which approach a linear velocity-dependence as transverse dispersion becomes velocity-independent. Upon confinement this pseudo-diffusive behavior can outweigh the performance advantage of the regular over the random morphology.

2.1 Introduction

The presence of a macroscopic confinement for any microscopically regular or random porous medium implies at least two fundamental time and length scales behind longitudinal dispersion with respect to the lateral equilibration of an analyte or a passive tracer in the nonuniform flow velocity field: the pore (short-time) scale and the macroscopic confinement (long-time) scale.[67,97] According to Giddings,[66] these scales reflect the transchannel and the transcolumn contribution to eddy dispersion, respectively. The effect of the confinement on dispersion (hereafter referred to as transcolumn contribution, regardless of the actual format of the confinement, i.e., cylindrical column or noncylindrical conduit) depends on the ratio of two lengths, one characteristic of the conduit cross-section and the other of the porous medium. For a particulate bed confined in the classical column format, for example, it is the ratio of column and particle diameter, referred to as particle-aspect ratio.

Hydrodynamic dispersion in cylindrically confined random sphere packings at low particle-aspect ratio (≤ 20) is a topic with a long tradition in chemical engineering.[98] For such packings eddy dispersion is dominated by the geometrical wall effect,[67,97,99] which describes the effects of the inability of spherical particles to form a close packing against the locally flat and hard surface of the column wall on the resulting lateral (external) porosity and velocity distributions. The first particle layer of the bed in contact with the wall is not only highly ordered, but also differs from subsequent layers, because the interstitial space between wall and first layer cannot be partially occupied by other particles. In subsequent particle layers (i.e., with increasing distance from the wall) the degree of microstructural order relaxes towards the packing bulk. The lateral external porosity profile of the packing starts at the wall with large oscillations, whose amplitudes decrease over a distance of a few (~ 5) particle diameters to a value associated with bulk behavior.[100–103] The short-ranged geometrical wall effect is distinct from a second and more extended wall effect,

[67] S. Khirevich et al. *Anal. Chem.*, 81, pp. 7057–7066, 2009.
[97] R. S. Maier et al. *Phys. Fluids*, 15, pp. 3795–3815, 2003.
[66] J. C. Giddings *Dynamics of Chromatography: principles and theory* Marcel Dekker, 1965
[98] J. M. P. Q. Delgado. *Heat Mass Transfer*, 42, pp. 279–310, 2006.
[99] M. Giese, K. Rottschäfer, and D. Vortmeyer. *AIChE J.*, 44, pp. 484–490, 1998.
[100] A. J. Sederman, P. Alexander, and L. F. Gladden. *Powder Technol.*, 117, pp. 255–269, 2001.
[101] A. de Klerk. *AIChE J.*, 49, pp. 2022–2029, 2003.
[102] J. Theuerkauf, P. Witt, and D. Schwesig. *Powder Technol.*, 165, pp. 92–99, 2006.
[103] G. E. Mueller. *Powder Technol.*, 203, pp. 626–633, 2010.

traditionally discussed in connection with much larger particle-aspect ratios (> 100).[104–106] The latter is related to the compressibility of pulverulent materials and the complex distribution of axial and radial stress during compression of the bed.[64] During the slurry-packing process, the friction between the particles, the resulting radial stress that forces the particles against the wall, and the friction between bed and wall,[104] effect a higher packing density near the wall (but beyond the $\sim 5\ d_\mathrm{p}$-distance from the wall that is governed by the geometrical wall effect) than in the core. As a consequence of this "frictional wall effect", external porosity and permeability are higher in the core than in the near-wall region, and a heterogeneous radial velocity profile develops. Under general conditions both wall effects (geometrical and frictional) influence the morphology of a confined packing, but depending on the actual particle-aspect ratio either wall effect may dominate hydrodynamic dispersion behavior.[96,105]

The geometrical wall effect was envisioned early in the chromatographic literature[107] and later carefully studied by Li et al.[108] in supercritical fluid chromatography and by Jorgenson and co-workers in capillary HPLC[49,109,110] with particle-packed cylindrical fused-silica capillaries. For example, Kennedy and Jorgenson[109] and subsequently Hsieh and Jorgenson[110] have shown that the performance of capillaries packed with 5 µm particles improves significantly when decreasing the capillary diameter from 50 to 12 µm. At these low particle-aspect ratios, the packed bed morphology is dominated by the geometrical wall effect; because the small column diameter does not enable full relaxation of the ordered wall region into bulk behavior, the packing is effectively more ordered and homogeneous over the whole conduit cross-section.

Packed beds with low particle-aspect ratios have shifted into the focus of research, since the "omics" era, requiring fast analysis of small amounts of complex samples, triggered the ongoing trend for miniaturization.[111–113] Liquid chromatography was successfully miniaturized in the form of nanoflow and microchip HPLC;[114–118] particle-aspect ratios of $10 - 20$ are typical, because downsizing of conduit dimensions is not accompanied by a similar reduction of particle size.[119,120]

[104] G. Guiochon, E. Drumm, and D. Cherrak. *J. Chromatogr. A*, 835, pp. 41–58, 1999.
[105] R. A. Shalliker, B. S. Broyles, and G. Guiochon. *J. Chromatogr. A*, 888, pp. 1–12, 2000.
[106] R. A. Shalliker et al. *J. Chromatogr. A*, 977, pp. 213–223, 2002.
[64] B. G. Yew et al. *AIChE J.*, 49, pp. 642–664, 2003.
[96] S. Bruns and U. Tallarek. *J. Chromatogr. A*, 1218, pp. 1849–60, 2011.
[107] J. H. Knox and J. F. Parcher. *Anal. Chem.*, 41, pp. 1599–1606, 1969.
[108] W. Li et al. *J. Microcolumn Sep.*, 8, pp. 259–268, 1996.
[49] K. D. Patel et al. *Anal. Chem.*, 76, pp. 5777–5786, 2004.
[109] R. T. Kennedy and J. W. Jorgenson. *Anal. Chem.*, 61, pp. 1128–1135, 1989.
[110] S. Hsieh and J. W. Jorgenson. *Anal. Chem.*, 68, pp. 1212–1217, 1996.
[111] P. S. Dittrich and A. Manz. *Nat. Rev. Drug Discovery*, 5, pp. 210–218, 2006.
[112] D. Janasek, J. Franzke, and A. Manz. *Nature*, 442, pp. 374–80, 2006.
[113] A. Ríos et al. *TrAC-Trend. Anal. Chem.*, 25, pp. 467–479, 2006.
[114] G. P. Rozing. *LC-GC Eur.*, 16, pp. 14–19, 2003.
[115] J. Hernández-Borges et al. *J. Sep. Sci.*, 30, pp. 1589–1610, 2007.
[116] J. M. Saz and M. L. Marina. *J. Sep. Sci.*, 31, pp. 446–458, 2008.
[117] D. Tao et al. *Anal. Bioanal. Chem.*, 399, pp. 229–41, 2011.
[118] K. Faure. *Electrophoresis*, 31, pp. 2499–511, 2010.
[119] S. Jung et al. *J. Chromatogr. A*, 1216, pp. 264–273, 2009.
[120] S. Ehlert, T. Rösler, and U. Tallarek. *J. Sep. Sci.*, 31, pp. 1719–1728, 2008.

Therefore, the geometrical wall effect is important to eddy dispersion in microchip packings as well as the cylindrical fused-silica capillaries used in nano-HPLC. An additional challenge of microchip HPLC is the noncylindrical conduit format for the chromatographic bed. The cross-sectional geometry of a microfluidic channel is mainly determined by the materials and methods used in its fabrication. Separation channels with approximately semicircular,[121,122] elliptical,[123] quadratic,[124] rectangular,[125,126] bell-shaped,[127] or trapezoidal cross-sections[128–133] are found on recent HPLC-microchips, and deviations from ideal geometry, such as introduced by curved sides, rough edges, and irregularly-angled corners, are the rule. Due to the pressure limitations of most microchips, the slurry-packing of these noncylindrical microchannels is a technological problem, but has been solved previously to yield dense beds (average external porosity around $\varepsilon = 0.40$).[134] The presence of corners in a noncylindrical conduit as well as the symmetry decrease of the cross-section, if its geometry deviates from a circle, increase eddy dispersion in a microchip packing relative to a cylindrical capillary packing.[70,71,119,135] Low particle-aspect ratios and noncylindrical conduits are therefore the main points of investigation for the effect of the confinement on eddy dispersion in miniaturized chromatographic packings.

Because the quality of their preparation is less affected by the downsized conduit dimensions, monolithic beds or regular pillar arrays often substitute for particulate packings on HPLC-microchips.[136,137] Organic polymer-based monolithic beds are simply prepared by carrying out the one-step polymerization reaction directly in the microchannel.[118,126,129,131,138–142] The photolithographic etching of a regular array of pillar columns into a microchip[136,137,143–145] requires

[121] I. M. Lazar, P. Trisiripisal, and H. A. Sarvaiya. *Anal. Chem.*, 78, pp. 5513–5524, 2006.
[122] K. W. Ro, J. Liu, and D. R. Knapp. *J. Chromatogr. A*, 1111, pp. 40–47, 2006.
[123] D. S. Reichmuth, T. J. Shepodd, and B. J. Kirby. *Anal. Chem.*, 77, pp. 2997–3000, 2005.
[124] Y. Yang et al. *Lab Chip*, 5, pp. 869–876, 2005.
[125] A. Bhattacharyya and C. M. Klapperich. *Anal. Chem.*, 78, pp. 788–792, 2006.
[126] J. Liu et al. *Anal. Chem.*, 81, pp. 2545–2554, 2009.
[127] S. Jung et al. *Anal. Chem.*, 81, pp. 10193–10200, 2009.
[128] H. Yin et al. *Anal. Chem.*, 77, pp. 527–533, 2005.
[129] A. Ishida et al. *J. Chromatogr. A*, 1132, pp. 90–98, 2006.
[130] C.-Y. Shih et al. *J. Chromatogr. A*, 1111, pp. 272–278, 2006.
[131] J. Liu et al. *Int. J. Mass Spectrom.*, 259, pp. 65–72, 2007.
[132] J. F. Borowsky et al. *Anal. Chem.*, 80, pp. 8287–8292, 2008.
[133] M. T. Koesdjojo, C. R. Koch, and V. T. Remcho. *Anal. Chem.*, 81, pp. 1652–1659, 2009.
[134] S. Ehlert et al. *Anal. Chem.*, 80, pp. 5945–5950, 2008.
[70] S. Khirevich et al. *Anal. Chem.*, 79, pp. 9340–9349, 2007.
[71] S. Khirevich et al. *Anal. Chem.*, 81, pp. 4937–4945, 2009.
[135] S. Khirevich et al. *Lab Chip*, 8, pp. 1801–1808, 2008.
[136] D. S. Peterson. *Lab Chip*, 5, pp. 132–139, 2005.
[137] M. De Pra, W. Th. Kok, and P. J. Schoenmakers. *J. Chromatogr. A*, 1184, pp. 560–572, 2008.
[138] K. W. Ro, R. Nayak, and D. R. Knapp. *Electrophoresis*, 27, pp. 3547–3558, 2006.
[139] D. A. Mair et al. *Lab Chip*, 6, pp. 1346–1354, 2006.
[140] P. A. Levkin et al. *J. Chromatogr. A*, 1200, pp. 55–61, 2008.
[141] M. Vázquez and B. Paull. *anal chim acta*, 668, pp. 100–13, 2010.
[142] I. Nischang, O. Brueggemann, and F. Svec. *Anal. Bioanal. Chem.*, 397, pp. 953–60, 2010.
[143] W. De Malsche et al. *Anal. Chem.*, 79, pp. 5915–5926, 2007.
[144] F. Detobel et al. *Anal. Chem.*, 82, pp. 7208–17, 2010.
[145] L. C. Taylor, N. V. Lavrik, and M. J. Sepaniak. *Anal. Chem.*, 82, pp. 9549–56, 2010.

substantially more fabrication efforts, followed by post-processing to yield porous pillars with chemical surface modifications, essential for the capacity and selectivity of HPLC separations. Regular pillar arrays benefit from a microscopically ordered geometry, which decreases fluid dispersion in unconfined arrays compared with unconfined particulate beds. The latter are bulk random sphere packings, which possess a microscopic disorder on the scale of $1 - 2\,d_{\mathrm{p}}$ that translates to a short-range interchannel contribution to eddy dispersion,[67] in addition to the transchannel dispersion inherent to all porous media, regular or random. But the concept of regular pillar arrays as spatially porous media has to be altered, when these are used as chromatographic supports, because the inevitable confinement engenders a macroscopic heterogeneity, which will affect the dispersion behavior and thus the efficiency of the array for HPLC separations.

Whereas the influence of transcolumn velocity gradients of various origins on eddy dispersion in packed columns is well known,[49,64,66,67,96–110,146–148] the precise nature of how the microstructure of a packed bed, local disorder, and the geometry of the confinement affect the flow heterogeneity, transverse equilibration as well as macroscopically resulting longitudinal dispersion, and how it interrelates with the velocity-dependent transverse rate of mass transfer is still largely unresolved. In this work, we investigate how a macroscopic confinement affects the dispersion behavior and ultimately the separation efficiency of particulate packings and regular pillar arrays at conduit dimensions and geometrical properties that reflect those in capillary and microchip HPLC practice. We employ explicit or direct numerical simulations,[91] where all important transport phenomena and parameters, including the volumetric representation of the morphology of the studied system, are considered explicitly rather than using a meanfield or average procedure. Besides reproducing experimental column behavior, direct numerical simulations of flow and transport have been instrumental in identifying key structure-transport relationships in chromatographic media[63,67] and to analyze the effect of relevant parameters, such as particle size and shape, particle size distribution, intraparticle porosity and associated diffusion-limited transport, bed density, packing disorder and defects, as well as column dimensions and

[146] G. Guiochon. *J. Chromatogr. A*, 1126, pp. 6–49, 2006.
[147] E. Vandre et al. *AIChE J.*, 54, pp. 2024–2028, 2008.
[148] F. Gritti and G. Guiochon. *AIChE J.*, 56, pp. 1495–1509, 2010.
[91] M. Sahimi *Flow and transport in porous media and fractured rock: From classical methods to modern approaches* Wiley-VCH, 1995
[63] S. Khirevich et al. *J. Chromatogr. A*, 1217, pp. 4713–4722, 2010.

cross-sectional geometry, on the hydrodynamic properties of fixed beds.[47,62,63,67,70–73,77,97,135,149–159] Transient dispersion is easily recorded, which allows to quantify (i) the time and length scales behind the long-time (asymptotic) limit of dispersion, and (ii) the flow velocity-dependence of longitudinal and transverse asymptotic dispersion coefficients.

Computer-generated random packings of monosized, solid (nonporous), spheres at a bed (average external) porosity of $\varepsilon = 0.40$ confined in conduits of circular, rectangular, and semicircular cross-section serve as examples for miniaturized particulate packings. We vary the confinement geometry at constant cross-sectional area, and the microstructural heterogeneity (introduced through the packing protocol) as well as the particle-aspect ratio (20 and 10) for cylindrically confined packings. The comparison with bulk packings (which mimic infinitely wide random sphere packings without confinement) enables a clear-cut distinction of the effects introduced by the confinement on the various eddy dispersion contributions. An extensive set of longitudinal dispersion coefficients collected over a wide range of reduced flow velocities ($0.5 \leq \nu \leq 500$) provides plate height curves for analysis with the comprehensive Giddings equation. The observation of asymptotic dispersion behavior requires complete lateral equilibration over the conduit cross-section, which, in turn, necessitates sufficiently extended packings in the longitudinal (macroscopic flow) direction. The required packing length increases with the average flow velocity, but also depends on the cross-sectional geometry of the conduit, because the presence of corners and the increased characteristic lateral distance of a noncylindrical compared with a cylindrical conduit costs additional simulation time or packing length to account for laterally fully equilibrated wall and corner effects on dispersion. The size of the generated cylindrical and noncylindrical packings, with a length on the order of 10^3 particle diameters, and the studied velocity range (four orders of magnitude) necessary to obtain a good fit to the Giddings equation, relegate the numerical simulations to the large-scale category performed on supercomputers. The dispersion behavior of confined random sphere packings is compared with those of hexagonal arrays of solid (nonporous), cylindrical pillars. Starting from an unconfined

[47] D. Kandhai et al. *Phys. Rev. Lett.*, 88, p. 234501, 2002.
[62] R. S. Maier et al. *Water Resour. Res.*, 44, W06S03, 2008.
[72] R. S. Maier et al. *Phys. Fluids*, 12, pp. 2065–2079, 2000.
[73] S. Khirevich, A. Höltzel, and U. Tallarek. *Philos. Trans. R. Soc. A*, 369, pp. 2485–93, 2011.
[77] M. R. Schure et al. *Anal. Chem.*, 74, pp. 6006–6016, 2002.
[149] B. Manz, L. F. Gladden, and P. B. Warren. *AIChE J.*, 45, pp. 1845–1854, 1999.
[150] M. D. Mantle, A. J. Sederman, and L. F. Gladden. *Chem. Eng. Sci.*, 56, pp. 523–529, 2001.
[151] R. S. Maier et al. *Philos. Trans. R. Soc. A*, 360, pp. 497–506, 2002.
[152] M. R. Schure et al. *J. Chromatogr. A*, 1031, pp. 79–86, 2004.
[153] D. Hlushkou, A. Seidel-Morgenstern, and U. Tallarek. *Langmuir*, 21, pp. 6097–6112, 2005.
[154] M. R. Schure and R. S. Maier. *J. Chromatogr. A*, 1126, pp. 58–69, 2006.
[155] R. S. Maier, D. M. Kroll, and H. T. Davis. *AIChE J.*, 53, pp. 527–530, 2007.
[156] H. Bai et al. *Ind. Eng. Chem. Res.*, 48, pp. 4060–4074, 2009.
[157] R. S. Maier and R. S. Bernard. *J. Comput. Phys.*, 229, pp. 233–255, 2010.
[158] A. Daneyko et al. *Anal. Chem.*, 83, pp. 3903–10, 2011.
[159] S. Khirevich et al. *J. Chromatogr. A*, 1218, pp. 6489–97, 2011.

array, simulated as a single unit cell with periodic boundary conditions;[23,160,161] we first add top and bottom walls, and then complete the confinement by the addition of side walls. The interstitial porosity and the cross-sectional area of the arrays match the bed porosity ($\varepsilon = 0.40$) and cross-sectional area ($100\,\pi d_\mathrm{p}^2$ or $25\,\pi d_\mathrm{p}^2$), respectively, of the random sphere packings. The fully confined arrays are flat, rectangular boxes with channel width-to-height ratios typically found on microchips.

The results section starts with random sphere packings (Section 2.3.1): the transient dispersion behavior of confined sphere packings is contrasted with that of bulk sphere packings to retrieve the effect of the confinement for the studied conduit geometries; monitoring transient dispersion up to the asymptotic (long-time) limit guarantees that the derived plate height curves account for fully equilibrated wall and corner effects. This is essential to evaluate support structures of radically different morphologies, as, e.g., packings and pillar arrays, for their potential as chromatographic adsorbents. Plate height curves are analyzed with the comprehensive Giddings equation, and the effect of microstructural heterogeneity on asymptotic dispersion is discussed. Section 2.3.2 covers regular pillar arrays, and explains the differences in longitudinal dispersion behavior between random sphere packings and regular pillar arrays on the basis of their transverse dispersion behavior. Section 2.3.3 compares confined sphere packings with confined pillar arrays and quantifies the loss of separation efficiency for microscopically random and regular chromatographic supports, respectively, upon macroscopic confinement.

2.2 Numerical simulations

2.2.1 Generation of random sphere packings

Packings of monosized, solid (nonporous) spheres were generated with a modified Jodrey-Tory algorithm[67,70] at a bed porosity (interstitial void fraction) of $\varepsilon = 0.40$. Bulk (unconfined) random sphere packings had dimensions of ca. $9.53\,d_\mathrm{p} \times 9.53\,d_\mathrm{p}$ (cross-section) $\times 76.43\,d_\mathrm{p}$ (length; longitudinal direction, the macroscopic flow direction in our simulations) and periodic boundary conditions in all three directions. Confined packings (with periodic boundary conditions in the longitudinal direction) were generated in containers of $100\,\pi d_\mathrm{p}^2$ cross-sectional area and circular, rectangular (with a side-aspect ratio of 2:1), or semicircular geometry. The respective packing dimensions were ca. $20\,d_\mathrm{p}$ (cylinder diameter) $\times 6554\,d_\mathrm{p}$ (length), $25\,d_\mathrm{p} \times 12.5\,d_\mathrm{p}$ (rectangle sides) $\times 8192\,d_\mathrm{p}$, and $14.1\,d_\mathrm{p}$ (semicircle radius) $\times 8192\,d_\mathrm{p}$. Additionally, smaller cylindrical sphere packings with a particle-aspect ratio of 10 and a cross-sectional area of $25\,\pi d_\mathrm{p}^2$ were generated with dimensions of ca. $10\,d_\mathrm{p}$ (cylinder diameter) $\times 1638\,d_\mathrm{p}$ (length).

Packing density ($\varepsilon = 0.40$), confinement geometry (with circular, rectangular, or semicircular cross-section), and particle-aspect ratio are typical for miniaturized HPLC columns in capillary or microchip format. For 5µm-sized particles, a particle-aspect ratio of 20 translates to a column

[23] H. Brenner. *Philos. Trans. R. Soc. A*, 297, pp. 81–133, 1980.
[160] H. Brenner and P. M. Adler. *Philos. Trans. R. Soc. A*, 307, pp. 149–200, 1982.
[161] D. L. Koch et al. *J. Fluid Mech.*, 200, pp. 173–188, 1989.

inner diameter of 100 μm, a conservative value in capillary HPLC. The packing length of the cylindrically confined sphere packing ($6554\,d_\mathrm{p}$) would then correspond to a bed length of ~3.3 cm. Such packing dimensions are sufficient for the analysis of laterally fully equilibrated wall and corner effects on dispersion, as observed with bed lengths on the order of centimeters in chromatographic practice.

For the bulk and the cylindrically confined packings we also varied the degree of microstructural heterogeneity. The Jodrey-Tory algorithm enables independent adjustment of bed porosity and degree of heterogeneity.[43,63,159] Packing generation starts from a random distribution of sphere centers in the simulation box, where sphere overlap is typical. Each iteration includes the search for two sphere centers with a minimum pair-wise distance that defines the maximal sphere diameter at which no sphere-overlap occurs in the current configuration, followed by a symmetrical displacement of the two sphere centers up to a new distance; the displacement length is scaled by a constant α. Our modification of the Jodrey-Tory algorithm considers in the searching procedure for the distance between two nearest points also the distance between a point and the container wall, which allows the generation of packings in containers of every shape. Three packing types were generated by varying (i) the initial distribution scheme of sphere centers and (ii) the value of the constant α scaling the displacement length. Generation of R- and Rx0.001-packings started from a random and uniform distribution of sphere centers in the simulation box, whereas for Sx2-packings the simulation box was first divided into equal cubes and then each sphere center placed in a random position into a cube. The scaling constant was set to $\alpha = 0.001$ (Rx0.001), $\alpha = 1$ (R), or $\alpha = 2$ (Sx2). If a small constant for scaling the displacement length is used, sphere centers remain close to their initial positions during packing generation, which preserves the randomness of the initial distribution. Using a larger constant for scaling the displacement length yields a more homogeneous distribution of sphere centers in the final configuration. The degree of microstructural heterogeneity increases among the three packing types as Sx2 <R <Rx0.001. Confined packings with rectangular or semicircular cross-section were generated as R-packings.

Packings were discretized with a spatial resolution of 30 nodes/d_p, which is sufficient for the accurate simulation of fluid flow[81] and mass transport.[72] Discrete lattices had dimensions of ca. $286 \times 286 \times 2293$ nodes (bulk), $600 \times 600 \times 196608$ nodes (circular), $752 \times 376 \times 245760$ nodes (rectangular), $848 \times 424 \times 245760$ nodes (semicircular), and $300 \times 300 \times 49140$ nodes (small circular). We used five random realizations of each packing; results given for a packing refer to the mean calculated from its five random realizations.

2.2.2 Regular pillar arrays

Regular, hexagonal arrays of uniform, solid (nonporous) cylinders were constructed with the same bed porosity ($\varepsilon = 0.40$) as the sphere packings. Porosity (ε), unit cell width (m), and pillar

[43] S. Khirevich "High-Performance Computing of Flow, Diffusion, and Hydrodynamic Dispersion in Random Sphere Packings" PhD thesis Germany: Philipps-Universität Marburg, 2010

[81] D. Kandhai et al. *Philos. Trans. R. Soc. A*, 360, pp. 521–534, 2002.

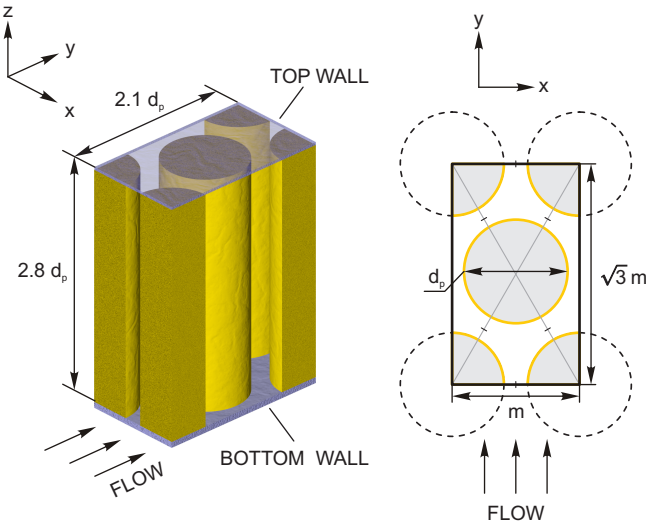

Figure 2.1: Hexagonal array of identical cylindrical pillars with a bed porosity of $\varepsilon = 0.40$. The three-dimensional unit cell with top and bottom confinement (left) was used as partially confined array (with periodic boundary conditions at the sides) and to build fully confined arrays of the desired width (x). Simulations in a bulk pillar array were performed with the two-dimensional unit cell (right). Periodic boundary conditions in the macroscopic flow direction (y) were generally used for all arrays and packings.

diameter (d_p) are related through

$$d_\mathrm{p}^2 = 2\frac{\sqrt{3}}{\pi}(1-\varepsilon)m^2, \tag{2.1}$$

as illustrated in Figure 2.1 with the two-dimensional unit cell. Simulations in a bulk array were performed in such a two-dimensional unit cell with periodic boundary conditions in x and y. The three-dimensional unit cell is shown alongside; the structure has a height (z) of $2.8\ d_\mathrm{p}$ and a length (y) of $2.1\ d_\mathrm{p}$. Simulations in a partially confined array were performed in such a unit cell with periodic boundary conditions along the sides (x) and in the macroscopic flow direction (length y), mimicking a flat configuration with wide top and bottom walls and open sides (top-bottom confinement). The fully confined pillar array was built from repetition of the three-dimensional unit cell up to the desired width (x) of $112.2 d_\mathrm{p}$ and is shown in Figure 2.2 next to the confined sphere packings. The high channel width-to-height ratio of $112.2\ d_\mathrm{p}/2.8\ d_\mathrm{p} = 40$ is typical for microfabricated pillar arrays on HPLC microchips.[143–145] Based on a particle or pillar diameter of $d_\mathrm{p} = 5$ µm, for example, the fully confined array would have a channel height of 14 µm and a channel width of 561 µm. The pillar array's cross-sectional area matches those of the confined sphere packings ($100\ \pi d_\mathrm{p}^2$). For comparison with the smaller cylindrical packing (particle-aspect ratio of 10 and cross-sectional area of $25\ \pi d_\mathrm{p}^2$), a fully confined pillar array with a correspondingly smaller width of $28.3\ d_\mathrm{p}$, but equal height ($2.8\ d_\mathrm{p}$) and length ($2.1\ d_\mathrm{p}$) than the other confined pillar arrays was built (Figure 2.3). Periodic boundary conditions in the flow direction (y) were used for all packings and arrays.

The pillar arrays were discretized with a grid resolution of 60 nodes$/d_\mathrm{p}$, i.e., twice the res-

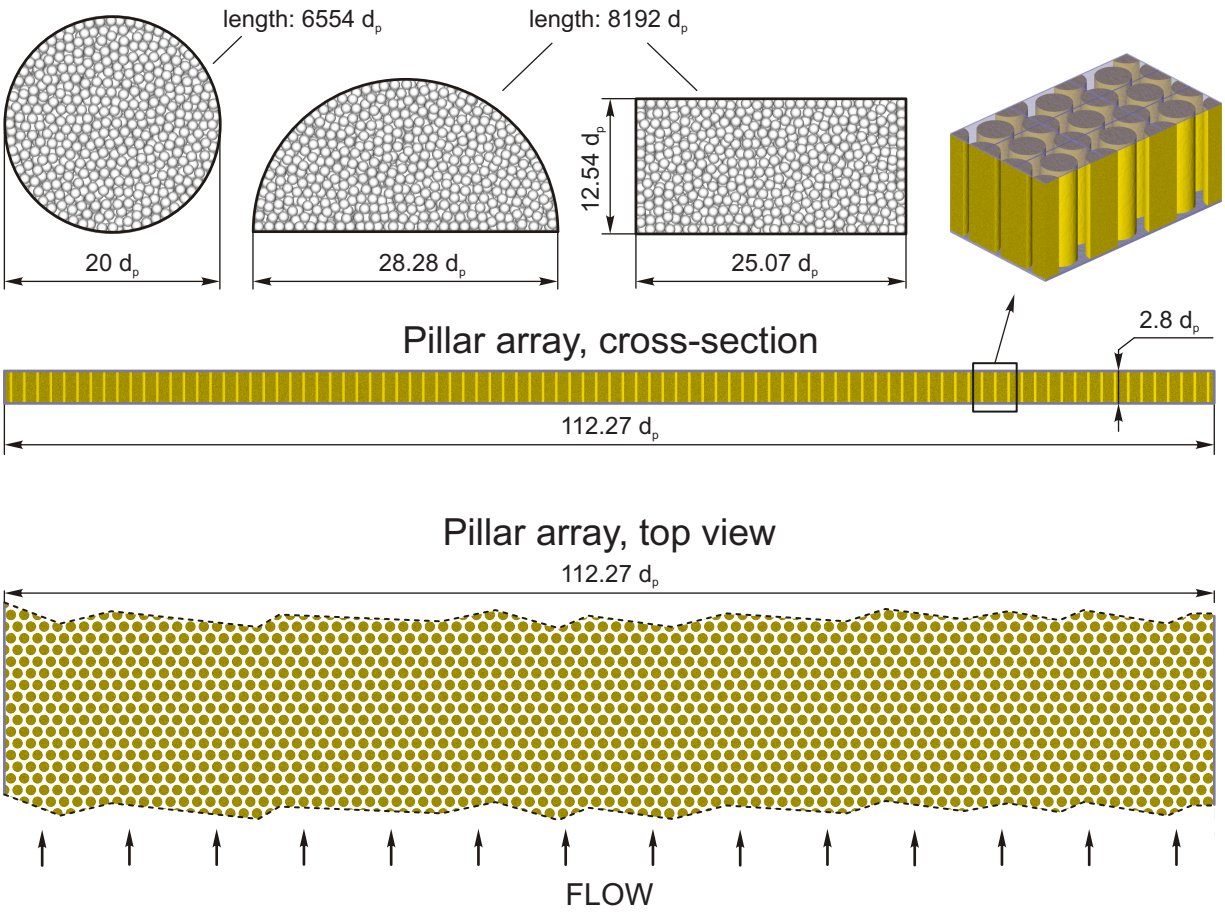

Figure 2.2: Confined chromatographic beds with a cross-sectional area of $100\,\pi d_\mathrm{p}^2$ (where d_p denotes the particle or pillar diameter) and a bed porosity of $\varepsilon = 0.40$. Shown are random sphere packings with circular (with a particle-aspect ratio of 20), rectangular, or semicircular cross-section (and dimensions as indicated) as well as the fully confined pillar array with flat, rectangular cross-section (with a channel width-to-height ratio of 40). Zoom and top view visualize the pillar array's two-dimensionally ordered, hexagonal microstructure.

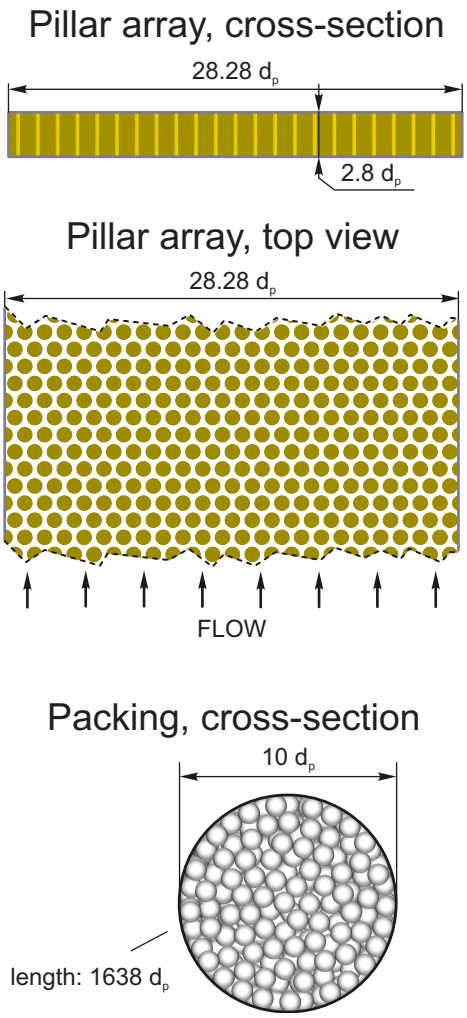

Figure 2.3: Confined chromatographic beds with a cross-sectional area of $25\,\pi d_{\mathrm{p}}^2$ (where d_{p} denotes the particle or pillar diameter) and a bed porosity of $\varepsilon = 0.40$. The cylindrical random sphere packing has a particle-aspect ratio of 10, which is also the channel width-to-height ratio of the regular pillar array's rectangular cross-section.

olution used for the random sphere packings, because calculation of dispersion coefficients for the arrays is more sensitive to the spatial resolution.[43] Discrete lattices of the representative geometrical elements (unit cells) from the pillar arrays, which were subjected to periodic boundary conditions as required in a given case, had dimensions of ca. 74×128 nodes (width x ×length y) for the bulk pillar array (two-dimensional geometry, Figure 2.1), $74 \times 128 \times 170$ nodes (width x ×length y ×height z) for the partially confined pillar array (Figure 2.1), $6736 \times 128 \times 170$ nodes for the fully confined pillar array (Figure 2.2), and $1704 \times 128 \times 169$ nodes for the small, confined pillar array (Figure 2.3).

2.2.3 Simulation of fluid flow

We consider low Reynolds number flow (Re $\sim 10^{-2}$) of an incompressible fluid in the interstitial void space of the generated sphere packings and pillar arrays. Velocity fields $\vec{u}(\vec{r})$ were simulated by the lattice-Boltzmann method (LBM).[162–165] The principal advantages of the LBM approach are its simple handling of topologically complex boundaries, such as those encountered in porous media, and its inherent parallelism that allows easy implementation of the developed numerical models at high-performance computational systems. The LBM approach is based on the connection between (i) the molecular kinetics and (ii) the phenomenological description which can be expressed in the form of the Navier-Stokes equations assuming the fluid as a continuum

$$\nabla \cdot \vec{u} = 0 \tag{2.2}$$

and

$$(\vec{u} \cdot \nabla)\, \vec{u} + \frac{\nabla p}{\rho} - \mu \nabla^2 \vec{u} = 0, \tag{2.3}$$

where p is pressure, and ρ and μ are the density and kinematic viscosity of the fluid, respectively. The kinetics of an ensemble of (in a physical sense) classical particles can be described in terms of the one-particle velocity distribution function $f(\vec{r}, \vec{v}, t)$ which defines the density of particles with velocity $\vec{v}$ around the space-time point ($\vec{r}$, t). Assuming molecular chaos, the Boltzmann equation describing the dynamics of $f(\vec{r}, \vec{v}, t)$ can be derived[166]

$$\frac{\partial f}{\partial t} + \vec{v} \cdot \nabla f = \left(\frac{\partial f}{\partial t} \right) \Big|_{\text{collision}}, \tag{2.4}$$

[162] R. Benzi, S. Succi, and M. Vergassola. *Phys. Rep.*, 222, pp. 145–197, 1992.
[163] S. Chen and G. D. Doolen. *Annu. Rev. Fluid Mech.*, 30, pp. 329–364, 1998.
[164] S. Succi *The lattice Boltzmann equation for fluid dynamics and beyond* Oxford University Press, 2001
[165] Ubertini S. et al. *Lectures on Lattice Boltzmann Methods for Complex Fluid Flows* Science4 Press, 2009
[166] S. Chapman and T. G. Cowling *The mathematical theory of non-uniform gases* 3rd ed. Cambridge University Press, 1990

where the right-hand side describes the time rate of change in $f(\vec{r},\vec{v},t)$ due to interparticle collisions (collision operator).

Only a small set of discrete particle velocities is needed to simulate the Navier-Stokes equation and much of the kinetic theory of classical particle ensembles can be represented in a discretized version.[167,168] In this version, the continuous velocity distribution function $f(\vec{r},\vec{v},t)$ is replaced by its discrete analogue $f_i(\vec{r},t)$, which defines the density of particles with a discrete velocity $\vec{e}_i$ at $(\vec{r},t)$. Particles move synchronously during time steps Δt along links of a spatial lattice. The values of the velocities $\vec{e}_i$ are chosen such that in one time step each particle moves from one lattice node to its neighbor. After every time step, the functions $f_i(\vec{r},t)$ are redistributed in lattice nodes according to the collision operator. The time evolution of $f_i(\vec{r},t)$ is described by the discrete (lattice) Boltzmann equation

$$f_i\left(\vec{r}+\vec{e}_i\Delta t,\, t+\Delta t\right) = f_i\left(\vec{r},\, t\right) + \Delta_i\left(\vec{r},\, t\right), \tag{2.5}$$

where Δ_i is the discrete interparticle collision operator. Local values of the fluid density and flow velocity are obtained from the statistical moments of the velocity distribution functions in corresponding lattice nodes:

$$\rho\left(\vec{r},\, t\right) = \sum_i f_i\left(\vec{r},\, t\right) \tag{2.6}$$

and

$$\vec{u}\left(\vec{r},\, t\right) = \sum_i \frac{\vec{e}_i f_i\left(\vec{r},\, t\right)}{\rho\left(\vec{r},t\right)}. \tag{2.7}$$

In this study, we used the so-called D3Q19 lattice, a cubic lattice with lattice spacing Δl and 18 links at each lattice node, which can be obtained by projecting the four-dimensional face-centered hypercubic lattice onto three-dimensional space.[169,170] In the D3Q19 lattice each node is connected to its six nearest and twelve diagonal neighbors. Additionally, we employ a linear BGK-collision operator[32]

$$\Delta_i = -\frac{f_i - f_i^{\mathrm{eq}}}{\tau}, \tag{2.8}$$

where τ is the relaxation time of the particle velocity distribution function to an equilibrium state f_i^{eq}. This parameter is connected with the lattice kinematic viscosity of the fluid:

$$\mu = \frac{2\tau - 1}{6}. \tag{2.9}$$

[167] U. Frisch, B. Hasslacher, and Y. Pomeau. *Phys. Rev. Lett.*, 56, pp. 1505–1508, 1986.
[168] G. R. McNamara and G. Zanetti. *Phys. Rev. Lett.*, 61, pp. 2332–2335, 1988.
[169] Rothman D. H. and Zaleski S. *Lattice-Gas Cellular Automata* Cambrige Unversity Press, 1997
[170] Y. H. Qian, D. D'Humières, and P. Lallemand. *EPL*, 17, pp. 479–484, 1992.
[32] P. L. Bhatnagar, E. P. Gross, and M. Krook. *Phys. Rev.*, 94, pp. 511–525, 1954.

By employing the Chapman-Enskog expansion, it can be shown that the equilibrium distribution

$$f_i^{\mathrm{eq}} = \rho w_i \left[1 + 3\vec{e}_i \cdot \vec{u} + \frac{9}{2}\left(\vec{e}_i \cdot \vec{u}\right)^2 - \frac{3}{2}\vec{u} \cdot \vec{u}\right], \tag{2.10}$$

with the weight coefficients

$$w_0 = \frac{1}{3}, \tag{2.11}$$

$$w_\alpha = \frac{1}{18}, \tag{2.12}$$

$$w_\beta = \frac{1}{36}, \tag{2.13}$$

properly recovers the Navier-Stokes equations.[166,171] Subscripts α and β refer, respectively, to lattice links with the nearest and diagonal neighbors, while 0 corresponds to the component of f_i^{eq} associated with the rest particles.

In our LBM simulations the uniform pressure gradient driving the flow was substituted by an equivalent body–force gradient. The validity of this approach for spatially periodic simulation domains was demonstrated by Zuzovsky et al.[172] and Adler et al.[74]; it was successfully applied by Edwards et al.[173] and Maier et al.[72]. Simulations were performed at very low lattice Mach numbers (Ma $<10^{-3}$), which minimizes the compressibility error introduced by LBM as Ma approaches $c_{\mathrm{s}} = 1/3^{1/2}$, the speed of sound in the system. A bounce-back (BB) rule[75] was employed to implement the no-slip velocity boundary condition at the solid-liquid interface (i.e., the surfaces of the solid spheres, solid cylinders, and the confinement). The lattice kinematic viscosity defined by Eq. (2.9) was set to a value of $1/6$ ($\tau = 1$). Pan et al.[76] have shown that this value gives the most accurate performance of the BB boundary condition. The lattice kinematic viscosity in Eq. (2.9) can be translated into the physical world using the spatial and temporal discretization steps (Δl and Δt) of the model by $\mu_{\mathrm{physical}} = \mu_{\mathrm{lattice}}(\Delta l)^2/\Delta t$.

The velocity field in a sphere packing or pillar array was first calculated at a low Reynolds number and then linearly rescaled,[77] relying on the properties of creeping flow (p. 48 in [66]), to cover the whole velocity range in simulations of hydrodynamic dispersion. In order to quantify the numerical error in the simulations introduced by the approximation of constant velocity

[171] X. He and L.-S. Luo. *J. Stat. Phys.*, 88, pp. 927–944, 1997.
[172] M. Zuzovsky. *Phys. Fluids*, 26, p. 1714, 1983.
[74] P. M. Adler, M. Zuzovsky, and H. Brenner. *Int. J. Multiphase Flow*, 11, pp. 387–417, 1985.
[173] D. A. Edwards et al. *Phys. Fluids A*, 2, pp. 45–55, 1990.
[75] M. A. Gallivan et al. *Int. J. Numer. Methods Fluids*, 25, pp. 249–263, 1997.
[76] C. Pan, L.-S. Luo, and C. T. Miller. *Comput. Fluids*, 35, pp. 898–909, 2006.

over a lattice voxel, we performed a detailed and computationally expensive resolution study (see [43], available online) using up to 90 grid nodes per sphere diameter for bulk packings as well as confined packings with different conduit cross-sections. This study demonstrated (i) convergence of the asymptotic longitudinal dispersion coefficient to a "grid independent" value with increasing resolution: the discretization error becomes small and the difference between resolutions of 75 and 90 nodes/d_p is less than 1%; and (ii) less than 10% error in the dispersion coefficients with the resolution used in the present work (30 nodes/d_p) relative to the highest resolution of 90 nodes/d_p over the whole simulated velocity range, from reduced velocities of 0.5 up to 500, i.e., from the diffusion-limited to the convection-dominated transport regime (cf. Figure 1.10 in Khirevich[43]).

The D3Q19 lattice requires storage of 19 lattice links per lattice node, which resulted in computer memory requirements of ca. 13 GB for bulk packings and of up to $5-6$ TB for the confined packings. Flow simulation in one realization of a confined packing required ca. 1500 LBM iterations and took ~ 0.8 hours on 16384 processor cores (cylindrical packing with particle-aspect ratio of 20, Figure 2.2) or ~ 0.4 hours on 2048 processor cores (cylindrical packing with particle-aspect ratio of 10, Figure 2.3) of a BlueGene/P system (Forschungszentrum Jülich and Rechenzentrum Garching, Germany). Flow simulation in the fully confined pillar array of Figure 2.2 required ca. 1500 LBM iterations and took ~ 0.5 hours on 1024 processor cores.

2.2.4 Simulation of advection-diffusion

Mass transport was simulated using a random-walk particle-tracking technique,[78] where a large number of inert (nonadsorbing and nonreacting), point-like tracers is distributed randomly and uniformly throughout the void space of a sphere packing or pillar array, and then the time evolution of the tracer coordinates due to fluid flow and molecular (Brownian) motion monitored. The transient hydrodynamic dispersion coefficient $D_y(t)$ along a direction y is determined from

$$D_y\left(t\right) = \frac{1}{2N}\frac{d}{dt}\sum_{i=1}^{N}\left(\Delta\vec{r}_{y,i}\left(t\right) - \left\langle\Delta\vec{r}_y\left(t\right)\right\rangle\right)^2, \tag{2.14}$$

where $\Delta\vec{r}_{y,i}(t) \overset{\mathrm{def}}{=} \vec{r}_{y,i}(t) - \vec{r}_{y,i}(0)$ and $\left\langle\Delta\vec{r}_y\left(t\right)\right\rangle$ denote the corresponding Cartesian components of the displacement of the ith tracer and the average displacement of the tracer ensemble after time t, respectively, in y-direction, and N is the number of tracers ($N = 5\times10^5$). Advective displacement of a tracer was calculated using the velocity vector from the nearest lattice node, assuming constant fluid velocity over a lattice voxel. A multiple-rejection scheme was implemented to restrict tracer movement to the void (fluid) space of the packings and pillar arrays.[79] Diffusive tracer displacement follows a Gaussian distribution in each spatial coordinate with zero mean and a variance of $(2D_m\delta\mathrm{t})^{1/2}$, where D_m is the diffusion coefficient in bulk solution and

[78] J. A. Rudnick and G. D. Gaspari *Elements of the random walk: an introduction for advanced students and researchers* Cambridge University Press, 2004

[79] P. Szymczak and A. J. C. Ladd. *Phys. Rev. E*, 68, p. 036704, 2003.

δt is the simulation time step. Longitudinal and transverse dispersion coefficients, $D_{\mathrm{L}}(t)$ and $D_{\mathrm{T}}(t)$, were calculated with Eq. (2.14) along and transverse to the macroscopic flow direction, respectively. Transient values are denoted as $D_{\mathrm{L}}(t)$ and $D_{\mathrm{T}}(t)$, while the absence of the time parameter denotes time-independence, i.e., asymptotic values, D_{L} and D_{T}, as determined from the $D(t)$-curves. We analyzed flow and dispersion for a velocity range of $0.5 \leq \nu \leq 500$, where $\nu = u_{\mathrm{av}} d_{\mathrm{p}} / D_{\mathrm{m}}$ is the reduced velocity calculated from the average velocity through a sphere packing or pillar array (u_{av}), the particle or pillar diameter (d_{p}), and the tracer diffusion coefficient in the bulk fluid (D_{m}).

The program realization of all algorithms was implemented as parallel codes in C/C++ languages using the Message Passing Interface standard.[80] Mass transport simulations were performed on 8192 processor cores of the BlueGene/P system and took about 768 hours for all confined packings. Mass transport simulations for all pillar arrays took about 600 hours on 1024 processor cores.

2.2.5 Validation of the simulation methodology

Over the last decade our modeling approach including the implementation of different (and systematically varied) packing generation protocols and a detailed study of their impact on the resulting packing microstructure, from random-close to random-loose packing of the beds, and how the resulting microstructure affects diffusion as well as fluid flow and dispersion over a wide velocity range, has been significantly developed and validated through comparison with analytical predictions, simulations, and experimental results.

In a simple case study, we simulated hydraulic flow between two parallel plates[43] and found a relative error in the flow velocity profile (compared to the analytical solution) of 0.5% using a spatial resolution of 25 nodes over the width of the channel. In a more complex case, we simulated flow through bulk random sphere packings and analyzed their hydraulic permeability as a function of the lattice spatial resolution.[81] For grid resolutions higher than ~ 25 nodes per sphere diameter we observed only a weak effect on permeability; a similar value has been given by Maier et al.[72]. Further, the absolute value of permeability agreed very well (within a few percents) with permeability values obtained from the Kozeny–Carman and Richardson–Zaki equations (cf. Figure 3 in [81]).

To compare simulated values of hydrodynamic dispersion coefficients with analytical predictions of Taylor[16] and Aris,[174] we simulated advective-diffusive mass transport between two parallel plates.[43] The relative difference between simulated and analytical values of the dispersion coefficient was 0.63%. Dispersion and mass transfer simulations in computer-generated bulk random packings of porous and nonporous spheres have also shown good agreement with experimental data obtained by pulsed magnetic-field gradient nuclear magnetic resonance (cf.

[80] W. Gropp and A. Lusk E. Skjellum *Using MPI: Portable Parallel Programming with the Message-Passing Interface* 2nd ed. MIT Press, 1999

[16] G. Taylor. *Philos. Trans. R. Soc. A*, 219, pp. 186–203, 1953.

[174] R. Aris. *Philos. Trans. R. Soc. A*, 252, pp. 538–550, 1959.

Figure 4 in [47]). Similarly, the velocity dependence of the dispersion coefficients for packed beds (described by a power law) was very close to the experimentally observed one, which is based on a large body of experimental data.[73] In closely related research, we validated our numerical simulation approach to three-dimensional electrokinetic flow and transport problems in porous media (ordered and random sphere packings as well as microfluidic channels) under general conditions, e.g., for arbitrary value and distribution of electrokinetic potential at the solid-liquid interface, electrolyte composition, and pore space morphology, by good agreement with results that have been either predicted theoretically, or obtained by alternative numerical methods.[153,175–177]

More recently, we reported systematic studies and derived correlations on the effect of the particle size distribution, packing density (bed porosity), and packing generation protocol on the resulting packing microstructure (degree of heterogeneity) and the observed transport behavior (diffusion, dispersion).[63,158,159] In particular, the diffusive tortuosities simulated for ordered sphere packings approached the analytical solution and the diffusive tortuosities simulated for random sphere packings reproduced the Weissberg equation;[159] Weissberg's equation was derived theoretically and has found corroboration from a number of experiments and simulations. Most striking, however, was the close agreement between data based on our simulations and those reported for porous sub-2 μm and core-shell particles by Gritti et al.[57] and Gritti and Guiochon[95] concerning parameters in the comprehensive Giddings plate height equation that characterize the disorder of the packing microstructure and its impact on eddy dispersion.[158] This excellent comparison between sophisticated experimental and modeling approaches shifts the acquisition, analysis, and interpretation of plate height data to a new level, which is required in the derivation of the key morphology-transport relationships. These relationships are essential to any improved HPLC stationary phase design and our general understanding of chromatographic band spreading through its individual contributions.[178]

We also simulated hydrodynamic dispersion in microfluidic separation channels with cross-sections derived from real HPLC microchips. The simulations were performed in both open (i.e., non-packed) as well as particle-packed channels (using the particle size distribution and packed-bed porosity from the experiments as input parameters), and very good agreement with experimental dispersion data was found in both cases.[71]

Very recently we demonstrated the physical reconstruction of packed beds of modern fine particles and monoliths.[96,179,180] In turn, these physical reconstructions can serve as benchmark in the

[175] D. Hlushkou, D. Kandhai, and U. Tallarek. *Int. J. Numer. Methods Fluids*, 46, pp. 507–532, 2004.
[176] D. Hlushkou et al. *Chem. Eng. Commun.*, 193, pp. 826–839, 2006.
[177] D. Hlushkou "Numerical Simulation of Flow and Mass Transport in (Electro)Chromatographic Systems" PhD thesis Magdeburg, Germany: Institute of Chemical and Process Engineering, Otto-von-Guericke-Universität, 2003
[57] F. Gritti et al. *J. Chromatogr. A*, 1217, pp. 3819–43, 2010.
[95] F. Gritti and G. Guiochon. *Chem. Eng. Sci.*, 65, pp. 6327–6340, 2010.
[178] F. Gritti and G. Guiochon. *J. Chromatogr. A*, 1221, pp. 2–40, 2012.
[179] S. Bruns et al. *Anal. Chem.*, 82, pp. 6569–75, 2010.
[180] S. Bruns et al. *J. Chromatogr. A*, 1218, pp. 5187–94, 2011.

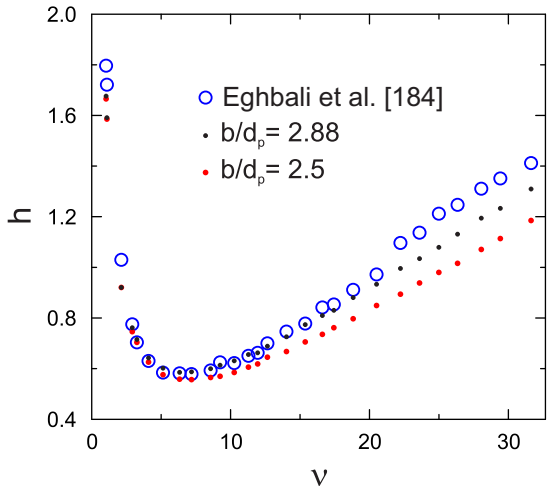

Figure 2.4: Comparison of simulated plate height data in a reconstructed hexagonal pillar array with top-bottom confinement with the experimental data of Eghbali et al.[184]. Dependence of the reduced plate height $h = 2(D_\mathrm{L}/D_\mathrm{m})/\nu$ on the reduced velocity $\nu = u_\mathrm{av} d_\mathrm{p}/D_\mathrm{m}$ for a bed porosity of $\varepsilon = 0.78$, a pillar diameter of $d_\mathrm{p} = 4$ µm, and channel height (distance between top and bottom walls) of $b = 10$ µm ($b/d_\mathrm{p} = 2.5$) or $b = 11.5$ µm ($b/d_\mathrm{p} = 2.88$).

simulations, and results for silica monoliths have been reported already.[181–183] These simulations have shown quantitative agreement between experimental and simulated Darcy permeabilities, validating our approach, because the only input parameters were the physically reconstructed geometrical structure of the macropore domain (without any assumptions or subsequent adjustments on monolith morphology), pressure drop, and mobile phase viscosity.[181] Quantitative agreement between experiment and simulations not only validated our approach to the reconstruction of porous media morphology and simulation of flow and transport, but also allowed us to present subsequently derived data characterizing the velocity field as well as hydrodynamic dispersion on solid grounds,[181–183] because these data are strictly based on a realistic macropore space morphology. Therefore, we have reached the stage where the individual contributions to chromatographic band spreading can be *quantified* through their morphological origin.

A final validation, which fits in the context of the present work (regular pillar arrays), is provided by Figure 2.4, where we compare chromatographic plate height data in a reconstructed hexagonal pillar array for top-bottom confinement with the experimental data of Eghbali et al.[184]. We used this system for our simulations, because (i) precise (on-column) experimental data for the plate heights are available, and (ii) the microstructure of the system can be reproduced exactly. For our simulations we adapted a porosity of $\varepsilon = 0.78$, a pillar diameter of $d_\mathrm{p} = 4$ µm, and a nominal channel height (distance between top and bottom walls) of $b = 10$ µm, i.e., $b/d_\mathrm{p} = 2.5$, as in [184]. The three-dimensional unit cell of the hexagonal array of identical cylindrical pillars with top-bottom confinement in Figure 2.1 (left panel) was adjusted accordingly and discretized

[181] D. Hlushkou, S. Bruns, and U. Tallarek. *J. Chromatogr. A*, 1217, pp. 3674–3682, 2010.
[182] D. Hlushkou et al. *Anal. Chem.*, 82, pp. 7150–9, 2010.
[183] D. Hlushkou et al. *J. Sep. Sci.*, 34, pp. 2026–37, 2011.
[184] H. Eghbali et al. *Anal. Chem.*, 81, pp. 705–715, 2009.

with a high spatial resolution of 200 grid nodes per d_p to minimize possible finite-size effects. Because the experimental plate height data reported in [184] represent equilibration of the injected tracer bands between top and bottom walls only, without equilibration between the two side walls, we also modeled dispersion for the top-bottom confinement.[43]

In Figure 2.4 we compare the normalized asymptotic longitudinal dispersion coefficients $D_\mathrm{L}/D_\mathrm{m}$, expressed in terms of plate heights $h = 2(D_\mathrm{L}/D_\mathrm{m})/\nu$, with experimental values from the work of Eghbali et al.[184] over the whole range of reduced velocities ν available from the experiments. Simulated plate heights slightly underestimate the experimental ones at higher velocities. The agreement improved when we increased the channel height from $b = 10$ µm to 11.5 µm ($b/d_\mathrm{p} = 2.88$). In [185], the authors noted a nominal pillar height of 10 µm, but according to Figure 2 in [185] the micropillars have a height of ~11.5 µm. The same value was also reported in [143]. Therefore, we performed an additional set of simulations with $b/d_\mathrm{p} = 2.88$, which provides close agreement with the experimental data (Figure 2.4). It is not clear why the experimental data for $\nu > 20$ show a common upward shift; a disturbance in the curve progression is probably due to an experimental artifact. Taking into account this shift of the data and also some uncertainty in the "exact" spatial dimensions of the experimental system, as well as deviations of the pillar shape from a perfect cylinder due to the etching process, which also has been shown to increase dispersion (cf. Figure 1.12 in [43]), we conclude that our model demonstrates good agreement with the experimental data in [184].

2.3 Results and discussion

2.3.1 Dispersion in bulk and confined sphere packings

Transient dispersion behavior

Dispersion in bulk random sphere packings ($\varepsilon = 0.366 - 0.46$), including transient behavior, has been studied in considerable detail in the past.[63,67,72,77,158] From these studies we know that the longitudinal dispersion coefficient $D_\mathrm{L}(t)$ attains its asymptotic (long-time) limit on a time scale of ca. $2-2.5t_\mathrm{D}$, where t_D is a characteristic transverse dispersive time defined as $t_\mathrm{D} = 2D_\mathrm{T}(\nu)t/d_\mathrm{p}^2$ and D_T is the asymptotic transverse dispersion coefficient at a given value of ν. The transverse dispersive time unit $2D_\mathrm{T}/d_\mathrm{p}^2$ corresponds to the time span $d_\mathrm{p}^2/2D_\mathrm{T}$, after which the tracer particles are dispersed laterally by one sphere diameter. The transverse dispersive time scale adequately describes the lateral equilibration between different velocities in a random packing, which is driven neither by pure diffusion nor by pure convection, but by their combined effects. The use of D_T in the dimensionless dispersive time scale reflects this combination of flow and diffusion. The asymptotic time scale of $\sim 2.25\, t_\mathrm{D}$ translates to a characteristic average transverse dispersion length in the bulk packings $\langle l_\mathrm{T}\rangle_\mathrm{bulk}$ of

$$\langle l_\mathrm{T}\rangle_\mathrm{bulk} = \sqrt{2D_\mathrm{T}t} \approx \sqrt{2.25d_\mathrm{p}} = 1.5d_\mathrm{p}, \tag{2.15}$$

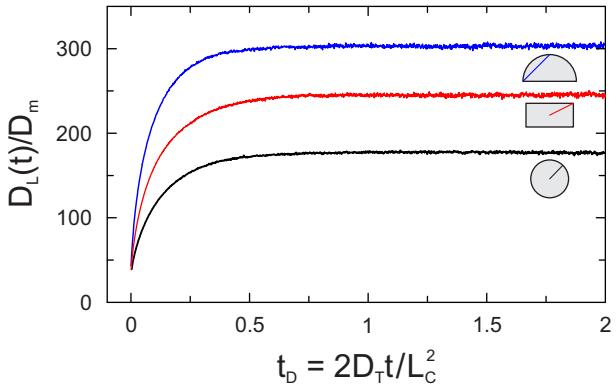

Figure 2.5: Transient longitudinal dispersion in confined random sphere packings with a cross-sectional area of $100\,\pi d_\mathrm{p}^2$ and a bed porosity of $\varepsilon = 0.40$ (cf. Figure 2.2) at an average reduced velocity of $\nu = 100$. $D_\mathrm{L}(t)/D_\mathrm{m}$ is a function of the transverse dispersive time $t_\mathrm{D} = 2D_\mathrm{T}t/L_\mathrm{C}^2$, where D_T is the transverse dispersion coefficient taken from the bulk packing (at $\nu = 100$) and L_C is the characteristic transverse length for each conduit geometry, i.e., the radius ($L_\mathrm{C} = 10\,d_\mathrm{p}$), half-diagonal ($L_\mathrm{C} = 14\,d_\mathrm{p}$), and corner-to-apex chord ($L_\mathrm{C} = 20\,d_\mathrm{p}$) for the circular, rectangular, and semicircular cross-section, respectively.

which means that longitudinal dispersion in a bulk packing is asymptotic after a distance of about $1.5\,d_\mathrm{p}$ has been sampled laterally by the tracer molecules. This heterogeneity on the order of $1-2\,d_\mathrm{p}$ Eq. (2.15) is associated with the short-scale disorder of a random sphere packing compared to a crystal-like structure, e.g., an ordered array of spheres. Giddings' estimate of $\sim 1.25\,d_\mathrm{p}$ for the distance behind the short-range interchannel contribution (see p. 45 in [66]) is close to our own result of $\sim 1.5\,d_\mathrm{p}$. Heterogeneities on larger time and length scales than $2-2.5\,t_\mathrm{D}$ have not been detected so far.

The transient behavior of longitudinal dispersion coefficients towards their asymptotic values was monitored for the confined sphere packings, expecting a transcolumn contribution due to the geometrical wall effect.[67,70,97,151,155] Figure 2.5 shows the development of $D_\mathrm{L}(t)/D_\mathrm{m}$ for a reduced velocity of $\nu = 100$. Elapsed time has been normalized through the transverse dispersive time $t_\mathrm{D} = 2D_\mathrm{T}(\nu)t/L_\mathrm{C}^2$, with the value for $D_\mathrm{T}(\nu)$ taken from the bulk packings. L_C is a characteristic transverse length for the three conduit geometries, which replaces the particle diameter used as a convenient measure for the bulk packings. This length characterizes the lateral distance that needs to be traversed by the tracer particles for a complete exchange between different velocities. Under consideration of the symmetry of the velocity fields it refers to the longest distance between different velocities. The highest velocities in cylindrical conduits are found along the wall due to the geometrical wall effect; complete exchange between velocity extremes in the fluid phase is then achieved by covering the lateral distance from wall to center. Consequently, the characteristic transverse length on the macroscopic (conduit cross-sectional) scale is the cylinder radius. For the noncylindrical conduits studied in this work the highest velocities are located in the corners. The characteristic transverse length for a conduit with rectangular cross-section is then the half-diagonal, and for a conduit with semicircular cross-section the distance between corner and apex.[70,73,135]

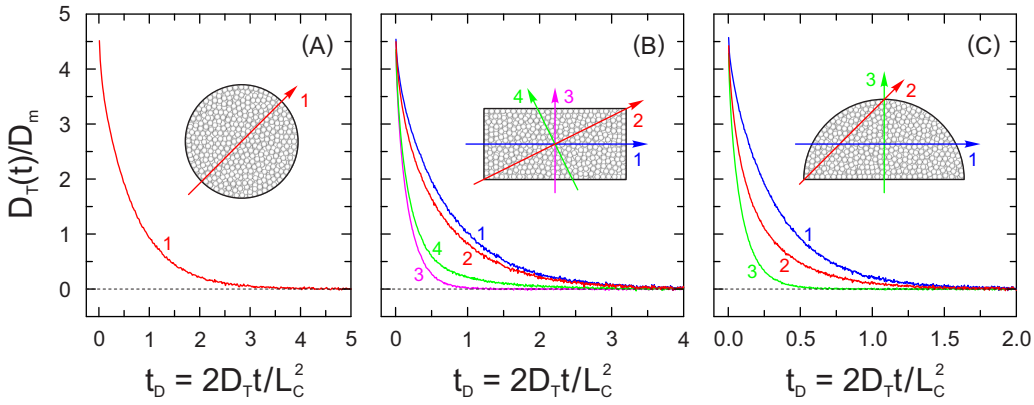

Figure 2.6: Transient transverse dispersion in confined random sphere packings with a cross-sectional area of $100\,\pi d_p^2$ and a bed porosity of $\varepsilon = 0.40$ (cf. Figure 2.2) at an average reduced velocity of $\nu = 100$. $D_T(t)/D_m$ is a function of the transverse dispersive time $t_D = 2D_Tt/L_C^2$, where D_T is the transverse dispersion coefficient taken from the bulk packing (at $\nu = 100$) and L_C is the characteristic transverse length for each conduit geometry, i.e., the radius ($L_C = 10\,d_p$), half-diagonal ($L_C = 14\,d_p$), and corner-to-apex chord ($L_C = 20\,d_p$) for the circular (A), rectangular (B), and semicircular (C) cross-section, respectively. Arrows indicate directions along which transverse dispersion was monitored.

The choices for the characteristic transverse lengths of the confined packings are validated in Figure 2.5, where the longitudinal dispersion data demonstrate asymptotic behavior after $\sim 1\,t_D$. This time scale corresponds to the time span after which the tracer particles are dispersed laterally by one L_C. For the cylindrical packing this result yields the anticipated characteristic average transverse dispersion length for longitudinal dispersion, $\langle l_T \rangle_{\text{cylinder,L}}$, of

$$\langle l_T \rangle_{\text{cylinder,L}} = \sqrt{2D_Tt} \approx L_C \equiv \frac{d_c}{2}. \tag{2.16}$$

The macroscopic flow heterogeneity caused by the cylindrical confinement of a sphere packing adds a transcolumn contribution to dispersion, which due to the cylindrical symmetry requires lateral equilibration on the scale of the cylinder radius, i.e., $L_C = d_c/2$. The asymptotic time span of $t \approx (d_c/2)^2/2D_T(\nu)$ for $D_L(t)$ is reminiscent of classical Taylor-Aris dispersion in laminar flow through a cylindrical pipe, where the asymptotic time span is proportional to $t \approx (d_c/2)^2/2D_m$.[16,174] The reduction of symmetry from circular to rectangular to semicircular cross-sections at constant cross-sectional area results in an increased characteristic transverse length of the velocity field (Figure 2.2 and Figure 2.5).

Before continuing with transient transverse dispersion in Figure 2.6, we note that Maier et al.[97,151,155] have studied enhanced, diameter-dependent dispersion in packed cylinders compared with bulk packings. They adopted a generalization of the Aris model of dispersion in a tube[174] to extrapolate their pore-scale simulations to the asymptotic time scale ($t_D > 1$, Figure 2.5) and used the radial velocity variation from the pore-scale simulation in a simplified transport model.[151] It is a qualitative model of how the radial velocity profile affects the development of asymptotic longitudinal dispersion. With this approach Maier et al.[155] demonstrated new evidence

for diameter-dependent dispersion in packed cylinders with particle-aspect ratios of $10 \leq d_c/d_p \leq 50$. Their approach is very useful for the comparison of dispersion in its pre-asymptotic regime and the determination of cross-over points for packed cylinders with different diameters. This is important for all experimental designs in which the asymptotic dispersion regime is never reached (e.g., in analytical and preparative HPLC). In our current work, we are not interested in a refinement of models that extrapolate from pore-scale simulations to the asymptotic time scale for dispersion in confined packings, but in the quantitative analysis on how laterally fully equilibrated wall and corner effects are reflected in the dependence of the reduced plate heights on the reduced velocity, as analyzed with the comprehensive Giddings equation.

Figure 2.6 illustrates transient transverse dispersion at $\nu = 100$ for the confined packings. Elapsed time has been normalized as in Figure 2.5, i.e., through $t_D = 2D_T(\nu)t/L_C^2$, with L_C as the radius, half-diagonal, and corner-apex-chord of the conduits with circular, rectangular, and semicircular cross-section, respectively. Figure 2.6A shows that transverse dispersion in the cylindrical packing decreases to zero on a time scale about four times longer than it takes to reach asymptotic longitudinal dispersion (Figure 2.5). Transverse asymptotic dispersion in the cylindrical packing is thus observed on a time scale of $\sim 4\, t_D$ (in any direction due to cylindrical geometry), which translates to a characteristic average transverse dispersion length for the transverse dispersion process, $\langle l_T \rangle_{cylinder,T}$, of

$$\langle l_T \rangle_{cylinder,T} = \sqrt{2D_T t} \approx 2L_C \equiv d_c. \tag{2.17}$$

This result is unsurprising given the limits that the confinement imposes on the tracers' lateral displacements: On their journey laterally through a sphere packing the tracer particles bounce back from the wall, so that their lateral displacement cannot exceed the cylinder diameter. Transverse dispersion has decayed to zero after the time $t \approx d_c^2/2D_T(\nu)$ has elapsed, i.e., the asymptotic time scale for a confined cylindrical packing is 2^2 times larger in transverse (Figure 2.6A) than in longitudinal direction (Figure 2.5) and therefore

$$\langle l_T \rangle_{cylinder,T} = 2 \langle l_T \rangle_{cylinder,L}\,. \tag{2.18}$$

The transverse dispersion behavior of confined packings with rectangular (Figure 2.6B) and semicircular (Figure 2.6C) cross-section is qualitatively similar, i.e., $D_T(t)/D_m$ decreases to zero. Because of the reduced symmetry of these conduits with respect to cylindrical packings, however, the process is anisotropic, as Figure 2.6B and Figure 2.6C show.

Figure 2.5 and Figure 2.6 reflect the dispersion behavior of packed capillaries[49,109,110] and separation channels used in nano-HPLC[114–117] and microchip-HPLC,[118] where the ratio of the packed-bed length to the column diameter (or the characteristic transverse channel size) reaches an order of thousands. For narrow-bore and analytical HPLC columns (which constitute the majority of HPLC columns in practice) the ratio of packed-bed length to column diameter is below 100. Thus analyte residence times in these columns are insufficient to allow for a fully relaxed transcolumn contribution to eddy dispersion, i.e., the dynamic process is truncated before

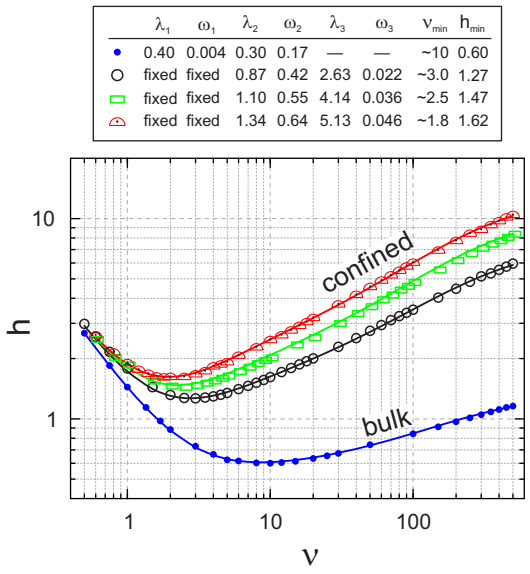

Figure 2.7: Dependence of the reduced plate height $h = H/d_\mathrm{p}$ on the reduced velocity $\nu = u_\mathrm{av} d_\mathrm{p}/D_\mathrm{m}$ (where d_p is the particle diameter) for bulk and confined random sphere packings with a cross-sectional area of $100\,\pi d_\mathrm{p}^2$ and a bed porosity of $\varepsilon = 0.40$ (cf. Figure 2.2). Symbols denote the cross-sectional geometry. Solid lines represent the best fits of the simulated data to Eq. (2.20). Characteristic parameters of the plate height curves (h_min, ν_min) and eddy dispersion contributions (λ_i, ω_i; cf. Eq. (2.20)) are summarized in the legend.

the asymptotic longitudinal dispersion coefficient is reached. Plate height curves acquired under such nonequilibrium conditions do not reflect the full lateral equilibration, and the absence of wall effects may erroneously be assumed.

Velocity-dependence of longitudinal dispersion

Longitudinal dispersion coefficients D_L usually discussed in the engineering literature[98] are related to the chromatographic plate heights H as well as their reduced values $h = H/d_\mathrm{p}$ through[66]

$$D_\mathrm{L} = \frac{H u_\mathrm{av}}{2} = \frac{h \nu D_\mathrm{m}}{2}. \tag{2.19}$$

The plate height curves obtained for the bulk and confined random sphere packings from collecting asymptotic longitudinal dispersion coefficients over a reduced velocity range of $0.5 \leq \nu \leq 500$ are shown in Figure 2.7. The use of nonporous spheres and nonadsorbing tracers in our model eliminates mass transfer resistance contributions due to intraparticle diffusion and adsorption from our data, as opposed to experimentally acquired plate heights.[66,67,186,187] Because plate heights in Figure 2.7 reflect only band broadening contributions that originate from eddy dispersion in the interparticle void space of the packings, they are overall lower than plate height data of a nonselective system.

[186] P. Magnico and M. Martin. *J. Chromatogr. A*, 517, pp. 31–49, 1990.
[187] J. H. Knox. *J. Chromatogr. A*, 960, pp. 7–18, 2002.

The effect of a macroscopic confinement and the associated transcolumn contribution to eddy dispersion is immediately recognizable from the large difference between the plate height curves of the bulk and those of the confined packings. The plate height minimum jumps from $h_{\min} = 0.60$ and $\nu_{\min} = 10$ for the bulk packing to $h_{\min} = 1.27$ and $\nu_{\min} = 3$ for the cylindrically confined packing. With decreasing conduit symmetry, the plate height curves shift upwards, from $h_{\min} = 1.47$ and $\nu_{\min} = 2.5$ for the rectangular cross-section to $h_{\min} = 1.62$ and $\nu_{\min} = 1.8$ for the semicircular cross-section. Figure 2.7 shows that the impact of the actual conduit geometry on the separation efficiency of random sphere packings–although secondary to that of the confinement *per se*–is by no means negligible. It is therefore advisable to consider the final geometry of a separation channel that is to be packed with adsorbent particles for chromatography, when choosing microfabrication materials and methods.[127]

The plate height data of Figure 2.7 were analyzed with the comprehensive plate height equation $h = f(\nu)$ derived by Giddings considering the coupling between transverse diffusion and spatial velocity fluctuations.[66] For our computer-generated packings of nonporous spheres and point-like, inert (nonadsorbing, nonreacting) tracers, the Giddings equation is[67]

$$h = h_{\text{diff}} + \sum_{i=1}^{3} h_{\text{eddy},i} = \frac{2\gamma}{\nu} + \sum_{i=1}^{3} \frac{2\lambda_i}{1 + (2\lambda_i/\omega_i)\,\nu^{-1}}. \tag{2.20}$$

The first term in Eq. (2.20), $h_{\text{diff}} = 2\gamma/\nu$, is the contribution from longitudinal diffusion in the packing and contains the obstruction factor $\gamma = D_{\text{eff}}/D_{\text{m}}$, which relates the effective (asymptotic) diffusion coefficient of a tracer in the packing (D_{eff}) to the diffusion coefficient of this tracer in the bulk solution (D_{m}).[159] The second, third, and fourth terms in Eq. (2.20) consider eddy dispersion contributions $h_{\text{eddy},i}$ to band broadening that originate from flow field inhomogeneities on different time and length scales:[178] the second term ($i = 1$) refers to the velocity inhomogeneity across individual flow channels between adjacent particles (transchannel contribution), whereas the third term ($i = 2$) covers the flow maldistribution on a lateral length scale of $1 - 2$ particle diameters (short-range interchannel contribution). While transchannel equilibration is required in any packed bed, ordered or random, the short-range interchannel contribution is associated with the disorder of a random compared with an ordered sphere packing, and also reflects individual degrees of disorder between different random packings.[63,158] The fourth term in Eq. (2.20) ($i = 3$) represents the confinement-based transcolumn velocity bias and associated dispersion (transcolumn contribution).[67] ω_i and λ_i in Eq. (2.20) are structural parameters characteristic of each eddy dispersion contribution. The ratio $\nu_{1/2,i} = 2\lambda_i/\omega_i$ is a reduced transition velocity at which the corresponding plate height term $h_{\text{eddy},i}$ reaches half of its limiting value and thereafter starts to flatten noticeably.[188] At high velocities $h_{\text{eddy},i}$ approaches the constant value $2\lambda_i$, whereas at low velocities $h_{\text{eddy},i}$ approaches $\omega_i\nu$ and then looks like an ordinary kinetics or mass transfer velocity-proportional term.

The obstruction factor γ was calculated for each packing from the respective effective dif-

[188] J. C. Giddings. *Nature*, 184, pp. 357–358, 1959.

fusion coefficients observed in the long-time limit in simulations of mass transport without advective flow ($\nu = 0$). For fitting the reduced plate height data to Eq. (2.20), γ was held fixed at the calculated value. The best fits of the plate height data to Eq. (2.20) as well as the derived values for the coefficients λ_i and ω_i are shown in Figure 2.7. (For fitting the plate height data of the bulk packings the term for the transcolumn contribution, $h_{\mathrm{eddy},3}$, was omitted from Eq. (2.20)). The adapted form of the comprehensive Giddings equation excellently fits the simulated plate heights over the whole velocity range of $0.5 \leq \nu \leq 500$, with $R^2 > 0.999$.

The values we obtained for the bulk packings (with $\gamma = 0.65$) of $\lambda_1 = 0.40$ and $\omega_1 = 0.004$ for the transchannel and $\lambda_2 = 0.30$ and $\omega_2 = 0.17$ for the short-range interchannel contribution are reminiscent of Giddings' estimates: $\lambda_1 \approx 0.5$, $\omega_1 \approx 0.01$, $\lambda_2 \approx 0.5$, and $\omega_2 \approx 0.5$.[66] The results for the bulk packings agree very well with our previous data for bulk monodisperse[63] and polydisperse[158] packings. λ_1 reflects the longitudinal length scale on which the velocity inequality between center and edge of an individual pore persists before the flow stream splits up into several subsequent pores down the packing; ω_1 depends on the lateral pore dimensions and thus increases with the bed porosity, but its overall impact is negligible due to its very small values ($0.003 < \omega_1 < 0.006$).[63,158] The reduced transition velocity for the transchannel contribution is estimated at $\nu_{1/2,1} = 2 \times 0.4/0.004 = 200$, i.e., it raises slowly over most of the velocity range shown in Figure 2.7 and reaches its full potential only at high velocities, which are outside the operational range in HPLC practice with modern fine particles[48,51,189–191] (typically $\nu < 30$). The parameters λ_2 and ω_2 both increase monotonously with the bed porosity,[63,158] reflecting that a looser random packing is more disordered on a short-range scale than a denser one, where the restricted available space narrows the possibilities for individual sphere placement. The value for $\omega_2 = 0.17$ agrees excellently with our previous results for bulk monodisperse and polydisperse packings at $\varepsilon = 0.40$ ($\omega_2 = 0.16 - 0.18$) generated with the same protocol.[158] λ_2 characterizes the longitudinal length scale on which flow inequalities over a lateral length scale of $1 - 2$ particle diameters persist in a packing, before being leveled out in (and by) the flow field.[66,67,178] Experimental values for λ_2 provided by Gritti et al.[57] and Gritti and Guiochon[95] for core-shell particle columns fall within the range of $0.2 < \lambda_2 < 0.5$, which we previously received for monodisperse and polydisperse packings at bed porosities of $\varepsilon = 0.366 - 0.460$:[158] they determined $\lambda_2 = 0.20$ and $\lambda_2 = 0.35$ for columns packed with, respectively, 2.6 µm Kinetex-C_{18} particles (100×4.6 mm) and 2.7 µm Halo-C_{18} particles (150×4.6 mm),[57] and later $\lambda_2 = 0.30$ and $\lambda_2 = 0.40$ for 150×4.6 mm columns packed with 2.6 µm Kinetex-C_{18} particles and with 2.7 µm Halo-C_{18} particles, respectively.[95] All columns had external (bed) porosities around $\varepsilon = 0.40$. For a packing with a narrow particle size distribution at this porosity, our previous simulations predicted $\lambda_2 = 0.31$,[158] and the value for the present monodisperse packing is very similar ($\lambda_2 = 0.30$).

[48] J. R. Mazzeo et al. *Anal. Chem.*, 77, 460 A–467 A, 2005.
[51] G. Guiochon and F. Gritti. *J. Chromatogr. A*, 1218, pp. 1915–38, 2011.
[189] J. E. MacNair, K. C. Lewis, and J. W. Jorgenson. *Anal. Chem.*, 69, pp. 983–989, 1997.
[190] J. E. MacNair, K. D. Patel, and J. W. Jorgenson. *Anal. Chem.*, 71, pp. 700–708, 1999.
[191] S. Fekete, K. Ganzler, and J. Fekete. *J. Pharmaceut. Biomed.*, 51, pp. 56–64, 2010.

To focus our analysis on the wall and corner effects and the resulting transcolumn contribution to eddy dispersion in the confined packings (Figure 2.7), we limited the number of unknown parameters in Eq. (2.20) by using the transchannel contribution of the bulk packings ($\lambda_1 = 0.4$ and $\omega_1 = 0.004$). This is a valid first approximation, because the transchannel contribution appears to be the most "universal" dispersion contribution, expected to show the least variations between different packings of similar packing density. Our previous work has shown that the values of λ_1 and ω_1 for $\varepsilon < 0.40$ are nearly insensitive to variations in the packings' microstructural degree of heterogeneity as well as to the particles' polydispersity.[63,158]

We now discuss the transcolumn contribution to eddy dispersion (λ_3 and ω_3) for laterally fully equilibrated wall and corner effects in our computer-generated packings. $D_\mathrm{L}(t)$ converges to its asymptotic value on a time span $t \propto L_\mathrm{C}^2/\langle D_\mathrm{T}\rangle$, where $\langle D_\mathrm{T}\rangle$ represents the mean value of D_T over a bed's cross-section[67,97,151,155,192] (cf. Figure 2.5). With sufficiently long packings tracers equilibrate over the entire cross-section by transverse dispersion. For this "equilibrium" transcolumn contribution pseudo-diffusive behavior is observed, characterized by a linear velocity dependence of the plate height contribution.[148] This dynamics is typical for capillary and microchip HPLC (where the ratio of bed length to column diameter or the characteristic transverse channel size reaches an order of thousands), but different from that in wider columns, especially as we consider fast separations. In that case, tracers cannot sample the complete cross-section and band broadening is directly related to the actual transcolumn flow profile. As a consequence, this "nonequilibrium" transcolumn contribution is controlled by a convective mechanism,[193] and the associated eddy dispersion contribution to a first approximation shows a linear velocity-dependence, while the corresponding plate height contribution becomes somewhat velocity-independent (see also the discussion of transcolumn dispersion in [194] and Figure 6 in that reference).

The significance of a macroscopic confinement for the overall eddy dispersion contribution to band broadening is apparent from the relatively large values of λ_3 (compared with the transchannel and the short-range interchannel contribution): $\lambda_3 = 2.63$ (circular cross-section), $\lambda_3 = 4.14$ (rectangular), and $\lambda_3 = 5.13$ (semicircular). The values for ω_3 demonstrate a similar increase with decreasing symmetry of the conduit cross-section, with $\omega_3 = 0.022$ (circular) $< \omega_3 = 0.036$ (rectangular) $< \omega_3 = 0.046$ (semicircular). As expected for laterally fully equilibrated wall and corner effects, the coefficients for the transcolumn contribution have high reduced transition velocities of $\nu_{1/2,3} = 2\lambda_3/\omega_3 > 200$, so that in the wide velocity range where $\nu \ll 2\lambda_3/\omega_3$, the transcolumn contribution can be approximated as $h_{\mathrm{eddy},3} \approx \omega_3\nu$, just like the transchannel contribution ($h_{\mathrm{eddy},1} \approx \omega_1\nu$). Both plate height contributions taper off at higher velocities, due to the coupling of classical eddy dispersion (pure flow mechanism) and transverse diffusion in random packings, inherent to Eq. (2.20).[66,146]

The qualitative dependence of the transcolumn contribution on the conduit geometry at constant cross-sectional area can be better understood with a closer look at the general form of

[192] E. Hamdan, J. Milthorpe, and J. Lai. *Chem. Eng. J.*, 137, pp. 614–635, 2008.
[193] F. Gritti and G. Guiochon. *J. Chromatogr. A*, 1217, pp. 6350–65, 2010.

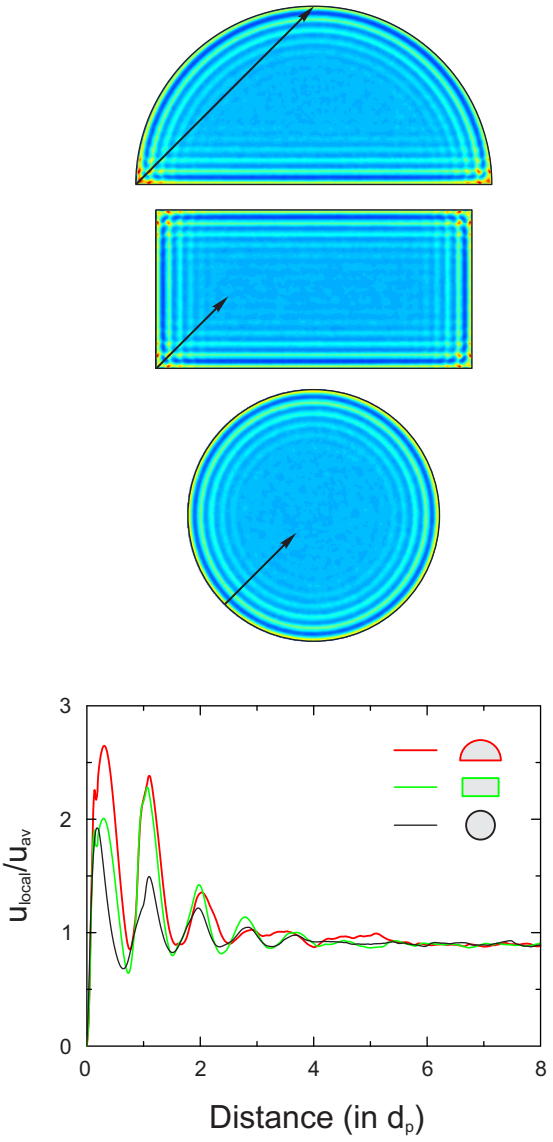

Figure 2.8: Lateral velocity distributions (averaged over the packing length) at an average reduced velocity of $\nu = 100$ in confined random sphere packings (cf. Figure 2.2) with a cross-sectional area of $100\ \pi d_\mathrm{p}^2$ and a bed porosity of $\varepsilon = 0.40$ (top), and one-dimensional distributions of the relative velocity $u_\mathrm{local}/u_\mathrm{av}$ (bottom) along the indicated directions.

ω_i in Eq. (2.20) according to Giddings[66]

$$\omega_i = \frac{\omega_{\alpha,i}^2 \omega_{\beta,i}^2}{2}. \tag{2.21}$$

Here, $\omega_{\alpha,i}$ is the ratio of the characteristic diffusion length to the particle diameter and $\omega_{\beta,i}$ is the ratio of the difference between the velocity extremes characterizing a particular type of velocity disparity (e.g., a transcolumn velocity heterogeneity) and the corresponding mean velocity. The influence of $\omega_{\alpha,i}$ can be explained by the characteristic transverse length L_C for the three conduit geometries, as derived from the transient dispersion behavior (Figure 2.5): L_C increases from circular ($L_\mathrm{C} = 10\ d_\mathrm{p}$; radius) to rectangular ($L_\mathrm{C} = 14\ d_\mathrm{p}$; half-diagonal) to semicircular ($L_\mathrm{C} = 20\ d_\mathrm{p}$; corner-apex-chord) geometry. Concerning the influence of the second parameter ($\omega_{\beta,i}$), Figure 2.8 (top panel) shows the lateral flow velocity distribution at $\nu = 100$ for each conduit geometry. As anticipated from the impossibility to pack conduit corners tightly, regions of advanced velocity appear in the corners of the noncylindrical packings.[70,71,73,135] Selected velocity profiles (Figure 2.8, bottom panel) over a distance of $8\ d_\mathrm{p}$ from the wall to the randomly packed core visualize the local velocity extremes for each conduit geometry. The difference in local velocities between wall and core region grows decidedly from cylindrical to noncylindrical conduits. The semicircular cross-section has worse dispersion characteristics than the rectangular one, partly because the corner region of the semicircular packing has more extended channels and carries higher velocities, partly because the semicircular cross-section has lower symmetry and a longer characteristic transverse length than the rectangular at equal area[70,73] (Figure 2.5).

From the dispersion analysis presented in Figure 2.7 we obtain the following estimates for the transition velocities characterizing the three eddy dispersion contributions: $\nu_{1/2,1} \approx 200$ (transchannel), $\nu_{1/2,2} \approx 4$ (short-range interchannel), and $\nu_{1/2,3} > 200$ (transcolumn). Because the reduced transition velocity is a rough dividing point between the dominance of diffusive and flow mechanisms of lateral exchange in a packing at lower and higher velocities, respectively, the high transition velocities of the transchannel and transcolumn contributions indicate that over a wide range of reduced velocities, certainly in chromatographic praxis ($\nu < 30$), these effects reduce to simple mass transfer velocity-proportional terms. Only the short-range interchannel contribution retains its coupling characteristics. The total effect of the component plate height curves to eddy dispersion can then be written as

$$h_\mathrm{eddy} = \sum_{i=1}^{3} h_{\mathrm{eddy},i} = (\omega_1 + \omega_3)\,\nu + \frac{2\lambda_2}{1 + (2\lambda_2/\omega_2)\,\nu^{-1}}. \tag{2.22}$$

This result agrees well with Giddings' scale analysis for these contributions.[66] The low impact of coupling between diffusive and flow mechanisms of eddy dispersion in the limited range of practical velocities ($5 < \nu < 30$) also explains why in this velocity range the plate height data are adequately described by the van Deemter equation, particularly for columns packed with

porous particles, when mass transfer terms associated with the stationary phase add to the plate height.[195,196]

Effect of the degree of microstructural heterogeneity on dispersion

Experimental chromatographic packings are produced with a wide range of packing conditions. The final column may be tested for its dispersion characteristics by acquisition of plate height curves, but the packing microstructure usually remains unknown, so that crucial knowledge about the relation between packing process parameters, packing microstructure, and the packing's transport properties remains unavailable. In contrast, the effect of the packing process parameters and protocols on the microstructure of computer-generated packings is far better understood.[43,63,159] We studied three packing types: Rx0.001, R, and Sx2. The Sx2-packing originates from a lattice-based initial distribution of sphere centers in the simulation box, whereas the generation of R- and Rx0.001-packings starts from a random distribution. The value of the constant α for scaling the displacement length determines how well inhomogeneities in the initial distribution of sphere centers are balanced out in the final packing microstructure: with a small displacement value ($\alpha = 0.001$) particle centers tend to stay closer to their initial positions so that the final configuration reflects the randomness of the initial distribution of particle centers; a larger displacement value ($\alpha = 2$) provides a more uniform distribution of particle centers in the final configuration. The three generated packing types therefore reflect a systematic decrease in the microstructural degree of heterogeneity (or packing disorder) in the sequence: Rx0.001 $>$ R $\gg$ Sx2.

In our previous work on disorder-dispersion correlations for bulk sphere packings at bed porosities of $\varepsilon = 0.366 - 0.46$, we subjected all packings to Voronoi tessellation[197] and subsequently correlated the statistical moments of the Voronoi volume distributions (standard deviation and skewness) with the porosity and the protocol-dependent microstructural disorder.[63] The conducted statistical analysis based on the Voronoi volume distributions revealed a porosity and protocol-dependent short-range disorder that was strongly correlated to the short-range interchannel contribution to eddy dispersion, whereas the transchannel contribution was much less affected by the packing disorder.

In the current work, we investigate cylindrically confined packings (Rx0.001, R, Sx2) with a particle-aspect ratio of 20 and a bed porosity of $\varepsilon = 0.40$. The complete $h - \nu$ data sets for these packings over a reduced velocity range of $0.5 \leq \nu \leq 500$ as well as the best fits of these data to Eq. (2.20) are available in Figure 2.9. Again, the obstruction factor γ was fixed at the value calculated independently for each confined packing at $\nu = 0$ and the values of the parameters for the transchannel contribution to eddy dispersion (λ_1 and ω_1) were taken from the respective bulk packings. Each curve in Figure 2.9 (similar to Figure 2.7) represents the mean calculated from five random realizations of a packing type (or confinement type, as in Figure 2.7). The adapted form of the comprehensive Giddings equation Eq. (2.20) excellently fits the simulated plate

[195] U. Tallarek, E. Bayer, and G. Guiochon. *J. Am. Chem. Soc.*, 120, pp. 1494–1505, 1998.
[196] K. M. Usher, C. R. Simmons, and J. G. Dorsey. *J. Chromatogr. A*, 1200, pp. 122–128, 2008.
[197] A. Okabe *Spatial tessellations: concepts and applications of Voronoi diagrams* 2nd ed. John Wiley & Sons, 2000

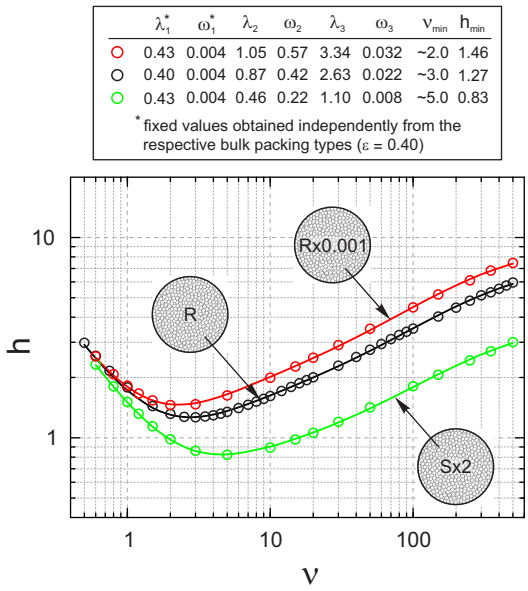

Figure 2.9: Dependence of the reduced plate height $h = H/d_\mathrm{p}$ on the reduced velocity $\nu = u_\mathrm{av} d_\mathrm{p}/D_\mathrm{m}$ (where d_p is the particle diameter) for cylindrically confined random sphere packings with a cross-sectional area of $100\,\pi d_\mathrm{p}^2$ and a bed porosity of $\varepsilon = 0.40$. The packings possess different degrees of microstructural heterogeneity (Rx0.001 > R ≫ Sx2) induced by systematic variations of the packing protocol. Solid lines represent the best fits of the simulated data to Eq. (2.20). Characteristic parameters of the plate height curves (h_min, ν_min) and eddy dispersion contributions (λ_i, ω_i; cf. Eq. (2.20)) are summarized in the legend.

height data over the whole velocity range, with $R^2 > 0.999$. The curve minimum (h_min and ν_min) shifts from $h_\mathrm{min} = 1.46$ and $\nu_\mathrm{min} = 2$ for the Rx0.001-packing via $h_\mathrm{min} = 1.27$ and $\nu_\mathrm{min} = 3$ for the R-packing to $h_\mathrm{min} = 0.83$ and $\nu_\mathrm{min} = 5$ for the Sx2-packing, i.e., separation efficiency increases with decreasing packing disorder. Whereas the transchannel contribution to eddy dispersion is practically unaffected by the protocol-dependent degree of microstructural heterogeneity, the values of the parameters for the short-range interchannel (λ_2, ω_2) and transcolumn (λ_3, ω_3) contributions show a trend consistent with the shift of the curve minimum, i.e., they decrease with decreasing packing disorder.

Figure 2.9 demonstrates the impact of the packing generation protocol (similar to the packing conditions and process parameters in HPLC practice) on the kinetic performance of a confined packing. The range of the plate height curves in Figure 2.9, where the span between different packing types is comparable (between R and Rx0.001) or even larger (between Sx2 and Rx0.001) than the change induced by different conduit cross-sectional geometries (cf. Figure 2.7), suggests that more research should be devoted to the preparation of highly efficient packed beds. Understanding how packing generation determines packing microstructure is admittedly easier for computer algorithms than for the slurry-packing process,[64] but the physical reconstruction of experimental column packings and the derivation of appropriate statistical parameters that describe the packing morphology is a promising step in this direction.[96]

2.3.2 Dispersion in bulk and confined pillar arrays

Velocity-dependence of longitudinal dispersion

Contrary to random sphere packings the studied pillar arrays possess an ordered microstructure due to the regular arrangement of equal cylindrical pillars. Modeling of flow and transport in bulk regular pillar arrays is relatively straightforward, because transport properties can be reduced to an advection-diffusion problem in a single unit cell.[23,160,161] Thus, unlike in random sphere packings, whose geometrical dimensions need to be sufficient to observe asymptotic dispersion behavior, dispersion simulations in a bulk pillar array can be limited to the two-dimensional unit cell (e.g., to the xy-plane, Figure 2.1). Upon confinement of the array, however, the no-slip velocity boundary condition at the surface of a wall causes flow and transport to become macroscopically inhomogeneous. A transcolumn velocity bias is generated parallel to the pillar axis (by the top and bottom walls) as well as perpendicular to it (due to the side walls), and dispersion simulations require consideration of the complete three-dimensional geometry of the confined array to take proper account of the four newly created 90°-corners (Figure 2.2 and Figure 2.3).

The two-dimensional problem of dispersion in bulk regular cylinder arrays (arrays of circles) was studied in the past[27,28,198–200] and received renewed interest with microfabricated pillar array columns for HPLC applications.[201] In contrast, dispersion simulations in confined pillar arrays, where the confinement effects on the scaling of dispersion were quantified, are rare and incomplete. Desmet and co-workers studied the effect of the two side walls and their geometrical adjustment for minimizing the engendered dispersion at a few velocities by employing a two-dimensional geometry (without top and bottom walls).[202] Later, they investigated the influence of top and bottom walls, using periodic boundary conditions at the sides.[203] But real, experimental microfabricated arrays are fully confined, with side walls and corners, and these partial confinement studies do not account for the long-term equilibration along the width of a flat confined pillar array (with a high channel width-to-height ratio, as in Figure 2.2). Tracer equilibration between the closely spaced top and bottom walls is much faster than between the wider spaced side walls and the accompanying corners. Because the envisioned length along the flow direction of the microfabricated pillar arrays for HPLC applications is on the order of centimeters,[143–145] the complete lateral equilibration between the side walls over a distance on the order of 100 μm also requires consideration in a full confinement analysis. Plate height data of partially confined (equilibration only between top and bottom walls, i.e., on the order of just

[27] D. A. Edwards et al. *Transp. Porous Media*, 6, pp. 337–358, 1991.
[28] J. Salles et al. *Phys. Fluids A*, 5, pp. 2348–2376, 1993.
[198] D. A. Edwards, M. Shapiro, and H. Brenner. *Phys. Fluids A*, 5, p. 837, 1993.
[199] H. P. A. Souto and C. Moyne. *Phys. Fluids*, 9, pp. 2253–2263, 1997.
[200] D. Buyuktas and W. W. Wallender. *Heat Mass Transfer*, 40, pp. 261–270, 2004.
[201] P. Gzil et al. *Anal. Chem.*, 75, pp. 6244–50, 2003.
[202] N. Vervoort et al. *Anal. Chem.*, 76, pp. 4501–7, 2004.
[203] J. De Smet et al. *J. Chromatogr. A*, 1154, pp. 189–197, 2007.

10 μm) or even unconfined pillar arrays are sometimes[143,201,204,205] compared with plate height data of particle-packed capillaries,[206,207] but this is inappropriate (as well as confusing to those interested more in technological advances than chromatographic theory), because the latter plate heights reflect laterally fully equilibrated wall and corner effects, which are absent in the former. In addition, the performance of particle-packed capillaries depends on the particle-aspect ratio, thus, also on the cross-sectional area (for a given particle size), and on the packing conditions, which largely determine the packing microstructure or quality.[49,108–110] As our transient dispersion analysis in Figure 2.5 shows, truncating the dispersion process in the pre-asymptotic regime reduces the apparent dispersion coefficient with respect to its long-time (asymptotic) limit and therefore mimics a better chromatographic performance. Thus, the comparison between different column morphologies is valid only under the condition of similar conduit cross-sectional area, bed porosity, support porosity (nonporous; partially or fully porous), and retention behavior (thermodynamic vs. kinetic), and moreover requires the careful analysis of time and length scales behind any velocity bias to quantify its impact on dispersion.

Figure 2.10 presents the comprehensive $h - \nu$ data set simulated for the fully confined pillar array with a channel width-to-height ratio of 40 (Figure 2.2), the bulk pillar array, and the top-bottom confined array (cf. Figure 2.1) over a velocity range of $0.5 \leq \nu \leq 500$, where the pillar diameter replaces the sphere diameter in the calculation of $\nu = u_{\mathrm{av}} d_{\mathrm{p}} / D_{\mathrm{m}}$. The longitudinal dispersion data simulated for the fully confined array reflect laterally fully equilibrated wall and corner effects. The $h - \nu$ curves in Figure 2.10A (double logarithmic) and Figure 2.10B (linear-logarithmic) reveal the following features:

(i) First and foremost, confinement causes a strong shift of the plate height minimum (best seen in Figure 2.10A), similar as observed in Figure 2.7 for the random sphere packings. Whereas the minimum coordinates are $h_{\mathrm{min}} = 0.07$ at $\nu_{\mathrm{min}} = 50$ for the bulk pillar array, they shift to $h_{\mathrm{min}} = 0.18$ and $\nu_{\mathrm{min}} = 20$ upon adding top and bottom walls, and to $h_{\mathrm{min}} = 0.46$ and $\nu_{\mathrm{min}} = 15$ after further enclosing the array with side walls. Thus, h_{min} increases by a factor of nearly seven from bulk to full confinement, whereas cylindrical confinement of the random sphere packing resulted only in a ca. twofold increase of h_{min} (Figure 2.7)! The explanation for this discrepancy between sphere packings and pillar arrays lies in their respective microstructures, random vs. regular: fluid dispersion in a bulk regular pillar array results only from transchannel equilibration, and thus the plate heights of an unconfined regular pillar array are lower than those of an unconfined random sphere packing, where due to the inherent short-range disorder of the microstructure additionally a short-range interchannel term contributes to eddy dispersion. Consequently, the regular pillar array experiences a much stronger loss of its (previously excellent) separation efficiency after the addition of a confinement-based macroscopic heterogeneity than a random sphere packing.

(ii) At low velocities ($\nu < 2$), all plate height curves approach and ultimately collapse

[204] M. De Pra et al. *Anal. Chem.*, 78, pp. 6519–6525, 2006.
[205] J. Eijkel. *Lab Chip*, 7, pp. 815–7, 2007.
[206] G. Stegeman, J. C. Kraak, and H. Poppe. *J. Chromatogr. A*, 634, pp. 149–159, 1993.
[207] N. Wu, Y. Liu, and M. L Lee. *J. Chromatogr. A*, 1131, pp. 142–50, 2006.

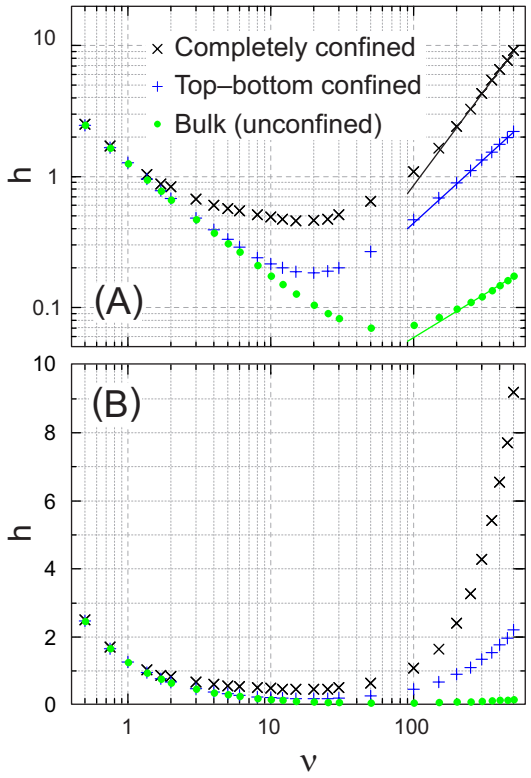

Figure 2.10: Dependence of the reduced plate height $h = H/d_\mathrm{p}$ on the reduced velocity $\nu = u_\mathrm{av} d_\mathrm{p}/D_\mathrm{m}$ (d_p is the pillar diameter) for bulk and confined regular pillar arrays with a cross-sectional area of $100\ \pi d_\mathrm{p}^2$ and a bed porosity of $\varepsilon = 0.40$ (cf. Figure 2.1 and Figure 2.2). Plate height curves are shown in double logarithmic (A) and linear-logarithmic (B) form to visualize individual aspects discussed in the text.

onto the pure diffusion result (best seen in Figure 2.10A) characterized by $h_{\mathrm{diff}} = 2\gamma/\nu$ with $\gamma = D_{\mathrm{eff}}/D_{\mathrm{m}} = 0.61$, i.e., at low flow velocities the tracers sample the microstructure primarily by diffusion. It is interesting to note that diffusion in the regular pillar arrays is more obstructed than in the random sphere packings at equal bed porosity, whereas diffusion in ordered sphere packings is less obstructed than in random sphere packings.[159] This marks a fundamental difference between structures that are ordered in two dimensions, like regular pillar arrays, and those that are ordered in three dimensions, like ordered sphere packings, with regard to diffusion.[208]

(iii) At high velocities ($\nu > 200$), all plate height curves demonstrate a linear velocity-dependence, highlighted by the straight lines in Figure 2.10A. Whereas this looks like an ordinary kinetics or mass transfer velocity-proportional term, we note again that the use of nonporous supports (nonporous spheres or cylinders) and passive tracers eliminates the mass transfer resistance contributions caused by diffusion inside the spheres or cylinders and by adsorption. The slope of the solid lines in Figure 2.10A, which serve as a guide to the eye, increases strongly from bulk to top-bottom confined to fully confined pillar array and represents the additional, pseudo-diffusive contributions to overall fluid dispersion from the laterally fully equilibrated wall and corner effects in the confined structures. For the bulk pillar array the indicated linear velocity-dependence of the plate heights originates in the perfectly ordered microstructure, which is known to result in a diffusion-limited contribution to dispersion. In spatially periodic porous media molecular diffusion is essential for the tracers to "forget" their initial position.[23,152,160,161,209] The deleterious effect of the confinement on the separation efficiency is best seen in the linear-logarithmic presentation of the $h - \nu$ data (Figure 2.10B), where at $\nu > 100$ the plate heights of the fully confined array visually shoot off. And Figure 2.10A shows that the fully confined array (black crosses) has an unusually wide and shallow plate height minimum (compared with the confined sphere packings in Figure 2.7) at $\nu = 5 - 50$, before the plate heights rise steeply at higher velocities. Plate height curves of the regular pillar arrays are analyzed in detail in the next section, where we also clarify why the Giddings equation and other familiar plate height equations (or correlations), which work well for sphere packings, fail to describe the data in Figure 2.10.

Transverse dispersion and tracer trajectories

Complementary information about the plate height curve characteristics was obtained from the velocity-dependence of the transverse dispersion coefficient. The dependence of $D_{\mathrm{T}}/D_{\mathrm{m}}$ in the bulk pillar array (measured perpendicular to the axis of the cylinders) is compared in Figure 2.11 with the corresponding curve for the bulk sphere packing. This figure reveals a fundamental difference in transverse dispersion behavior between regular cylinder arrays and random sphere packings, which in turn affects longitudinal dispersion and the velocity-dependence of the plate height data. $D_{\mathrm{T}}/D_{\mathrm{m}}$-values of the sphere packing increase monotonously over the whole velocity range, whereas for the pillar array the values—after an initially faster increase than observed for the sphere packing—approach an asymptotic value of $D_{\mathrm{T}}/D_{\mathrm{m}} \approx 10$ at $\nu > 200$. Thus, transverse

[208] S. Torquato *Random heterogeneous materials: microstructure and macroscopic properties* Springer, 2002
[209] D. J. Gunn and C. Pryce. *Trans. Inst. Chem. Eng.*, 47, T341, 1969.

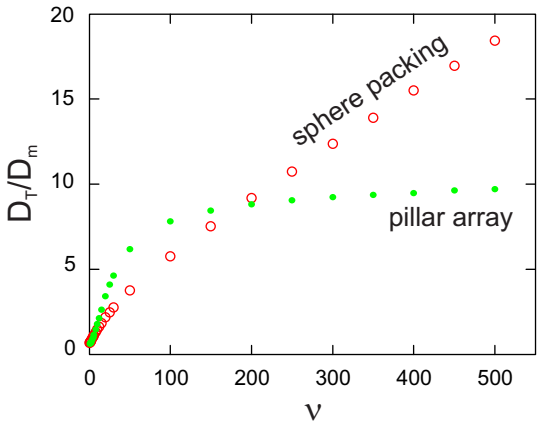

Figure 2.11: Dependence of the normalized asymptotic transverse dispersion coefficient $D_{\mathrm{T}}/D_{\mathrm{m}}$ on the reduced velocity $\nu = u_{\mathrm{av}} d_{\mathrm{p}}/D_{\mathrm{m}}$ for the bulk sphere packing and the bulk pillar array (d_{p} is the particle or pillar diameter, respectively). Dispersion in the array is recorded perpendicular to the pillar axis.

dispersion in the regular pillar array shows a very weak velocity-dependence at $\nu > 200$ and manifests itself as a pseudo-diffusive mechanism; however, with a faster transverse equilibration (characterized by $D_{\mathrm{T}} \approx 10 D_{\mathrm{m}}$) than achieved by pure molecular diffusion (D_{m}). This development of D_{T} towards an asymptotic value[161] is reflected in the plate height curves of Figure 2.10A, where the consequences of the transverse dispersion process are again most apparent for the fully confined pillar array (black crosses). For $\nu < 50$, transverse dispersion increases noticeably with the velocity (Figure 2.11). The increase of D_{T} to some extent counteracts the increase of D_{L}, i.e., the increased transverse dispersion (and faster equilibration) moderates the extent of longitudinal dispersion. As a consequence, the plate height data show only a small increase with velocity, resulting in the wide, shallow plate height minimum at $\nu = 5 - 50$ (black crosses in Figure 2.10A). For $50 < \nu < 200$, the velocity-dependence of transverse dispersion weakens ($D_{\mathrm{T}}/D_{\mathrm{m}}$-data in Figure 2.11 taper off strongly) and the slope of the plate height curve in Figure 2.10A increases. When at $\nu > 200$ transverse dispersion is almost velocity-independent (Figure 2.11), plate height data (black crosses in Figure 2.10A) increase linearly with velocity, as expected for mobile phase mass transfer resistance characterized by a constant diffusivity or, as here, a (nearly) constant transverse dispersivity.

Whereas transverse equilibration of tracers perpendicular to the pillar axis occurs through transverse dispersion, which may or may not be velocity-dependent as analyzed with Figure 2.11, transverse equilibration parallel to the pillar axis (between top and bottom walls of the confined arrays) occurs – at any velocity – solely by molecular diffusion. The situation in the regular pillar arrays, where we either have a constant transverse diffusivity or a flow-rate dependent, but at higher flow rates also constant transverse dispersivity,[161] contrasts with the monotonous increase of $D_{\mathrm{T}}/D_{\mathrm{m}}$ over the whole velocity range observed for random sphere packings (Figure 2.11). Consequently, transverse dispersion in random sphere packings remains flow-rate dependent at higher velocities and is thus a more efficient moderator of longitudinal dispersion than the velocity-independent transverse diffusivity or dispersivity in regular pillar arrays. Thus, the plate

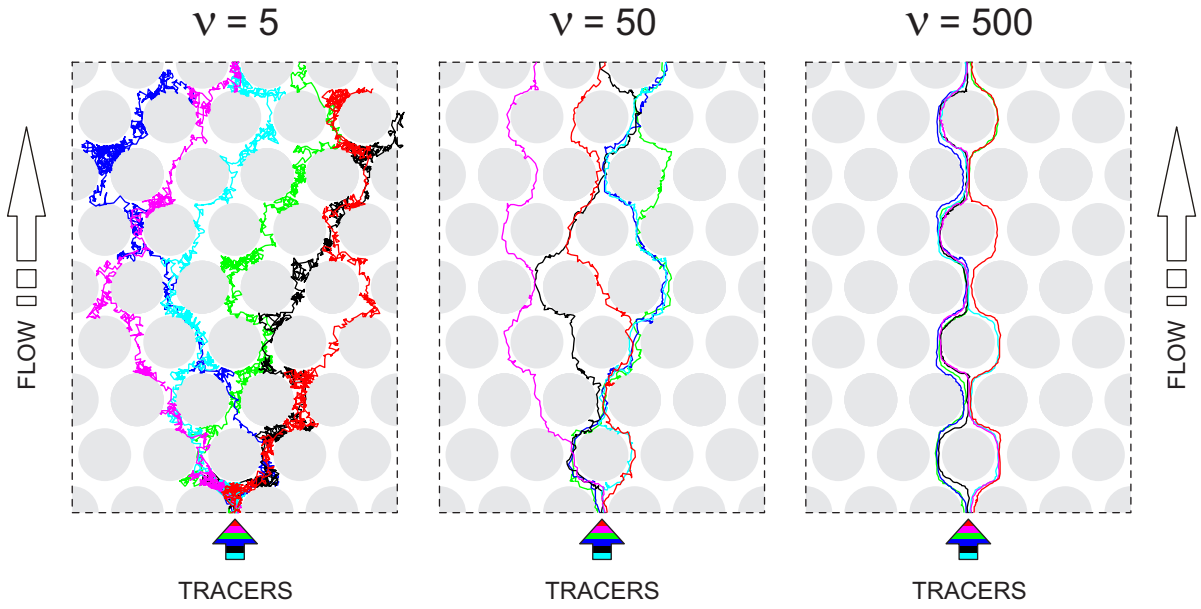

Figure 2.12: Tracer trajectories in a two-dimensional hexagonal pillar array ($\varepsilon = 0.40$) at reduced velocities of $\nu = 5$, 50, and 500, illustrating the velocity-dependent, effective interplay between longitudinal advection and transverse diffusion. Six color-coded tracers were released at the same location (as indicated by the striped arrow) and their pathways within the predefined section (fixed spatial window) monitored.

height contribution from transcolumn dispersion in the confined sphere packings, which depends on the rate of transverse equilibration between the involved velocity extremes, tapers off at higher velocities ($\nu_{1/2,3} > 200$, Figure 2.7), whereas the plate heights of the confined pillar array show a linear velocity-dependence at higher velocities (Figure 2.10A, black crosses, $\nu > 200$).

To visualize the interplay between longitudinal advection and transverse diffusion behind the transverse dispersion behavior of the regular pillar array (Figure 2.11) at the scale of individual tracers, we recorded tracer trajectories at low, medium, and high velocities ($\nu = 5$, 50, and 500; Figure 2.12). Six color-coded tracers were simultaneously released in the central pore at the selected pillar array section's upstream border ("starting point" at the bottom; indicated by the striped arrow), and their paths due to fluid flow (the macroscopic flow direction is from bottom to top in Figure 2.12) and diffusion were monitored, until the downstream border of the selected section ("finish line" at the top) was reached. Because tracers reach the downstream border faster at higher velocities, trajectories for larger values of ν in Figure 2.12 correspond to a shorter time scale. Comparison of trajectories over comparable distances, i.e., within a fixed spatial window instead of a fixed temporal domain, better visualizes the developing diffusion-limitation to transverse dispersion with increasing velocity. At low velocities ($\nu = 5$, left panel of Figure 2.12), diffusion is an effective mechanism for lateral exchange between flow streamlines from neighboring pores. The coupling of diffusion and advection spans a velocity-responsive network of longitudinal and lateral mass transport (due to the circular pillar shape the pore walls are curved, so that longitudinal as well as lateral velocity components exist at the pillar array's pore scale). An increase of ν results in an increase of lateral advective mixing, which

together with the diffusive coupling explains the increase of D_T/D_m with ν in Figure 2.11 at low velocities. At high velocities ($\nu = 500$, right panel of Figure 2.12), tracer motion due to longitudinal advection between individual pillars is so fast that transverse diffusion enables only comparatively small jumps, which are ineffective to further increase lateral mixing with the velocity. Within the fixed spatial window visible in Figure 2.12, tracers adhere to the bundle of streamlines into which they were released originally and undergo stream splitting and merging along the row of pillars behind the tracers' starting point. Eventually, tracers hop into neighboring streamlines by diffusion, but to visualize this process at $\nu = 500$, the observation window would have to be much longer.

Figure 2.12 illustrates the diffusion-limitation of the regular pillar arrays clearly: at high reduced velocities lateral mixing across the streamlines occurs only by diffusion, unaffected by the velocity. This explains the near-asymptotic regime in Figure 2.11, where the D_T/D_m-values become almost constant ($D_T/D_m \approx 10$ for $\nu > 200$). As a result, the longitudinal dispersion coefficients D_L/D_m grow quadratically with the velocity (and plate heights linearly), similar to Taylor-Aris dispersion in an open tube.[16,174] (But D_T/D_m levels off at a significantly higher value than for pure diffusion, because lateral velocity components in the pillar array increase lateral equilibration at the pore scale.) The microstructure of the pillar array plays a key role behind that behavior: Unlike a random sphere packing the regular pillar array cannot function as a mixer, which explains the observed difference in the velocity-dependence of D_T/D_m compared with random sphere packings (Figure 2.11). In a regular pillar array diffusion lets a tracer forget its initial position (cf. Figure 2.12), whereas in a random sphere packing the tracer experiences a stochastic velocity, which becomes uncorrelated as soon as a sufficient length of streamline has been traversed.[161]

The tracer dynamics of Figure 2.12 complement the averaged transverse dispersion data of Figure 2.11 and explain the slopes of the plate height curves in Figure 2.10 for the pillar arrays, particularly the linear dependence of the reduced plate height on the reduced velocity for $\nu > 200$. Our analysis shows that fluid dispersion in regular pillar arrays does not resemble eddy dispersion in random sphere packings. This is also the reason why we did not present best fits of any form of the Giddings equation or other familiar plate height equations (or correlations) to the data in Figure 2.10. Whereas the Giddings equation as well as the Knox correlation describe the *bending* of the plate height curves of random sphere packings at higher velocities,[66,146] they do not capture the nature of the transverse dispersion behavior behind longitudinal dispersion and the plate height curves of regular pillar arrays. These plate height curves approach a *constant slope* (linear increase of h with ν) as transverse dispersion becomes velocity-independent (Figure 2.10 and Figure 2.11). The statement that the Knox equation remains valid for regular pillar arrays[201] is therefore unfounded from a fundamental, hydrodynamic point of view. In our present study, the fitting of the Knox equation to the comprehensive data sets in Figure 2.10 resulted in obvious, systematic deviations, whereas application of the Giddings equation provided eddy dispersion parameters (λ_i and ω_i) without physical meaning. Schure et al.[152] have reached similar conclusions about dispersion in ordered packed beds.

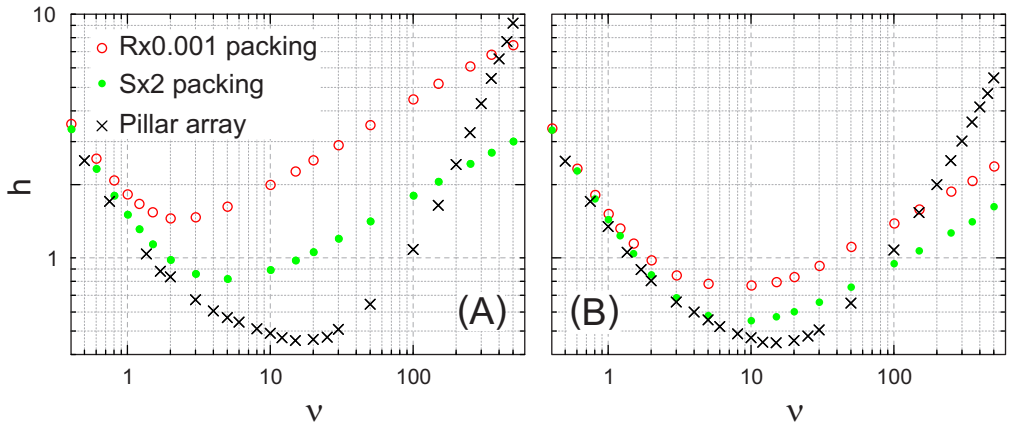

Figure 2.13: Comparison of plate height curves for confined cylindrical sphere packings and fully confined pillar arrays at $\varepsilon = 0.40$. (A) Confined beds of Figure 2.2 with a cross-sectional area of $100\,\pi d_\mathrm{p}^2$, corresponding to a particle-aspect ratio of 20 for the cylindrical packings and a channel width-to-height ratio of 40 for the confined array. (B) Confined beds of Figure 2.3 with a cross-sectional area of $25\,\pi d_\mathrm{p}^2$, a particle-aspect ratio of 10 for the cylindrical packings, and a channel width-to-height ratio of 10 for the confined array. Confined random sphere packings were generated with different degrees of microstructural heterogeneity (Rx0.001 $\gg$ Sx2) induced by systematic variations of the packing protocol.

2.3.3 Comparison of confined sphere packings and pillar arrays

In Figure 2.13 we compare the separation efficiencies ($h - \nu$ curves) of confined cylindrical sphere packings and confined pillar arrays under the condition of identical porosity ($\varepsilon = 0.40$) and cross-sectional area as well as laterally fully equilibrated wall and corner effects over a wide velocity range ($0.5 \leq \nu \leq 500$). In particular, Figure 2.13A contains the data obtained for the chromatographic beds with a cross-sectional area of $100\,\pi d_\mathrm{p}^2$ (i.e., a particle-aspect ratio of 20 for the cylindrical packings), and Figure 2.13B shows the data for the smaller dimensioned beds (Figure 2.3) with a cross-sectional area of $25\,\pi d_\mathrm{p}^2$ (i.e., a particle-aspect ratio of 10 for the cylindrical packings). The effect of the varied packing generation parameters on the final packing microstructure and the plate height curves is reflected in the data range spanned by the Rx0.001 and the Sx2 packing types (cf. Section 2.3.1.3 and Figure 2.9). For the smaller particle-aspect ratio (Figure 2.13B), the difference in plate heights between the more homogeneous Sx2-packings and the less homogeneous Rx0.001-packings narrows, and the plate height curves are lower than for the larger particle-aspect ratio (Figure 2.13A). The lower particle-aspect ratio implies that the wall region (characterized by porosity oscillations over a distance of $\sim 5\ d_\mathrm{p}$ from the cylinder wall towards the bulk due the geometrical wall effect) constitutes a larger fraction of the overall cross-section, so that these packings are effectively more homogeneous. This results in lower plate heights and damps the impact of the packing generation parameters on morphology (and separation efficiency), because the influence of the bulk properties ultimately disappears. Thus, the restraint the geometrical confinement and accompanying wall effect places on the possible positions of spheres forces random sphere packings from different generation protocols to become more homogeneous as well as more similar to each other. Because reducing the channel width-to-height ratio from 40 (Figure 2.13A) to 10 (Figure 2.13B) has no effect on

the ordered microstructure of the regular pillar arrays, their plate height curves are much less affected than those of the random sphere packings by decreasing confinement dimensions.

The confined pillar arrays are superior to the cylindrical sphere packings over most of the velocity range shown in Figure 2.13. However, the plate height curves of the pillar arrays come out of the minimum with a much steeper slope than those of the sphere packings and finally overtake them at higher velocities. For the larger beds in Figure 2.13A, this occurs at rather high velocities ($\nu \approx 180$ and $\nu \approx 450$ for the Sx2- and the Rx0.001-packing, respectively), but when the bed dimensions are decreased to a cross-sectional area of $25\,\pi d_\mathrm{p}^2$ (Figure 2.13B), the difference between random sphere packings and regular pillar arrays decreases, and the velocity at which arrays and packings are comparable is down to $\nu \approx 60-150$. For chromatographic praxis, Figure 2.13 implies that regular pillar arrays have better efficiency than random sphere packings for HPLC separations of small analytes (typically $\nu < 30$), but not for the envisioned high-speed analyses of larger analytes, e.g., fast bioseparations. For example, at an average velocity of $u_\mathrm{av} = 5$ mm/s, a pillar diameter of $d_\mathrm{p} = 5$ µm, and a diffusivity of $D_\mathrm{m} = 1.510^{-10}\mathrm{m}^2/\mathrm{s}$ (comparable to the bulk diffusion coefficients of insulin or lysozyme in typical mobile phases[87]), the reduced velocity of $\nu = u_\mathrm{av} d_\mathrm{p}/D_\mathrm{m} = 166.7$ puts the separation into a regime, where the plate heights of the pillar arrays are already comparable to those of the sphere packings (Figure 2.13).

Our analysis of the dispersion behavior of pillar arrays shows that their regular microstructure can be beneficial or problematic:[90] The absence of mechanical mixing capabilities reduces longitudinal dispersion at lower velocities compared with random sphere packings, but limits transverse equilibration at higher velocities, which strikes back onto longitudinal dispersion. Regular pillar arrays differ fundamentally from random sphere packings in their dispersion-scaling at higher velocities: Lateral mixing in confined pillar arrays occurs by purely diffusive (along the pillar axis) or pseudo-diffusive (perpendicular to the pillar axis) dynamics, which results in a steep, linear rise of the plate heights with the velocity, whereas lateral mixing in confined sphere packings is due to a coupling of transverse diffusion and spatial velocity fluctuations (absent in regular pillar arrays), a mechanism that remains “flow-responsive” (velocity-dependent) and causes the bending (tapering off) of the plate height curves.

2.4 Summary and conclusions

To quantify the impact of the macroscopic confinement of chromatographic supports on flow heterogeneity and the resulting dispersion, we investigated flow and mass transport in computer-generated bulk and confined (i) random packings of monosized, solid (nonporous), spherical particles, and (ii) hexagonal arrays of monosized, solid cylinders (pillar arrays) over a wide range of reduced velocities ($0.5 \leq \nu \leq 500$). Comprehensive data sets were obtained with a quantitative numerical analysis scheme comprising (i) the generation of bulk and confined packings by a modified Jodrey-Tory algorithm, (ii) three-dimensional flow field calculations by

[87] F. Gritti et al. *J. Chromatogr. A*, 1217, pp. 1589–603, 2010.

[90] S. G. Weber and P. W. Carr “High Performance Liquid Chromatography” in: ed. by P. R. Brown and R. A. Hartwick John Wiley & Sons, 1989 chap. 1

the lattice-Boltzmann method, and (iii) modeling of advective-diffusive transport with a random-walk particle-tracking technique. Programs were implemented and scaled on publicly accessible supercomputing platforms. We employed a basic set of confined sphere packings with identical cross-sectional area and bed porosity ($\varepsilon = 0.40$), to quantify the impact of the confinement geometry (circular, rectangular, and semicircular), to study the influence of packing-protocol induced microstructural disorder and of the particle-aspect ratio (20 and 10), and to evaluate the general consequences of the confinement-induced porosity and velocity heterogeneity on dispersion.

Transient behavior of longitudinal and transverse dispersion was analyzed and the time scale of asymptotic dispersion correlated with the spatial scales of heterogeneity in bulk and confined sphere packings. For the cylindrical packings asymptotic longitudinal dispersion is achieved on a time scale proportional to the square of the column radius, but transverse dispersion decays to zero on a time scale proportional to the square of the column diameter, i.e., four times more slowly. The reduced conduit cross-sectional symmetry from circular to rectangular to semicircular geometry at constant cross-sectional area resulted in an increased characteristic transverse length of the velocity field and the associated dispersion. This length characterizes the straight lateral distance through a packing that needs to be covered by the tracers for complete exchange between different velocities.

The velocity-dependence of asymptotic longitudinal dispersion as reflected in the plate height curves was analyzed with the comprehensive Giddings equation, which was carefully adapted to the confined packings Eq. (2.20) based on insight gained from the bulk packings. Due to the geometrical wall effect and the presence of corners in the noncylindrical packings, a significant transcolumn contribution to eddy dispersion could be resolved and analyzed. The extremes values of the velocities characterizing the transcolumn velocity bias increase from circular to rectangular to semicircular geometry, because (i) the channels in the corners of the semicircular geometry are more extended and display higher flow velocity than the channels in the corners of the rectangular geometry, and (ii) the semicircle has the lowest symmetry among the investigated geometries and a longer characteristic transverse length.

Confined random sphere packings were compared with confined regular pillar arrays under the condition of identical bed porosity ($\varepsilon = 0.40$), conduit cross-sectional area ($100\pi d_{\mathrm{p}}^2$ or $25\pi d_{\mathrm{p}}^2$), as well as laterally fully equilibrated geometrical wall and corner effects on dispersion, to quantify the actual separation efficiency loss for microscopically regular and random chromatographic media upon macroscopic confinement. We showed that the plate height curves of regular pillar arrays are more affected by the confinement than those of the random sphere packings, and that fluid dispersion in the pillar arrays does not resemble eddy dispersion in random packings. The plate height curves of the pillar arrays were analyzed and explained in detail on the basis of the transverse dispersion behavior, illustrated with tracer trajectories. Whereas the Giddings equation and the Knox correlation describe the bending (tapering off) of the plate height curves at higher velocities for random packings due to the coupling of transverse diffusion and spatial velocity fluctuations, they do not capture the nature of the transverse dispersion behavior behind

longitudinal dispersion for regular arrays. Instead of tapering off, the plate height curves of the pillar arrays increase to approach a constant, steep slope as transverse dispersion becomes velocity-independent (pseudo-diffusive). The regular microstructure of a pillar array plays a key role in that regard, because it cannot function as a mechanical mixer like a random sphere packing. As a result, longitudinal dispersion grows quadratically with the velocity, like Taylor-Aris dispersion in a tube. This pseudo-diffusive behavior (linear plate height increase with velocity) is amplified upon confinement and can outweigh the performance advantage of a regular pillar array over a random sphere packing.

Acknowledgement

This work was supported by the Deutsche Forschungsgemeinschaft DFG (Bonn, Germany) under grants TA 268/4-1 and TA 268/5-1. Computational resources on IBM BlueGene/P platforms were provided by “Genius“ at RZG (Rechenzentrum Garching, Germany) and “Jugene“ at FZJ (Forschungszentrum Jülich, Germany). We thank the DEISA Consortium (www.deisa.eu) cofunded through the EU FP6 project RI-031513 and the FP7 project RI-222919 for support within the DEISA Extreme Computing Initiative. We are also grateful to the Jülich Supercomputing Centre (JSC) for allocation of a special CPU-time grant (project HMR10).

Chapter 3

From random sphere packings to regular pillar arrays: Analysis of transverse dispersion

Authors:

Anton Daneyko, Dzmitry Hlushkou, Siarhei Khirevich, and Ulrich Tallarek

State of publication:

Published August 14, 2012 in Journal of Chromatography A, Vol. 1257, pp 98–115
DOI: 10.1016/j.chroma.2012.08.024

Abstract

We study the impact of microscopic order on transverse dispersion in the interstitial void space of bulk (unconfined) chromatographic beds by numerical simulations of incompressible fluid flow and mass transport of a passive tracer. Our study includes polydisperse random sphere packings (computer-generated with particle size distributions of modern core–shell and sub-2 μm particles), the macropore space morphology of a physically reconstructed silica monolith, and computer-generated regular pillar arrays. These bed morphologies are analyzed by their velocity probability density distributions, transient dispersion behavior, and the dependence of asymptotic transverse dispersion coefficients on the mobile phase velocity. In our work, the spherical particles, the monolith skeleton, and the cylindrical pillars are all treated as impermeable solid phase (nonporous) and the tracer is unretained, to focus on the impact of microscopic order on flow and (particularly transverse) hydrodynamic dispersion in the interstitial void space. The microscopic order of the pillar arrays causes their velocity probability density distributions to start and end abruptly, their transient dispersion coefficients to oscillate, and the asymptotic transverse dispersion coefficients to plateau out of initial power law behavior. The microscopically disordered beds, by contrast, follow power law behavior over the whole investigated velocity

range, for which we present refined equations (i.e., Eq. (3.13) and the data in Table 3.2 for the polydisperse sphere packings; Eq. (3.17) for the silica monolith). The bulk bed morphologies and their intrinsic differences addressed in this work determine how efficient a bed can relax the transverse concentration gradients caused by wall effects, which exist in all confined separation media used in chromatographic practice. Whereas the effect of diffusion on transverse dispersion decreases and ultimately disappears at increasing velocity with the microscopically disordered chromatographic beds, it dominates in the pillar arrays. The pillar arrays therefore become the least forgiving bed morphology with macroscopic heterogeneities and the engendered longitudinal dispersion in chromatographic practice. Wall effects in pillar arrays and the monolith caused by their confinement impact band broadening, which is traditionally observed on a macroscopic scale, more seriously than in the packings.

3.1 Introduction

In chromatography, the height equivalent to a theoretical plate (H) is defined as the slope of the dependence of the variance of an analyte band (σ^2) on its migration distance. In a first approximation, assuming a homogeneous chromatographic bed and an incompressible mobile phase, this slope (hence H) is constant along the column. A similar definition applies to the band broadening in longitudinal ($z-$) and transverse directions, i.e., parallel and perpendicular with respect to the macroscopic flow direction. Longitudinal and transverse dispersion coefficients D_L and D_T usually discussed in the engineering literature[98] are related to the chromatographic plate heights H_L and H_T by[66]

$$D_\mathrm{L} = \frac{H_\mathrm{L} u_\mathrm{av}}{2} = \frac{h_\mathrm{L} \nu D_\mathrm{m}}{2} = \frac{u_\mathrm{av}}{2} \cdot \frac{\partial \sigma_\mathrm{L}^2}{\partial z}, \tag{3.1}$$

and

$$D_\mathrm{T} = \frac{H_\mathrm{T} u_\mathrm{av}}{2} = \frac{h_\mathrm{T} \nu D_\mathrm{m}}{2} = \frac{u_\mathrm{av}}{2} \cdot \frac{\partial \sigma_\mathrm{T}^2}{\partial z}, \tag{3.2}$$

where h is the reduced plate height and ν is the reduced velocity, which characterizes the ratio of longitudinal advective to diffusive transport in a chromatographic bed (u_av is the average mobile phase velocity through the bed and D_m is the analyte's diffusion coefficient in the bulk fluid). Importantly, the band broadening in longitudinal direction controls the resolution between the peaks of the different components of the sample and is of paramount importance in all applications of chromatography; band broadening in the transverse direction controls the lateral homogeneity of the band and relaxes concentration gradients caused by nonuniform distributions of the local velocity.[90,146]

[98] J. M. P. Q. Delgado. *Heat Mass Transfer*, 42, pp. 279–310, 2006.
[66] J. C. Giddings *Dynamics of Chromatography: principles and theory* Marcel Dekker, 1965
[90] S. G. Weber and P. W. Carr "High Performance Liquid Chromatography" in: ed. by P. R. Brown and R. A. Hartwick John Wiley & Sons, 1989 chap. 1
[146] G. Guiochon. *J. Chromatogr. A*, 1126, pp. 6–49, 2006.

As an analyte zone migrates along a chromatographic bed, it is dispersed in longitudinal and transverse directions by a combination of diffusive and advective processes. When a streamlet hits, e.g., a particle in a randomly packed bed, it splits into several, unequal streamlets that flow around the hit particle, between it and its different neighbors, and merge with other different streamlets of similar origin. Thus, the migration of the mobile phase along a packed column is accompanied by the constant shearing and merger of streamlets. This process is involved in the eddy dispersion contribution to longitudinal dispersion; it is also the essential source of transverse dispersion, because transverse diffusion in the new streamlets and a cascade succession of similar events at each additional particle promote transverse dispersion. In this case, the process is known as "stream-splitting". Because the streamlets are much smaller than the particles between which they flow, transverse dispersion causes rapid local homogenization of the stream composition. However, in the absence of significant transverse advection, homogenization is extremely slow at the column scale, where it relaxes transcolumn concentration gradients that arise from macroscopic variations in the local flow velocity. This implies that at least two fundamental length and time scales exist for eddy dispersion and the associated transverse equilibration between different velocities of the flow field in a confined chromatographic bed: the pore (short-time) scale and the confinement or transcolumn (long-time) scale.[67,97]

If a chromatographic bed (e.g., an *in situ* prepared monolith, a slurry-packed column, or a microfabricated pillar array) is macroscopically inhomogeneous, which is usually related to its confinement, it will show a transcolumn flow heterogeneity. This, in turn, leads to the formation of transverse concentration gradients, which are eventually relaxed with transverse dispersion. Recent work of Gritti and Guiochon[148,193] has provided an in-depth analysis of transcolumn dispersion in packed chromatographic columns. In particular, they demonstrated that transcolumn concentration gradients relax differently depending on whether the bed is made of porous or nonporous particles. When the particles are porous, the analytes can diffuse either through the interparticle void space or through the intraparticle pores (impossible with nonporous particles). The diffusion flux across a particle is the sum of the contributions of diffusion through the mobile phase contained in the pores of the particle and of surface diffusion (along the adsorbent surface).[210,211] The latter contribution increases rapidly with increasing concentration gradient along this surface, hence the diffusion flux increases rapidly with increasing retention of the analyte. Furthermore, the time spent by the analytes in the column is longer when the particles are porous. Thus, transverse concentration gradients are more effectively relaxed. Gritti and Guiochon[148,193] presented a new model of transcolumn eddy dispersion based on Giddings' coupling theory for diffusive and flow mechanisms,[66] in which transcolumn flow profiles were approximated with experimental data and also the importance of surface diffusion (enhancing the rate of mass trans-

[67] S. Khirevich et al. *Anal. Chem.*, 81, pp. 7057–7066, 2009.
[97] R. S. Maier et al. *Phys. Fluids*, 15, pp. 3795–3815, 2003.
[148] F. Gritti and G. Guiochon. *AIChE J.*, 56, pp. 1495–1509, 2010.
[193] F. Gritti and G. Guiochon. *J. Chromatogr. A*, 1217, pp. 6350–65, 2010.
[210] K. Miyabe. *J. Chromatogr. A*, 1183, pp. 49–64, 2008.
[211] F. Gritti and G. Guiochon. *AIChE J.*, 57, pp. 346–358, 2011.

fer through porous particles, along the adsorbent surface) was accounted for. To summarize, the impact of transcolumn velocity biases is minimized when the pores of the particles are accessible; it decreases with increasing retention and transverse dispersion coefficient of the analytes.

Transcolumn velocity biases of different origin can be a serious problem with all kinds of chromatographic beds. For example, the presence of two wall effects has been reported for slurry-packed columns:[96,105] (i) Stress and strain that take place in the bed during the slurry packing process and bed consolidation cause the distribution of mobile phase velocities across the column to become heterogeneous.[64,104,106] Consequently, the sample zones warp during elution and concentration gradients build up.[95,212] This frictional wall effect is traditionally discussed in connection with analytical and preparative columns. (ii) A geometrical wall effect[101,213] dominates the kinetic column performance at low column-to-particle diameter ratio, which becomes important for packed capillaries[214] and microchips.[119,134] In general, both wall effects contribute to the bed morphology, but depending on the actual column-to-particle diameter ratio either wall effect may dominate the macroscopic velocity heterogeneity and transcolumn eddy dispersion.

Compared with packed (particulate) beds, transcolumn velocity biases in silica monoliths are caused by their radial heterogeneity, which is supposed to stem from chemical and/or temperature gradients that form across the column bed during the monolith preparation.[215] Also, strain resulting from the stress caused by the shrinkage of the monolithic rod after formation of a solid network may cause the interface between monolith and column wall to break due to inelastic deformations. The monolith may separate from the wall causing slightly higher local porosities in the wall region. By placing electrochemical detectors at various points of the cross-section at the column exit of semi-preparative (10 mm i.d.) and analytical (4.6 mm i.d.) silica monoliths, Guiochon and co-workers[216,217] found 4% and 1.5% velocity difference, respectively, between the wall and the core region. Even at only a few percent, morphological differences, e.g., in local macroporosity, cause a noticeable loss of separation efficiency. Another, severe form of radial heterogeneity occurs in capillary monoliths: As opposed to larger-diameter monolithic rods, capillary monoliths are prepared directly in the tube then used for chromatographic separations; so that gaps where the bed has snapped back from the wall allow the mobile phase to bypass

[96] S. Bruns and U. Tallarek. *J. Chromatogr. A*, 1218, pp. 1849–60, 2011.
[105] R. A. Shalliker, B. S. Broyles, and G. Guiochon. *J. Chromatogr. A*, 888, pp. 1–12, 2000.
[64] B. G. Yew et al. *AIChE J.*, 49, pp. 642–664, 2003.
[104] G. Guiochon, E. Drumm, and D. Cherrak. *J. Chromatogr. A*, 835, pp. 41–58, 1999.
[106] R. A. Shalliker et al. *J. Chromatogr. A*, 977, pp. 213–223, 2002.
[95] F. Gritti and G. Guiochon. *Chem. Eng. Sci.*, 65, pp. 6327–6340, 2010.
[212] F. Gritti and G. Guiochon. *J. Chromatogr. A*, 1218, pp. 1592–602, 2011.
[101] A. de Klerk. *AIChE J.*, 49, pp. 2022–2029, 2003.
[213] G. E. Mueller. *Powder Technol.*, 159, pp. 105–110, 2005.
[214] S. Bruns et al. *Anal. Chem.*, 84, pp. 4496–503, 2012.
[119] S. Jung et al. *J. Chromatogr. A*, 1216, pp. 264–273, 2009.
[134] S. Ehlert et al. *Anal. Chem.*, 80, pp. 5945–5950, 2008.
[215] G. Guiochon. *J. Chromatogr. A*, 1168, 101–68; discussion 100, 2007.
[216] K. S. Mriziq et al. *J. Chromatogr. A*, 1193, pp. 97–103, 2008.
[217] J. A. Abia, K. S. Mriziq, and G. A Guiochon. *J. Chromatogr. A*, 1216, pp. 3185–91, 2009.

the bed.[182] Efforts directed against this problem have been reported recently for capillary[180,218–221] and analytical[222–224] silica monoliths.

Compared to microscopically disordered, macroscopically inhomogeneous packings and monoliths, even microscopically ordered pillar arrays suffer from substantial wall effects as we distort the perfect microstructure by a macroscopic confinement. The concept of pillar arrays as spatially periodic porous media has to be altered when these stationary phases are used as chromatographic supports, because the inevitable confinement engenders a macroscopic heterogeneity, which affects the dispersion behavior and thus the efficiency of the array for separations in liquid chromatography.[225] The effect of a straightforward confinement (resulting in a rectangular bed cross-section and side walls containing a layer of embedded half cylinders) on hydrodynamic dispersion is illustrated with Figure 3.1. We employ numerical simulations of the transient normalized longitudinal hydrodynamic dispersion coefficient obtained with a passive (nonadsorbing, nonreacting) tracer in the inertstitial void space between nonporous pillars of diameter d_p.[225] Upon confinement of the pillar array, the no-slip velocity boundary condition at the surface of the top and bottom as well as the two side walls causes flow and transport to become macroscopically inhomogeneous. The transcolumn velocity bias is generated parallel to the pillar axis (by the top and bottom walls) as well as perpendicular to it (due to the side walls). To obtain reliable plate height data the dispersion simulations require consideration of the complete three-dimensional geometry of the confined array to take proper account of the four newly created $90°$-corners.[225] Starting from an unconfined, i.e., bulk regular pillar array, simulated as a single unit cell with periodic boundary conditions, we first add top and bottom walls (indicated in the upper right panel of Figure 3.1 by the semi-transparent faces), and then complete the confinement with the addition of side walls. The two fully confined exemplary pillar arrays in Figure 3.1 (with a height of $2.8\ d_\mathrm{p}$ each and a width of $28.37\ d_\mathrm{p}$ and $112.27\ d_\mathrm{p}$, respectively) are flat, rectangular boxes with channel width-to-height ratios typically found on microchips.[145]

Importantly, Figure 3.1 illustrates that the asymptotic dispersion coefficient at the selected velocity of $\nu = u_\mathrm{av} d_\mathrm{dom}/D_\mathrm{m} = 61.5$ (d_dom is the domain size of a pillar array taken as the sum of d_p and the shortest interpillar distance) increases from $D_\mathrm{L}/D_\mathrm{m} = 1.75$ for the bulk pillar array (blue curve in Figure 3.1) to 6.64 for top-bottom confined pillar array (black curve) to ca. 16.2 for both fully confined pillars (overlaid red and green horizontal lines). Thus, the dispersion coefficients and the corresponding plate heights increase by a factor of ~ 9 when we progress

[182] D. Hlushkou et al. *Anal. Chem.*, 82, pp. 7150–9, 2010.
[180] S. Bruns et al. *J. Chromatogr. A*, 1218, pp. 5187–94, 2011.
[218] K. Kanamori et al. *J. Sep. Sci.*, 27, pp. 874–886, 2004.
[219] M. Motokawa et al. *J. Sep. Sci.*, 29, pp. 2471–2477, 2006.
[220] R. Roux, M. Abi Jaoudé, and C Demesmay. *J. Chromatogr. A*, 1216, pp. 3857–63, 2009.
[221] T. Hara et al. *J. Chromatogr. A*, 1217, pp. 89–98, 2010.
[222] K. Hormann et al. *J. Chromatogr. A*, 1222, pp. 46–58, 2012.
[223] F. Gritti and G. Guiochon. *J. Chromatogr. A*, 1225, pp. 79–90, 2012.
[224] F. Gritti and G. Guiochon. *J. Chromatogr. A*, 1227, pp. 82–95, 2012.
[225] A. Daneyko et al. *J. Chromatogr. A*, 1218, pp. 8231–48, 2011.
[145] L. C. Taylor, N. V. Lavrik, and M. J. Sepaniak. *Anal. Chem.*, 82, pp. 9549–56, 2010.

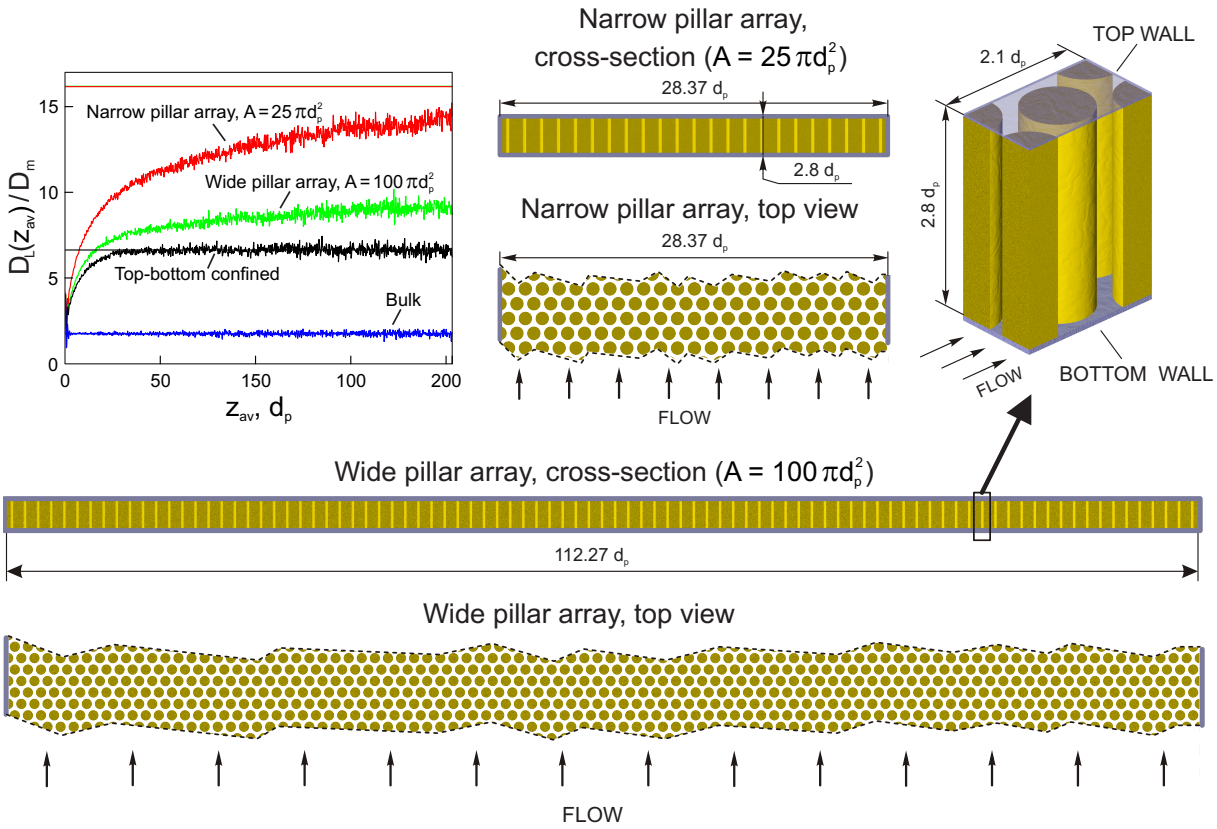

Figure 3.1: Influence of the macroscopic confinement on longitudinal dispersion in hexagonal arrays of solid (nonporous), cylindrical pillars at a bed porosity (interstitial void volume fraction) of $\varepsilon = 0.40$. The graph compares transient longitudinal dispersion as well as the corresponding asymptotic values (horizontal lines) for a bulk pillar array (blue curve), which represents an unconfined pillar array without walls, with a top-bottom confined pillar array of $2.8\ d_\mathrm{p}$ height (illustrated in the top right panel of the figure; black curve and line in the graph) and two fully confined pillar arrays with a width (cross-sectional area A) of $28.37\ d_\mathrm{p}$ ($25\ \pi d_\mathrm{p}^2$) and $112.27\ d_\mathrm{p}$ ($100\ \pi d_\mathrm{p}^2$), respectively (d_p is the pillar diameter). Top and cross-sectional views onto the confined pillar arrays are provided in the figure. Their side walls contain a layer of embedded half cylinders, reflecting a simple, regular truncation of the microstructure at the unit cell boundaries upon confinement. Dimensionless longitudinal dispersion coefficients $D_\mathrm{L}(z_\mathrm{av})/D_\mathrm{m}$ are plotted as a function of the longitudinal ($z-$) position of the center of gravity of the tracer ensemble z_av (in d_p). The reduced velocity is $\nu = u_\mathrm{av} d_\mathrm{dom}/D_\mathrm{m} = 61.5$ (d_dom is the domain size taken as the sum of d_p and the shortest interpillar distance). Asymptotic values $D_\mathrm{L}/D_\mathrm{m}$ of the two fully confined pillar arrays are identical (overlaid red and green horizontal lines at $D_\mathrm{L}/D_\mathrm{m} = 16.2$), because of their identical height. Due to their different widths, however, they realize asymptotic behavior after different times.

from the bulk pillar array (which is a mathematical abstraction) to the fully confined arrays. In addition, asymptotic dispersion for the fully confined, wide array (with a width of $112.27\,d_\mathrm{p}$ and a cross-sectional area of $A = 100\,\pi d_\mathrm{p}^2$) is reached after the center of gravity of the tracer ensemble has travelled downstream by a distance of $\sim 15,700\,d_\mathrm{p}$ with the flow. Only then does the green curve in Figure 3.1 coincide with its horizontal asymptote (at $D_\mathrm{L}/D_\mathrm{m} = 16.2$). Our analysis demonstrates that the simple addition of confining walls to a pillar array with regular microstructure, even with side walls containing a layer of embedded half cylinders, already changes dramatically time and length scales of dispersion as well as the asymptotic dispersion coefficients and plate heights associated with the new transcolumn velocity bias.

This effect is enhanced when the side wall regions cannot be prepared homogeneously and even differ from each other, as reported by Op de Beeck et al.[226]. In that case, the whole width of the confined pillar array is required to relax the (also nonsymmetrical) transcolumn concentration gradients seen in an unsymmetrical warping of the sample zones over the whole width of the microchip (see, e.g., Figure 6 in [226]). The dramatic consequences of these nonsymmetrical side wall effects in confined pillar arrays for dispersion are similar to those observed earlier with capillary silica monoliths,[182] where local gaps have formed irregularly along the column and its circumference. This wall effect has a noncylindrical symmetry, so that the capillary diameter as opposed to the capillary radius is the characteristic equilibration length for transcolumn eddy dispersion.[67]

The preceding discussion highlights the insurmountable evidence for wall effects in modern chromatographic supports and their impact on kinetic performance of HPLC columns. It has also indicated the key role played by transverse dispersion in the mass transfer across the beds, relaxing the transverse concentration gradients that are caused by the various transcolumn velocity biases. The efficient transverse relaxation of concentration gradients in the interstitial void space of a chromatographic bed specifically addresses the bed morphology in regard to its ability to mix mechanically between velocity biases that are associated with the macroscopic confinement. There is general consensus[98] that measurements of transverse dispersion are more difficult to perform than the analysis of the much easier accessible longitudinal dispersion data. Unsurprisingly, the precise nature of how the microstructure of a chromatographic bed affects the transverse flow heterogeneity (velocity probability density distribution), transverse equilibration (transient behavior), and the velocity-dependent transverse rate of mass transfer (scaling of the asymptotic transverse dispersion coefficients with the velocity) still remains largely unresolved. A profound insight into the transverse dispersion behavior of modern chromatographic beds (packings, monoliths, pillars) improves our understanding of mass transfer mechanisms in different morphologies and the quantitation of phenomena that limit kinetic column performance.

In this work we analyze transverse dispersion (velocity distributions, transient dispersion, and the velocity-dependence of D_T) in the important bulk domain of chromatographic beds, because the morphology of the bulk domain determines how efficient the bed can relax transverse concentration gradients that are caused by the various transcolumn velocity biases. Our

[226] J. Op de Beeck et al. *J. Chromatogr. A*, 1239, pp. 35–48, 2012.

analysis includes random sphere packings computer-generated with a narrow and a wide particle size distribution (PSD), which reflect the PSDs of modern core–shell and sub-2 μm particles, respectively;[158] the macropore space morphology of a silica-monolith, which has been physically reconstructed using confocal laser scanning microscopy;[179,181,183] and computer-generated hexagonal pillar arrays (cf. Figure 3.1). These microscopically disordered (packed beds, monolith) and ordered (pillar arrays) bed morphologies form a set of materials, which are currently intensively discussed and investigated for their use in highly efficient chromatographic separations. From a fundamental point of view, our study addresses the key influence of the bed morphology (the impact of microscopic order, in particular) on both transverse and longitudinal dispersion behavior. It employs realistic bed morphologies, and as a potential benefit for the knowledge base of the chromatographer, it provides correlations on the velocity-dependence of transverse dispersion, which contribute to a reliable analysis of mass transfer mechanisms in modern HPLC. In the current work, the spherical particles of the random sphere packings, the continuous skeleton of the monolith, and the cylindrical pillars of the regular pillar arrays are all treated as impermeable solid phase (nonporous) and the tracer is unretained. This approach allows us to focus on the impact of microscopic order on flow and (particularly transverse) hydrodynamic dispersion in the interstitial void space of the beds, which is most important in chromatographic practice when advection dominates over diffusion. It also avoids unnecessary complexity added by the specification and discussion of intraparticle transport properties.

In the remainder of this work we first summarize the generation of the employed bed morphologies, then describe briefly our approach to the simulation of flow and mass transport, and finally present simulation results on velocity probability density distributions, transient dispersion behavior, and the velocity-dependence of asymptotic dispersion coefficients.

3.2 Employed bed morphologies

3.2.1 Polydisperse random sphere packings

The study of polydisperse sphere packings is motivated by the use of sub-2 μm[48,49] and of solid core–porous shell particles[50,51] as modern HPLC packing materials, which reflect two of the newer developments in separation science. The basic idea of the sub-2 μm particles is to increase separation efficiency by a reduction of particle size, albeit at the expense of increased

[158] A. Daneyko et al. *Anal. Chem.*, 83, pp. 3903–10, 2011.
[179] S. Bruns et al. *Anal. Chem.*, 82, pp. 6569–75, 2010.
[181] D. Hlushkou, S. Bruns, and U. Tallarek. *J. Chromatogr. A*, 1217, pp. 3674–3682, 2010.
[183] D. Hlushkou et al. *J. Sep. Sci.*, 34, pp. 2026–37, 2011.
[48] J. R. Mazzeo et al. *Anal. Chem.*, 77, 460 A–467 A, 2005.
[49] K. D. Patel et al. *Anal. Chem.*, 76, pp. 5777–5786, 2004.
[50] J. J. Kirkland, T. J. Langlois, and J. J. DeStefano. *Am. Lab.*, 39, pp. 18–21, 2007.
[51] G. Guiochon and F. Gritti. *J. Chromatogr. A*, 1218, pp. 1915–38, 2011.

pressure requirements, necessitating specialized equipment.[227–229] The concept of core–shell particles is to improve mass transfer kinetics by restricting intraparticle diffusion to the thin porous shell,[52,53,230,231] while maintaining the hydraulic permeability associated with the particle diameter. Core–shell particles differ not only in their architecture from fully porous particles, but also in their PSDs: Fully porous sub-2 μm particles come in broad PSDs (relative standard deviation: $20-25\%$), because traditional particle sizing methods are ineffective for these particles;[54] core–shell particles come in narrow PSDs with a relative standard deviation of $5-6\%$, because the size of the solid cores and the thickness of the porous shell can be strictly controlled.[51]

We have studied narrow PSD and wide PSD bulk packings based on the experimental PSDs of sub-3 μm core–shell and sub-2 μm fully porous particles, respectively, as determined by scanning electron microscopy.[158] Packings were computer-generated with a fixed packing protocol over a range of bed porosities (interparticle void volume fractions) between $\varepsilon = 0.366$ and $\varepsilon = 0.460$ (representing the range from random-close to random-loose packing for monosized spheres) to simulate fluid flow and advective-diffusive mass transport in the packings' interparticle void space. The comparison of wide PSD, narrow PSD, and monodisperse packings revealed no systematic differences in hydraulic permeability and only small differences in hydrodynamic dispersion. This observation indicates a slight intrinsic advantage of a narrow PSD with respect to hydrodynamic dispersion in bulk packings. The effect of the PSD width on the plate height curves, however, is negligible compared with the influence of the bed porosity and is also too small to be noticed in chromatographic practice.[158] These simulations have demonstrated that the reduced eddy dispersion reported for columns packed with core–shell particles cannot result from the intrinsic (i.e., unrelated to the packing process) advantage of a narrow PSD.

In this work we apply these packings as well as the simulation approach to the analysis of transverse dispersion. These packings are unconfined (bulk) packings that mimic infinitely wide packings without walls. The size distributions of the spheres in the narrow PSD and the wide PSD packings were modeled after the experimentally determined PSDs of sub-3 μm core–shell and sub-2 μm fully porous particles, respectively. Important steps are repeated here for the ease of reading. PSDs of porous-shell 2.6 μm Kinetex particles (Phenomenex, Torrance, CA) and of fully porous 1.7 μm Acquity particles (Waters, Milford, MA) were determined with a JSM-7500F scanning electron microscope (JEOL, Eching, Germany). Of Kinetex particles (C_{18}, endcapped, carbon load: 12%; core: 1.9 μm, shell: 0.35 μm, pore size: 100 Å) 44 images were acquired, from which 976 particle diameters were measured. Of Acquity particles (BEH 300 C_{18}, endcapped, carbon load: 18%; pore size: 300 Å) 93 images were acquired, from which 2608 particle diameters were measured. Histograms were converted into smooth, continuous probability density

[227] N. Wu, J. A. Lippert, and M. L Lee. *J. Chromatogr. A*, 911, pp. 1–12, 2001.
[228] J. A. Anspach et al. *Anal. Chem.*, 77, pp. 7489–94, 2005.
[229] J. W. Jorgenson. *Annu. Rev. Anal. Chem.*, 3, pp. 129–150, 2010.
[52] A. Cavazzini et al. *Anal. Chem.*, 79, pp. 5972–9, 2007.
[53] J. O. Omamogho et al. *J. Chromatogr. A*, 1218, pp. 1942–53, 2011.
[230] A. Felinger. *J. Chromatogr. A*, 1218, pp. 1939–41, 2011.
[231] F. Gritti, J. Omamogho, and G. Guiochon. *J. Chromatogr. A*, 1218, pp. 7078–93, 2011.
[54] J. Will Thompson, R. A. Lieberman, and J. W Jorgenson. *J. Chromatogr. A*, 1216, pp. 7732–8, 2009.

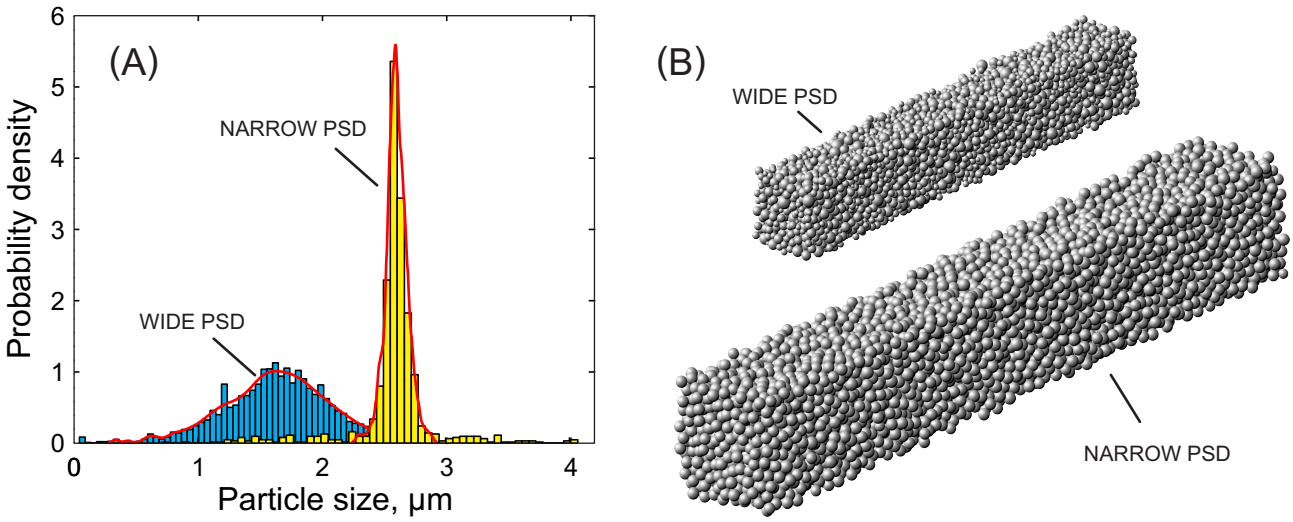

Figure 3.2: (A) Particle size distributions (PSDs) of sub-2 µm fully porous particles (wide PSD) and sub-3 µm core–shell particles (narrow PSD) as experimentally determined by scanning electron microscopy. The histograms were converted into probability density functions f_{W} and f_{N} (red curves) for the computer-generation of polydisperse random sphere packings (cf. Table 3.1). (B) Wide PSD and narrow PSD packings of solid (nonporous) particles of $10\,d_{\mathrm{A}} \times 10\,d_{\mathrm{A}} \times 70\,d_{\mathrm{A}}$ (where d_{A} is the number-mean diameter) at a bed porosity of $\varepsilon = 0.40$.

functions f_{N} (narrow PSD) and f_{W} (wide PSD) using the kernel density estimation method with Gaussian kernel and restriction to positive values.[68] Experimental PSDs and resulting probability density functions are shown in Figure 3.2A. Sets of random numbers to represent the sphere diameters in the computer-generated polydisperse sphere packings were generated from the probability density functions f_{N} and f_{W} with an acceptance-rejection method.[69]

Of the various statistical parameters that can be calculated for PSDs, we use number-mean diameter $d_{\mathrm{A}} = \Sigma\, n_i\, d_i / \Sigma\, n_i$ and surface-mean (or Sauter) diameter $d_{\mathrm{S}} = \Sigma\, n_i\, d_i^3 / \Sigma\, n_i\, d_i^2$. The narrow PSD of the core–shell particles contains particle diameters between 2.3 and 2.9 µm, has a relative standard deviation of 3.4%, and closely spaced number-mean and surface-mean diameters of $d_{\mathrm{A}} = 2.60$ µm and $d_{\mathrm{S}} = 2.61$ µm, respectively (Table 3.1). The wide PSD of the 1.7 µm particles covers particle diameters from 0.30 to 2.79 µm and has a relative standard deviation of 25.3%; its number-mean diameter ($d_{\mathrm{A}} = 1.64$ µm) is somewhat smaller than its surface-mean diameter ($d_{\mathrm{S}} = 1.83$ µm).

Based on the two probability density functions, f_{W} and f_{N} (cf. Figure 3.2A), two types of bulk, isotropic, random packings of solid (nonporous) spheres, a wide PSD and a narrow PSD type, respectively, at a bed porosity of $\varepsilon = 0.40$ were generated with a modified Jodrey-Tory algorithm, as described previously,[63,159] using periodic boundaries. The realization of periodic

[68] A. W. Bowman and A. Azzalini *Applied Smoothing Techniques for Data Analysis: The Kernel Approach with S-Plus Illustrations* Oxford University Press, 1997
[69] J. E. Gentle *Random Number Generation and Monte Carlo Methods* 2nd ed. Springer, 2003
[63] S. Khirevich et al. *J. Chromatogr. A*, 1217, pp. 4713–4722, 2010.
[159] S. Khirevich et al. *J. Chromatogr. A*, 1218, pp. 6489–97, 2011.

Table 3.1: Statistical properties of the experimentally determined particle size distributions (PSDs) for sub-2 µm fully porous particles (wide PSD) and for sub-3 µm core-shell particles (narrow PSD) and of the corresponding probability density functions f_W and f_N derived from the experimental PSDs.

	Wide PSD 1.7µm fully porous particles	f_W	Narrow PSD 2.6µm core-shell particles	f_N
Number of measured particle diameters	2608	–	976	–
Number-mean diameter (d_A)	1.64	1.64	2.60	2.60
Surface-mean diameter (d_S)	1.83	1.84	2.61	2.61
Relative standard deviation	25.3%	25.9%	3.4%	3.4%
Minimum diameter	0.30	0.27	2.27	2.24
Maximum diameter	2.79	3.01	2.90	2.93
Quantiles $d_{10}/d_{50}/d_{90}$	1.10/1.64/2.16	1.09/1.65/2.17	2.50/2.60/2.71	2.50/2.60/2.71

boundaries assumes that the position of a sphere on one side of the packing (within the representative domain) influences the position of spheres at the opposite side. As a result, space is filled regularly at the macroscale, while reproducing the representative domain, but randomness prevails locally at the microscale, within this domain. When a physical parameter (e.g., velocity field lines) or matter (e.g., a tracer molecule) is passing through one face of the representative domain, it reappears on the opposite face with the same properties (e.g., tracer velocity). Packing dimensions of $10\,d_A \times 10\,d_A \times 70\,d_A$ were chosen to avoid recorrelation artifacts observed when the representative domain is too small.[232] The bed porosity of $\varepsilon = 0.40$ is used as a representative value for packed beds and needs to be fixed in a comparison of different packings, because it is the parameter on which hydrodynamic dispersion and thus column performance depend first and foremost.[158]

Examples of the two packing types are shown in Figure 3.2B. They illustrate the packing cross-section ($10d_A \times 10d_A$) and the longest packing dimension ($70d_A$), which is the macroscopic fluid flow direction in our simulations. The respective width of the two PSDs and relative particle sizes are well reflected in the appearance of the generated packing types. With each PSD, ten individual packings were generated, and the results shown in the figures represent the average from these ten packings of the same type and porosity.

3.2.2 Silica monolith

A research sample of a ca. 60 cm long bare-silica Chromolith CapRod™ monolith with a nominal macropore size of ~2 µm and a nominal skeleton thickness of ~1 µm in a 100 µm i.d. cylindrical fused-silica capillary was provided by Merck KGaA (Darmstadt, Germany). For physical reconstruction of the monolith's macropore space morphology by confocal laser scanning microscopy, a 10 cm long segment was cut from the monolith. A bulk segment from the monolith's core region was physically reconstructed to receive a 60 µm ×60 µm ×12 µm matrix (consisting of 1.6×10^9 cubic voxels of 30 nm edge length) with an interskeleton macroporosity of $\varepsilon = 0.70$, shown in Figure 3.3. Experimental details behind the reconstruction of the bulk macropore space

[232] S. Khirevich, A. Höltzel, and U. Tallarek. , 13, pp. 801–822, 2013.

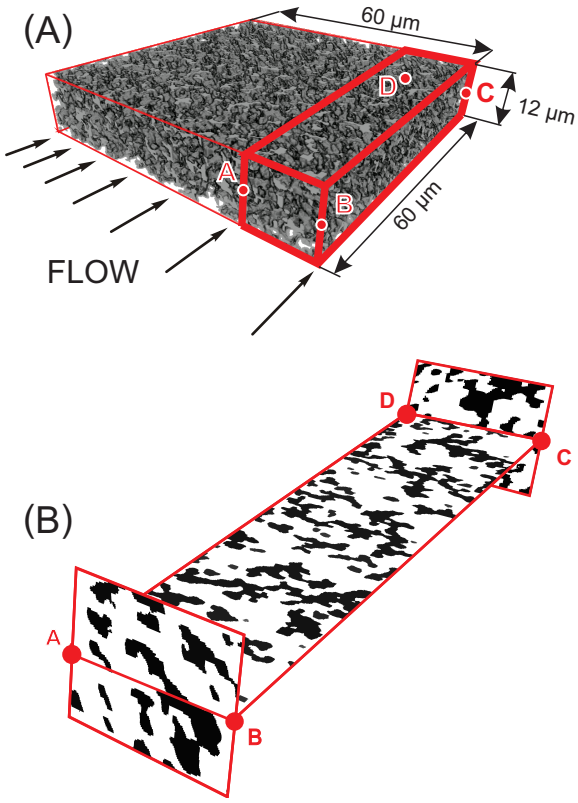

Figure 3.3: (A) Bulk macropore domain (60 µm ×60 µm ×12 µm) of a silica monolith reconstructed using confocal laser scanning microscopy. The 60 µm ×12 µm ×12 µm sub-domain used for the simulations of fluid flow and dispersion (encased by the thick red lines) contains 3.2×10^8 cubic voxels with an edge length of 30 nm. (B) Two transverse sections and one longitudinal section of the sub-domain. The solid (nonporous) monolith skeleton is shown in black. The bed porosity (interstitial void volume fraction) is $\varepsilon = 0.70$.

morphology of the silica monolith can be found in our previous publications.[181,182]

We have combined the physical reconstruction of silica monolith morphology with direct numerical simulations of fluid flow and mass transport in the monolith's interskeleton macropore space:[181,182] Three-dimensional flow simulations gave quantitative agreement between experimental and simulated Darcy permeabilities; only the physically reconstructed three-dimensional geometrical structure of the macropore domain (without assumptions or subsequent adjustments on the monolith morphology), pressure drop, and mobile phase viscosity were used as input parameters in these simulations.[181] We also quantified eddy dispersion contributions originating in the bulk macropore heterogeneity and correlated them with structural features of the monolith.[182] This new insight has substantially improved morphology-transport relationships for silica monoliths.[183,233] In particular, the results have shown that both the intraskeleton transport properties and a stochastic variation of the macropore space characteristics can be neglected compared with the ultimate challenge of reducing the column radial heterogeneity.

[233] F. Gritti and G. Guiochon. *J. Chromatogr. A*, 1218, pp. 5216–27, 2011.

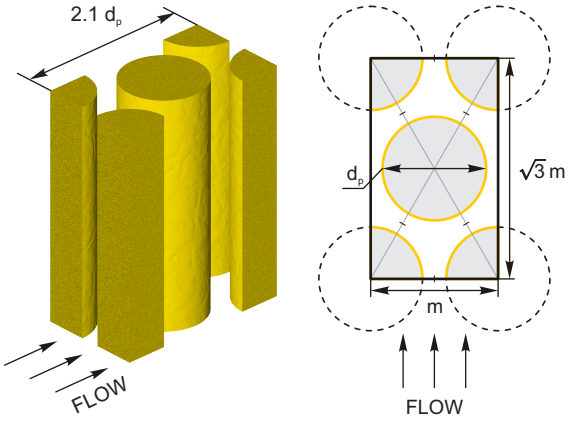

Figure 3.4: Hexagonal array of solid (nonporous), identical cylindrical pillars. Simulations in bulk pillar arrays with a bed porosity of $\varepsilon = 0.40$ (shown) and $\varepsilon = 0.70$ were performed using the two-dimensional unit cell (right), where d_p denotes the pillar diameter and m is the unit cell width. Periodic boundary conditions were used in all directions.

In this work, we apply the bulk silica monolith with a solid (nonporous) skeleton depicted in Figure 3.3 and the simulation approach to study transverse dispersion of a passive (unretained) tracer and compare it with the random sphere packings and regular pillar arrays.

3.2.3 Regular pillar arrays

Regular, hexagonal arrays of uniform, solid (nonporous) cylinders were computer-generated with the same bed porosities as the polydisperse sphere packings ($\varepsilon = 0.40$, Figure 3.2) and the silica monolith ($\varepsilon = 0.70$, Figure 3.3) for the sake of comparison. Porosity (ε), unit cell width (m), and pillar diameter (d_p) are related through

$$d_\mathrm{p}^2 = 2\frac{\sqrt{3}}{\pi}\,(1-\varepsilon)\,m^2, \tag{3.3}$$

as illustrated in Figure 3.4 with the two-dimensional unit cell. The simulations in bulk regular pillar arrays with porosities of $\varepsilon = 0.40$ and $\varepsilon = 0.70$ were performed in such two-dimensional unit cells with periodic boundary conditions in all directions. The three-dimensional unit cell is shown alongside. This structure has a height of $2.8\,d_\mathrm{p}$ and a length of $2.1\,d_\mathrm{p}$ ($\varepsilon = 0.40$). It has previously been used to construct flat configurations with wide top and bottom walls and open or closed sides to study by simulations the impact of the stepwise confinement of a bulk pillar array (from bulk to top-bottom confined to fully confined) on the engendered fluid dispersion (cf. Figure 3.1) in:[225]

In this work, we apply two-dimensional unit cells (Figure 3.4) and the simulation approach to analyze transverse mixing in these perfectly ordered microstructures and compare it with the behavior observed in disordered microstructures represented by the polydisperse sphere packings and the silica monolith. This approach allows us to resolve an intrinsic bottleneck of regular pillar arrays concerning their use in highly efficient chromatographic separations.

3.3 Simulation of fluid flow

The lattice-Boltzmann method (LBM)[162–165] was used for the simulation of low Reynolds number flow of an incompressible fluid through the interparticle void space of the bulk, polydisperse random sphere packings, the interskeleton macropore space of the reconstructed monolith, and the interstitial void space of the regular pillar arrays. At present, the LBM is arguably the best tool for pore-scale simulations of fluid flow in porous media, mostly due to its ability to accurately describe flow in complex pore space geometries without need for simplification or extensive meshing.[46,164] A distinct advantage is its inherent parallelism, which allows easy parallelization of the developed numerical models for effective use on supercomputing systems.[42,43] Until now, this approach has demonstrated great potential in the modeling of flow and transport in chromatographic media like randomly packed beds[47,62,63,67,70,71,73,77,97,135,149–154,158,159,225,232] and monoliths.[181–183,234,235] Besides reproducing experimental column behavior, these simulations have been instrumental in resolving morphology-transport relationships and to analyze the effect of the particle size distribution, intraparticle porosity and associated diffusion-limited transport, bed density, packing disorder and defects, as well as column dimensions and cross-sectional geometry on dispersion. We have previously described in much detail the whole modeling approach, e.g., in [43] (available online), and in a directly preceding paper, which analyzed the impact of the macroscopic confinement on flow and dispersion in regular pillar arrays and random sphere packings.[225] Therefore, only a brief summary is given here.

In the LBM a discretized version of the Boltzmann equation with linearized collision operator

[162] R. Benzi, S. Succi, and M. Vergassola. *Phys. Rep.*, 222, pp. 145–197, 1992.
[163] S. Chen and G. D. Doolen. *Annu. Rev. Fluid Mech.*, 30, pp. 329–364, 1998.
[164] S. Succi *The lattice Boltzmann equation for fluid dynamics and beyond* Oxford University Press, 2001
[165] Ubertini S. et al. *Lectures on Lattice Boltzmann Methods for Complex Fluid Flows* Science4 Press, 2009
[46] D. Kandhai et al. *Int. J. Numer. Methods Fluids*, 31, pp. 1019–1033, 1999.
[42] S. Khirevich, A. Daneyko, and U. Tallarek "Simulation of fluid flow and mass transport at extreme scale" in: *Jülich Blue Gene/P Extreme Scaling Workshop 2010* ed. by B. Mohr and W. Frings Forschungszentrum Jülich, Jülich Supercomputing Centre, 2010
[43] S. Khirevich "High-Performance Computing of Flow, Diffusion, and Hydrodynamic Dispersion in Random Sphere Packings" PhD thesis Germany: Philipps-Universität Marburg, 2010
[47] D. Kandhai et al. *Phys. Rev. Lett.*, 88, p. 234501, 2002.
[62] R. S. Maier et al. *Water Resour. Res.*, 44, W06S03, 2008.
[70] S. Khirevich et al. *Anal. Chem.*, 79, pp. 9340–9349, 2007.
[71] S. Khirevich et al. *Anal. Chem.*, 81, pp. 4937–4945, 2009.
[73] S. Khirevich, A. Höltzel, and U. Tallarek. *Philos. Trans. R. Soc. A*, 369, pp. 2485–93, 2011.
[77] M. R. Schure et al. *Anal. Chem.*, 74, pp. 6006–6016, 2002.
[135] S. Khirevich et al. *Lab Chip*, 8, pp. 1801–1808, 2008.
[149] B. Manz, L. F. Gladden, and P. B. Warren. *AIChE J.*, 45, pp. 1845–1854, 1999.
[150] M. D. Mantle, A. J. Sederman, and L. F. Gladden. *Chem. Eng. Sci.*, 56, pp. 523–529, 2001.
[151] R. S. Maier et al. *Philos. Trans. R. Soc. A*, 360, pp. 497–506, 2002.
[152] M. R. Schure et al. *J. Chromatogr. A*, 1031, pp. 79–86, 2004.
[153] D. Hlushkou, A. Seidel-Morgenstern, and U. Tallarek. *Langmuir*, 21, pp. 6097–6112, 2005.
[154] M. R. Schure and R. S. Maier. *J. Chromatogr. A*, 1126, pp. 58–69, 2006.
[234] H. Koku et al. *J. Chromatogr. A*, 1218, pp. 3466–75, 2011.
[235] H. Koku et al. *J. Chromatogr. A*, 1237, pp. 55–63, 2012.

is solved.[162–165] The method simulates hydrodynamic phenomena by tracking the time evolution of distribution functions of fictitious particles that are confined to a cubic lattice and move with discrete velocity $\vec{c}_i$ during discrete time steps. The particle distribution function $f_i(\vec{r},t)$ represents the probability of finding a particle with velocity $\vec{c}_i$ at position $\vec{r}$ and time t. Each time step Δt is divided into separate streaming and collision steps. Velocities $\vec{c}_i$ are chosen such that in one streaming step a particle moves along a lattice link from one lattice node to its neighbor. Subsequently, particle distribution functions f_i are redistributed according to the collision operator.

For our LBM, we used the BGK (Bhatnagar-Gross-Krook) collision operator[32] and the evolution equation for the distribution function is[162–165]

$$f_i(\vec{r}+\Delta t\vec{c}_i, t+\Delta t) = f_i(\vec{r},t) - \frac{f_i(\vec{r},t) - f_i^{eq}(\vec{r},t)}{\tau}, \tag{3.4}$$

where f_i^{eq} denotes the equilibrium distribution function and τ is the relaxation parameter, which is related to the kinematic viscosity by $\mu = (2\tau - 1)/6$.[163] The local fluid density $\rho(\vec{r},t)$ and velocity $\vec{u}(\vec{r},t)$ are obtained from the zero-order and first-order moments of the particle distribution functions:

$$\rho(\vec{r},t) = \sum_i f_i(\vec{r},t), \tag{3.5}$$

and

$$\vec{u}(\vec{r},t) = \frac{\sum_i \vec{c}_i f_i(\vec{r},t)}{\rho(\vec{r},t)}. \tag{3.6}$$

The equilibrium distribution function depends on the local density $\rho(\vec{r},t)$ and the local velocity $\vec{u}(\vec{r},t)$

$$f_i^{eq}(\rho,\vec{u}) = w_i\rho\left(1 + \frac{\vec{c}_i\vec{u}}{c_S^2} + \frac{(\vec{c}_i\vec{u})^2}{2c_S^4} - \frac{\vec{u}\vec{u}}{2c_S^2}\right), \tag{3.7}$$

where c_S is the speed of sound and w_i are weight factors that depend on the employed lattice. Usually, the LBM models are designated as DxQy, where x is the lattice dimensionality and y refers to the number of lattice links from a given lattice node to its neighbors (including the node itself) located on a simple cubic lattice. In this work we used the D3Q19 lattice, a cubic lattice with 18 links at each lattice node, which can be obtained by projecting the four-dimensional face-centered hypercubic lattice onto three-dimensional space.[169,170] Each node is connected to its

[32] P. L. Bhatnagar, E. P. Gross, and M. Krook. *Phys. Rev.*, 94, pp. 511–525, 1954.
[169] Rothman D. H. and Zaleski S. *Lattice-Gas Cellular Automata* Cambrige Unversity Press, 1997
[170] Y. H. Qian, D. D'Humières, and P. Lallemand. *EPL*, 17, pp. 479–484, 1992.

six nearest and twelve diagonal neighbors. The following weight factors were used: $w_i = 1/3$ for $i = 0$; $w_i = 1/18$ for $i = 1, 3, 5, 7, 10, 13$; and $w_i = 1/36$ for $i = 2, 4, 6, 8, 9, 11, 12, 14, 15, 16, 17, 18$ (conventional numbering for lattice links). It can be shown[166,171] that the equilibrium distribution function and the given weight coefficients recover the macroscopic fluid properties represented by the Navier-Stokes equation[7]

$$(\vec{u} \cdot \nabla)\, \vec{u} + \frac{\nabla p}{\rho} - \mu \nabla^2 \vec{u} = 0, \tag{3.8}$$

with

$$\nabla \cdot \vec{u} = 0. \tag{3.9}$$

To summarize, the LBM uses a mesoscopic description, where the fluid is represented by an ensemble of identical particles, and although these fictitious particles do not resemble real molecules and the particle dynamics is limited to random moves and binary collisions on a regular lattice, macroscopic fluid properties described by Eqs. (3.8) and (3.9) can be properly recovered from the ensemble properties by a statistical approach. The LBM is based on a connection between the molecular kinetics and phenomenological description; the latter can be expressed with the Navier-Stokes equation assuming the fluid as a continuum.

We substituted the uniform pressure gradient driving the flow by an equivalent body force.[163,164,169] A bounce-back rule[75] was applied to implement the no-slip velocity boundary condition at the solid-liquid interface (i.e., the surfaces of the solid spheres, solid monolith skeleton, and solid pillars). The lattice kinematic viscosity was set to a value of $1/6$ ($\tau = 1$), which was shown to provide an accurate performance for the modeling scheme we employ.[76] Periodic boundary conditions were imposed at the external faces of the representative domains for the chromatographic beds. Their application assumes identical local values of the flow velocity field in opposite points lying at the corresponding edges of a domain. To avoid artifacts in the flow field originating from abrupt changes in the pore space structure due to the connection of monolith slices from opposite faces, we introduced additionally a gap space that separates the periodically reproduced monolith domain in three-dimensional space. If the gap is large enough to allow flow field equilibration, this eliminates any mutual effects between neighboring monolith domains.[181]

The typical flow regime in the employed chromatographic beds is low Reynolds number flow (Re $\ll 1$). According to Darcy's law the pressure gradient driving the flow and the average flow velocity are directly proportional as long as Re $\ll 1$ is satisfied,[12] and the local flow vector

[166] S. Chapman and T. G. Cowling *The mathematical theory of non-uniform gases* 3rd ed. Cambridge University Press, 1990

[171] X. He and L.-S. Luo. *J. Stat. Phys.*, 88, pp. 927–944, 1997.

[7] L. D. Landau and E. M. Lifschitz *Fluid mechanics* 2nd ed. Butterworth–Heinemann, 2007

[75] M. A. Gallivan et al. *Int. J. Numer. Methods Fluids*, 25, pp. 249–263, 1997.

[76] C. Pan, L.-S. Luo, and C. T. Miller. *Comput. Fluids*, 35, pp. 898–909, 2006.

[12] D. Hlushkou and U. Tallarek. *J. Chromatogr. A*, 1126, pp. 70–85, 2006.

components follow the same linear scaling. This allows to calculate the flow field for a given packing, monolith, or pillar array at low Reynolds number ($\mathrm{Re} < 0.01$) and realize the required range of velocities in our dispersion simulations by linear rescaling of the flow field components.[77]

For simulations of fluid flow in the interstitial void space of the chromatographic beds with the LBM, the polydisperse sphere packings, the monolith, and the pillar arrays are discretized to obtain a simulation grid. The accuracy of the simulation results depends on the grid resolution, which in turn affects the required amount of computational resources. For monodisperse sphere packings, a grid resolution of 30 nodes/d_A is sufficient.[81] For polydisperse sphere packings, the appropriate grid resolution depends on the number and diameter of the smallest spheres in the PSD.[71] We evaluated the effect of the grid resolution on the numerical simulation results by calculating the flow velocity field at grid resolutions between 10 and 90 nodes/d_A and observed that for the employed wide PSD and narrow PSD packings (Figure 3.2) a grid resolution of 60 nodes/d_A is the best compromise between accuracy and required computational resources.[158]

For the silica monolith (Figure 3.3) the three-dimensional lattice spacing was adjusted to the pixel resolution in the confocal laser scanning microscopy image stack (30 nm). All simulations were performed in a 60 µm $\times 12$ µm $\times 12$ µm sub-domain (encased by the thick red lines in Figure 3.3A) of the reconstructed 60 µm $\times 60$ µm $\times 12$ µm monolith domain. The sub-domain contains $2000 \times 400 \times 400 = 3.2 \times 10^8$ cubic voxels and was characterized as large enough (by systematic variation of its size) for determining bulk properties of the monolith (hydraulic permeability, asymptotic diffusion and dispersion coefficients) and realizing a velocity range for the dispersion and plate height analysis, which is representative of chromatographic practice with this type of monolith.[181–183]

The pillar arrays were discretized with a grid resolution of 60 nodes/d_p, because the calculation of dispersion coefficients for the ordered structures is more sensitive to spatial resolution than for the random packings.[43] Discrete lattices of the representative geometrical elements (unit cells) from the bulk pillar arrays, which were subjected to periodic boundary conditions, had dimensions of 74×128 nodes (width $\times$ length) for the two-dimensional geometry shown in Figure 3.4 ($\varepsilon = 0.40$) and of 104×178 nodes for $\varepsilon = 0.70$ (due to the larger unit cell, cf. Eq. (3)).

The flow field simulations for each packing consisted of 2500 LBM iterations, which required ~ 2.2 hours on 1024 BlueGene/P processor cores and 110 GB of RAM. Flow simulation for the monolith consisted of 10000 LBM iterations, which required ~ 40 hours on 64 Power6 processor cores and 50 GB of RAM. The demand of resources for flow simulations in the pillar arrays is negligibly small in comparison (20000 LBM iterations, requiring only 12 seconds on 16 Power6 processor cores and 5 MB of RAM).

[81] D. Kandhai et al. *Philos. Trans. R. Soc. A*, 360, pp. 521–534, 2002.

3.4 Simulation of advection-diffusion

Mass transport in the polydisperse sphere packings, in the monolith, and in the pillar arrays was simulated with a random-walk particle-tracking technique;[36,37,78] where a large number of inert, point-like tracers is distributed randomly and uniformly throughout the whole void space of a chromatographic bed, and then the time evolution of tracer coordinates due to fluid flow and molecular (Brownian) motion is monitored. The transient dispersion coefficient $D_\alpha(t)$ along a direction α, e.g., parallel or perpendicular to the direction of macroscopic fluid flow is determined from

$$D_\alpha(t) = \frac{1}{2N}\frac{d}{dt}\sum_{i=1}^{N}\left(\Delta r_{\alpha,i}(t) - \langle \Delta r_\alpha(t)\rangle\right)^2, \tag{3.10}$$

where $\Delta r_{\alpha,i}(t) \stackrel{\text{def}}{=} r_{\alpha,i}(t) - r_{\alpha,i}(0)$ and $\langle \Delta r_\alpha(t)\rangle$ denote corresponding Cartesian components of the displacement of the ith tracer and the average displacement of the tracer ensemble after time t, respectively, in α-direction, and N is the number of the employed tracers (in this work up to $N = 2 \times 10^6$). Advective displacement of a tracer was calculated using the velocity vector from the nearest lattice node, assuming constant fluid velocity over a lattice voxel. A multiple-rejection scheme was implemented to restrict the tracer movement to the void (fluid) space of a chromatographic bed.[79] Diffusive tracer displacement follows a Gaussian distribution in each spatial coordinate with zero mean and a variance of $2D_\mathrm{m}\delta t$, where D_m is the diffusion coefficient of the tracers in the bulk fluid and δt is the simulation time step (defined such that the average diffusive displacement did not exceed half of the lattice spacing used to calculate a flow velocity field).

Longitudinal and transverse dispersion coefficients (cf. Eqs. (3.1) and (3.2)) were determined by Eq. (3.10) parallel and perpendicular to the macroscopic flow direction, respectively. Transient values are denoted as $D_\mathrm{L}(t)$ and $D_\mathrm{T}(t)$, while the absence of the time parameter indicates time-independence, i.e., asymptotic values, D_L and D_T, as determined from the $D(t)$-curves. For calculation of any $D_\alpha(t)$ with Eq. (3.10), the individual and ensemble displacements of the tracer particles ($\Delta\vec{r}_i$ and $\langle\Delta\vec{r}\rangle$) during their movement in the artificially introduced gap space between the periodically reproduced monolith domain were excluded.

The program realization of all algorithms was implemented as parallel codes in C/C++ languages using the Message Passing Interface standard.[80] All dispersion simulations took $\sim$600 hours on 1024 processor cores of a BlueGene/P system.

[36] P. Salamon, D. Fernàndez-Garcia, and J. J. Gómez-Hernández. *J. Contam. Hydrol.*, 87, pp. 277–305, 2006.
[37] F. Delay, P. Ackerer, and C. Danquigny. *Vadose Zone J.*, 4, pp. 360–379, 2005.
[78] J. A. Rudnick and G. D. Gaspari *Elements of the random walk: an introduction for advanced students and researchers* Cambridge University Press, 2004
[79] P. Szymczak and A. J. C. Ladd. *Phys. Rev. E*, 68, p. 036704, 2003.
[80] W. Gropp and A. Lusk E. Skjellum *Using MPI: Portable Parallel Programming with the Message-Passing Interface* 2nd ed. MIT Press, 1999

3.5 Validation of the simulation approach

Over the last decade our modeling approach including the implementation of different (and systematically varied) sphere-packing generation protocols and a detailed study of their impact on the resulting packing microstructure, from random-close to random-loose packing of the beds, and how the microstructure affects diffusion as well as fluid flow and dispersion over a wide range of velocities, has been significantly developed and validated through comparison with analytical predictions, simulations, and experimental results. For a summary of these results and achievements, which cover random sphere packings, silica monoliths, and pillar arrays, the reader is referred to Chapter 2.5 in [225], a directly preceding paper to the current one. The validation of the employed boundary conditions, including bed length, grid resolution, multiple-rejection scheme for implementation of the no-flux boundary condition at the solid-liquid interface, approximation of constant velocity over a lattice voxel, etc., is summarized in [232] and in Chapters 1.3 and 1.4 in [43].

3.6 Results and discussion

We sub-divide our dispersion study (with an emphasis on transverse dispersion) into the following aspects, which are analyzed for each chromatographic bed type: (i) Velocity probability density distributions; (ii) transient dispersion $D_{\mathrm{T}}(t)/D_{\mathrm{m}}$; and (iii) dependence of the asymptotic $D_{\mathrm{T}}/D_{\mathrm{m}}$ on the average mobile phase velocity u_{av}. The gained insight helps us to compare the different bed types (packings, monolith, pillars) concerning their intrinsic morphology and capability to function as an efficient transverse mechanical mixer in view of wall effects and the engendered longitudinal dispersion with confined supports traditionally used, analyzed, and discussed in chromatographic practice.[67,182,225]

3.6.1 Polydisperse random sphere packings

The aforementioned aspects are illustrated in Figures 3.5–3.7 for the polydisperse sphere packings. Figure 3.5 begins with transverse (panel A) and longitudinal (panel B) velocity probability density distributions $P(u_{\mathrm{T}}/u_{\mathrm{av}})$ and $P(u_{\mathrm{L}}/u_{\mathrm{av}})$, where u_{T} and u_{L} denote transverse and longitudinal velocity components in a packing, respectively. The area under these curves has been normalized to unity, and they can be regarded as providing the relative fraction of a velocity component u_{T} or u_{L} in the flow field. $P(u_{\mathrm{T}}/u_{\mathrm{av}})$ in Figure 3.5A is symmetric with respect to zero velocity, because there is no net flow in transverse direction; its center of gravity is at $u_{\mathrm{T}}/u_{\mathrm{av}} = 0$. $P(u_{\mathrm{L}}/u_{\mathrm{av}})$ in Figure 3.5B has a sharp peak close to zero velocity (due to the no-slip boundary condition at the surface of the particles) and decays exponentially, quickly towards negative velocities and with a much smaller slope towards positive velocities; its center of gravity is at $u_{\mathrm{L}}/u_{\mathrm{av}} = 1$.

The distribution functions in Figure 3.5 characterize fluid flow through the packings in the low Reynolds number regime, where they are invariant to changes in u_{av}.[12] The PSD has

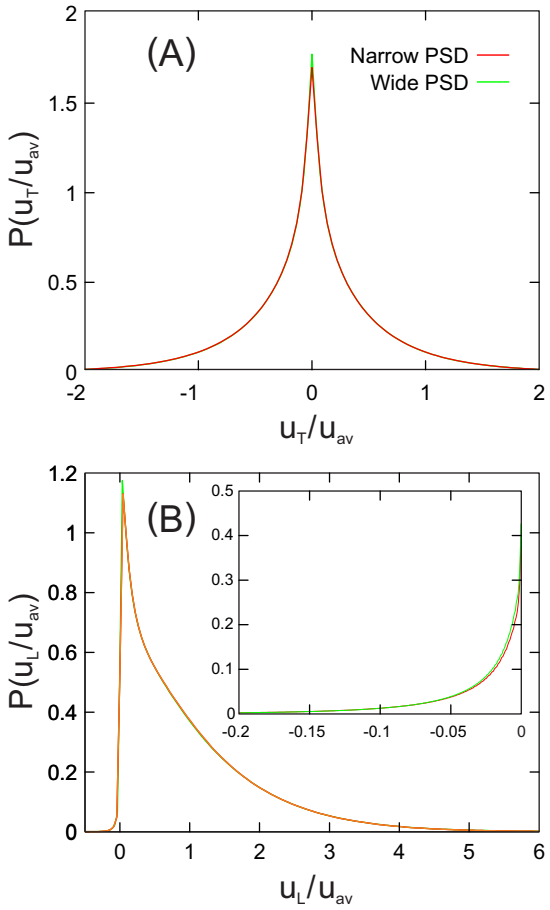

Figure 3.5: Transverse (A) and longitudinal (B) velocity probability density distributions $P(u_{\mathrm{T}}/u_{\mathrm{av}})$ and $P(u_{\mathrm{L}}/u_{\mathrm{av}})$ for the polydisperse sphere packings (cf. Figure 3.2), where u_{T} and u_{L} are the transverse and longitudinal velocity components and u_{av} is the average mobile phase velocity. The area under these curves has been normalized to unity, and they can be regarded as providing the relative fraction of a velocity component u_{T} or u_{L} in the flow field. The inset in panel B is a zoom into the negative velocity tail of $P(u_{\mathrm{L}}/u_{\mathrm{av}})$.

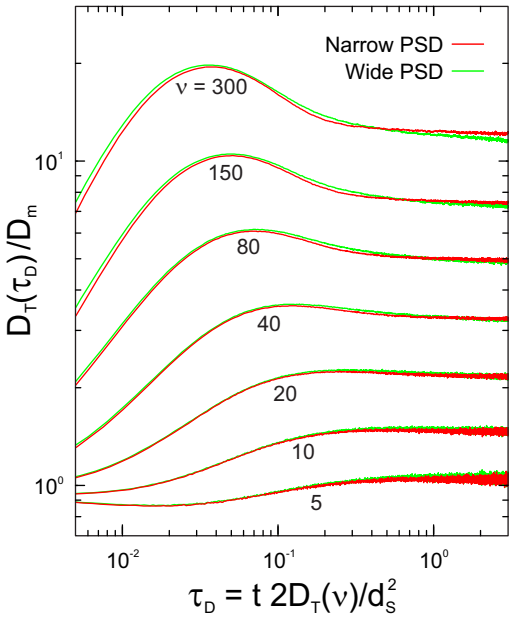

Figure 3.6: Transient behavior of the transverse dispersion coefficient $D_{\mathrm{T}}(\tau_D)/D_{\mathrm{m}}$ for the polydisperse sphere packings at selected values of the reduced velocity $\nu = u_{\mathrm{av}} d_{\mathrm{S}}/D_{\mathrm{m}}$, where d_{S} is the Sauter mean diameter (cf. Table 3.1). Elapsed time t is plotted as dimensionless transverse dispersive time $\tau_{\mathrm{D}} = 2D_{\mathrm{T}}t/d_{\mathrm{S}}^2$, where $D_{\mathrm{T}}(\nu)$ is the asymptotic transverse dispersion coefficient at a given value of ν.

a negligible effect in this regard, as evidenced by the almost indistinguishable distributions $P(u_{\mathrm{T}}/u_{\mathrm{av}})$ and $P(u_{\mathrm{L}}/u_{\mathrm{av}})$ for packings with narrow and wide PSD at identical bed porosity ($\varepsilon = 0.40$). The slow exponential decay of $P(u_{\mathrm{L}}/u_{\mathrm{av}})$ towards positive velocities and its small, but distinct tail towards negative velocities (visualized by the inset in Figure 3.5B) agrees with previous simulated and experimental data.[236,237] The occurrence of negative velocities in laminar flow through random sphere packings due to back-flow regions and stationary eddy patterns is well-known.[12,238–243] Stationary vortices in a flow velocity field are not necessarily a sign of the turbulent regime. Turbulent flow is highly unsteady; all fluid properties fluctuate with extremely chaotic spatio-temporal pattern, and inertial dominate over viscous forces.[12] In laminar flow, fluid layers glide smoothly over adjacent ones, with a stationary spatio-temporal pattern and molecular interchange of momentum only.

Figure 3.6 illustrates transient behavior of the transverse dispersion coefficient $D_{\mathrm{T}}(\tau_{\mathrm{D}})/D_{\mathrm{m}}$ for selected values of $\nu = u_{\mathrm{av}} d_{\mathrm{S}}/D_{\mathrm{m}}$ from the investigated range of reduced velocities ($0.5 \leq \nu \leq 500$). Elapsed time t in Figure 3.6 is plotted as dimensionless transverse dispersive time

[236] L. Lebon et al. *Phys. Fluids*, 8, p. 293, 1996.
[237] R. S. Maier et al. *Phys. Fluids*, 10, pp. 60–74, 1998.
[238] M. L. Johns et al. *AIChE J.*, 46, pp. 2151–2161, 2000.
[239] Y. E. Kutsovsky et al. *Phys. Fluids*, 8, p. 863, 1996.
[240] M. Rashidi et al. *Adv. Water Resour.*, 19, pp. 163–180, 1996.
[241] J. Götz et al. *Chem. Eng. Process.*, 41, pp. 611–629, 2002.
[242] X. Ren, S. Stapf, and B. Blümich. *AIChE J.*, 51, pp. 392–405, 2005.
[243] N. W. Halpern-Manners et al. *J. Phys. Chem. A*, 115, pp. 4023–30, 2011.

$\tau_{\mathrm{D}} = 2D_{\mathrm{T}}t/d_{\mathrm{S}}^2$, where the dispersive time unit $2D_{\mathrm{T}}/d_{\mathrm{S}}^2$ corresponds to the time span $d_{\mathrm{S}}^2/2D_{\mathrm{T}}$, after which the tracer particles are dispersed laterally by one Sauter diameter d_{S}, and $D_{\mathrm{T}}(\nu)$ is the asymptotic transverse dispersion coefficient at the given value of ν. The use of D_{T} in the dimensionless dispersive time scale reflects the actual combination of flow and diffusion and describes adequately the lateral equilibration between different velocities in a random sphere packing, which – in the investigated velocity range – is driven neither by pure diffusion nor by pure convection, but by their combined effects[66] (see also analysis of dispersion regimes following below).

For reduced velocities in Figure 3.6 ($5 \leq \nu \leq 300$), $D_{\mathrm{T}}(\tau_D)/D_{\mathrm{m}}$ demonstrates the attainment of asymptotic values after $\tau_{\mathrm{D}} = 2-3$ with both narrow and wide PSD packings, i.e., transverse dispersion becomes asymptotic after a distance of $\sim 1.5 d_{\mathrm{S}}$ has been sampled laterally by the tracer particles. Absolute time required for this process decreases with increasing velocity ν due to the concomitant increase of $D_{\mathrm{T}}(\nu)$. Figure 3.6 illustrates that transverse dispersion curves develop an intermediate peak for $\nu > 10$, i.e., as advection dominates over diffusion. With increasing velocity the peak is shifted towards very short times τ_D.[67,97] The form of the curves is caused by longitudinal advection, which initially forces the average tracer particle to make a transverse displacement on the order of $d_{\mathrm{S}}/2$ around a sphere. Afterwards, the tracer may either move back towards its initial transverse position or further increase its transverse displacement, yielding a net reduction in the rate of spreading. The transverse dispersion curves of the narrow PSD and the wide PSD packings for a given velocity are generally very similar, like their asymptotic values.

Figure 3.7 presents asymptotic values $D_{\mathrm{T}}/D_{\mathrm{m}}$ for the polydisperse sphere packings as a function of the reduced velocity ($\nu = u_{\mathrm{av}} d_{\mathrm{S}}/D_{\mathrm{m}}$), in Figure 3.7A in double-logarithmic form for the whole investigated velocity range ($0.5 \leq \nu \leq 500$), and in Figure 3.7B in linear form for $5 \leq \nu \leq 300$. The relevance of the velocity range selected in Figure 3.7B (as well as in Figure 3.6) will become evident below. Transverse dispersion coefficients D_{T} in Figure 3.7 were calculated from the transient dispersion curves (cf. Figure 3.6) as the average value over the interval $\tau_{\mathrm{D}} = 2-3$. The data in Figure 3.7A can be analyzed with the following dispersion regimes.[91,244] At very low velocities ($\nu < 0.3$) we enter the diffusion regime, where advection is so weak that diffusion controls transverse dispersion almost completely and

$$\frac{D_{\mathrm{T}}}{D_{\mathrm{m}}} \approx \gamma_{\mathrm{e}}. \tag{3.11}$$

Here, γ_{e} is the external (or interparticle) obstruction factor. It characterizes effective diffusion in the interparticle void space of the packings[66,159]

$$\gamma_{\mathrm{e}} = \frac{D_{\mathrm{eff}}}{D_{\mathrm{m}}} = \lim_{t\to\infty} \frac{D(t)}{D_{\mathrm{m}}}, \tag{3.12}$$

[91] M. Sahimi *Flow and transport in porous media and fractured rock: From classical methods to modern approaches* Wiley-VCH, 1995

[244] J. M. P. Q. Delgado. *Chem. Eng. Res. Des.*, 85, pp. 1245–1252, 2007.

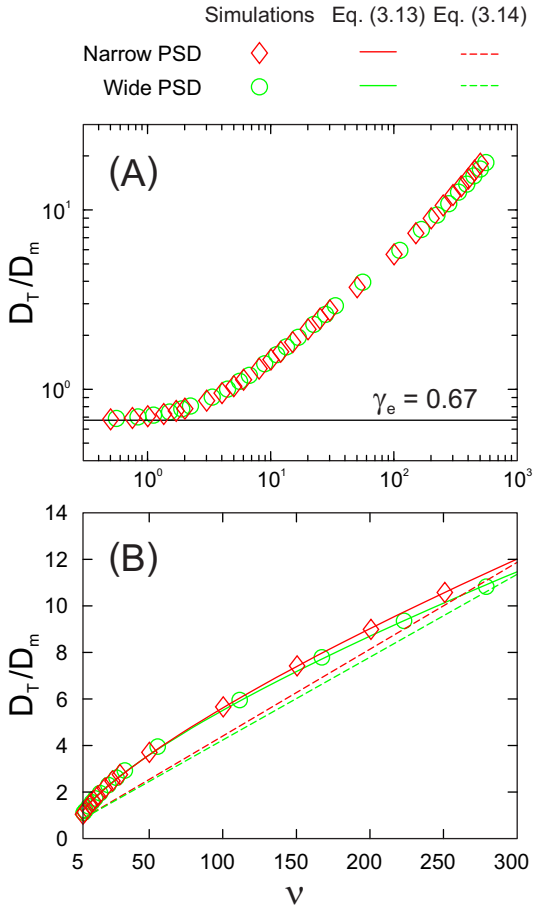

Figure 3.7: Asymptotic values $D_\mathrm{T}/D_\mathrm{m}$ for the polydisperse sphere packings as a function of the reduced velocity $\nu = u_\mathrm{av} d_\mathrm{S}/D_\mathrm{m}$, where d_S is the Sauter mean diameter (cf. Table 3.1). (A) Double-logarithmic plot for the whole investigated velocity range ($0.5 \leq \nu \leq 500$). (B) Linear plot for $5 \leq \nu \leq 300$. Transverse dispersion coefficients D_T were calculated from the transient dispersion curves (cf. Figure 3.6) as the average value over the interval $\tau_\mathrm{D} = 2-3$.

where D_m is the diffusion coefficient in the bulk fluid, $D(t)$ is the pre-asymptotic diffusion coefficient in a packing, and D_{eff} is its effective, i.e., asymptotic (long-time) value. We determined γ_e by monitoring the long-time limit of the diffusion coefficient in the packings, analogous to $D_T(\tau_D)/D_m$ in Figure 3.6, but for $\nu = 0$.[159] The following values were obtained: $\gamma_e = 0.670$ and 0.672 for the narrow PSD and the wide PSD packings, respectively. This limiting behavior is indicated in Figure 3.7A by the horizontal line.

The velocity range $0.3 < \nu < 5$ denotes a transition or superposition regime, where the contributions of advection and diffusion to dispersion are of similar magnitude; the functional dependence $D_T/D_m = f(\nu)$ is difficult to quantify by an equation. The velocity range $5 \leq \nu \leq 300$ (Figures 3.6 and 3.7B) characterizes the power law regime, where advection dominates dispersion, but the effect of diffusion cannot be neglected:[91,244]

$$\frac{D_T}{D_m} = \gamma_e + a_T \nu^{\beta_T}. \tag{3.13}$$

This regime is also referred to as boundary-layer dispersion in recognition of the presence and importance of the viscous boundary layer at the spheres' surfaces, in which mass transport normal to the surface is diffusion limited.[89] Sahimi[91] mentions that the average value of β_T in Eq. (3.13) from all the available experimental data (including beadpacks and unconsolidated sandpacks) is $\beta_T \approx 0.9$, whereas typical values of a_T, which depend on the heterogeneity of the pore space, are $a_T \approx 0.01 - 0.05$. For reduced velocities $\nu > 300$ we enter the pure mechanical dispersion regime, where the effect of diffusion is negligible and transverse dispersion results simply from the stochastic velocity field that is imposed by the randomly distributed pore boundaries in a packing[91,244]

$$\frac{D_T}{D_m} = \gamma_e + b_T \nu. \tag{3.14}$$

Based on this overview of relevant dispersion regimes, we fitted Eq. (3.13) to our D_T/D_m-data in the velocity range of $5 \leq \nu \leq 300$ (Figure 3.7B), representing the power law or boundary-layer dispersion regime of the whole investigated velocity range shown in Figure 3.7A ($0.5 \leq \nu \leq 500$). Values of γ_e for the narrow PSD and wide PSD packings were used as fixed input parameters. The results are illustrated in Figure 3.7B and summarized in Table 3.2. The fit of Eq. (3.13) to the D_T/D_m-data in the velocity range of $5 \leq \nu \leq 300$ is excellent. Interestingly, as we fit Eq. (3.13) to the D_T/D_m-data over the whole velocity range, the parameters are only slightly modified (Table 3.2).

The transverse dispersion data in Figure 3.7 strictly refer to bulk packings of nonporous particles (without wall and extracolumn effects) and a nonadsorbing tracer. They allow us to focus on the impact of the bed morphology on flow and mass transport in the interparticle void space of the packings, which is most important when advection dominates over diffusion. Thereby,

[89] D. L. Koch and J. F. Brady. *J. Fluid Mech.*, 154, pp. 399–427, 1985.

Table 3.2: Analysis of the transverse dispersion data $D_T/D_m = f(\nu)$ in Figure 3.7 for the bulk wide PSD and narrow PSD packings (cf. Figure 3.2 and Table 3.1) at a bed porosity of $\varepsilon = 0.40$[a]

Velocity range[b]	Wide PSD packings[c]	Narrow PSD packings[c]
$5 \leq \nu \leq 300$	Eq. (3.13): $a_T = 0.167$, $\beta_T = 0.731$, $R^2 = 0.9992$	Eq. (3.13): $a_T = 0.152$, $\beta_T = 0.756$, $R^2 = 0.9994$
$0.5 \leq \nu \leq 500$	Eq. (3.13): $a_T = 0.146$, $\beta_T = 0.758$, $R^2 = 0.9996$	Eq. (3.13): $a_T = 0.133$, $\beta_T = 0.782$, $R^2 = 0.9996$
$0.5 \leq \nu \leq 500$	Eq. (3.14): $b_T = 0.034$, $R^2 = 0.9847$	Eq. (3.14): $b_T = 0.037$, $R^2 = 0.9879$

[a] Transverse dispersion coefficients D_T were calculated from the transient dispersion curves (cf. Figure 3.6) as the average value over the interval $\tau_D = 2 - 3$.
[b] Reduced velocity was calculated as $\nu = u_{av} d_S / D_m$, where d_S is the Sauter mean diameter (cf. Table 3.1).
[c] Best fits of Eq. (3.13) to the D_T/D_m-data for $5 \leq \nu \leq 300$ and of Eq. (3.14) to the D_T/D_m-data for $0.5 \leq \nu \leq 500$ are visualized in Figure 3.7B.

these data also avoid unnecessary complexity caused by the specification and discussion of intra-particle transport properties. On the other hand, it is known that the retention of an analyte and the porosity of the particles affect transverse equilibration.[148,193] The effects of analyte retention and particle porosity will be absorbed in the effective diffusion coefficient for the packings. Then, Eqs. (3.11)–(3.14) may be generalized based on the expressions for D_{eff} discussed by Gritti and Guiochon in a recent review on mass transfer kinetics, band broadening, and column efficiency in liquid chromatography (see Chapter 2.3.1 in [178]).

As such, our data and results in Table 3.2 (nonporous particles, inert tracer; $D_{eff} = \gamma_e D_m$) should be compared with the work of Knox et al.[245] and Eon,[246] who studied transverse dispersion and plate height data in the bulk region of cylindrical confined packings prepared from nonporous glass beads over approximate velocity ranges of $16 < \nu < 250$[245] and $0.6 < \nu < 1000$.[246] For these full velocity ranges the following equation was fitted to their transverse reduced plate height data

$$h_T = \frac{2\gamma_e}{\nu} + A_T, \tag{3.15}$$

which is directly obtained from Eq. (3.14) using Eq. (3.2), with $A_T = 2b_T$. Whereas the first term on the right-hand-side of Eq. (3.15) accounts for obstructed diffusion in a packing (cf. Eq. (3.12)), the constant A_T in Eq. (3.15) can be identified as arising from a "stream-splitting" mechanism dependent only upon the packing geometry.[247] Knox et al.[245] and Eon[246] obtained values of $A_T = 0.060$ and 0.075, respectively. After applying Eq. (3.14) to our transverse dispersion data over the whole investigated velocity range in Figure 3.7A ($0.5 \leq \nu \leq 500$), which reflects the procedure of Knox et al.[245] and Eon,[246] we obtain $A_T = 2b_T = 0.073$ and 0.068 for the narrow PSD and the wide PSD packings, respectively. On the one hand, we note the excellent agreement between our analysis with Eq. (3.14) and that of Knox et al.[245] and Eon[246] with Eq. (3.15) regarding the values of the constant $A_T = 2b_T$ obtained for similar systems (bulk packings of nonporous particles). On the other hand, we caution the limited use of these equations, as they relate to the pure mechanical dispersion regime, where the effect of diffusion is completely

[245] J. H. Knox, G. R. Laird, and P. A. Raven. *J. Chromatogr. A*, 122, pp. 129–145, 1976.
[246] C. H. Eon. *J. Chromatogr. A*, 149, pp. 29–42, 1978.
[247] D. S. Horne, J. H. Knox, and L. McLaren. *Separ. Sci.*, 1, pp. 531–554, 1966.

negligible ($\nu > 300$). In the power law or boundary-layer dispersion regime ($5 \leq \nu \leq 300$), however, diffusion cannot be neglected. Unsurprisingly, the above mentioned representation of our $D_\mathrm{T}/D_\mathrm{m}$-data with Eq. (3.14) is unsatisfactory in this regime (see dashed lines in Figure 3.7B and R^2-values in Table 3.2). Instead, Eq. (3.13) should be used for the adequate representation of the transverse dispersion data, both from the achievable fit quality (see solid lines in Figure 3.7B and R^2-values in Table 3.2) and the underlying hydrodynamic boundary-layer dispersion mechanism.

To summarize, our careful analysis with the bulk narrow PSD and wide PSD packings suggests to adapt the following equation (obtained from Eqs. (3.2) and (3.13)) for characterization of transverse reduced plate height data in the chromatographically most relevant velocity range represented by the power law or boundary-layer dispersion regime:

$$h_\mathrm{T} = \frac{2\gamma_\mathrm{e}}{\nu} + 2a_\mathrm{T}\nu^{(\beta_\mathrm{T}-1)}. \tag{3.16}$$

For the employed polydisperse sphere packings ($\varepsilon = 0.40$) all parameters relevant to this equation can be found in Table 3.2. Our analysis shows that the PSD has a negligible impact on transverse dispersion, which agrees with the conclusions of other investigations.[248,249] We note that the Sauter mean diameter should be employed in comparative studies with polydisperse sphere packings to account for their different surface-to-volume ratios (even at identical bed porosity), which impact the hydrodynamics in the boundary-layer dispersion regime[158,250] (for clarity, d_S has been used to prepare Figures 3.6 and 3.7).

3.6.2 Silica monolith

Figures 3.8–3.10 illustrate the results of a similar analysis for the reconstructed silica monolith (cf. Figure 3.3) as performed above for the polydisperse sphere packings (Figures 3.5–3.7). In particular, Figure 3.8 shows the transverse (panel A) and longitudinal (panel B) velocity probability density distributions $P(u_\mathrm{T}/u_\mathrm{av})$ and $P(u_\mathrm{L}/u_\mathrm{av})$, where corresponding functions of the wide PSD packings from Figure 3.5 are included for comparison. As Figure 3.8 demonstrates, these distributions are very similar for the two bed morphologies and reveal common features explained already for the packings. The most notable difference is observed with the higher distribution maxima for the monolith, which are associated with slow fluid. While such a difference may be caused by different degrees of heterogeneity in the bed structures, as observed, e.g., for bead packs with artificially placed defects[62,152,154,234] (where zones of slow fluid dominate throughout, forming an intense, narrow peak of the distribution, whereas faster regions occur with much lower frequency but carry the bulk of the flow), the computer-generated sphere packings (Figure 3.2) and the physically reconstructed silica monolith (Figure 3.3) have relatively homogeneous morphologies.[63,158,182,183] Another, straightforward explanation can be found in the

[248] N. W. Han, J. Bhakta, and R. G. Carbonell. *AIChE J.*, 31, pp. 277–288, 1985.
[249] J. R. F. Guedes de Carvalho and J. M. P. Q. Delgado. *AIChE J.*, 46, pp. 1089–1095, 2000.
[250] F. Gritti et al. *J. Chromatogr. A*, 1218, pp. 8209–21, 2011.

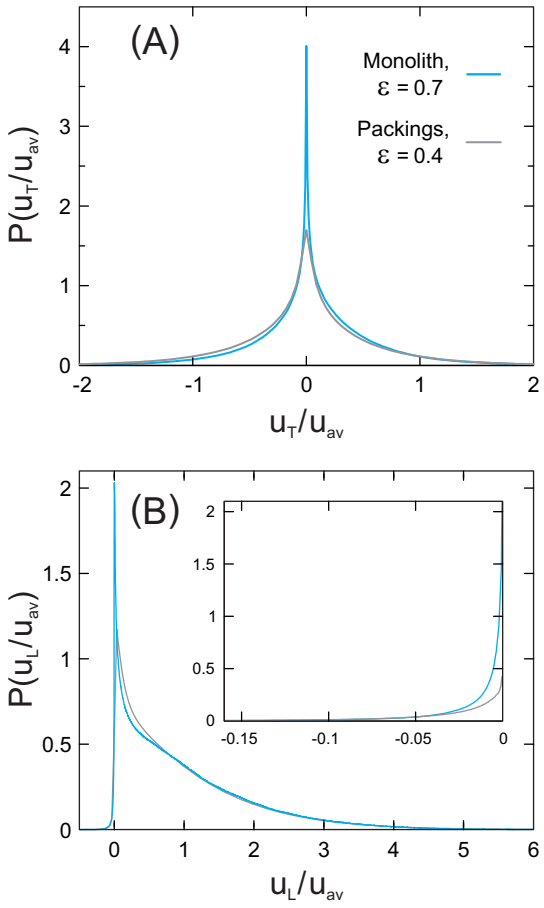

Figure 3.8: Transverse (A) and longitudinal (B) velocity probability density distributions $P(u_{\mathrm{T}}/u_{\mathrm{av}})$ and $P(u_{\mathrm{L}}/u_{\mathrm{av}})$ for the reconstructed silica monolith (cf. Figure 3.3), where u_{T} and u_{L} are the transverse and longitudinal velocity components and u_{av} is the average mobile phase velocity. The area under these curves has been normalized to unity, and they can be regarded as providing the relative fraction of a velocity component u_{T} or u_{L} in the flow field. The inset in panel B is a zoom into the negative velocity tail of $P(u_{\mathrm{L}}/u_{\mathrm{av}})$. Distributions for the wide PSD packings are included for comparison.

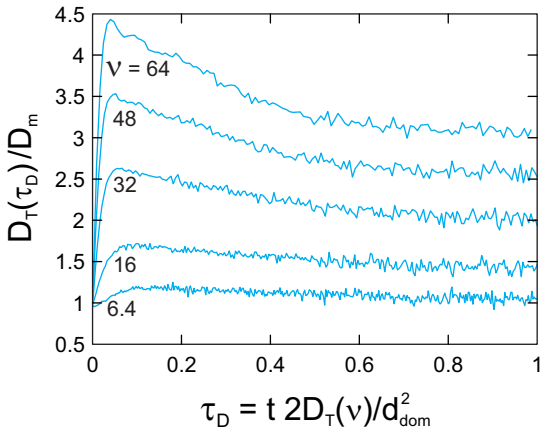

Figure 3.9: Transient behavior of the transverse dispersion coefficient $D_{\mathrm{T}}(\tau_D)/D_{\mathrm{m}}$ for the silica monolith at selected values of the reduced velocity $\nu = u_{\mathrm{av}} d_{\mathrm{dom}}/D_{\mathrm{m}}$, where $d_{\mathrm{dom}} = 3.2$ µm is the monolith's domain size.[183] Elapsed time t is plotted as dimensionless transverse dispersive time $\tau_{\mathrm{D}} = 2D_{\mathrm{T}}t/d_{\mathrm{dom}}^2$, where $D_{\mathrm{T}}(\nu)$ is the asymptotic transverse dispersion coefficient at a given value of ν.

higher external surface-to-volume ratio of the silica monoliths compared to sphere packings.[251] Consequently, the peaks of both $P(u_{\mathrm{T}}/u_{\mathrm{av}})$ in Figure 3.8A and $P(u_{\mathrm{L}}/u_{\mathrm{av}})$ in Figure 3.8B become sharper and more intense for the monolith. Like the packings, the monolith shows a distinct tail of negative velocities in $P(u_{\mathrm{L}}/u_{\mathrm{av}})$. The volumetric fraction of regions with negative longitudinal flow velocity components (inset in Figure 3.8B) amounts to ∼1.3% of the total macropore space of the reconstructed 60 µm ×12 µm ×12 µm monolith sub-domain (encased by the thick red lines in Figure 3.3A). It is somewhat smaller for the packings (∼0.8%).

For the sake of completeness we note that the comparison of $P(u_{\mathrm{L}}/u_{\mathrm{av}})$ of a silica monolith with that of a polymeric monolith (a commercial "convective interaction media" sample) shows that the silica monolith has a wider, lower peak around zero and comparatively fewer negative velocities.[234] This difference may originate in the relatively homogeneous morphology of the silica monolith,[182,183] which results in a more uniformly distributed flow field compared to the heterogeneous polymeric monolith structure with a much broader distribution of the pore sizes available for fluid flow and therefore pores that enable varying degrees of advective flow.[234]

Figure 3.9 illustrates transient behavior of the transverse dispersion coefficient $D_{\mathrm{T}}(\tau_{\mathrm{D}})/D_{\mathrm{m}}$ in the monolith for selected reduced velocities $\nu = u_{\mathrm{av}} d_{\mathrm{dom}}/D_{\mathrm{m}}$. Elapsed time is plotted as transverse dispersive time $\tau_{\mathrm{D}} = 2D_{\mathrm{T}}t/d_{\mathrm{dom}}^2$. We have now used the domain size $d_{\mathrm{dom}} = 3.2$ µm of this monolith in the calculation of both ν and τ_D. The value of d_{dom} (i.e., the sum of the monolith's macropore size and skeleton thickness) originates from the results of our previous morphological analysis of the reconstructed silica monolith using chord length distributions for the skeleton and the macropore space.[183] As an illustration, a chord length in the monolith's macropore space is a straight distance between two encounters with the monolith skeleton. The mode of the chord length distribution represents the most frequent skeleton wall-to-wall distance.

[251] U. Tallarek, F. C. Leinweber, and A. Seidel-Morgenstern. *Chem. Eng. Technol.*, 25, pp. 1177–1181, 2002.

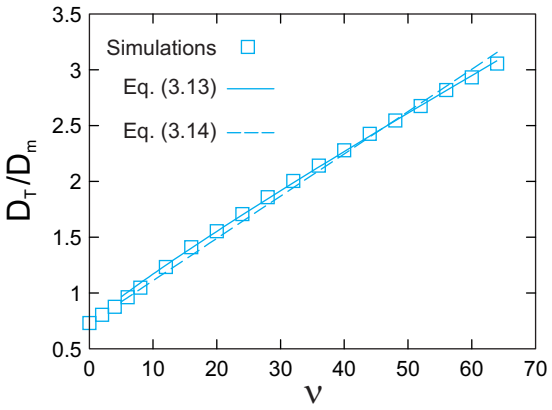

Figure 3.10: Asymptotic values $D_\mathrm{T}/D_\mathrm{m}$ for the silica monolith as a function of the reduced velocity $\nu = u_\mathrm{av} d_\mathrm{dom}/D_\mathrm{m}$, where $d_\mathrm{dom} = 3.2$ µm is the monolith's domain size.[183] Transverse dispersion coefficients D_T were calculated from the transient dispersion curves (cf. Figure 3.9) as the average value over the interval $\tau_\mathrm{D} = 1.0$-1.5.

Gille et al.[252] have shown that for an infinitely long cylindrical pore the mode of the chord length distribution corresponds to the pore diameter. We have analyzed modes of 2.25µm and 0.95µm, respectively, for the macropore space and the skeleton, providing an estimate for the domain size of $d_\mathrm{dom} = 3.2$ µm.[183] In Figure 3.9 the dispersive time unit $2D_\mathrm{T}/d_\mathrm{dom}^2$ now corresponds to the time span $d_\mathrm{dom}^2/2D_\mathrm{T}$, after which the tracer particles are dispersed laterally by one domain d_dom, and $D_\mathrm{T}(\nu)$ is the asymptotic transverse dispersion coefficient at the given value of ν, as before.

The $D_\mathrm{T}(\tau_\mathrm{D})/D_\mathrm{m}$ curves in Figure 3.9 demonstrate the attainment of asymptotic values after ca. one τ_D, i.e., transverse dispersion becomes asymptotic in the monolith after a distance on the order of just one domain size (d_dom) has been sampled laterally by the tracer particles. It shows that the macropore space morphology of the silica monolith can be considered as very homogeneous.[183] Figure 3.9 also illustrates that the transverse dispersion curves for the monolith develop an intermediate peak for $\nu > 10$ (when advection dominates over diffusion), as for the packings. The "stream-splitting" mechanism, mentioned with the packings, takes place now along the curved surface of the monolith skeleton.

Figure 3.10 presents asymptotic values $D_\mathrm{T}/D_\mathrm{m}$ for the monolith as a function of the reduced velocity ($\nu = u_\mathrm{av} d_\mathrm{dom}/D_\mathrm{m}$). Transverse dispersion coefficients D_T in Figure 3.10 were calculated from the transient dispersion curves (cf. Figure 3.9) as the average value over the interval $\tau_\mathrm{D} = 1.0 - -1.5$. Although the macroscopic dimensions of the monolith (cf. Figure 3.3) limit the realizable velocity range in the dispersion simulations, we could still extend this range (with values of ν up to 64) beyond typical operating conditions in HPLC practice. Based on our experience with the packings (Figure 3.7), Eq. (3.13) was fitted to the $D_\mathrm{T}/D_\mathrm{m}$-data for the monolith in the velocity range of $5 \leq \nu \leq 64$ in Figure 3.10, which represents the power law or boundary-layer dispersion regime. The value of γ_e for the macropore space of the monolith has been analyzed independently by monitoring the long-time limit of the diffusion coefficient (cf. Eq. (3.12)), analogous to $D_\mathrm{T}(\tau_\mathrm{D})/D_\mathrm{m}$ in Figure 3.9, but for $\nu = 0$, and was used as a fixed input

[252] W. Gille, D. Enke, and F. Janowski. *J. Porous. Mat.*, 8, pp. 179–191, 2001.

parameter ($\gamma_e = 0.730$). The best fit of Eq. (3.13)) to the data in Figure 3.10 gives ($R^2 = 0.9993$):

$$\frac{D_T}{D_m} = 0.730 + 0.056\nu^{0.897}, \tag{3.17}$$

with $\nu = u_{av} d_{dom}/D_m$ and $d_{dom} = 3.2$ µm. As expected from our experience with the packings (Figure 3.7 and Table 3.2), the application of Eq. (3.14) to the transverse dispersion data of the monolith provided an inadequate description. The best fit with Eq. (3.14) is included in Figure 3.10 for comparison ($D_T/D_m = 0.730 + 0.038\nu$, $R^2 = 0.9919$). To summarize, our careful analysis with the reconstructed silica monolith suggests to adapt Eq. (3.17) for characterization of transverse dispersion coefficients and reduced plate height data (together with Eq. (3.2)) in the chromatographically most relevant velocity range represented by the power law or boundary-layer dispersion regime.

3.6.3 Regular pillar arrays

After having analyzed the hydrodynamics in microscopically disordered, macroscopically homogeneous chromatographic beds in Sections 3.6.2 and 3.6.1, we complement this insight by a similar study with microscopically ordered pillar arrays at bed porosities ($\varepsilon = 0.40$ and 0.70), which reflect the packings and the monolith. Figure 3.4 shows that the pillar arrays have an ordered microstructure due to the regular arrangement of equal cylindrical pillars. The modeling of flow and transport in unconfined regular pillar arrays is straightforward, because transport properties can be reduced to an advection-diffusion problem in a single unit cell.[23,160,161] Unlike in random packings and monoliths, whose geometrical dimensions need to be sufficient to observe asymptotic dispersion behavior, the dispersion simulations in bulk pillar arrays can be limited to the two-dimensional unit cell (Figure 3.4) with periodic boundary conditions in all directions. On the other hand, this simple picture needs to be revised upon confinement of an array, because the no-slip velocity boundary condition at the surface of a wall causes flow and mass transport to become macroscopically inhomogeneous.[225] This has already been pointed out in the Introduction of this paper and illustrated with Figure 3.1. A transcolumn velocity bias is generated parallel to the pillar axis (by the top and bottom walls) as well as perpendicular to it (due to the side walls). Dispersion simulations then require consideration of the complete three-dimensional geometry of the confined array to take proper account of the four newly created 90°-corners.[225] For confined pillar arrays their bulk transverse mixing rates play a key role, because they determine how quickly the significant transcolumn concentration gradients caused by even simple confinement and wall effects, as in Figure 3.1, are relaxed over the whole cross-section, and therefore how much band broadening is finally engendered after full transcolumn equilibration.

There are only few studies available which provide information on transverse dispersion

[23] H. Brenner. *Philos. Trans. R. Soc. A*, 297, pp. 81–133, 1980.
[160] H. Brenner and P. M. Adler. *Philos. Trans. R. Soc. A*, 307, pp. 149–200, 1982.
[161] D. L. Koch et al. *J. Fluid Mech.*, 200, pp. 173–188, 1989.

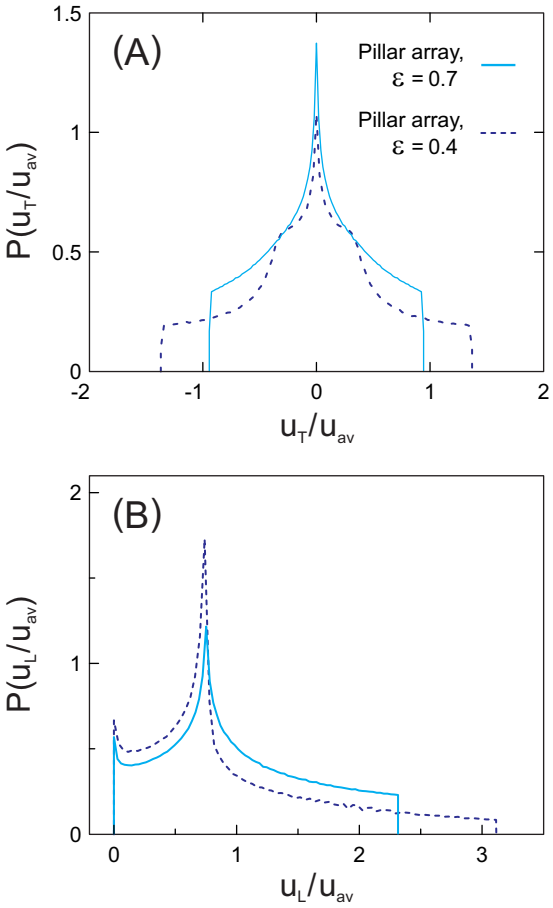

Figure 3.11: Transverse (A) and longitudinal (B) velocity probability density distributions $P(u_{\mathrm{T}}/u_{\mathrm{av}})$ and $P(u_{\mathrm{L}}/u_{\mathrm{av}})$ for the regular pillar arrays (cf. Figure 3.4), where u_{T} and u_{L} are the transverse and longitudinal velocity components and u_{av} is the average mobile phase velocity. The area under these curves has been normalized to unity, and they can be regarded as providing the relative fraction of a velocity component u_{T} or u_{L} in the flow field.

in bulk regular cylinder arrays.[27,28,199,200,253,254] We particularly note the recent work of Porter et al.[255] (and references therein). Here, we extend this knowledge and furthermore compare microscopically ordered with microscopically disordered chromatographic beds in regard to their transverse dispersion behavior. Figures 3.11–3.14 for the pillar arrays complement the earlier presentation and analysis of data for the polydisperse sphere packings (Figures 3.5–3.7) and the silica monolith (Figures 3.8–3.10). In particular, Figure 3.11 depicts the transverse (panel A) and longitudinal (panel B) velocity probability density distributions $P(u_\mathrm{T}/u_\mathrm{av})$ and $P(u_\mathrm{L}/u_\mathrm{av})$ for bed porosities of $\varepsilon = 0.40$ and 0.70. The striking difference between these distributions (Figure 3.11) and those of the microscopically disordered beds (Figure 3.5 and Figure 3.8) is recognized from their abrupt termination for the pillar arrays. With $P(u_\mathrm{T}/u_\mathrm{av})$ and the positive velocity tail of $P(u_\mathrm{L}/u_\mathrm{av})$ it appears as if the exponential decay functions have been truncated; in addition, the negative velocity tail of $P(u_\mathrm{L}/u_\mathrm{av})$, observed for the packings and the monolith, is absent for the pillar arrays. The microscopic order of the pillar arrays limits the set of available velocities $u_\mathrm{T}/u_\mathrm{av}$ and $u_\mathrm{L}/u_\mathrm{av}$, which explains the discreteness of $P(u_\mathrm{T}/u_\mathrm{av})$ and $P(u_\mathrm{L}/u_\mathrm{av})$ seen in Figure 3.11 and the narrower velocity ranges than for the microscopically disorded beds. A similar observation has been made with ordered sphere packings.[152] The drop-off in $P(u_\mathrm{L}/u_\mathrm{av})$ for the pillar arrays (Figure 3.11B) is reminiscent of the boxcar shape of $P(u_\mathrm{L}/u_\mathrm{av})$ in Hagen-Poiseuille flow through a straight cylindrical tube,[256,257] where each velocity ($0 \leq u_\mathrm{L}/u_\mathrm{av} \leq 2$) has identical probability density. The different velocity ranges for the pillar arrays in Figure 3.11 reflect their bed porosities: the lower bed porosity produces wider velocity spectra to realize a targeted value of u_av.

As we will see below, the transient dispersion curves for the pillar arrays are visually more complex than for the packings (Figure 3.6) and the monolith (Figure 3.9). However, this apparent complexity is the mere result of simplicity, i.e., the strict monodispersity of the pillar diameter d_p and the microscopic order compared with the polydisperse, disordered chromatographic beds. Figure 3.12 analyzes dispersion exemplarily for the pillar array with $\varepsilon = 0.70$. Figure 3.12A illustrates transient transverse and Figure 3.12B transient longitudinal dispersion. For better visualization, the tracers were initially ($t = 0$) distributed uniformly in a plane between two pillars, as indicated in panel 2 of Figure 3.12 by the thick red lines ("initial distribution"). This simulates the local pulse injection into a bulk pillar array. The tracer zone then moves downstream with the flow (from left to right), shown in more detail by two movies uploaded in the Supporting Information (available at http://dx.doi.org/10.1016/j.chroma.2012.08.024). The position of the center of gravity of the tracer ensemble z_av corresponds to the first moment of the tracer

[27] D. A. Edwards et al. *Transp. Porous Media*, 6, pp. 337–358, 1991.
[28] J. Salles et al. *Phys. Fluids A*, 5, pp. 2348–2376, 1993.
[199] H. P. A. Souto and C. Moyne. *Phys. Fluids*, 9, pp. 2253–2263, 1997.
[200] D. Buyuktas and W. W. Wallender. *Heat Mass Transfer*, 40, pp. 261–270, 2004.
[253] A. Eidsath. *Chem. Eng. Sci.*, 38, pp. 1803–1816, 1983.
[254] M. Quintard and S. Whitaker. *Adv. Water Resour.*, 17, pp. 221–239, 1994.
[255] M. L. Porter, F. J. Valdés-Parada, and B. D. Wood. *Adv. Water Resour.*, 33, pp. 1043–1052, 2010.
[256] M. J. E. Golay and J. G. Atwood. *J. Chromatogr. A*, 186, pp. 353–370, 1979.
[257] U. Tallarek et al. *Anal. Chem.*, 72, pp. 2292–2301, 2000.

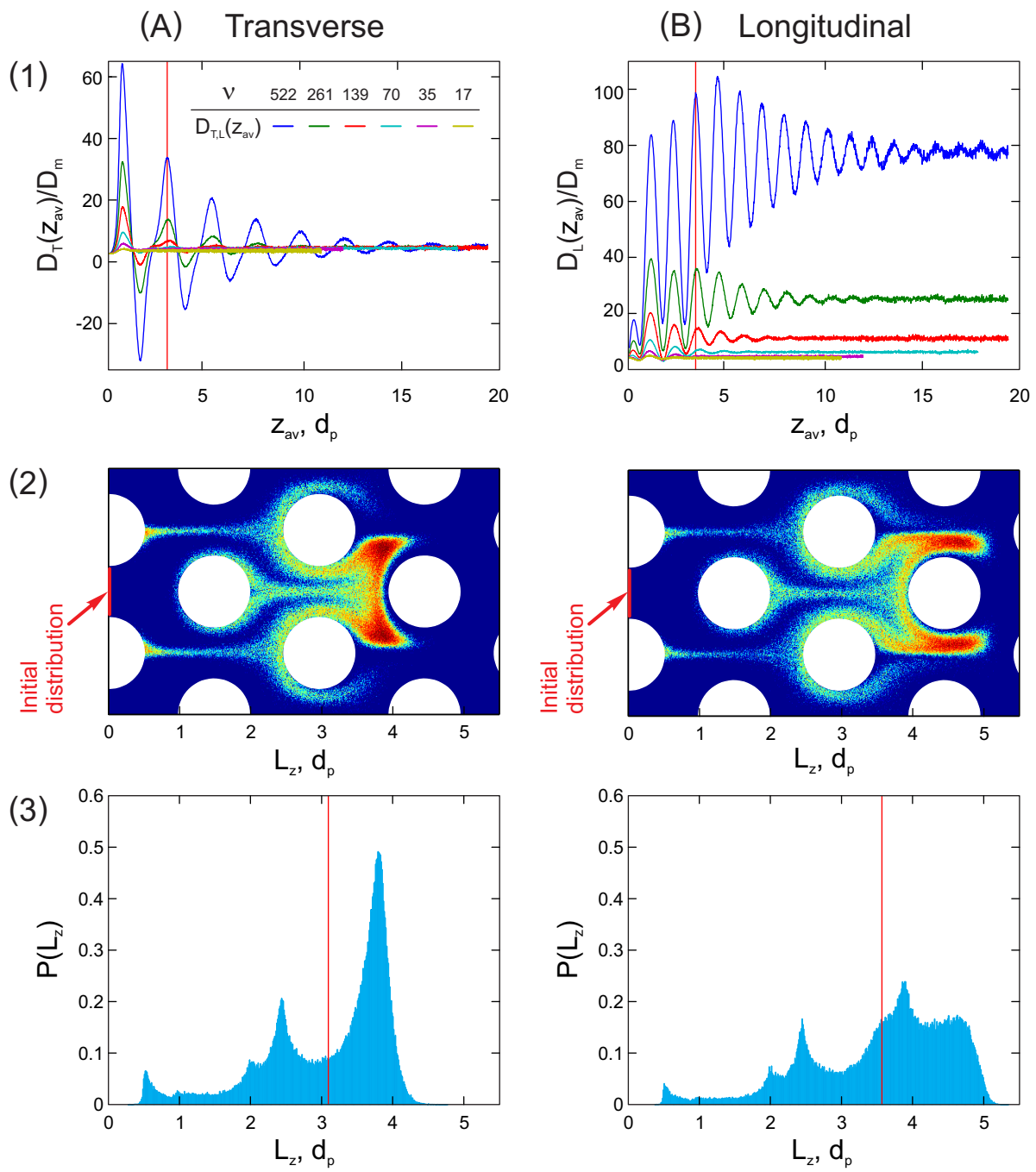

Figure 3.12: Analysis of transient transverse (A) and longitudinal (B) dispersion in the bulk pillar array with $\varepsilon = 0.70$ at selected values of the reduced velocity $\nu = u_{\mathrm{av}} d_{\mathrm{dom}}/D_{\mathrm{m}}$, where d_{dom} is the domain size taken as the sum of the pillar diameter d_{p} and the shortest interpillar distance ($d_{\mathrm{dom}} \equiv m$ in Figure 3.4). Transverse and longitudinal dispersion coefficients (panel 1) are plotted as a function of the position of the center of gravity of the tracer ensemble z_{av} (cf. Eq. (3.18)). The 2×10^5 tracers were initially ($t = 0$ distributed uniformly in a plane between two pillars, as indicated in panel 2 by the thick red lines ("initial distribution"), which simulates local pulse injection. The tracer zone then moves downstream with the flow (from left to right), which is monitored by the travelled longitudinal distance of the tracers L_{z} (in d_{p}). Two-dimensional concentration snapshots and associated one-dimensional distribution profiles in panel 2 and panel 3 correspond to $z_{\mathrm{av}} = 3.1\ d_{\mathrm{p}}$ and $z_{\mathrm{av}} = 3.6\ d_{\mathrm{p}}$ (indicated by the red vertical lines in panel 3). These values of z_{av} reflect local maxima of the transient dispersion curves in panel 1 (also marked by red vertical lines). The data shown in panel 2 and panel 3 were obtained for $\nu = 522$ (cf. blue curves in panel 1). The movies in the Supporting Information (available at http://dx.doi.org/10.1016/j.chroma.2012.08.024), which visualize the transverse and longitudinal dispersion dynamics in more detail, were obtained for this $\nu = 522$ (Movie_1.mp4) as well as for $\nu = 139$ (Movie_2.mp4).

coordinates

$$z_{\mathrm{av}} = \frac{1}{N}\sum_{i=1}^{N} z_i, \tag{3.18}$$

where N is the total number of tracers (here, $N = 2 \times 10^5$) and z_i denotes the individual tracer coordinates. Two-dimensional concentration snapshots and associated one-dimensional distribution profiles in panel 2 and panel 3 of Figure 3.12 correspond to $z_{\mathrm{av}} = 3.1\ d_{\mathrm{p}}$ (Figure 3.12A) and $z_{\mathrm{av}} = 3.6\ d_{\mathrm{p}}$ (Figure 3.12B). These values of z_{av} are indicated by the red vertical lines in panel 3. They reflect local maxima in the transient dispersion curves in panel 1 of Figure 3.12, which are also marked by red vertical lines. In panel 1 the dispersion coefficients are plotted as a function of z_{av} for different reduced velocities $\nu = u_{\mathrm{av}} d_{\mathrm{dom}}/D_{\mathrm{m}}$, where d_{dom} is the domain size of a pillar array taken as the sum of d_{p} and the shortest interpillar distance, i.e., $d_{\mathrm{dom}} \equiv m$ in Figure 3.4. We employed d_{dom} for the calculation of ν to compare supports with different bed porosity. The data shown in panel 2 and panel 3 of Figure 3.12 were obtained for $\nu = 522$ (cf. blue curves in panel 1). The movies in the Supporting Information (available at http://dx.doi.org/10.1016/j.chroma.2012.08.024), which visualize the transverse and longitudinal dispersion dynamics in more detail, were obtained for this $\nu = 522$ (Movie_1.mp4) as well as for $\nu = 139$ (Movie_2.mp4).

Panel 2 of Figure 3.12 indicates that local maxima in the transient transverse and longitudinal dispersion coefficients (cf. panel 1) are observed when the highly concentrated (red) part of the tracer zone flows through regions of the pillar array, where high transverse and high longitudinal velocity components are found, respectively. This can be explained using the transverse and longitudinal velocity fields in Figure 3.13, shown for the same geometrical section of the pillar array as in panel 2 of Figure 3.12. Each stream of fluid which impinges directly on the top of a pillar is divided equally around it. Therefore, high positive (and high negative) transverse velocities are observed in regions where this "stream-splitting" is strong (Figure 3.13A), i.e., near the upstream hemisphere of a pillar. Due to the cylindrical geometry, the positive transverse velocities decrease (and negative velocities increase) to zero towards the equator of the pillars, where the longitudinal velocities dominate (Figure 3.13B). When the highly concentrated (red) part of the tracer zone flows near the upstream hemisphere of a pillar, as in panel 2 of Figure 3.12A, the locally strong transverse spreading affects a large number of tracers, which results in a local maximum of the transient transverse dispersion coefficient seen in panel 1 of Figure 3.12A (red vertical line). This process is repeated with each pillar further downstream. It is blurred only by transverse diffusion, which results in decreasing amplitudes of the oscillations with the distance travelled by the tracer zone. Similarly, when the highly concentrated (red) part of the tracer zone flows near the equator of the same pillar (now panel 2 of Figure 3.12B), the locally strong longitudinal spreading (cf. Figure 3.13B) results in a local maximum of the transient longitudinal dispersion coefficient seen in panel 1 of Figure 3.12B (red vertical line). Eventually, the oscillations in the transient transverse and longitudinal dispersion coefficients disappear and asymptotic values D_{T} and D_{L} can be extracted (see also movies in the Supporting

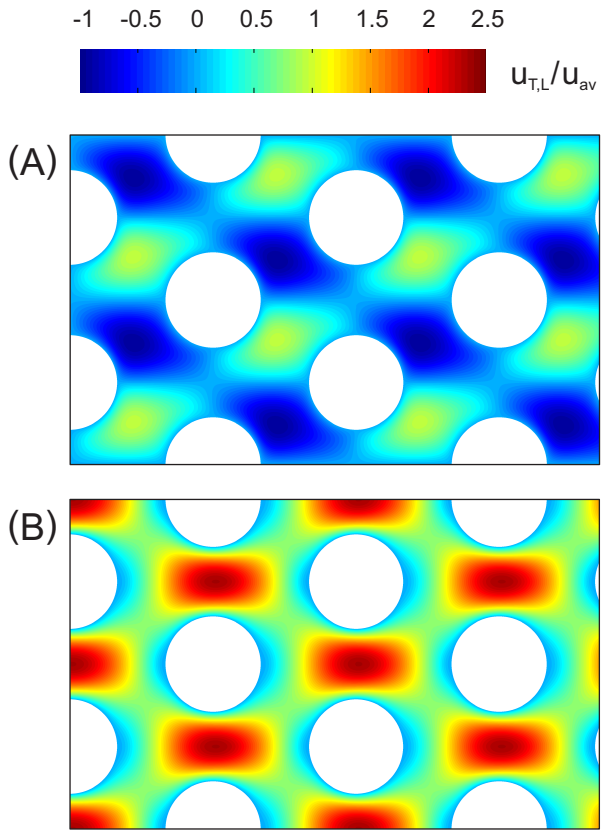

Figure 3.13: Normalized transverse ($u_{\mathrm{T}}/u_{\mathrm{av}}$, A) and longitudinal ($u_{\mathrm{L}}/u_{\mathrm{av}}$, B) velocity fields in the bulk pillar array with $\varepsilon = 0.70$. The geometrical section of the pillar array corresponds to that shown in panel 2 of Figure 3.12, and also the flow direction is from left to right (as in Figure 3.12).

Information at http://dx.doi.org/10.1016/j.chroma.2012.08.024).

The clear, separate pictures of the transverse and longitudinal velocity fields in Figure 3.13 explain the oscillating behavior observed for transient transverse and longitudinal dispersion coefficients in Figure 3.12: The periodic changes between positive and negative transverse velocities (Figure 3.13A) and between high and low positive longitudinal velocities (Figure 3.13B), which are experienced during downstream flow, produce periodic transverse and longitudinal spreading behavior, respectively. While asymptotic values D_T and D_L are also obtained for the pillar arrays, as for the polydisperse sphere packings and the monolith, the damped oscillations observed in Figure 3.12, which are absent in Figure 3.6 (packings) and Figure 3.9 (monolith), result from the strict monodispersity of the pillar diameter d_p and the microscopic order compared with the polydisperse, disordered chromatographic beds. "Stream-splitting" in the random morphologies of the packings and the monolith produces a single peak only in the transient dispersion curves (and only at sufficiently high velocities, where the effect of diffusion, as a random process, becomes small). To summarize, the random arrangement of obstacles and their polydispersity weaken spatio-temporal correlations in flow through packings and monoliths compared with regular pillar arrays, which is reflected by their transient dispersion curves (Figures 3.6, 3.9, and 3.12). Similar conclusions on spatio-temporal correlations in flow and transport through porous media can be reached using dedicated pulsed magnetic-field gradient nuclear magnetic resonance techniques.[258–260]

Figure 3.14 presents asymptotic values $D_\mathrm{T}/D_\mathrm{m}$ for the two pillar arrays ($\varepsilon = 0.40$ and 0.70) as a function of the reduced velocity $\nu = u_\mathrm{av} d_\mathrm{dom}/D_\mathrm{m}$ (up to $\nu = 615$). This figure reveals an important difference in the transverse dispersion curves for random sphere packings (Figure 3.7) and regular pillar arrays.[199,225,255] Whereas the $D_\mathrm{T}/D_\mathrm{m}$-data of the packings increase significantly over the whole velocity range in Figure 3.7A, the data for the pillar arrays approach porosity-dependent plateaus (Figure 3.14A) after an initial increase (Figure 3.14B): They taper off strongly and show a weak velocity-dependence for $\nu > 100$ ($\varepsilon = 0.40$) and $\nu > 30$ ($\varepsilon = 0.70$). The plateaus in Figure 3.14A demonstrate a diffusion-limitation that occurs in the pillar arrays. It is manifested as a pseudo-diffusive mechanism in the transverse dispersion characteristics, however, with a faster transverse equilibration (characterized by $D_\mathrm{T} \approx 10\, D_\mathrm{m}$ for $\varepsilon = 0.40$ and by $D_\mathrm{T} \approx 3\, D_\mathrm{m}$ for $\varepsilon = 0.70$ in the plateau region) than by pure molecular diffusion (D_m). Although the $D_\mathrm{T}/D_\mathrm{m}$-data of the pillar arrays indicate intitial power law behavior (Figure 3.14B), as observed for the packings (Figure 3.7B) and the monolith (Figure 3.10), which can be explained by enhanced "stream-splitting" along individual pillars, the regular microstructure of the pillar arrays (compared with the packings and the monolith) limits transverse advective mixing to the unit cell of a pillar array; a larger transverse "mixing network" based on advective flow cannot develop.

This is illustrated by Figure 3.15, which shows normalized transverse velocity fields $u_\mathrm{T}/u_\mathrm{av}$

[258] P. T. Callaghan, S. L. Codd, and J. D. Seymour. *Concept. Magnetic. Res.*, 11, pp. 181–202, 1999.
[259] P. T. Callaghan and S. L. Codd. *Phys. Fluids*, 13, pp. 421–427, 2001.
[260] S. Stapf et al. *Concept. Magnetic. Res.*, 14, pp. 172–211, 2002.

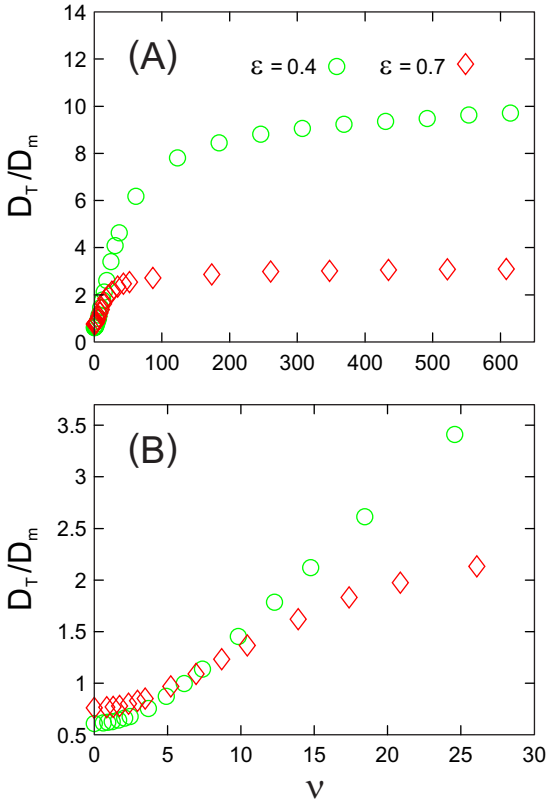

Figure 3.14: Asymptotic values $D_{\mathrm{T}}/D_{\mathrm{m}}$ for the two pillar arrays ($\varepsilon = 0.40$ and 0.70) as a function of the reduced velocity $\nu = u_{\mathrm{av}} d_{\mathrm{dom}}/D_{\mathrm{m}}$, where d_{dom} is the domain size of an array taken as the sum of the pillar diameter d_{p} and the shortest interpillar distance ($d_{\mathrm{dom}} \equiv m$ in Figure 3.4). After an initial power law behavior ($\nu < 30$, panel B), the data approach porosity-dependent plateaus at higher velocity (A). For $\nu = 0$, we obtain $\gamma_{\mathrm{e}} = 0.610$ ($\varepsilon = 0.40$) and $\gamma_{\mathrm{e}} = 0.761$ ($\varepsilon = 0.70$). The plateaus are at $D_{\mathrm{T}}/D_{\mathrm{m}} \approx 10$ ($\varepsilon = 0.40$) and $D_{\mathrm{T}}/D_{\mathrm{m}} \approx 3$ ($\varepsilon = 0.70$).

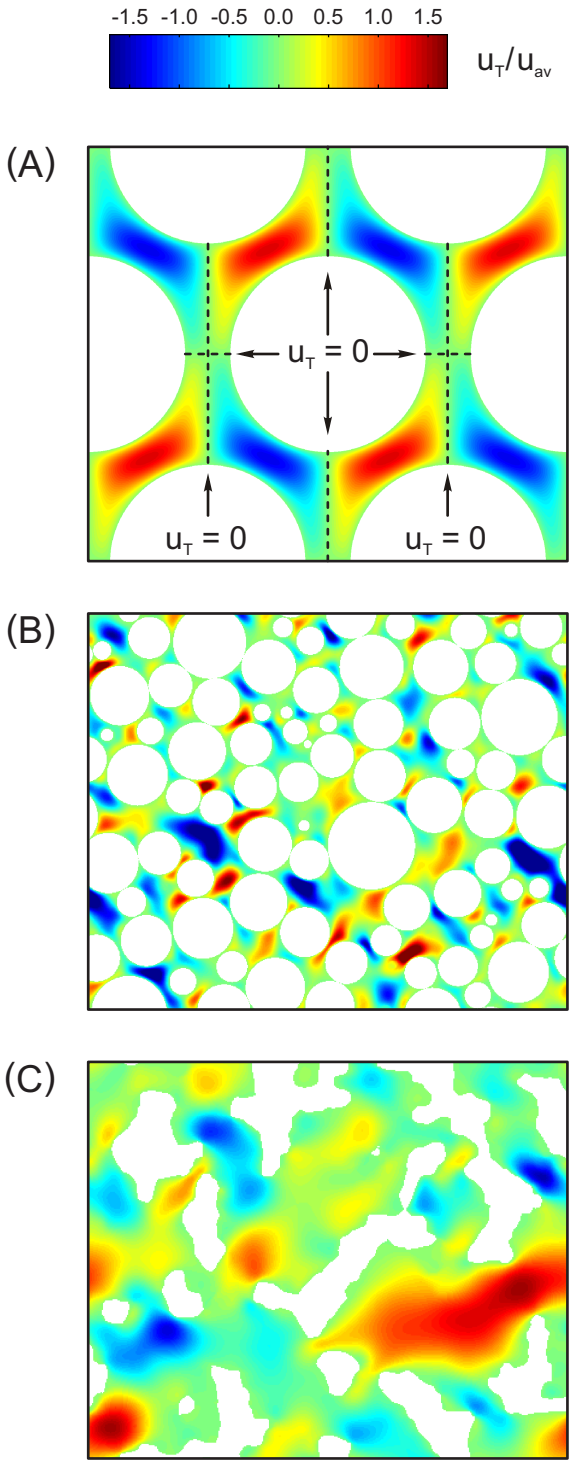

Figure 3.15: Normalized transverse velocity fields $u_{\mathrm{T}}/u_{\mathrm{av}}$ for (A) the pillar array ($\varepsilon = 0.40$, (B) a wide PSD packing ($\varepsilon = 0.40$), and (C) the silica monolith ($\varepsilon = 0.70$). The pillar, particle, and monolith dimensions are not drawn to scale. Dashed lines in the pillar array indicate symmetry lines, where transverse velocity is zero.

for the pillar array with $\varepsilon = 0.40$ (Figure 3.15A), a wide PSD packing (Figure 3.15B), and the monolith (Figure 3.15C). Strikingly, the strict monodispersity of the pillar diameter d_p and the microscopic order compared with the polydisperse, disordered chromatographic beds results in lines of symmetry in each unit cell of the pillar array, for which velocity is zero in transverse direction ($u_\mathrm{T}/u_\mathrm{av} = 0$, highlighted by the dashed black lines in Figure 3.15A). The fluid of the complete unit cell (cf. Figure 3.4) is encased by these lines of zero transverse velocity. Additional lines exist within the unit cell both parallel and perpendicular to the macroscopic flow direction (see Figure 3.15A). Due to this high symmetry, which is conserved throughout the whole chromatographic bed, a diffusion-limitation develops in the $D_\mathrm{T}/D_\mathrm{m}$-data for a pillar array as the velocity is increased (Figure 3.14). In regions with very low (or even zero) transverse velocities, i.e., near (or on) the symmetry lines, transverse dispersion is diffusion-controlled and overall increases little with the velocity. Thus, as the velocity and the "stream-splitting" along individual pillars increase, these regions ultimately limit the transverse dispersion beyond the individual pillar scale, i.e., between different unit cells. This can be rationalized with the symmetry lines at the equator of the pillars, which are perpendicular to the macroscopic flow direction. In Figure 3.15A these symmetry lines are the two horizontal ones (the flow direction is vertical). The hydrodynamics along these lines reflects Taylor-Aris dispersion in a straight channel, where transverse equilibration (and the entrance into the neighbored unit cell in Figure 3.15A) can occur only by diffusion. In addition, these lines contain the highest longitudinal velocities (cf. Figure 3.13B, where the flow direction is horizontal and $\varepsilon = 0.70$). Consequently, as longitudinal velocity increases, available time for transverse diffusive equilibration between neighbored unit cells decreases.

This analysis identifies the bottleneck of transverse dispersion in the regular pillar arrays: Transverse equilibration between unit cells is diffusion-limited and, because the symmetry indicated in Figure 3.15A is conserved throughout the whole pillar array, limits the maximal value of $D_\mathrm{T}/D_\mathrm{m}$ observed in the plateau (Figure 3.14A). The higher bed porosity of $\varepsilon = 0.70$ results in longer symmetry lines and a stronger diffusion-limitation, as seen in the lower $D_\mathrm{T}/D_\mathrm{m}$ plateau values compared with $\varepsilon = 0.40$ ($D_\mathrm{T}/D_\mathrm{m} \to 1$ as $\varepsilon \to 1$). By contrast, the transverse velocity fields for the polydisperse, disordered chromatographic beds (Figure 3.15B and 15C) do not reveal the symmetry observed with the pillar array in Figure 3.15A (and Figure 3.13). Instead, positive and negative velocities appear in a random fashion, reflecting the individual microstructural degree of heterogeneity. This illustrates that the random bed morphologies can build an efficient, three-dimensional network of longitudinal and transverse velocities, which allows them to function as a more efficient transverse mechanical mixer at high velocities than a regular pillar array (which can only mix by "stream-splitting" on the local pillar level). For the sake of completeness, we note that the symmetry lines of zero transverse velocity shown in Figure 3.15A ($u_\mathrm{T}/u_\mathrm{av} = 0$) also explain the difference at zero velocity between bed porosities observed in the longitudinal and transverse velocity probability density distributions of the pillar arrays (Figure 3.11): The longer lines for $\varepsilon = 0.70$ cause a higher overall peak at $u_\mathrm{T}/u_\mathrm{av} = 0$ (Figure 3.11A), whereas the lower peak at $u_\mathrm{L}/u_\mathrm{av} = 0$ for $\varepsilon = 0.70$ in Figure 3.11B results from the smaller surface (which imposes

the no-slip velocity boundary condition). Thus, the lines of zero transverse velocity within the fluid space outweigh the effect of a smaller surface (at which both longitudinal and transverse velocities are zero) on $P(u_\mathrm{T}/u_\mathrm{av})$ at higher bed porosity. By contrast, the monolith ($\varepsilon = 0.70$) in Figure 3.8 demonstrates higher population of zero velocities in both $P(u_\mathrm{T}/u_\mathrm{av})$ and $P(u_\mathrm{L}/u_\mathrm{av})$ than the packings ($\varepsilon = 0.40$). It is explained by its higher ratio of external surface to volume, which originates from its different bed morphology.[251]

To summarize, the local transverse velocity components in a regular pillar array arise due to "stream-splitting" around individual pillars. While they increase with the velocity on this very local scale, the transverse equilibration between neighbored unit cells (on the next larger scale) remains diffusion-limited. It restricts the maximal available transverse dispersion coefficients and causes the $D_\mathrm{T}/D_\mathrm{m}$-data to plateau out of the initial power law behavior (Figure 3.14) originating in the above-mentioned "stream-splitting". This developing dominance of diffusion is in contrast to the disappearing effect of diffusion on transverse dispersion with the polydisperse, disordered chromatographic beds (cf. Figure 3.7): In the power law or boundary-layer dispersion regime the effect of diffusion is small, but not yet negligible; then, in the pure mechanical dispersion regime diffusion can be neglected and dispersion, which results from the stochastic velocity field that is imposed by the randomly distributed pore boundaries, increases linearly with the velocity. It is therefore unsurprising that Eqs. (3.13) and (3.14) were inadequate to represent the transverse dispersion data of the pillar arrays (Figure 3.14).

3.7 Summary and conclusions

All chromatographic beds are heterogeneous over the column cross-section for reasons, which are specific to the diverse conditions of their preparation processes. These macroscopic heterogeneities cause noticeable or even deleterious transcolumn velocity biases responsible for the warping of analyte bands and transverse concentration gradients. This is highlighted by the unsymmetrical wall effects, which are not symmetrical with respect to the column axis, observed in capillary silica monoliths[182] and pillar arrays.[226] They cause persistent transients in the longitudinal dispersion coefficients and high asymptotic values (if asymptotic behavior can be realized at all). At this point transverse dispersion is important. It contributes to mass transfer across the column, relaxing transverse concentration gradients that are caused by these velocity biases. The efficient transverse mixing by a particular bed morphology therefore is a key component in the overall morphology-transport relationships underlying advanced material design and performance optimization.

In this work we have analyzed the transverse dispersion behavior of bulk, i.e., unconfined chromatographic bed morphologies, which comprise polydisperse random sphere packings (reflecting the PSDs of modern core–shell and sub-2 μm particles), a silica monolith, and two regular (hexagonal) pillar arrays. Our study shows that the effect of these PSDs on the velocity probability density distributions (Figure 3.5), transient dispersion (Figure 3.6), as well as the dependence of asymptotic dispersion on the reduced velocity (Figure 3.7) is negligible. As an

important result, we found that Eq. (3.13) and the parameters listed in Table 3.2 should be used to scale the transverse dispersion coefficients of the polydisperse sphere packings in the (chromatographically most relevant) power law or boundary-layer dispersion regime, where the influence of diffusion becomes small but not negligible (equivalently, Eq. (3.16) and the parameters listed in Table 3.2 should be used for the transverse plate heights). Similarly, Eq. (3.17) should be used to scale transverse dispersion coefficients for the silica monolith (cf. Figure 3.10). Both bed morphologies (packings and monolith) are macroscopically homogeneous ("infinite" bulk morphologies), but microscopically disordered. By contrast, the pillar arrays are microscopically ordered, which has unique consequences for their flow and dispersion behavior. First, the velocity probability density distributions (Figure 3.11) start and end abruptly, because the ordered microstructure limits the set of available velocities ("cutting off" the tails observed for the microscopically disordered chromatographic beds, Figure 3.8). Second, transient dispersion oscillates (Figure 3.12) due to the periodic nature of spreading in transverse and longitudinal directions along the pillars, as explained with the transverse and longitudinal velocity fields (Figure 3.13) and visualized using tracer pulse injection (Figure 3.12). Third, their asymptotic transverse dispersion coefficients plateau out of an initial power law behavior (Figure 3.14), whereas the microscopically disordered chromatographic beds demonstrate power law behavior throughout the whole investigated velocity range (Figures 3.7 and 3.10, Eqs. (3.13) and (3.17)).

The impact of the microscopic order of the pillar arrays on flow and dispersion can be rationalized with a closer look at the transverse velocity field (Figure 3.15). The fluid of the complete unit cell is encased by symmetry lines of zero transverse velocity; further symmetry lines exist within the unit cell. As a consequence, transverse equilibration between unit cells is diffusion-limited, which – together with the bed porosity – determines the maximal value in the plateau of the transverse dispersion curves (Figure 3.14A). By contrast, the random bed morphologies construct an efficient, three-dimensional network of longitudinal and transverse velocities, which allows them to function as a more efficient transverse mechanical mixer at high velocities than a regular pillar array.

This different behavior of microscopically ordered and disordered chromatographic beds has important consequences for the band broadening in chromatographic practice. Our analysis shows that the regular microstructure of pillar arrays can be beneficial or problematic when we add a confinement :[90,225] The limited (longitudinal as well as transverse) mechanical mixing capabilities still result in a lower longitudinal dispersion compared to confined sphere packings at low velocities, but increase longitudinal dispersion even beyond that of the packings at higher velocities (Figure 13 in [225]). Due to the diffusion-limitation in the transverse dispersion curves longitudinal dispersion already in bulk pillar arrays grows quadratically with the velocity, when the transverse dispersion data plateau out of their initial power law behavior (Figure 3.14). This pseudo-diffusive behavior translates to a linear increase of longitudinal plate heights with velocity. It is amplified upon confinement and eventually outweighs the performance advantage of a regular pillar array over a random sphere packing: Lateral mixing in confined pillar arrays occurs by purely diffusive (along the pillar axis) and pseudo-diffusive (perpendicular to the

pillar axis) dynamics, which results in a steep, linear rise of the longitudinal plate heights with the velocity (see straight lines in Figure 10A in [225]). By contrast, lateral mixing in confined packings is promoted via a coupling of transverse diffusion and spatial velocity fluctuations (absent in regular pillar arrays beyond the individual pillar scale), a mechanism that remains velocity-dependent and is responsible for the familiar bending ("tapering off") of the eddy dispersion contribution in the longitudinal plate height curves at increasing velocity.[66,225]

Due to the limited transverse dispersion originating in their ordered microstructure, regular pillar arrays experience a much stronger loss of separation efficiency upon confinement than random sphere packings. This is also revealed by the strong shift of the coordinates for the minimum of their longitudinal plate height curves, as analyzed previously (Figure 10 in [225]): Whereas the coordinates of the plate height minimum for the bulk pillar array in Figure 3.1 ($\varepsilon = 0.40$) are $h_{\min} = 0.07$ and $\nu_{\min} = 50$, they shift to $h_{\min} = 0.18$ and $\nu_{\min} = 20$ for the top-bottom confined pillar array (indicated in the upper right panel of Figure 3.1 by the semi-transparent faces), and to $h_{\min} = 0.46$ and $\nu_{\min} = 15$ for the fully confined, wide pillar array also shown in Figure 3.1 ($\mathrm{A} = 100\,\pi d_{\mathrm{p}}^2$). Thus, $h_{\min}$ of the longitudinal plate height curves increases by a factor of nearly seven from bulk to full confinement in Figure 3.1, whereas cylindrical confinement of random sphere packings (also with $\varepsilon = 0.40$ and $\mathrm{A} = 100\,\pi d_{\mathrm{p}}^2$) resulted only in a ca. twofold increase of $h_{\min}$.[225]

To summarize, the transverse dispersion data of the polydisperse sphere packings ($\varepsilon = 0.40$) and the monolith ($\varepsilon = 0.70$) are similar to those of the pillar arrays (with $\varepsilon = 0.40$ and $\varepsilon = 0.70$, respectively) in an initial power law regime. However, while the effect of diffusion on transverse dispersion decreases and ultimately disappears at increasing velocity with the microscopically disordered chromatographic beds, it dominates in the pillar arrays. At increasing velocity, regular pillar arrays therefore become the least forgiving morphology with macroscopic heterogeneities and the engendered longitudinal dispersion. Wall effects with pillar arrays and the monolith impact band spreading more seriously than for packings; the efficiency loss with respect to the bulk bed morphologies is tremendous (cf. Figure 3.1).[182,225]

Acknowledgement

This work was supported by the Deutsche Forschungsgemeinschaft DFG (Bonn, Germany) under grants TA 268/5-1 and TA 268/6-1. Computational resources on IBM BlueGene/P and Power6 platforms were provided by RZG (Rechenzentrum Garching, Germany) and FZJ (Forschungszentrum Jülich, Germany). We are grateful to the John von Neumann Institute for Computing (NIC) and the Jülich Supercomputing Center (JSC) for allocation of a special CPU-time grant (NIC project number: 4717, JSC project ID: HMR10).

Chapter 4

Computational investigation of longitudinal diffusion, eddy dispersion, and trans-particle mass transfer in bulk, random packings of core–shell particles with varied shell thickness and shell diffusion coefficient

---

Authors:

Anton Daneyko, Dzmitry Hlushkou, Vasili Baranau, Siarhei Khirevich, Andreas Seidel-Morgenstern, and Ulrich Tallarek

State of publication: Submitted on April 8, 2015 to Journal of chromatography A

Abstract

In recent years, chromatographic columns packed with core–shell particles have been widely used for efficient and fast separations at comparatively low operating pressure. However, the influence of the porous shell properties on the mass transfer kinetics in core–shell packings is still not fully understood. We report on results obtained with a modeling approach to simulate three-dimensional advective–diffusive transport in bulk random packings of monosized core–shell particles, covering a range of reduced mobile phase flow velocities from 0.5 up to 1000. The impact of the effective diffusivity of analyte molecules in the porous shell and the shell thickness on the resulting plate height is investigated. We present an extension of Giddings' coupling theory of eddy dispersion to account for the analyte retention due to stagnant fluid regions in the porous shells of the particles, where the mobile phase flow velocity is zero. The plate height equation involving the modified eddy dispersion term excellently describes the simulated data for sphere

packings with varied shell thickness and shell diffusion coefficient. It is shown that the model of trans-particle mass transfer resistance for core–shell particles by Kaczmarski and Guiochon[261] is applicable up to a constant factor. We analyze individual contributions to the plate height from different mass transfer mechanisms in dependence of the shell parameters. Simulations demonstrate that a reduction of the plate height in packings of core–shell relative to fully porous particles arises mainly due to a reduced trans-particle mass transfer resistance and transchannel eddy dispersion.

4.1 Introduction

Core–shell particles have recently been intensively studied and employed for highly efficient, fast separations.[50,51,262–275] They consist of a nonporous fused-silica core surrounded by a porous layer having essentially the properties of fully porous particles. The performance of columns packed with sub-3 μm core–shell particles challenges that of columns packed with sub-2 μm fully porous particles, with the advantages of operating at back-pressures close to 3 μm-particle packings and smaller efficiency losses due to thermal effects at high flow rates.[87,262,276,277] The efficiency of a column with a given length and bed characteristic scale is inversely proportional to its height equivalent to a theoretical plate (HETP), which is mainly a function of the linear velocity of the mobile phase during an isocratic run. Nearly 60 years ago, van Deemter et al.[278] have formulated an empirical equation describing the essence of band broadening in chromatographic columns. These authors simplified the solution of the kinetic model developed earlier by Lapidus and Amundson[279] by assuming a Dirac pulse shape of the injection pulse. They established that the broadening of an analyte band during its migration along the column and the HETP are controlled by three independent factors: (i) longitudinal diffusion of analyte molecules along the

[261] K. Kaczmarski and G. Guiochon. *Anal. Chem.*, 79, pp. 4648–56, 2007.
[50] J. J. Kirkland, T. J. Langlois, and J. J. DeStefano. *Am. Lab.*, 39, pp. 18–21, 2007.
[51] G. Guiochon and F. Gritti. *J. Chromatogr. A*, 1218, pp. 1915–38, 2011.
[262] J. J. Destefano, T. J. Langlois, and J. J. Kirkland. *J. Chromatogr. Sci.*, 46, pp. 254–260, 2008.
[263] S. A. Schuster et al. *J. Chromatogr. Sci.*, 48, pp. 566–571, 2010.
[264] F. Gritti and G. Guiochon. *Anal. Chem.*, 85, pp. 3017–35, 2013.
[265] S. Fekete and D. Guillarme. *J. Chromatogr. A*, 1308, pp. 104–13, 2013.
[266] F. Gritti and G. Guiochon. *J. Chromatogr. A*, 1333, pp. 60–9, 2014.
[267] F. Gritti and G. Guiochon. *J. Chromatogr. A*, 1348, pp. 87–96, 2014.
[268] R. Hayes et al. *J. Chromatogr. A*, 1357, pp. 36–52, 2014.
[269] F. Gritti and G. Guiochon. *LC GC N. Am.*, 32, pp. 928–940, 2014.
[270] N. Lambert, I. Kiss, and A. Felinger. *J. Chromatogr. A*, 1366, pp. 84–91, 2014.
[271] J. C. Heaton and D. V. McCalley. *J. Chromatogr. A*, 1371, pp. 106–116, 2014.
[272] S. Fekete, D. Guillarme, and M. W. Dong. *LC GC N. Am.*, 32, p. 420, 2014.
[273] L. E. Blue and J. W. Jorgenson. *J. Chromatogr. A*, 1380, pp. 71–80, 2015.
[274] H. Dong and J. D. Brennan. *J. Colloid Interface Sci.*, 437, pp. 50–7, 2015.
[275] P. Jandera, T. Hájek, and M. Staňková. *Anal. Bioanal. Chem.*, 407, pp. 139–51, 2015.
[87] F. Gritti et al. *J. Chromatogr. A*, 1217, pp. 1589–603, 2010.
[276] R. W. Brice, X. Zhang, and L. A. Colón. *J. Sep. Sci.*, 32, pp. 2723–31, 2009.
[277] F. Gritti and G. Guiochon. *Chem. Eng. Sci.*, 65, pp. 6310–6319, 2010.
[278] J. J. van Deemter, F. J. Zuiderweg, and A. Klinkenberg. *Chem. Eng. Sci.*, 5, pp. 271–289, 1956.
[279] L. Lapidus and N. R. Amundson. *J. Phys. Chem. US*,, pp. 984–988, 1952.

concentration gradient in the eluent, (ii) eddy dispersion due to sample transport and exchange between the anastomosed flow paths in a packed bed, and (iii) mass transfer resistance due to finite rates for the transfer of analyte molecules between bulk eluent and stationary phase. These contributions to the HETP are referred to in chromatography as, respectively, the B, A, and C terms (or coefficients) of the van Deemter equation

$$H = \frac{B}{u_{\mathrm{av}}} + A + C u_{\mathrm{av}}, \tag{4.1}$$

where H is the plate height and u_{av} the average mobile phase velocity. The three contributions to the HETP account for all the band broadening due to mass transfer processes encountered in any type of chromatographic column. For instance, the B term is related to an apparent, complex diffusion coefficient accounting for the sample diffusivity in the interparticle bulk eluent and in the pore network of the stationary phase. The A term includes contributions due to flow velocity biases taking place over different characteristic lengths in the column, which can be divided into transchannel (associated with the dimension of the interparticle channels between neighboring particles), short-range interchannel (associated with the scale of a few particle diameters), long-range interchannel, and transcolumn effects.[66] The flow velocity biases behind the two latter contributions (long-range interchannel, transcolumn) occur only in macroscopically inhomogeneous packed beds. The C term accounts for all mechanisms resulting in a finite response time that analyte molecules need for transfer between solid and bulk liquid phase. As a consequence, the coefficients in Eq. (4.1) are semi-empirical and cannot be related directly to a physical description of the individual mass transfer mechanisms. A comprehensive approach to the efficiency of chromatographic beds therefore must distinguish between the individual contributions to band broadening arising from different mass transfer mechanisms and physiochemical phenomena. Then, the general HETP equation can be written as[178]

$$H = H_{\mathrm{long}} + H_{\mathrm{eddy}} + H_{\mathrm{film}} + H_{\mathrm{stat}} + H_{\mathrm{ads}} + H_{\mathrm{fe}}, \tag{4.2}$$

where the subscripts "long", "eddy", "film", "stat", "ads", and "fe" denote the contribution of longitudinal diffusion, eddy dispersion, external film mass transfer resistance, mass transfer resistance across the stationary phase including pore and surface diffusion, the rate of adsorption–desorption at the surface of an adsorbent, and the friction–expansion of the mobile phase, respectively.

Using peak parking experiments with a diffusion model based on the effective medium theory, Gritti and Guiochon[59] analyzed individual contributions to band broadening in columns packed with Halo and Kinetex core–shell particles. They demonstrated that the high efficiencies for core–shell particles in resolving low molecular weight compounds result from a combination of a smaller longitudinal diffusion term (B term in Eq. (4.1) and H_{long} term in Eq. (4.2) and

[66] J. C. Giddings *Dynamics of Chromatography: principles and theory* Marcel Dekker, 1965
[178] F. Gritti and G. Guiochon. *J. Chromatogr. A*, 1221, pp. 2–40, 2012.
[59] F. Gritti and G. Guiochon. *J. Chromatogr. A*, 1217, pp. 5069–5083, 2010.

significantly reduced eddy dispersion (A term in Eq. (4.1) and H_{eddy} term in Eq. (4.2) compared to those in columns packed with conventional fully porous particles.[51,59] Later, numerical simulations of hydrodynamic dispersion in bulk random packings of polydisperse particles[158] and the morphological analysis of physically reconstructed packed beds[280] revealed that the smaller eddy dispersion contribution to band broadening in columns packed with core–shell particles should be attributed to a higher transcolumn homogeneity rather than an improved bed morphology on smaller length scales. The origin for the decrease of B and H_{long} terms can be explained by a reduction of the total packed-bed volume accessible for diffusion due to the presence of the particles' solid cores. However, a rigorous theoretical analysis of the interrelation between physiochemical properties of the porous shells, analyte molecules, and column efficiency is still an unresolved problem.

The theoretical determination of the terms in the HETP equations is generally a big problem as it requires resolvable and accurate mathematical models for all mass transfer phenomena occurring in chromatographic columns. The greatest challenge results from the random and heterogeneous nature of the packed particulate beds. In this regard, computer simulations provide the exceptional possibility to evaluate the mass transfer characteristics in packed beds and analyze systematically the dependence of separation efficiency on individual parameters of the chromatographic system.

In this contribution, we present the results of a numerical investigation of advective–diffusive mass transfer in bulk random packings of spherical core–shell particles. We analyze the impact of the effective diffusivity of analyte molecules in the porous shell as well as the shell thickness on the plate height. For this purpose, we computer-generated random packings of 16,000 monosized particles. Then, we computed the three-dimensional flow velocity field in the interparticle void space using the lattice-Boltzmann method (LBM). Finally, the transport of point-like tracers in the interparticle void space and porous shells of the packing particles was modeled by a random-walk particle-tracking (RWPT) technique. A similar simulation approach was previously applied to study the effect of the packing porosity, morphology, and particle size distribution on the effective diffusivity and eddy dispersion in packed beds;[63,67,152,154,158,281] to analyze the impact of the packing confinement on eddy dispersion;[97,225] to study hydrodynamic dispersion in

[158] A. Daneyko et al. *Anal. Chem.*, 83, pp. 3903–10, 2011.
[280] S. Bruns et al. *J. Chromatogr. A*, 1268, pp. 53–63, 2012.
[63] S. Khirevich et al. *J. Chromatogr. A*, 1217, pp. 4713–4722, 2010.
[67] S. Khirevich et al. *Anal. Chem.*, 81, pp. 7057–7066, 2009.
[152] M. R. Schure et al. *J. Chromatogr. A*, 1031, pp. 79–86, 2004.
[154] M. R. Schure and R. S. Maier. *J. Chromatogr. A*, 1126, pp. 58–69, 2006.
[281] A. Daneyko et al. *J. Chromatogr. A*, 1257, pp. 98–115, 2012.
[97] R. S. Maier et al. *Phys. Fluids*, 15, pp. 3795–3815, 2003.
[225] A. Daneyko et al. *J. Chromatogr. A*, 1218, pp. 8231–48, 2011.

silica and polymeric chromatographic monoliths;[182,183,234,235,282] and to investigate the influence of analyte retention and adsorption kinetics on mass transport in open channels and packed beds.[77,283,284] In this study, we mainly focus on the analysis of the influence of two core–shell particle characteristics – the shell thickness and the value of the effective diffusion coefficient in the shell – on the plate height. The plate height equation for the system we investigate consists of three terms

$$H = H_{\mathrm{long}} + H_{\mathrm{eddy}} + H_{\mathrm{stat}}, \tag{4.3}$$

where the H_{eddy} term is associated with the flow velocity biases on only the transchannel and short-range interchannel characteristic lengths, because the packings are bulk packings, i.e., unconfined (no wall effects) and macroscopically homogeneous. The H_{long} term associated with the apparent diffusivity of tracers in the entire packing (including the interparticle void space and pore network in the particles' porous shells) is obtained by the RWPT simulation in the absence of flow. Then, we determine the plate height at different mobile phase flow velocities (with reduced velocities between 0.5 and 1000), while keeping the same structure of the packing, and vary the following two parameters: the diameter of the particles' solid core from zero (fully porous particles) to the particle diameter (nonporous particles) and the value of the effective diffusion coefficient in the porous shells. We analyze individual contributions to the plate height arising from different mass transfer mechanisms, using a proposed extension of the Giddings coupled eddy dispersion model to packings of core–shell particles and the model of Kaczmarski and Guiochon[261] originally developed for mass transfer in a single core–shell particle.

4.2 Numerical methods

4.2.1 Overview of the employed simulation methods

The numerical simulations of mass transport in packings of core–shell particles as performed in this work involve three distinct methods: (i) simulation of the bed structure, (ii) simulation of fluid flow in the interparticle void space, (iii) simulation of advective–diffusive transport of inert (non-reactive) point-like tracers. Firstly, a collective-rearrangement algorithm based on the Jodrey–Tory method was employed to generate random packings of spheres (Section 4.2.2). The method reproduces the morphological properties of the interstitial void space of the bulk region of a chromatographic bed. The LBM was used to calculate the three-dimensional flow velocity field in the interparticle void space of the packings (Section 4.2.3). And finally, a RWPT

[182] D. Hlushkou et al. *Anal. Chem.*, 82, pp. 7150–9, 2010.
[183] D. Hlushkou et al. *J. Sep. Sci.*, 34, pp. 2026–37, 2011.
[234] H. Koku et al. *J. Chromatogr. A*, 1218, pp. 3466–75, 2011.
[235] H. Koku et al. *J. Chromatogr. A*, 1237, pp. 55–63, 2012.
[282] D. Hlushkou et al. *J. Chromatogr. A*, 1303, pp. 28–38, 2013.
[77] M. R. Schure et al. *Anal. Chem.*, 74, pp. 6006–6016, 2002.
[283] D. Hlushkou et al. *J. Phys. Chem. C*, 117, pp. 22974–22985, 2013.
[284] D. Hlushkou et al. *Anal. Chem.*, 86, pp. 4463–4470, 2014.

technique was applied to simulate advective–diffusive transport of the tracers in the interparticle void space and diffusive transport in the porous shells of the particles (Section 4.2.4). To analyze the effect of the porous shell on the plate height, the shell thickness was systematically changed, while the arrangement of the spheres remained identical. In addition, two values of the effective shell diffusivity were used in the simulations.

4.2.2 Bed morphologies

Ten different bulk random packings of monosized spheres with an external (interparticle) porosity of $\varepsilon_e = 0.4$ were generated employing a modified Jodrey–Tory algorithm. A detailed description of this procedure can be found in.[63,232] Each packing had dimensions of $10\,d_p \times 10\,d_p \times 140\,d_p$, where d_p is the sphere diameter. All packings had periodic boundaries along every dimension. The implementation of periodic boundaries assumes that the sphere position on one side of the packing (i.e., within the representative domain) influences the position of spheres at the opposite side. Moreover, when a flow velocity field line or a tracer molecule is passing through one face of the representative domain, it reappears on the opposite face with the same properties. The length of the packings ($140\,d_p$) was chosen to avoid recorrelation artifacts observed when the packing length is too short.[43,72,232] These artifacts manifest themselves in an increasing value of the hydrodynamic dispersion coefficient with time. The tracer transport in the porous shells of the particles was assumed to be purely diffusive due to the much higher hydraulic resistance of the shell layer compared with the interparticle void space. The morphology of the particles was characterized by the core-to-particle diameter ratio, $\rho = d_{core}/d_p$. In this study, we analyzed packings composed of core–shell particles with nine values of $\rho = 0.0, 0.2, 0.5, 0.6, 0.74, 0.8, 0.9, 0.95$, and 1.0, covering the range from fully porous particles ($\rho = 0.0$) to nonporous particles ($\rho = 1.0$). The shell porosity in all particles was assumed as $\varepsilon_{shell} = 0.44$.[87] The diffusivity of tracers in the porous shells was characterized by the ratio $\Omega = D_{shell}/D_m$ of the effective diffusion coefficient in the shell (D_{shell}) to the molecular diffusion coefficient in the bulk solution (D_m). We used two values $\Omega = 0.2$ and 0.9, which represent the range of this parameter from a small nonretained to a moderately retained compound.[178,285]

4.2.3 Velocity field computations

The velocity field was computed using the LBM – a kinetic approach with discrete space and time based on resolving the microscopic Boltzmann equation instead of the macroscopic Navier–Stokes equation. Among the advantages of the LBM are its inherent parallelism in view of computational efficiency and the capability to handle topologically complex solid−liquid interfaces like those in random sphere packings. We employed a three-dimensional cubic lattice with

[232] S. Khirevich, A. Höltzel, and U. Tallarek. , 13, pp. 801–822, 2013.
[43] S. Khirevich “High-Performance Computing of Flow, Diffusion, and Hydrodynamic Dispersion in Random Sphere Packings” PhD thesis Germany: Philipps-Universität Marburg, 2010
[72] R. S. Maier et al. *Phys. Fluids*, 12, pp. 2065–2079, 2000.
[285] F. Gritti, K. Horvath, and G. Guiochon. *J. Chromatogr. A*, 1263, pp. 84–98, 2012.

19 links at each lattice node, the so-called D3Q19 lattice.[170] The lattice spacing Δl was adjusted to $\Delta l = d_\mathrm{p}/60$, i.e., 60 nodes per particle diameter.[158,232] After discretization of the generated bed structures the LBM lattice had dimensions of $600 \times 600 \times 8400$ nodes. Depending on the position, each lattice node was marked as either solid (inside the particles) or liquid (in the interparticle void space). At the solid−liquid interface, a halfway bounce-back rule was applied to implement the no-slip velocity boundary condition.[75] Periodic boundary conditions were imposed at the external faces of the computational domain. Further parameters and implementation details used for the LBM in this work can be found in:[43,158,225,232]

4.2.4 Hydrodynamic dispersion simulation

Mass transport of tracers in the interparticle void space of the packing and in the porous shells of the particles was modeled with a RWPT method.[37,78,286] The idea of the RWPT approach is to distribute a large number N of point-like tracers in the volume of interest and let them move according to the local flow velocity and local diffusion properties (in this work we employed $N = 3 \times 10^5$). The velocity of a tracer in the interparticle volume of the packing was determined by using its position in the discrete velocity field as obtained with the LBM (nearest-point interpolation with resolution $d_\mathrm{p}/60$). At each time step Δt of the algorithm, the position of the individual tracer is updated according to the following rule

$$\vec{r}\,(t + \Delta t) = \vec{r}\,(t) + \vec{u}\,(\vec{r}\,(t))\,\Delta t + \vec{\xi}\sqrt{2D\,(\vec{r}\,(t))\,\Delta t}, \tag{4.4}$$

where $\vec{u}(\vec{r}(t))$ is the flow velocity at $\vec{r}(t)$, $\vec{\xi}$ is a random vector whose Cartesian components have a standard normal distribution ($\vec{\xi}$ is independently generated on each iteration for each tracer), and $D(\vec{r}(t))$ is the diffusion coefficient at $\vec{r}(t)$. The diffusion coefficient of a tracer depends on its current position and is either equal to the molecular diffusion coefficient D_m (if the tracer is in the interparticle void space of the packing) or to $D_\mathrm{shell} = \Omega D_\mathrm{m}$ (if the tracer is in the porous shell of a particle, i.e., the shells of the particles are treated as homogeneous medium with an effective diffusion coefficient D_shell).

The transient hydrodynamic dispersion coefficient $D_\psi(t)$ along direction ψ is determined via the second central statistical moment of the coordinates of the tracer ensemble $\sigma_\psi^2\,(t)$ as

$$D_\psi(t) = \frac{1}{2}\frac{d\sigma_\psi^2\,(t)}{dt} = \frac{1}{2N}\frac{d}{dt}\sum\nolimits_i^N \left(\Delta r_{\psi,i}\,(t) - \langle \Delta r_{\psi,i}\,(t)\rangle\right)^2, \tag{4.5}$$

where $\Delta r_{\psi,i}\,(t) \equiv r_{\psi,i}\,(t) - r_{\psi,i}\,(0)$, $r_{\psi,i}\,(t)$ is the ψ-coordinate of the ith tracer and $\langle \Delta r_{\psi,i}\,(t)\rangle$ is the displacement along the ψ-direction averaged over the tracer ensemble. The asymptotic value

[170] Y. H. Qian, D. D'Humières, and P. Lallemand. *EPL*, 17, pp. 479–484, 1992.
[75] M. A. Gallivan et al. *Int. J. Numer. Methods Fluids*, 25, pp. 249–263, 1997.
[37] F. Delay, P. Ackerer, and C. Danquigny. *Vadose Zone J.*, 4, pp. 360–379, 2005.
[78] J. A. Rudnick and G. D. Gaspari *Elements of the random walk: an introduction for advanced students and researchers* Cambridge University Press, 2004
[286] P. Salamon, D. Fernàndez-Garcia, and J. J. Gómez-Hernández. *Water Resour. Res.*, 43, W08404, 2007.

of the dispersion coefficient $D_\psi = \lim_{t\to\infty} D_\psi(t)$ is related to the chromatographic plate height H_ψ in the corresponding direction as

$$D_\psi = \frac{H_\psi u_{\mathrm{av}}}{2} = \frac{h_\psi \nu D_{\mathrm{m}}}{2} = \frac{u_{\mathrm{av}}}{2}\frac{\partial \sigma_\psi^2}{\partial L}, \tag{4.6}$$

where h_ψ is the reduced plate height, $\nu = u_{\mathrm{av}} d_{\mathrm{p}}/D_{\mathrm{m}}$ is the reduced flow velocity (in this work, $0.5 \leq \nu \leq 1000$), L is the distance traveled by the analyte zone along the column (or generally, along the macroscopic flow direction), and σ_ψ^2 is the variance of the analyte zone.

The simulation of the effective diffusion coefficient D_{eff} – obstructed diffusion of the analyte through the interstitial void space of the bed *and* porous shells of the particles – is a special case of the hydrodynamic dispersion simulation, for which we use Eqs. (4.4) and (4.5) but set the velocity field to zero.

4.2.5 Mass balance in simulations with core–shell particles

Given a packing of mesoporous core–shell particles, let us consider the analyte concentration in the interparticle (macroporous) void space and in the mesopore volume of the shells. We assume that the tracers are inert, i.e., no adsorption takes place and the shell of the particle is merely a rigid mesoporous structure (Figure 4.1, top panel). If the size of the tracers is infinitely small (no finite-size effects occur) and the system is at equilibrium, the concentration of tracers in the interparticle macropores c_{e} should be equal to the concentration of tracers in the mesopores of the shell, $c_{\mathrm{e}} = c_{\mathrm{mesopore}}$ (see Figure 4.1, top panel).

Since the concentrations c_{mesopore} and c_{e} are equal, the amount of tracers in the shells N_{shell} should relate to the amount of the tracers in the interparticle void space N_{e} as

$$\frac{N_{\mathrm{shell}}}{N_{\mathrm{e}}} = \frac{(1-\varepsilon_{\mathrm{e}})\,(1-\rho^3)\,\varepsilon_{\mathrm{shell}}}{\varepsilon_{\mathrm{e}}}. \tag{4.7}$$

Tracers move in the pores of the shells, which occupy the volume $V_{\mathrm{shell,void}} = \varepsilon_{\mathrm{shell}} V_{\mathrm{shell}}$ (where V_{shell} is the total volume of the shells). When we switch from the microscopic approach to the effective medium approach the volume accessible for the tracers increases and becomes V_{shell}. This increase in volume accessible for tracers requires a decrease in their apparent effective concentration c_{eff} in the shell as $c_{\mathrm{eff}} = N_{\mathrm{shell}}/V_{\mathrm{shell}}$ (Figure 4.1, bottom panel). Since c_{eff} is less than c_{mesopore} the straightforward implementation of the random walk method will lead to an artificial diffusive flux that will eventually equilibrate c_{eff} and c_{mesopore} and thus violate the theoretically correct distribution of tracers governed by Eq. (4.7). To preserve the distribution according to Eq. (4.7), one needs to introduce a probability for tracers to cross the bulk liquid–shell boundary. This approach was developed empirically and validated experimentally by Hoteit et al.[287] Lim[288] extended that work to account for the porosity of the media. According to [287,

[287] H. Hoteit et al. *Math. Geol.*, 34, pp. 435–456, 2002.
[288] D. Lim. *Nucl. Technol.*, 156, pp. 222–245, 2006.

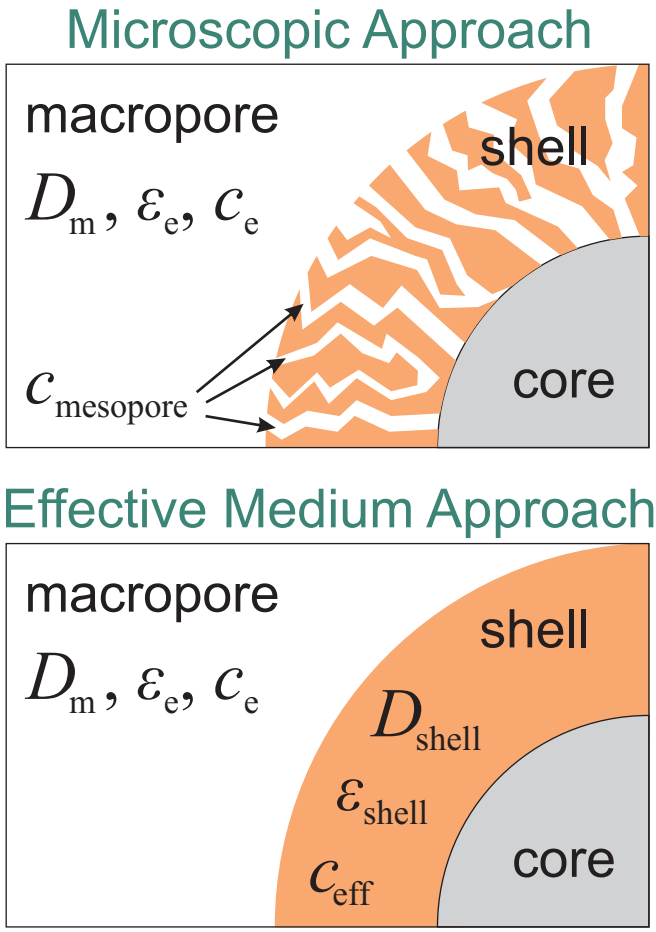

Figure 4.1: Comparison of the microscopic approach and the effective medium approach to core–shell particles. D_{shell} is the effective diffusion coefficient in the shell, D_{m} is the diffusion coefficient in the bulk fluid, c_{mesopore} is the analyte concentration in the mesopores of the shell, c_{e} is the concentration in the interparticle (macroporous) void space, $\varepsilon_{\mathrm{shell}}$ is the porosity of the shell, ε_{e} is the external porosity of the packing, and c_{eff} is the apparent effective concentration in the shell.

288], when a tracer hits the interface between medium M_1 and medium M_2 (regardless of the direction, i.e., whether this event occurs from M_1 to M_2 or from M_2 to M_1), the probability P_1 that a tracer ends up in medium M_1 is

$$P_1 = \frac{\varepsilon_1\sqrt{D_1}}{\varepsilon_1\sqrt{D_1} + \varepsilon_2\sqrt{D_2}}, \tag{4.8}$$

where ε_i and D_i ($i = 1, 2$) are the porosities and diffusion coefficients of the respective media. The probability that the tracer ends up in medium M_2 is

$$P_2 = 1 - P_1 = \frac{\varepsilon_2\sqrt{D_2}}{\varepsilon_1\sqrt{D_1} + \varepsilon_2\sqrt{D_2}}. \tag{4.9}$$

Later, Ramirez et al.[289] mathematically proved the empirical findings of Hoteit et al.[287], i.e., the validity of Eqs. (4.8) and (4.9), using the theory of α-skew Brownian motion. Bechtold et al.[290] proposed a modification to Eqs. (4.8) and (4.9) that makes them less expensive in terms of the numerical implementation. They showed that, since tracers cross the interface in *both* directions, one can achieve the same mass flux through the interface by letting tracers cross the interface from one side unconditionally and adjusting the probability to cross the interface from the other side. With these considerations in mind, they transformed Eqs. (4.8) and (4.9) into the following form:

$$\begin{cases} P_1 = \dfrac{\varepsilon_1\sqrt{D_1}}{\varepsilon_2\sqrt{D_2}} \text{ and } P_2 = 1 \text{ if } \dfrac{\varepsilon_1\sqrt{D_1}}{\varepsilon_2\sqrt{D_2}} \leq 1 \\ P_1 = \dfrac{\varepsilon_2\sqrt{D_2}}{\varepsilon_1\sqrt{D_1}} \text{ and } P_2 = 1 \text{ if } \dfrac{\varepsilon_1\sqrt{D_1}}{\varepsilon_2\sqrt{D_2}} > 1 \end{cases} \tag{4.10}$$

Here, P_1 is the probability for a tracer to enter medium M_1 when it hits the interface coming from medium M_2; P_2 is the probability to enter medium M_2 when the tracer hits the interface coming from medium M_1.

The work of Bechtold et al.[290] describes an efficient general RWPT method for porous media with discontinuous dispersion and diffusion coefficients. In the next section, we will show how this approach is adopted to our system.

4.2.6 RWPT method for core–shell particles

When a tracer moves in the interparticle void space of a packing its diffusive component of the displacement at each RWPT algorithm step is computed as

$$\Delta\vec{r} = \vec{\xi}\sqrt{2D_{\mathrm{m}}\Delta t}. \tag{4.11}$$

[289] J. M. Ramirez et al. *Water Resour. Res.*, 44, pp. 1–5, 2008.
[290] M. Bechtold et al. *Water Resour. Res.*, 47, W10526, 2011.

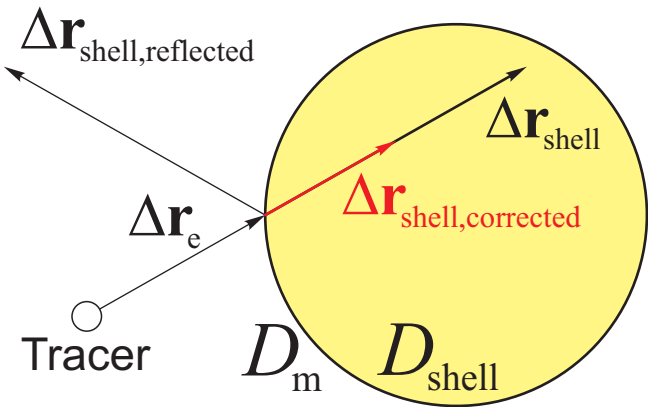

Figure 4.2: Illustration of random-walk particle-tracking method for media with discontinuous diffusion coefficients. The initial move of the tracer is split into external and internal components Δr_{e} and $\Delta r_{\mathrm{shell}}$. If the tracer is reflected, then $\Delta r_{\mathrm{shell}}$ is transformed into $\Delta r_{\mathrm{shell,reflected}}$; if the tracer stays in the particle, the $\Delta r_{\mathrm{shell}}$ component is transformed into $\Delta r_{\mathrm{shell,corrected}}$ according to Eq. (4.16) because of the difference between diffusion coefficients outside and inside the porous shell (D_{m} and D_{shell}).

If the tracer ends up in the shell of a particle after a $\Delta\vec{r}$ displacement, we need to decide if the tracer enters the shell or is reflected from the particle surface. According to Eq. (4.10), the probability that a tracer enters the shell from the interparticle space (P_{shell}) and the probability that a tracer enters the interparticle space from the shell (P_{e}) shall be calculated as follows:

$$P_{\mathrm{shell}} = \sqrt{\frac{D_{\mathrm{shell}}}{D_{\mathrm{m}}}}\varepsilon_{\mathrm{shell}} \text{ and } P_{\mathrm{e}} = 1. \tag{4.12}$$

Any time a tracer hits the particle boundary from the interparticle void space, we generate a random number χ from a [0, 1] uniform distribution. If $\chi \leq P_{\mathrm{shell}}$, the tracer is allowed to enter the particle; otherwise, it is reflected specularly from the surface of the particle (Figure 4.2). Since we know the position of the particle, we can split the tracer displacement $\Delta\vec{r}$ into the external $\Delta\vec{r}_{\mathrm{e}}$ and internal $\Delta\vec{r}_{\mathrm{shell}}$ components with respect to the particle surface and determine their values (see Figure 4.2):

$$\Delta\vec{r} = \Delta\vec{r}_{\mathrm{e}} + \Delta\vec{r}_{\mathrm{shell}} \tag{4.13}$$

If the tracer enters the particle, the $\Delta\vec{r}_{\mathrm{shell}}$ part of the total tracer displacement $\Delta\vec{r}$ should be corrected, as it was computed with D_{m} instead of D_{shell} in Eq. (4.11). The correction procedure was implemented according to the nonlinear time-splitting scheme by Bechtold et al.[290]

$$\sqrt{\Delta t} = \sqrt{\Delta t_{\mathrm{e}}} + \sqrt{\Delta t_{\mathrm{shell}}}, \tag{4.14}$$

where Δt_{e} is the time spent in the interparticle space and $\Delta t_{\mathrm{shell}}$ the time spent in the shell during a single iteration when the tracer crosses the bulk liquid–particle interface. Using the Einstein

diffusion formula, we can obtain the expression for the time of the external displacement $\Delta\vec{r}_e$:

$$\sqrt{\Delta t_\mathrm{e}} = |\Delta\vec{r}_\mathrm{e}| \Big/ \left|\vec{\xi}\sqrt{2D_\mathrm{m}}\right| \tag{4.15}$$

Using Eqs. (4.14), (4.15), and the Einstein diffusion formula, we can compute a corrected displacement inside the particle $\Delta\vec{r}_{\mathrm{shell,corrected}}$ as:

$$\Delta\vec{r}_{\mathrm{shell,corrected}} = \vec{\xi}\sqrt{2D_\mathrm{shell}\Delta t_\mathrm{shell}} = \vec{\xi}\sqrt{2D_\mathrm{shell}\Delta t}\left(1 - \frac{|\Delta\vec{r}_\mathrm{e}|}{|\Delta\vec{r}|}\right) \tag{4.16}$$

When a tracer starts its displacement in the shell of a particle and ends up in the interparticle space of the packing, we let it out unconditionally ($P_\mathrm{e} = 1$) according to Eq. (4.10).

We also have to correct the external part $\Delta\vec{r}_\mathrm{e}$ of the total tracer displacement $\Delta\vec{r}$. The expression for the corrected displacement $\Delta\vec{r}_{\mathrm{e,corrected}}$ is derived similar to Eq. (4.16):

$$\Delta\vec{r}_{\mathrm{e,corrected}} = \vec{\xi}\sqrt{2D_\mathrm{m}\Delta t_\mathrm{e}} = \vec{\xi}\sqrt{2D_\mathrm{m}\Delta t}\left(1 - \frac{|\Delta\vec{r}_\mathrm{shell}|}{|\Delta\vec{r}|}\right) \tag{4.17}$$

If the tracer hits a nonporous core of the particle it is always reflected specularly.

To simulate mass transport with different reduced velocities, we scaled linearly the velocity field. This is a valid approach, as the velocity fields were determined for the laminar regime, which means that local flow velocity scales linearly with applied pressure and average flow velocity.[225] To prevent instability and numerical dispersion, the cell Péclet number $Pe_\mathrm{cell} = u_\mathrm{av}\Delta l/D_\mathrm{m}$ was always kept below 20 (Δl is the lattice spacing in the LBM).[72]

4.2.7 Validation of the simulation approach

The LBM implementation was validated by comparing the velocity fields with analytical solutions of the Navier–Stokes equation in an open channel having circular cross-section and between two infinite parallel plates. Using the same LBM implementation, Khirevich[43] simulated flow in the body-centered cubic (BCC) sphere packing and compared permeability with analytical solutions of Sangani and Acrivos[292] and Zick and Homsy;[293] the deviation was within 2%. Hlushkou et al.[181] simulated hydraulic flow in a physically reconstructed silica monolith and compared the simulated permeability with experimental data; the relative difference was 2–4%.

The precision of our implementation of the RWPT method was investigated in [232]. The authors compared simulated hydrodynamic dispersion in an open channel with the analytical solution of Taylor and Aris[16,17] and found excellent agreement in the range of Péclet numbers of $1 \leq Pe \leq 1000$. In previous work,[225] we compared the results of hydrodynamic dispersion simu-

[292] A. S. Sangani and A. Acrivos. *Int. J. Multiphas. Flow.*, 8, pp. 343–360, 1982.
[293] A. A. Zick and G. M. Homsy. *J. Fluid Mech.*, 115, pp. 13–26, 1982.
[181] D. Hlushkou, S. Bruns, and U. Tallarek. *J. Chromatogr. A*, 1217, pp. 3674–3682, 2010.
[16] G. Taylor. *Philos. Trans. R. Soc. A*, 219, pp. 186–203, 1953.
[17] R. Aris. *P. Roy. Soc. A-Math. Phy.*, 235, pp. 67–77, 1956.

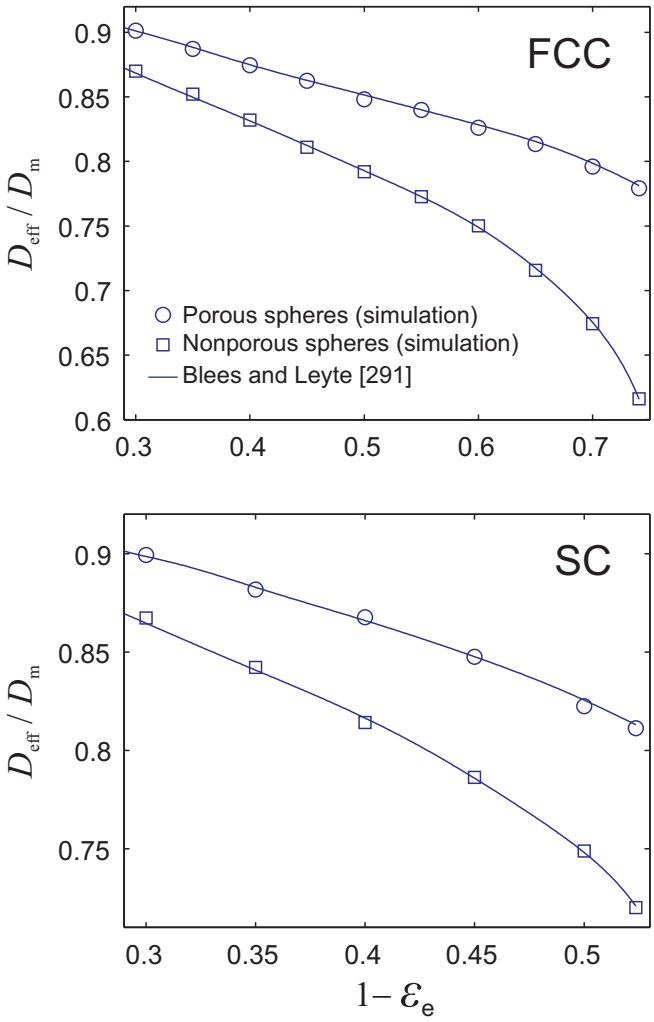

Figure 4.3: Comparison of our simulated data with the solution of Blees and Leyte.[291] Normalized effective diffusion coefficient $D_{\mathrm{eff}}/D_{\mathrm{m}}$ as a function of the packing density $(1-\varepsilon_{\mathrm{e}})$. Data of Blees and Leyte were taken from Figures 2 and 4 in [291]. The top panel shows diffusivities for the face-centered cubic (FCC) geometry. The bottom panel shows diffusivities for the simple cubic (SC) geometry.

lations in periodic arrays of cylinders with experiments of Eghbali et al.[184] and found excellent agreement. A recent comparison of our simulated data for packed beds of nonporous particles with pulsed field gradient nuclear magnetic resonance experiments in [294] has revealed a maximum deviation between simulation and experiment of 5 to 10% for longitudinal and transverse dispersion coefficients, respectively.

For this work, we have conducted additional simulations to validate the implementation of the RWPT method for systems with discontinuous diffusion coefficients, described in Section 4.2.4. We have simulated diffusion in periodic arrays of spheres. The spheres were centered in the lattice points of the face-centered cubic (FCC) and simple cubic (SC) crystals. The porosity of the structures was varied through the variation of the sphere size. Both cases of nonporous and fully porous spheres where investigated. Figure 4.3 reveals excellent agreement between our simulations and the analytical results of Blees and Leyte.[291] In the case of fully porous particles the ratio of the concentrations in the interparticle void space c_e and inside the particles c_eff was $c_\mathrm{e}/c_\mathrm{eff} = 10$. In terms of Blees and Leyte,[291] the parameters were $D_1C_1 = 0.1\ D_2C_2$ and $D_1 = D_2$, where $(D_1,\ C_1)$ and $(D_2,\ C_2)$ are the diffusion coefficient and concentration for the intraparticle and interparticle space, respectively.

In the course of every simulation, the monitored distribution of tracers conformed to Eq. (4.7). We also monitored the spatial distribution of tracers near the surface of the particles to ensure their concentration is not distorted – an effect known if the multiple-rejection boundary condition is used instead of specular reflection.[79]

4.3 Motivation for the extension of the Giddings theory

In this section, we briefly show that the original Giddings theory of coupled eddy dispersion cannot explain the behavior of the plate height curves obtained by simulations of advective–diffusive mass transport in the packings of core–shell particles. The reduced plate height for the packings under study can be represented as the sum of three independent contributions associated with three distinct mass transport mechanisms: longitudinal diffusion (h_long), eddy dispersion (h_eddy), and trans-particle mass transfer resistance (h_shell)

$$h = h_\mathrm{long} + h_\mathrm{eddy} + h_\mathrm{shell} = \frac{2D_\mathrm{eff}\,(\rho)}{D_\mathrm{m}R\nu} + A\,(\nu) + C_\mathrm{p}\nu, \tag{4.18}$$

where $D_\mathrm{eff}(\rho)$ is the effective diffusion coefficient for a given value of the core-to-particle diameter ratio ρ, $A(\nu)$ is the eddy dispersion term, and C_p is the trans-particle mass-transfer resistance coefficient. The retention ratio can be defined according to Giddings[66] as $R = N_\mathrm{e}/(N_\mathrm{e} + N_\mathrm{shell})$ and determined in terms of the external porosity of a packing ε_e, the shell porosity $\varepsilon_\mathrm{shell}$, and the

[184] H. Eghbali et al. *Anal. Chem.*, 81, pp. 705–715, 2009.
[291] M.H. Blees and J.C. Leyte. *J. Colloid Interface Sci.*, 166, pp. 118–127, 1994.
[79] P. Szymczak and A. J. C. Ladd. *Phys. Rev. E*, 68, p. 036704, 2003.

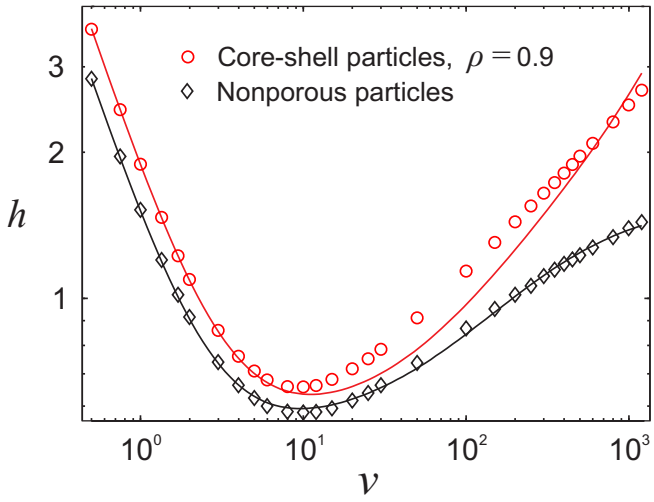

Figure 4.4: Comparison of simulated plate heights for core–shell particles (red circles) with the plate height model (red solid line) that uses structural parameters λ_i and ω_i obtained for nonporous particles (black diamonds and black solid line) in the eddy dispersion term $A(\nu)$ of Eq. (4.18). The maximum relative deviation of the model (red solid line) from the simulation results (red circles) for core–shell particles with a core-to-particle diameter ratio of $\rho = 0.9$ is 15%. The external porosity of the packings is $\varepsilon_e = 0.4$, the particles' shell porosity is $\varepsilon_{shell} = 0.44$.

core-to-particle diameter ratio ρ as

$$R = \frac{\varepsilon_e}{(1-\varepsilon_e)\,\varepsilon_{shell}\,(1-\rho^3)+\varepsilon_e}. \tag{4.19}$$

The retention ratio R is related to the zone retention factor k_1 often used in the literature as

$$R = 1/(1+k_1). \tag{4.20}$$

The origin of retention for nonadsorbed molecules is the zero-velocity field of stagnant fluid regions in the porous shells, accessible by diffusion.

According to Giddings' theory of coupled eddy dispersion,[66] the $A(\nu)$ term for bulk, macroscopically homogeneous packings of nonporous particles includes the transchannel ($i = 1$) and short-range interchannel ($i = 2$) contributions:

$$A(\nu) = \sum_{i=1}^{2} \frac{2\lambda_i}{1+\left(\frac{2\lambda_i}{\omega_i}\right)\nu^{-1}}, \tag{4.21}$$

where λ_i and ω_i are parameters that depend *only* on the geometrical structure of the packing ("structural parameters"). Equation (4.18) involving the A term determined by Eq. (4.21) was already used for describing successfully the reduced plate height curves (h–ν) simulated for bulk packings of nonporous particles,[63,158] when the trans-particle mass-transfer resistance coefficient C_p is zero and the retention ratio $R = 1$. An example of such a fitting result is shown in Figure 4.4 from the current study: The black diamonds in that figure are the values of h obtained with the

modeling approach described in Section 4.2 for a bulk packing of nonporous spheres ($\rho = 1.0$); the black solid line represents the fitting of the simulated data by Eqs. (4.18) and (4.21) with $C_{\mathrm{p}} = 0$ and $R = 1$. For this fitting procedure, we first determined D_{eff} in Eq. (4.18) from the simulation of purely diffusive transport in the packing ($\nu = 0$). As a consequence, the only free fitting parameters were λ_1, λ_2, ω_1, and ω_2 (the structural parameters) determining the eddy dispersion term (h_{eddy}) in Eq. (4.18).

We attempted to exploit the same model, Eqs. (4.18) and (4.21), to fit the reduced plate height curve for a packing of core–shell particles. For this purpose, we used the same packing, i.e., with the same particle size and arrangement, but with porous shells ($\rho = 0.9$) introduced into the particles. The value of D_{eff} for this packing was determined from the simulation of purely diffusive transport in the interparticle void space and the porous shells. To demonstrate the inapplicability of the original Giddings theory to porous particles, we used in Eq. (4.21) values of the structural parameters (λ_1, λ_2, ω_1, ω_2) determined for the same packing but composed of nonporous particles. Thus, the only unknown parameter to be fitted in Eq. (4.18) was C_{p}. The red circles and red solid line in Figure 4.4 represent, respectively, the simulated values of h in the core–shell particle-packing and the fit of Eqs. (4.18) and (4.21) with structural parameters of the nonporous particles and adjustable C_{p}. Fitting quality is much lower than for the nonporous particles and the relative difference between simulated data and the fitted curve reaches 15%. This disagreement originates in the fact that Giddings' coupled eddy dispersion theory does not account for analyte retention due to stagnant mobile phase in the porous shells. Giddings speculated that for porous particles (R <1) ω_1 may increase tenfold, whereas the parameter ω_2 should be less affected by changes in solute retention (conclusion of Chapter 2.8 in [66]). However, the theory of coupled eddy dispersion as presented in [66] does not provide any explicit dependency of the structural parameters (ω_i, λ_i) on retention due to analyte adsorption or due to the presence of stagnant mobile phase.

In the next section, we will present an extension of the original Giddings model to the case of core–shell particles.

4.4 Giddings theory of and its extension to packings of core–shell particles

In Sections 4.4.1 through 4.4.6, we present the derivation of the Giddings theory of coupled eddy dispersion for nonporous particles, which combines a cell model and effective medium approach with a discrete representation of the velocity field. Then, in Section 4.4.7, we extend this theory to the case of core–shell particles, using the same formalism.

4.4.1 Prerequisites

We need three equations to follow the reasoning of Giddings.

(i) Definition of plate height as the ratio of the variance of the analyte zone to the distance

traveled by the center of the band:

$$H = \frac{\sigma^2}{L} \tag{4.22}$$

(ii) Einstein's mean square displacement formula (for one-dimensional diffusion):

$$\sigma^2 = 2D_{\mathrm{m}}t \tag{4.23}$$

(iii) The relation for the variance of the displacement of a random walker:

$$\sigma^2 = l^2 n \tag{4.24}$$

Here, l is the length of the random walker step and n is the number of steps.

It is assumed that the chromatographic zone spreading follows Fick's law (pseudo-diffusive behavior) and yields a Gaussian profile, which obeys Eq. (4.23) but with D_{m} replaced by some effective coefficient. If the solute is unretained, the center of the zone moves with the average mobile phase velocity (u_{av}).

4.4.2 Cell model

Following Giddings' arguments in [66], we assume that the continuous velocity field in a packing can be represented by the simplified velocity field depicted in Figure 4.5, which is a superposition of two different velocity field layers. Each layer consists of neatly connected rectangular cells, which are $\gamma_i d_{\mathrm{p}}$ long and $\alpha_i d_{\mathrm{p}}$ wide ($i = 1, 2$). The mobile phase velocity in a cell of each field i in the frame of reference of the zone center is $\pm\Delta u_i$. Thus, the velocity at a given point in the laboratory frame of reference is $u_{\mathrm{av}} \pm \Delta u_1 \pm \Delta u_2$.

The velocity layer with smaller cells or layer 1 (black grid in Figure 4.5) is referred to as "transchannel", since it is associated with a transport process in the channels formed by the spheres in the packing. The size of a transchannel cell in the model is supposed to correspond to the average channel dimensions in a packing. It is assumed that the velocity in a given channel is constant and persists throughout its whole length, until the channel splits or merges with another one. The larger cells of the second velocity layer (red grid in Figure 4.5) represent regions, where a variation of the velocity occurs due to irregularities of the sphere packing on a spatial scale larger than in the first (transchannel) layer. Layer 2 is referred to as "short-range interchannel" and is associated with mass transport between the channels that are represented by layer 1. Unlike the transchannel layer, the short-range interchannel layer does not directly correspond to any physical boundary in the packing. The original estimates of the cell dimensions for typical chromatographic beds by Giddings[66] were $\alpha_1 = 1/6$, $\alpha_2 = 1.25$, $\gamma_1 = 1$, and $\gamma_2 = 1.5$. Giddings also included long-range interchannel and transcolumn layers in the velocity field superposition. These layers arise from velocity inhomogeneities on scales larger than those considered in this study. Consequently, they are not included in the further reasoning.

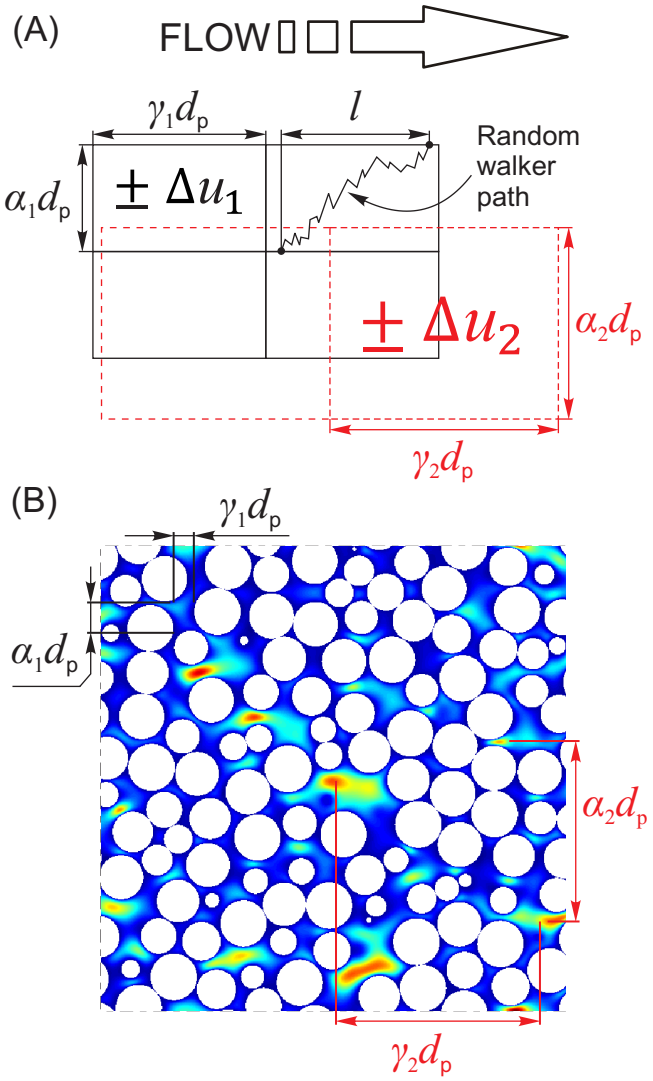

Figure 4.5: Top panel: Schematic of the velocity field in the eddy dispersion theory of Giddings, as seen from the frame of reference of the center of the analyte zone. The black cells are from the transchannel layer of the velocity field (index 1) and the red cells are from the short-range interchannel layer (index 2). Although we have only drawn four transchannel and two short-range interchannel cells, they fill up space regularly and infinitely. The distance l represents the jump of the random walker relative to the center of the analyte zone. Bottom panel: Slice of a simulated velocity field with the corresponding length scales, $\alpha_1 d_\mathrm{p}$ (transchannel) and $\alpha_2 d_\mathrm{p}$ (short-range interchannel). The color map indicates the velocity component along the superficial flow direction (red regions correspond to high velocity, blue regions to low velocity).

The model implies that the sign of Δu_i is chosen randomly with probability 1/2. This rule ensures that there are as much $+\Delta u_i$ cells as $-\Delta u_i$ cells (so that the average velocity u_{av} is not affected) and velocity biases on different levels, i.e., Δu_1 and Δu_2 are spatially uncorrelated. We now consider a single molecule as a random walker that moves in *one of the velocity layers*, whose parameters l and n we need to determine, so we could use Eq. (4.24) to compute the variance of its displacement. The step length l is defined as the distance that a molecule travels in the flow direction without velocity change relative to the center of the analyte zone. Transport of molecules with different velocities is one of the origins for zone dispersion. The top panel of Figure 4.5 illustrates two possibilities for a molecule to change velocity: due to a diffusion-controlled process or a flow-controlled process. The first scenario is realized when the molecule diffuses the distance $\alpha_i d_{\mathrm{p}}$ $(i = 1, 2)$ laterally into the neighboring cell. The second scenario is realized when the molecule travels the distance $\gamma_i d_{\mathrm{p}}$ $(i = 1, 2)$ along the flow into the next cell. These two mechanisms of velocity switch give rise to the different plate height contributions, which are described in Sections 4.4.3 and 4.4.4.

4.4.3 Diffusion-controlled dynamics of random walk

Let us consider the first scenario, when the dynamics of the random walk is determined by diffusion along the direction transverse to the average flow velocity (we use the subscript D for the diffusion-related quantities). Giddings assumed that this diffusion happens on both velocity layers with molecular diffusion coefficient D_{m} and used Einstein's diffusion formula, Eq. (4.23), to obtain the time needed to diffuse from the border of one cell into its neighbor (i.e., to travel the distance $\alpha_i d_{\mathrm{p}}$ in one dimension):

$$t_{\mathrm{D},i} = \alpha_i^2 d_{\mathrm{p}}^2 / 2D_{\mathrm{m}} \tag{4.25}$$

Since the center of the zone has the velocity u_{av}, the length of the random walker step in the frame of reference that moves with the center of the zone is:

$$l_{\mathrm{D},i} = \Delta u_i t_{\mathrm{D},i} \tag{4.26}$$

Given that L is the distance travelled by the zone center, the number of steps needed for the molecule to be displaced by L is

$$n_{\mathrm{D},i} = \frac{L}{S_{\mathrm{D},i}}, \tag{4.27}$$

where $S_{\mathrm{D},i}$ is the distance that the random walker travels on average in the laboratory frame of reference between diffusion-controlled cell changes. Since the average speed of the molecule is the same as the speed of the zone u_{av}, then:

$$S_{\mathrm{D},i} = u_{\mathrm{av}} t_{\mathrm{D},i} \tag{4.28}$$

We can now write down the expression for the plate height $H_{D,i}$ that originates from the diffusion-controlled dynamics, using Eqs. (4.22)–(4.28):

$$H_{\mathrm{D},i} = \frac{\sigma_{\mathrm{D},i}}{L} = \frac{l_{\mathrm{D},i}^2 n_{\mathrm{D},i}}{L} = \frac{\Delta u_i^2 t_{\mathrm{D},i}^2 n_{\mathrm{D},i}}{L} = \frac{\Delta u_i^2 t_{\mathrm{D},i}^2}{S_{\mathrm{D},i}} = \frac{\Delta u_i^2 t_{\mathrm{D},i}}{u_{\mathrm{av}}} = \frac{\Delta u_i^2 \alpha_i^2 d_{\mathrm{p}}^2}{u_{\mathrm{av}} 2 D_{\mathrm{m}}} \tag{4.29}$$

If we introduce the relative velocity difference as

$$\beta_i = \frac{\Delta u_i}{u_{\mathrm{av}}}, \tag{4.30}$$

then the result of Eq. (4.29) can be rewritten as

$$H_{\mathrm{D},i} = \frac{\alpha_i^2 \beta_i^2}{2} \frac{d_{\mathrm{p}}^2 u_{\mathrm{av}}}{D_{\mathrm{m}}}, \tag{4.31}$$

which is formula (2.8-9) in [66]. Equation (4.31) can be rewritten in the form that was used by Giddings to derive the coupling formula:

$$H_{\mathrm{D},i} = \beta_i^2 S_{\mathrm{D},i} \tag{4.32}$$

4.4.4 Flow-controlled dynamics of random walk

The second scenario for a molecule to change its velocity is the elution into the neighboring cell by fluid flow. This is the case when the dynamics of the random walker is controlled by changes in the flow field (subscript F). The distance $S_{\mathrm{F},i}$ that the random walker travels in the laboratory frame of reference between flow-controlled cell changes is:

$$S_{\mathrm{F},i} = \gamma_i d_{\mathrm{p}} \tag{4.33}$$

Accordingly, the number of steps for a random walker to travel the distance L is:

$$n_{\mathrm{F},i} = \frac{L}{S_{\mathrm{F},i}} \tag{4.34}$$

The time that a molecule spends in the cell on average is:

$$t_{\mathrm{F},i} = \frac{\gamma_i d_{\mathrm{p}}}{u_{\mathrm{av}}} \tag{4.35}$$

The average length of the step between velocity changes in the frame of reference of the zone center is:

$$l_{\mathrm{F},i} = \Delta u_i t_{\mathrm{F},i} \tag{4.36}$$

Using Eqs. (4.22), (4.24), (4.30), and (4.33)–(4.36) we obtain the flow-controlled contribution to the plate height:

$$H_{\mathrm{F},i} = \frac{\sigma_{\mathrm{F},i}}{L} = \frac{l_{\mathrm{F},i}^2 n_{F,i}}{L} = \frac{\left(\Delta u_i t_{\mathrm{F},i}\right)^2 n_{F,i}}{L} = \frac{\left(\Delta u_i t_{\mathrm{F},i}\right)^2}{S_{\mathrm{F},i}} = \frac{\left(\Delta u_i \gamma_i d_{\mathrm{p}}\right)^2}{u_{\mathrm{av}}^2 S_{\mathrm{F},i}} = \gamma_i \left(\frac{\Delta u_i}{u_{\mathrm{av}}}\right)^2 d_{\mathrm{p}} = \gamma_i \beta_i^2 d_{\mathrm{p}} \quad (4.37)$$

4.4.5 Interdependence of diffusion- and flow-controlled dynamics (coupling)

Earlier theory of eddy dispersion argued that its contribution to the plate height was constant for a given column,[295] i.e., it did not depend on velocity. If one assumes that the diffusion-controlled and flow-controlled processes are independent of each other, then according to the random-walk theory the variances of their respective random walks should sum up. This will lead to a linear dependence of plate height from velocity. However, experiments have shown that the plate height approaches a plateau with increasing velocity.[295–297] Since the velocity field affects the concentration field, which in turn drives diffusion, we cannot consider the diffusion-controlled mass transport as independent from flow-controlled mass transport. Thus, the addition of variances of the random walk processes should not hold true.

To introduce the interdependence of diffusion- and flow-controlled random walks, Giddings assumed that the length of the random walker step in the laboratory frame of reference is controlled by a combination of the diffusion- and flow-controlled dynamics (subscript C for coupled):

$$S_{\mathrm{C},i} = L/(n_{\mathrm{D},i} + n_{\mathrm{F},i}) \quad (4.38)$$

Then, he *postulated* that the expression for the coupled plate height $H_{C,i}$ has a functional form similar to the expression for the diffusion-controlled plate height $H_{D,i}$ defined by Eq. (4.32). This assumption leads to the following expression:

$$H_{\mathrm{C},i} = \beta_i^2 S_{\mathrm{C},i} \quad (4.39)$$

Equations (4.38) and (4.39) were used to derive the coupled plate height H_{C} as a combination of diffusion- and flow-controlled contributions (H_{D} and H_{F}). Notably, Klinkenberg and Sjenitzer[298] have pointed out the lack of justification for the conceptually similar assumption made in the very first publication of Giddings[188] on the coupling effect. Several other authors have also pointed

[295] J. C. Giddings and R. A. Robison. *Anal. Chem.*, 34, pp. 885–890, 1962.
[296] J. C. Giddings. *Anal. Chem.*, 35, pp. 1338–1341, 1963.
[297] A. Klinkenberg. *Anal. Chem.*, 38, pp. 489–490, 1966.
[298] A. Klinkenberg and F. Sjenitzer. *Nature*, 187, p. 1023, 1960.
[188] J. C. Giddings. *Nature*, 184, pp. 357–358, 1959.

out the empirical nature of the coupling formula.[247,299,300] In the remainder of this section, we derive the coupling formula on a mathematically more rigorous basis than the one originally presented by Giddings in [66, 188].

We first derive a set of simple asymptotic behaviors for the coupled plate height H_C as a function of the diffusion- and flow-controlled plate heights $H_\mathrm{C} = H_C\left(H_\mathrm{D}, H_\mathrm{F}\right)$. This allows us to specify a Taylor expansion for H_C in terms of H_D and H_F. We derive one possible form of coupling by neglecting unknown higher-order terms in this expansion. As far as H_C shall be fully described by H_D and H_F, our derivation does not depend on the physical mechanisms we choose for specifying the asymptotic behaviors of H_D and H_F. We utilize the cell model from Figure 4.5 to analyze the behavior of these terms.

Let us examine the case of infinitely wide cells ($\alpha_i \to \infty$ in Figure 4.5): The diffusion-controlled process will never be able to bring a molecule out of its cell, so the only mechanism that is going to participate in switching between the cells is the flow-controlled process. Thus, the coupled plate height will be equal to the flow-controlled plate height, $H_\mathrm{C} = H_\mathrm{F}$. At the same time, if $\alpha_i \to \infty$, then according to Eq. (4.29) $H_\mathrm{D} \to \infty$. Let us examine another case – that of infinitely long cells ($\gamma_i \to \infty$ in Figure 4.5): The flow-controlled process will never be able to bring a molecule out of its cell, so the cell switch will be accomplished by the diffusion-controlled process only. Thus, $H_\mathrm{C} = H_\mathrm{D}$, and according to Eq. (4.37) $H_\mathrm{F} \to \infty$. We now have the following set of asymptotic conditions:

$$\begin{cases} H_\mathrm{D} \to \infty \implies H_\mathrm{C} = H_\mathrm{F} \\ H_\mathrm{F} \to \infty \implies H_\mathrm{C} = H_\mathrm{D} \end{cases} \tag{4.40}$$

If we introduce a set of reciprocal variables $\phi = 1/H$, we transform the infinities in Eq. (4.40) into zeros:

$$\begin{cases} \phi_\mathrm{D} \to 0 \implies \phi_\mathrm{C} = \phi_\mathrm{F} \\ \phi_\mathrm{F} \to 0 \implies \phi_\mathrm{C} = \phi_\mathrm{D} \end{cases} \tag{4.41}$$

Despite the function $\phi_\mathrm{C} = \phi_C\left(\phi_D, \phi_\mathrm{F}\right)$ – a reciprocal of function H_C – is unknown, we can write its Taylor expansion at the point $\phi_\mathrm{D} = 0$, $\phi_\mathrm{F} = 0$ as

$$\phi_\mathrm{C} = \phi_\mathrm{C}\left(0,\, 0\right) + \frac{\partial \phi_\mathrm{C}}{\partial \phi_\mathrm{F}}\left(0, 0\right)\phi_\mathrm{F} + \frac{\partial \phi_\mathrm{C}}{\partial \phi_\mathrm{D}}\left(0, 0\right)\phi_\mathrm{D} + R_\mathrm{T}(\phi_\mathrm{F}, \phi_\mathrm{D}), \tag{4.42}$$

where $R_\mathrm{T}(\phi_\mathrm{F}, \phi_\mathrm{D})$ is a remainder of the series. If we truncate Eq. (4.42) – use only linear terms

[247] D. S. Horne, J. H. Knox, and L. McLaren. *Separ. Sci.*, 1, pp. 531–554, 1966.
[299] C. Horvath and H.-J. Lin. *J. Chromatogr. A*, 126, pp. 401–420, 1976.
[300] A. L. Berdichevsky and U. D. Neue. *J. Chromatogr. A*, 535, pp. 189–198, 1990.

– and combine it with the set of asymptotic conditions (4.41), we get:

$$\begin{cases} \phi_{\mathrm{C}}(0,0) + \dfrac{\partial \phi_{\mathrm{C}}}{\partial \phi_{\mathrm{F}}}(0,0)\,\phi_{\mathrm{F}} = \phi_{\mathrm{F}} \\ \phi_{\mathrm{C}}(0,0) + \dfrac{\partial \phi_{\mathrm{D}}}{\partial \phi_{\mathrm{F}}}(0,0)\,\phi_{\mathrm{D}} = \phi_{\mathrm{D}} \end{cases} \tag{4.43}$$

The system of Eq. (4.43) can only hold true if

$$\begin{cases} \phi_{\mathrm{C}}(0,0) = 0 \\ \dfrac{\partial \phi_{\mathrm{C}}}{\partial \phi_{\mathrm{F}}}(0,0) = 1 \\ \dfrac{\partial \phi_{\mathrm{D}}}{\partial \phi_{\mathrm{F}}}(0,0) = 1 \end{cases} \tag{4.44}$$

Using Eq. (4.44) in Eq. (4.42) and discarding higher order terms of ϕ_F and ϕ_{D}, we get:

$$\phi_{\mathrm{C}} = \phi_{\mathrm{F}} + \phi_{\mathrm{D}} \tag{4.45}$$

If we rewrite Eq. (4.45) in the form of plate heights, we obtain the coupling formula of Giddings for the ith velocity field layer:

$$1/H_{\mathrm{C},i} = 1/H_{\mathrm{F},i} + 1/H_{\mathrm{D},i} \tag{4.46}$$

Thus, the coupling can be derived through the cell model by neglecting higher-order terms in the Taylor expansion of ϕ_{C} Eq. (4.42).

The last assumption of the coupled eddy dispersion theory is that the processes happening in different layers of the velocity field are uncorrelated. Thus, their contributions are additive and the total eddy dispersion is the sum of the transchannel and short-range interchannel contributions:

$$H_{\mathrm{eddy}} = H_{\mathrm{C},1} + H_{\mathrm{C},2} \tag{4.47}$$

To obtain the most common representation of the coupling formula, Eq. (4.21), we need to use a different set of variables:

$$\begin{cases} \omega_i = \alpha_i^2 \beta_i^2 / 2 \\ \lambda_i = \gamma_i \beta_i^2 / 2 \end{cases} \tag{4.48}$$

As seen from Eq. (4.48), the parameters ω_i and λ_i do not depend on retention. In Section 4.4.7, we will extend the theory of coupled eddy dispersion to account for retention.

4.4.6 Comments on the original Giddings theory and further modifications

In Sections 4.4.2–4.4.5 it has been shown that the Giddings model is a combination of the cell model and effective-medium approach with a discrete representation of the velocity field. A mathematically rigorous cell model was developed by Schettler and Giddings in [301]. They introduced a correlation parameter that determined the order in which cells with different velocity bias alternate, but unfortunately the theory assumed a simpler geometrical structure. The authors showed how the choice of the correlation parameter (that determines the order in which cells with different velocity bias alternate) leads either to the classical or coupled model of eddy dispersion. The derivation that we have laid out in the previous sections is based on the uniform random distribution of the $\pm\Delta u_i$ cells, however the real velocity field is spatially correlated, i.e., regions of high velocity do not abruptly follow after low-velocity regions. The focus on spatial correlations of the velocity field might be the key to further advancements in the theory of dispersion in packed beds. Using Fourier analysis it might be possible to expand the discrete case described in [301] to a computed flow field and establish a quantitative link between the spatial correlations of the velocity field and eddy dispersion.

In [302] Giddings and Schettler developed a mathematically rigorous but at the same time very general theory that included the retention factor, i.e., it was not constrained to nonporous particles. The partial differential equations of this theory were solved for extremely high and extremely low velocity and conform to the coupling formula for the plate height:

$$H_{\text{low}} = -\frac{2}{D}\langle u(\vec{r})g(\vec{r},R)\rangle \tag{4.49}$$

$$H_{\text{high}} = -2\frac{\langle u(\vec{r})f(\vec{r})\rangle}{\langle u(\vec{r})\rangle} \tag{4.50}$$

Here, $\vec{r}$ is a point in the packing, R is the retention ratio, $g(\vec{r},R)$ and $f(\vec{r})$ are some unknown functions, and $u(\vec{r})$ is the projection of the velocity vector onto the direction of the superficial flow. The theory, however, does not offer solutions for the intermediate velocity range, i.e., it does not provide any direct corroboration of the coupling formula, Eq. (4.46), in the range of velocities where chromatography usually operates. However, the coupling formula shows good quantitative agreement with simulations and experimental data for nonporous particles.[63,158,186,294] The treatment of *porous* or *core–shell* particles ($R \neq 1$) in the framework of this theory has not yet been undertaken and is considered in the next section.

4.4.7 Extension of the Giddings formula for core–shell particles

We now derive expressions for the diffusion- and flow-controlled plate height contributions for the case when the packing particles have porous shells. Physical quantities associated with the

[186] P. Magnico and M. Martin. *J. Chromatogr. A*, 517, pp. 31–49, 1990.

core–shell particles will be denoted with primes.

Dependence of the cell model parameters on retention

The average velocity of analyte molecules through a bed of core–shell particles ($u_{\mathrm{av}}^{'}$) is a function of the retention ratio R and the average velocity in the interparticle void space u_{av}:

$$u_{\mathrm{av}}^{'} = Ru_{\mathrm{av}} \tag{4.51}$$

The relative velocity difference for the case of core–shell particles ($\beta_i^{'}$) can be obtained from Eqs. (4.30) and (4.51)

$$\beta_i^{'} = \Delta u_i / u_{\mathrm{av}}^{'} = \Delta u_i / Ru_{\mathrm{av}} = \beta_i / R, \tag{4.52}$$

where we assume that the velocity differences Δu_i remain unchanged. The spatial structure of the velocity field changes with the variation of the core-to-particle diameter ratio, i.e., the volume occupied by a porous shell is a zero-velocity region available for diffusion, which should affect the cell model. The characteristic length for such a region is comparable to the size of the particle and the size of the short-range interchannel velocity cells. We therefore assume that the dimensions of the short-range interchannel velocity cells should be a function of R or ρ, since $R = R(\rho)$ (cf. Eq. (4.19). With the assumption that the aspect ratio of the cells is preserved, the functional dependence of the cell length $\gamma_2^{'}$ and width $\alpha_2^{'}$ can be expressed as

$$\gamma_2^{'} = \gamma_2 R^{\eta} \text{ and } \alpha_2^{'} = \alpha_2 R^{\eta}, \tag{4.53}$$

where η is the unknown parameter and γ_2 and α_2 are the length and width of the short-range interchannel cell for the case of nonporous particles. Since the transchannel velocity layer represents the velocity field *between* particles, the cell dimensions of this layer are assumed to be independent from R. Thus, the whole set of the cell model parameters is:

$$\begin{cases} \beta_1^{'} = \beta_1 / R \\ \alpha_1^{'} = \alpha_1 \\ \gamma_1^{'} = \gamma_1 \\ \beta_2^{'} = \beta_2 / R \\ \alpha_2^{'} = \alpha_2 R^{\eta} \\ \gamma_2^{'} = \gamma_2 R^{\eta} \end{cases} \tag{4.54}$$

Eddy-dispersion formula for core–shell particles

Dimensions of the short-range interchannel cells (Figure 4.5) in the Giddings model reach beyond the size of a pore between the particles. Since diffusion on this length scale will be obstructed by the spheres of the packing and their shells, it is reasonable to use the effective diffusion coefficient D_{eff} instead of the molecular diffusion coefficient D_{m} in the diffusion-controlled contribution

described by Eq. (4.31). Therefore, for the case of core–shell particles, Eq. (4.31) becomes:

$$H_{\mathrm{D},2}^{'} = \frac{\alpha_2^{'2}\beta_2^{'2}}{2}\frac{d_\mathrm{p}^2 u_\mathrm{av}^{'}}{D_\mathrm{eff}} \tag{4.55}$$

It should be noted that the influence of ρ and Ω is already taken into account by the use of the effective diffusion coefficient D_eff. We now have all prerequisites to write down the full eddy dispersion plate height expression for core–shell particles. First, from Eqs. (4.46), (4.47), and (4.54) we obtain the following expression:

$$\begin{aligned} H_\mathrm{C}^{'} &= \sum\nolimits_{i=1}^{2}\left(1\Big/H_{\mathrm{D},i}^{'} + 1\Big/H_{\mathrm{F},i}^{'}\right)^{-1} = \\ &\left[\left(\frac{\alpha_1^{'2}\beta_1^{'2}}{2}\frac{d_\mathrm{p}^2 u_\mathrm{av}^{'}}{D_\mathrm{m}}\right)^{-1} + \left(\gamma_1^{'}\beta_1^{'2} d_\mathrm{p}\right)^{-1}\right]^{-1} + \left[\left(\frac{\alpha_2^{'2}\beta_2^{'2}}{2}\frac{d_\mathrm{p}^2 u_\mathrm{av}^{'}}{D_\mathrm{eff}}\right)^{-1} + \left(\gamma_2^{'}\beta_2^{'2} d_\mathrm{p}\right)^{-1}\right]^{-1} = \\ &\left[\left(\frac{\alpha_1^2\beta_1^2}{2R}\frac{d_\mathrm{p}^2 u_\mathrm{av}}{D_\mathrm{m}}\right)^{-1} + \left(\frac{\gamma_1\beta_1^2}{R^2} d_\mathrm{p}\right)^{-1}\right]^{-1} + \left[\left(\frac{\alpha_2^2\beta_2^2}{2R^{1-2\eta}}\frac{d_\mathrm{p}^2 u_\mathrm{av}}{D_\mathrm{eff}}\right)^{-1} + \left(\frac{\gamma_2\beta_2^2}{R^{2-\eta}} d_\mathrm{p}\right)^{-1}\right]^{-1} \end{aligned} \tag{4.56}$$

Next, we simplify Eq. (4.56) by introducing a set of parameters $\lambda_i^{'}$ and $\omega_i^{'}$:

$$\begin{cases} \omega_1^{'} = \alpha_1^2\beta_1^2/2R \\ \lambda_1^{'} = \gamma_1\beta_1^2/2R^2 \\ \omega_2^{'} = \alpha_2^2\beta_2^2/2R^{1-2\eta} \\ \lambda_2^{'} = \gamma_2\beta_2^2/R^{2-\eta} \end{cases} \tag{4.57}$$

Using Eq. (4.57), we can rewrite Eq. (4.56) in a simpler form:

$$H_\mathrm{C}^{'} = \left[\left(\omega_1^{'}\frac{d_\mathrm{p}^2 u_\mathrm{av}}{D_\mathrm{m}}\right)^{-1} + \left(2\lambda_1^{'} d_\mathrm{p}\right)^{-1}\right]^{-1} + \left[\left(\omega_2^{'}\frac{d_\mathrm{p}^2 u_\mathrm{av}}{D_\mathrm{eff}}\right)^{-1} + \left(2\lambda_2^{'} d_\mathrm{p}\right)^{-1}\right]^{-1} \tag{4.58}$$

Finally, from Eq. (4.58) we obtain the reduced plate height:

$$\begin{aligned} h_\mathrm{C}^{'} = \frac{H_\mathrm{C}^{'}}{d_\mathrm{p}} &= \left[\left(\omega_1^{'}\nu\right)^{-1} + \left(2\lambda_1^{'}\right)^{-1}\right]^{-1} + \left[\left(\omega_2^{'}\nu D_\mathrm{m}/D_\mathrm{eff}\right)^{-1} + \left(2\lambda_2^{'}\right)^{-1}\right]^{-1} = \\ &\frac{2\lambda_1^{'}}{1+\left(\dfrac{2\lambda_1^{'}}{\omega_1^{'}}\right)\nu^{-1}} + \frac{2\lambda_2^{'}}{1+\dfrac{D_\mathrm{eff}}{D_\mathrm{m}}\left(\dfrac{2\lambda_2^{'}}{\omega_2^{'}}\right)\nu^{-1}} \end{aligned} \tag{4.59}$$

Equations (4.57) and (4.59) represent our extension of the eddy dispersion theory to core–shell particles that takes retention into account. The main expression, Eq. (4.59), has a form similar to the one in the original theory of Giddings, with two distinctions: (i) The effective diffusion in the short-range interchannel term accounts for the influence of both ρ and Ω on transverse

mixing due to diffusion, and (ii) the parameters $\lambda_i^{'}$ and $\omega_i^{'}$ depend on the retention ratio R as described by Eq. (4.57).

4.4.8 Sum of the relative velocity differences

The velocity within the cell of an ith layer in the Giddings model is:

$$u_i^{\text{cell}} = \begin{cases} +\Delta u_i, \ p_+ = 0.5 \\ -\Delta u_i, \ p_- = 0.5 \end{cases} \tag{4.60}$$

That is, the magnitude of the velocity in the frame of reference of the zone center is Δu and its direction is a random variable with probability $p_+ = p_- = 0.5$. The variance of the velocity field defined by Eq. (4.60) is:

$$\text{Var}\left(u_i^{\text{cell}}\right) = \Delta u_i^2 \tag{4.61}$$

In the Giddings theory, the velocity fields in transchannel (u_1^{cell}) and short-range interchannel (u_2^{cell}) layers are chosen in a way that they are spatially uncorrelated to another, a prerequisite for splitting the eddy dispersion into *independent* transchannel and short-range interchannel contributions. Due to the absence of correlation the following property holds

$$\sum_i \text{Var}\left(u_i^{\text{cell}}\right) = \text{Var}\left(\sum_i u_i^{\text{cell}}\right) = \text{Var}\left(u^{\text{cell}}\right), \tag{4.62}$$

where u^{cell} is the total discrete velocity in the Giddings theory. The expression for the sum of the relative velocity differences β_{sum} can be obtained using Eqs. (4.30), (4.61), and (4.62):

$$\beta_{\text{sum}}^2 \overset{\text{def}}{=} \sum_i \beta_i^2 = \sum\nolimits_i \frac{\Delta u_i^2}{u_{\text{av}}^2} = \sum\nolimits_i \frac{\text{Var}\left(u_i^{\text{cell}}\right)}{u_{\text{av}}^2} = \frac{\text{Var}\left(u^{\text{cell}}\right)}{u_{\text{av}}^2} \tag{4.63}$$

We assume that the variance of the discrete velocity field u^{cell} defined in the Giddings theory is equal to the variance of the velocity field obtained from the LBM simulations, which gives us the opportunity to compute β_{sum}^2 for the simulated flow field. We will use Eq. (4.63) in Section 4.5.3 to extract the parameters α_i, γ_i, and β_i from our simulated data.

4.5 Results and discussion

4.5.1 Plate height

The numerical approach presented in Section 4.2 was used to simulate the reduced plate height h in packings of core–shell particles with different values of ρ (solid core-to-particle diameter ratio) and Ω (ratio of the effective diffusion coefficient in the porous shell to the diffusion coefficient in bulk solution). Figure 4.6 shows the simulated reduced plate height (symbols) as a function

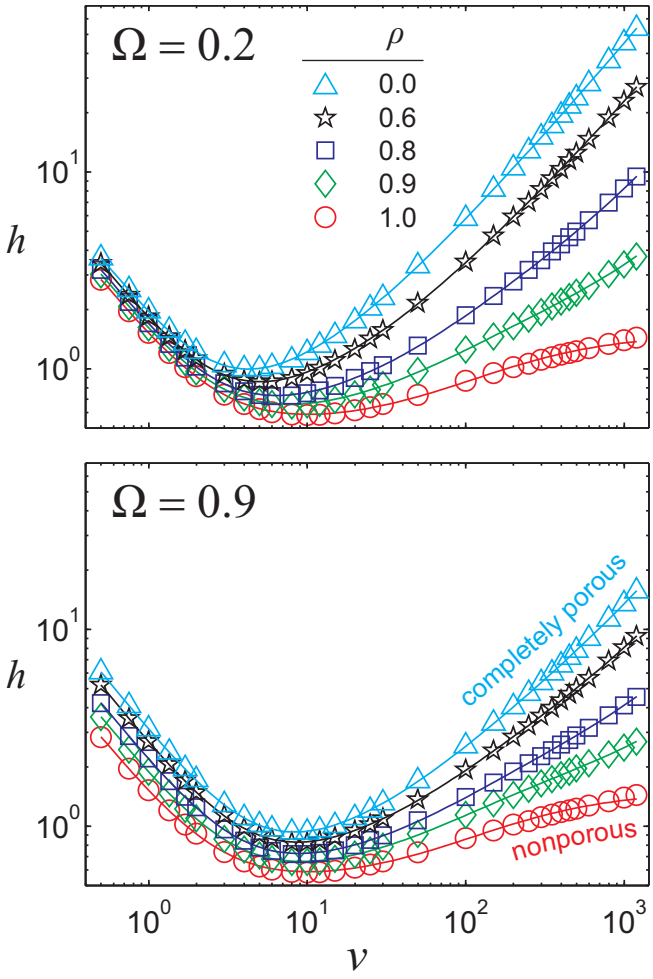

Figure 4.6: Simulated reduced plate height h (symbols) as a function of the reduced velocity ν for different normalized shell diffusivities $\Omega = D_{\mathrm{shell}}/D_{\mathrm{m}}$ and core-to-particle diameter ratios $\rho = d_{\mathrm{core}}/d_{\mathrm{p}}$. Solid lines correspond to fits of the data by Eq. (4.64). The size of the 95% confidence interval for each data point is smaller than the size of the markers. Data for some of the nine employed ρ-values are omitted from the figure for better visualization. The external porosity of the packings is $\varepsilon_{\mathrm{e}} = 0.4$, the particles' shell porosity is $\varepsilon_{\mathrm{shell}} = 0.44$.

of the reduced velocity ν. At each given value of ρ and Ω, simulations were carried out for ten packings (with different particle arrangements), obtained using the same packing protocol. Each symbol in Figure 4.6 corresponds to a h-value averaged over its ten values for the different beds. Statistical variation due to the random nature of the packings is represented by 95% prediction intervals. These intervals, however, were smaller than the size of the markers in Figure 4.6. For all values of ν and both values of Ω the reduced plate height decreases systematically with increasing ρ, i.e., with decreasing shell thickness from fully porous ($\rho = 0$) to nonporous particles ($\rho = 1$). The results in Figure 4.6 agree with experimental observations of increased efficiency for columns packed with core–shell particles compared to fully porous particles.[51,59] Further analysis of the data in the bottom panel of Figure 4.6 indicates that for the higher value of Ω (0.9) the optimal reduced velocity ν_{opt} (corresponding to the minimum of h) does not change markedly with ρ, i.e., with the shell thickness, whereas the value of ν_{opt} increases with smaller ρ at $\Omega = 0.2$ (top panel of Figure 4.6). Thus, for larger analyte molecules (lower intraparticle diffusivity) a reduction of the shell thickness will result in a noticeable increase of ν_{opt} (shorter analysis time). But it should be noted that a reduction of the shell thickness also lowers the column capacity, which may eliminate the benefit of using particles with thinner porous shells. The solid lines in Figure 4.6 represent the fitting results obtained using the following expression:

$$h(\nu) = h_{\mathrm{long}}(\nu) + h_{\mathrm{eddy},1}(\nu) + h_{\mathrm{eddy},2}(\nu) + h_{\mathrm{shell}}(\nu) = \frac{2D_{\mathrm{eff}}(\rho,\Omega)}{D_{\mathrm{m}}R\nu} + \frac{2\lambda_1'}{1+\left(\frac{2\lambda_1'}{\omega_1'}\right)\nu^{-1}} + \frac{2\lambda_2'}{1+\frac{D_{\mathrm{eff}}(\rho,\Omega)}{D_{\mathrm{m}}}\left(\frac{2\lambda_2'}{\omega_2'}\right)\nu^{-1}} + C_{\mathrm{p}}\nu \quad (4.64)$$

Here, $h_{\mathrm{eddy},1}$ and $h_{\mathrm{eddy},2}$ are the transchannel and the short-range interchannel contribution to eddy dispersion, respectively. In Eq. (4.64), we used the explicit forms of $h_{\mathrm{eddy},1}$ and $h_{\mathrm{eddy},2}$ that were obtained in Section 4.4, Eq. (4.59), by an extension of the Giddings coupled eddy dispersion model. Values of $D_{\mathrm{eff}}(\rho, \Omega)$ were acquired from independent simulations of purely diffusive transport in the packings (without fluid flow). Therefore, five parameters were free during the fitting procedure: λ_1', λ_2', ω_1', ω_2', and C_{p}. The retention ratio R in dependence of ρ was computed according to Eq. (4.19). The fitting quality with Eq. (4.64) in Figure 4.6 is much better than with Eq. (4.18) in Figure 4.4, which used the hydrodynamic dispersion term from the original Giddings model of coupled eddy dispersion Eq. (4.21) and structural parameters for packings of nonporous particles. It allows to conclude that our extension of the Giddings model, developed and presented in Section 4.4, adequately describes dispersion in the packings of core–shell particles. The fit of the simulated plate height data by Eq. (4.64) using the known $D_{\mathrm{eff}}(\rho, \Omega)$ allows us to quantify the individual contributions h_{long}, $h_{\mathrm{eddy},1}$, $h_{\mathrm{eddy},2}$, and h_{shell} to the total reduced plate height h and analyze the dependence of these contributions from the porous shell parameters, ρ and Ω.

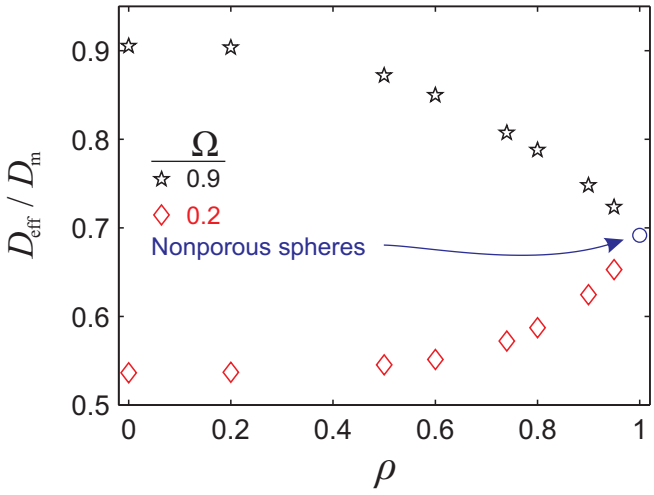

Figure 4.7: Normalized effective diffusion coefficient $D_{\mathrm{eff}}/D_{\mathrm{m}}$ for different $\Omega = D_{\mathrm{shell}}/D_{\mathrm{m}}$ as a function of the core-to-particle diameter ratio ρ. The size of the 95% prediction intervals for each data point is smaller than the size of the markers.

4.5.2 Effective diffusion coefficient

With the RWPT simulation approach presented in Section 4.2.4, we determined the effective diffusion coefficient D_{eff} in the packings of core–shell particles as a function of ρ and Ω. To recall, D_{eff} characterizes the effective diffusivity in both the interparticle void space and the porous shells. The results of the simulations are shown in Figure 4.7. Remarkably, the behaviors of D_{eff} in dependence of ρ are opposite at $\Omega = 0.2$ and 0.9: With a reduction of ρ (i.e., with increasing shell thickness) the effective diffusion coefficient in the packings increases for $\Omega = 0.9$ and decreases for $\Omega = 0.2$. This finding can be explained as follows. In a packing of core–shell particles, the solute fraction R resides in the interparticle void space where diffusive transport is characterized by D_{m}. The other solute fraction $(1 - R)$ resides in the porous shells of the particles, where the diffusion coefficient is $D_{\mathrm{shell}} = \Omega D_{\mathrm{m}}$. The value of R depends on ρ according to Eq. (4.19). Diffusion in both intraparticle and interparticle regions is obstructed: molecules in the interparticle void space follow the tortuous paths around the spheres, while molecules inside the particles follow the tortuous paths around the solid cores. The effective diffusion coefficient in the packing D_{eff} is a combination of effective diffusion coefficients in the interparticle space and in the particles. When the core diameter increases (ρ increases), the effective diffusion coefficient decreases for molecules in the spheres, but at the same time the solute fraction in the shell also decreases, thus reducing the influence of the decreasing effective diffusivity in the sphere on D_{eff}.

The D_{eff}-behavior in Figure 4.7 can be interpreted in the following way: A tracer moving between two points in the interparticle void space of the packing can follow a path either through the shell of a particle or around the particle. Effective diffusion is either enhanced or hindered, depending on Ω. As ρ increases the shell gets thinner and less analyte molecules reside in the shell. Consequently, the respective effect of the shell (enhancing or hindering diffusion) decreases

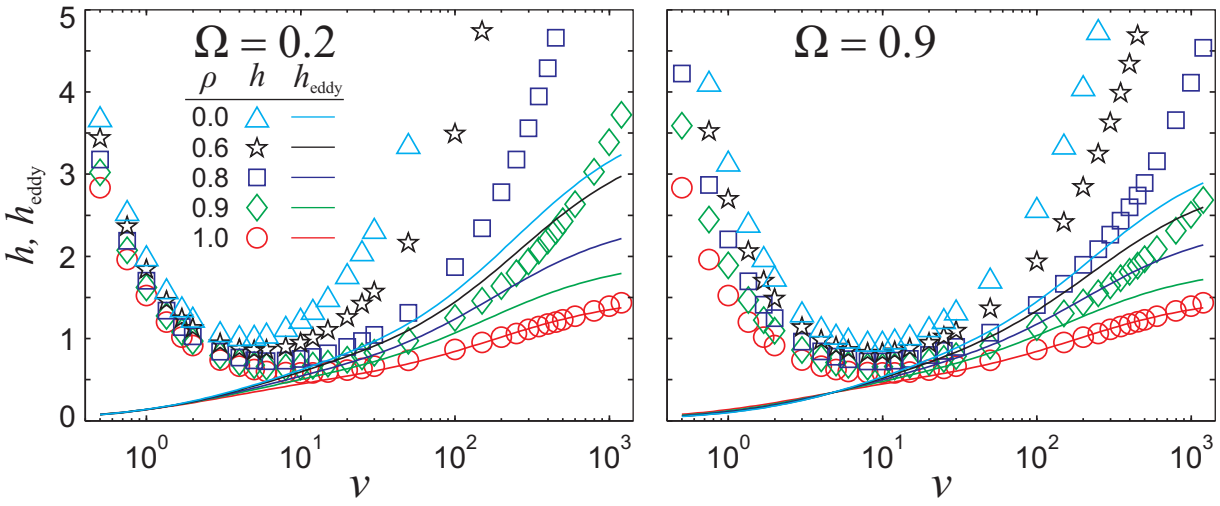

Figure 4.8: Comparison of the total reduced plate height h (symbols) and the contribution from eddy dispersion $h_{\mathrm{eddy}} = h_{\mathrm{eddy},1} + h_{\mathrm{eddy},2}$ (solid lines) as a function of the reduced velocity ν for the different values of ρ and Ω.

and D_{eff} converges to the value for nonporous particles (blue circle, Figure 4.7).

Therefore, the effect of D_{eff} on the reduced plate height term $h_{\mathrm{long}} = 2D_{\mathrm{eff}}/D_{\mathrm{m}}R\nu$ may be either beneficial or adverse: at a given value of ν, h_{long} may either decrease or increase depending on the value of Ω, and the magnitude of either effect is controlled by the shell thickness, as shown in Figure 4.7.

4.5.3 Eddy dispersion

Using the fits from Figure 4.6, we were able to extract the contribution of eddy dispersion $h_{\mathrm{eddy}} = h_{\mathrm{eddy},1} + h_{\mathrm{eddy},2}$ to the total reduced plate height and analyze its dependence on ρ and Ω. Figure 4.8 shows h_{eddy} as a function of the reduced velocity for different values of Ω and a systematic variation of ρ. The magnitude of h_{eddy} systematically grows with a decrease of ρ, i.e., the eddy dispersion term is higher in packings of fully porous particles ($\rho = 0$) than in the core–shell packings. This finding agrees with experimental results obtained by Gritti and Guiochon.[59] However, the difference between the contributions of h_{eddy} at different ρ-values to the overall reduced plate height near the plate height minima is marginal. It supports the conclusion from a morphological analysis of the wall region in core–shell packings,[280] i.e., the reduced eddy dispersion contribution should be basically attributed to a higher transcolumn homogeneity rather than an improved bed morphology on smaller length scales.

Up until now, no model for transchannel or short-range interchannel eddy dispersion took retention into account in a quantitative manner. As described in Section 4.3, it was previously assumed that the coefficients λ_i and ω_i obtained for nonporous particles under unretained conditions have the same values as for porous particles. In this case, it would leave C_{p} as the only parameter to be determined in Eq. (4.18). The discrepancy between this assumption and the simulation results favors rejecting of this model (cf. Figure 4.4). In Section 4.4.7, we have shown

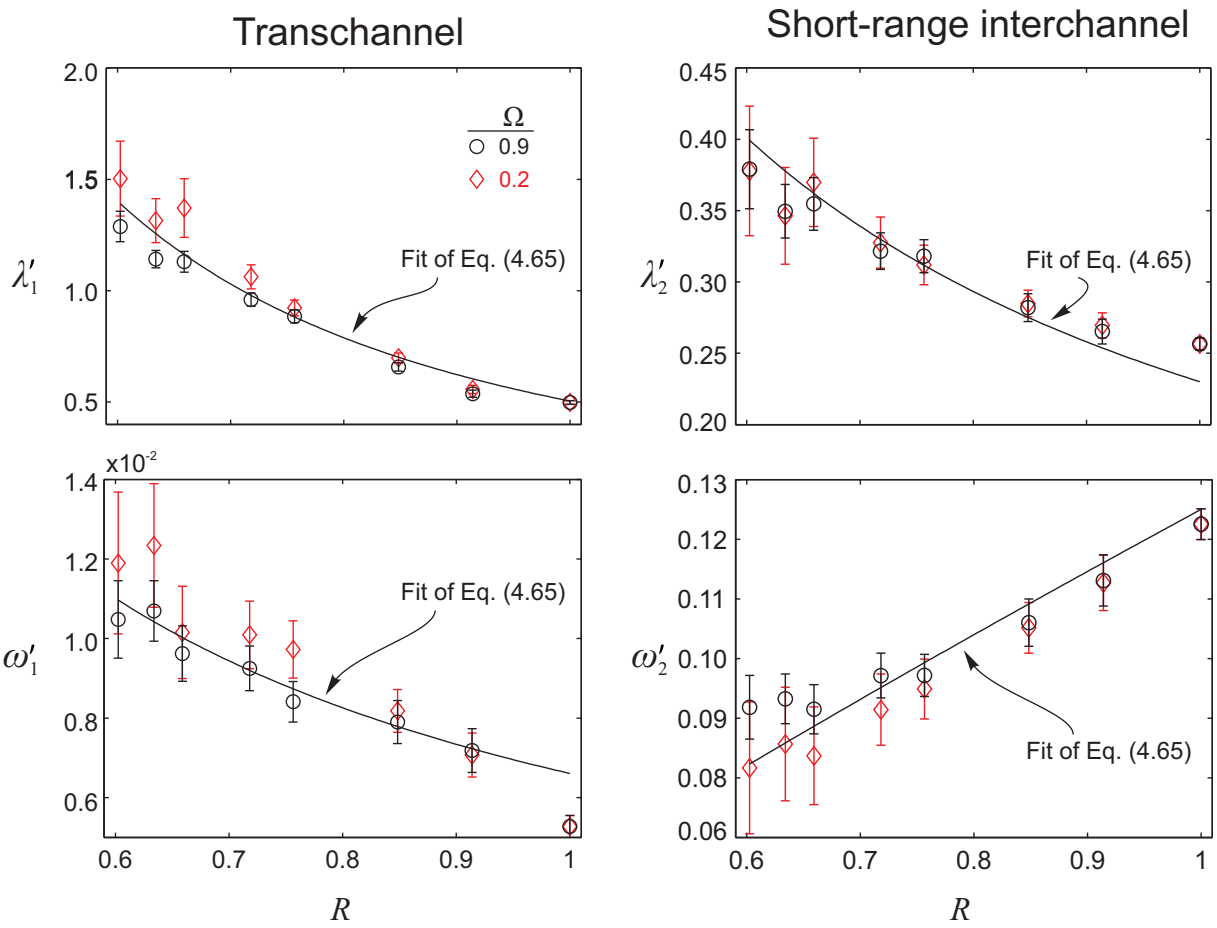

Figure 4.9: Giddings parameters for the transchannel and short-range interchannel eddy dispersion terms as a function of the retention ratio R, obtained by fitting Eq. (4.64) to the reduced plate height curves in Figure 4.6. The 95% confidence intervals are obtained from the fitting procedure. The parameters are plotted as a function of R, since it is the principal variable that affects their value, but they can be displayed also as a function of ρ using Eq. (4.19).

that the Giddings parameters for core–shell packings should depend on retention, as described by Eq. (4.54). Figure 4.9 shows how $\lambda_i^{'}$ and $\omega_i^{'}$ ($i = 1, 2$) obtained from the fit of Eq. (4.64) to the simulated plate height data behave as a function of the retention ratio R.

With our extended theory of eddy dispersion, we can express the Giddings parameters $\lambda_i^{'}$ and $\omega_i^{'}$ for core–shell particles described by Eq. (4.57) through the parameters for the nonporous particles λ_i and ω_i described by Eq. (4.48):

$$\begin{cases} \omega_1^{'} = \omega_1/R \\ \lambda_1^{'} = \lambda_1/R^2 \\ \omega_2^{'} = \omega_2 R^{1-2\eta} \\ \lambda_2^{'} = \lambda_2/R^{2-\eta} \end{cases} \tag{4.65}$$

The black solid lines in Figure 4.9 result from the fit of Eq. (4.65) to the displayed values of $\lambda_i^{'} = \lambda_i^{'}(R)$ and $\omega_i^{'} = \omega_i^{'}(R)$. Parameters of the fit were the coefficients λ_i, ω_i, and η. Eq. (4.65) fits the data well and thus corroborates our extension of the original Giddings theory of coupled eddy dispersion. The fit yields the following values: $\lambda_1 = 0.51$, $\omega_1 = 6.6 \times 10^{-3}$, $\lambda_2 = 0.23$, $\omega_2 = 0.13$, and $\eta = 0.91$, which are in accord with predictions of Giddings.[66] The behavior of $\lambda_i^{'}$ and $\omega_i^{'}$ in Figure 4.9 for different values of Ω are hardly distinguishable, because the influence of Ω on eddy dispersion has been already accounted for in the short-range interchannel term $h_{\mathrm{eddy},2}$ of Eq. (4.64) by the extended theory of coupled eddy dispersion, Eq. (4.55).

The parameters λ_i and ω_i ($i = 1, 2$) can be used to recover the parameters of the cell model γ_i, α_i, and β_i – the length, width, and relative velocity difference, respectively (cf. Section 4.4). However, such a recovery necessitates an additional set of constraints, because the system (4.48), which connects the parameters λ_i and ω_i with the parameters γ_i, α_i, and β_i has more unknowns (six) than equations (four). We now specify a set of additional constraints that limit the range for the original parameters.

Using the velocity field obtained from our LBM simulations and Eq. (4.63), we computed the sum of the relative velocity differences:

$$\beta_{\mathrm{sum}}^2 = \beta_1^2 + \beta_2^2 = 0.934 \tag{4.66}$$

Equation (4.66) helps us eliminate one variable from Eq. (4.48). However, there are still five unknowns in four equations. We utilize an additional set of constraints:

$$\begin{cases} \beta_2^2 > 0 \\ \gamma_2^{'} > \gamma_1^{'} \end{cases} \tag{4.67}$$

The first inequality is trivial, because the square cannot have negative values. The inequality $\gamma_2^{'} > \gamma_1^{'}$ results from the assumption that the short-range interchannel cell should be longer than the transchannel cell at each shell thickness (the other possible restriction, $\alpha_2^{'} > \alpha_1^{'}$, was automatically satisfied by Eq. (4.67) for the fitted values of λ_i and ω_i). Equation (4.67), together

with Eqs. (4.48), (4.53), and (4.66), allows to determine a range for γ_1

$$2\lambda_1\beta_{\text{sum}}^{-2} < \gamma_1 < 2\left(\lambda_1 + \lambda_2 R_{\text{min}}^{\eta}\right)\beta_{\text{sum}}^{-2}, \tag{4.68}$$

where $R_{\text{min}} = 0.6$ is the retention ratio for the system of fully porous particles, computed for our system using Eq. (4.19). Substituting the values for λ_1, λ_2, and η obtained from the fit of the plate height data (Figure 4.6) with Eqs. (4.64) and (4.65) into Eq. (4.68), we get $\gamma_1 \in (1.07, 1.35)$. If we choose any γ_1 from this range, we eliminate another unknown variable from the system of Eq. (4.48), which now becomes well determined. We have chosen $\gamma_1 = 1.25$ – in the middle of the allowed interval – because it minimizes the proximity to both constraints of Eq. (4.68). Table 4.1 compares the original guess of Giddings[66] for α_i, β_i, and γ_i with our recovered parameters (given that $\gamma_1 = 1.25$). The values presented in Table 4.1 can be used to assess the length scales on which mixing occurs in packed beds.

Table 4.1: Structural parameters of the Giddings model

	γ_1	α_1	β_1	γ_2	α_2	β_2
This work, Section 4.5.3	1.25	0.11	0.9	2.0	1.37	0.36
After Giddnigs[66]	1.00	0.17	1.0	1.5	1.25	0.80

4.5.4 Trans-particle mass transfer resistance

Fitting of the plate height curves by Eq. (4.64) (Section 4.5.1, Figure 4.6) allows us to analyze the dependence of the trans-particle mass-transfer coefficient C_{p} on ρ and Ω. We compare the behavior of $C_{\text{p}} = C_p(\rho, \Omega)$ obtained from that fitting with predictions from the theoretical model of Kaczmarski and Guiochon,[261] which determines C_{p} as:

$$\begin{cases} C_{\text{p}}(\rho, \Omega) = F\dfrac{1}{30}\dfrac{\varepsilon_{\text{e}}}{1-\varepsilon_{\text{e}}}\left(\dfrac{k_1}{1+k_1}\right)^2\dfrac{f(\rho)}{\Omega} \\ f(\rho) = \dfrac{1+2\rho+3\rho^2-\rho^3-5\rho^4}{\left(1+\rho+\rho^2\right)^2} \end{cases} \tag{4.69}$$

The parameter F is (implicitly assumed as) unity in [261] and is a model parameter in [303] with an estimated value close to unity. We have fitted the model represented by Eq. (4.69), with F as an adjustable parameter, to the values of C_{p} determined from the fit of the reduced plate height curves (Figure 4.6) with Eq. (4.64) and obtained $F = 2.41$ and 2.84 for $\Omega = 0.2$ and 0.9, respectively. These values of C_{p} obtained from the fitted plate height curves, together with their $C_{\text{p}} = C_p(\rho, \Omega)$ fit by Eq. (4.69), are shown in Figure 4.10 by the symbols and solid lines, respectively. We also include the original model of Kaczmarski and Guiochon[261] with $F = 1$ (dash-dotted lines).

The disagreement in Figure 4.10 between the behavior of $C_{\text{p}} = C_p(\rho, \Omega)$ as determined by

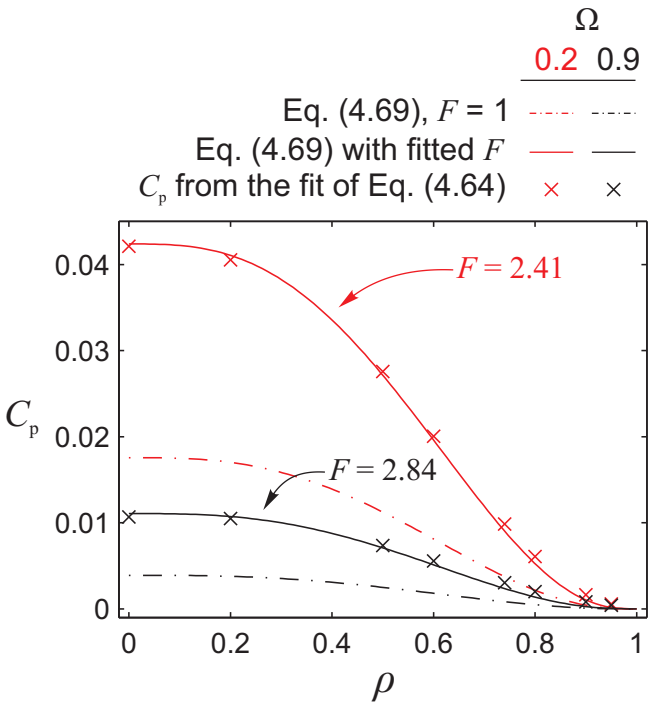

Figure 4.10: Trans-particle mass transfer-resistance coefficient C_p as a function of the core-to-particle diameter ratio ρ for different values of the normalized shell diffusivity Ω. Symbols represent C_p-values determined from fitting the simulated h–ν curves in Figure 4.6 with Eq. (4.64). The solid lines represent fitting of Eq. (4.69) to the determined C_p values, where F is a fitted parameter (given in the figure). The dash-dotted lines represent the original model of Kaczmarski and Guiochon[261] with $F = 1$. The 95% confidence intervals obtained from the fitting procedure are significantly smaller than the size of the markers.

the simulations and predicted with Eq. (4.69) using $F = 1$ (as in [261]) can be attributed to the assumptions of the general rate model used to derive Eq. (4.69). The derivation in [261] does not take into account the actual interparticle pore space morphology but rather uses volume-averaging: (i) the nonuniform flow velocity field in the interparticle void space is replaced by a constant velocity field, and (ii) a nonuniform radial concentration distribution of analyte is neglected. Consequently, these assumptions reduce a three-dimensional problem to a one-dimensional. Our simulation approach does not involve this simplification and resolves both analyte concentration and velocity fields in the three-dimensional pore space of the beds. Despite the before-mentioned assumptions, Eq. (4.69) is valid up to a factor F that does not depend on the shell thickness and changes only with Ω.

4.5.5 Analysis of h_{long}, $h_{\mathrm{eddy},1}$, $h_{\mathrm{eddy},2}$, and h_{shell} contributions to the total reduced plate height

In Figure 4.11, we present the individual reduced plate height contributions (h_{long}, $h_{\mathrm{eddy},1}$, $h_{\mathrm{eddy},2}$, and h_{shell}) to h in packings of core–shell particles ($\rho = 0.9$) and fully porous particles ($\rho = 0$) as a function of the reduced velocity. For these plots, we used $\lambda_i^{'}$ and $\omega_i^{'}$ from the fit of Eq. (4.65) (black lines in Figure 4.9) and C_{p} from Eq. (4.69) with the fitted values of F (solid lines in Figure 4.10). For D_{eff}, we used the values directly obtained from the simulations of diffusive transport in the packings (see Figure 4.7).

At low velocities (ν <1), the value of the reduced plate height is mainly determined by the h_{long} term. At a given value of ν <1, the most pronounced contribution of this term among the four ρ–Ω data sets (represented in Figure 4.11 with the red-colored areas) is observed for $\rho = 0$ (fully porous particles) and $\Omega = 0.9$ (high intraparticle diffusivity). At increasing ν (1 <ν <10), the h_{long} contribution decreases and transchannel eddy dispersion ($h_{\mathrm{eddy},1}$) becomes dominant. Moreover, the value of $h_{\mathrm{eddy},1}$ increases further with ν and is strongly affected by ρ and Ω (blue-colored areas in Figure 4.11). By contrast, $h_{\mathrm{eddy},2}$ (green) hardly changes for ν >10 and depends much less on ρ and Ω. The behavior of the transchannel ($h_{\mathrm{eddy},1}$) and short-range interchannel ($h_{\mathrm{eddy},2}$) eddy dispersion contributions in dependence of ν can be explained by considering the mechanisms resulting in tracer velocity equilibration on these two different length scales.

Transchannel eddy dispersion arises due to the flow velocity heterogeneity within individual channels formed by neighboring particles. The velocity bias in the interparticle void space of a packing of nonporous particles is determined by the difference between the highest local flow velocity in the central region of a channel and zero velocity at the solid–liquid interface, where the no-slip velocity boundary condition applies. The only mechanism resulting in the equilibration of transport velocities for tracers at different lateral positions in the channel is diffusion. The presence of porous shells (in which the velocity is also zero) slows down the equilibration process between tracers in an interparticle channel and a particle shell. The rate of this equilibration process is determined by ρ and Ω: The smaller ρ and Ω become, the slower is the velocity equilibration, resulting in a higher $h_{\mathrm{eddy},1}$ contribution to h (blue areas in Figure 4.11). The increase in ν results in a growth of the velocity bias in the channels and in a corresponding

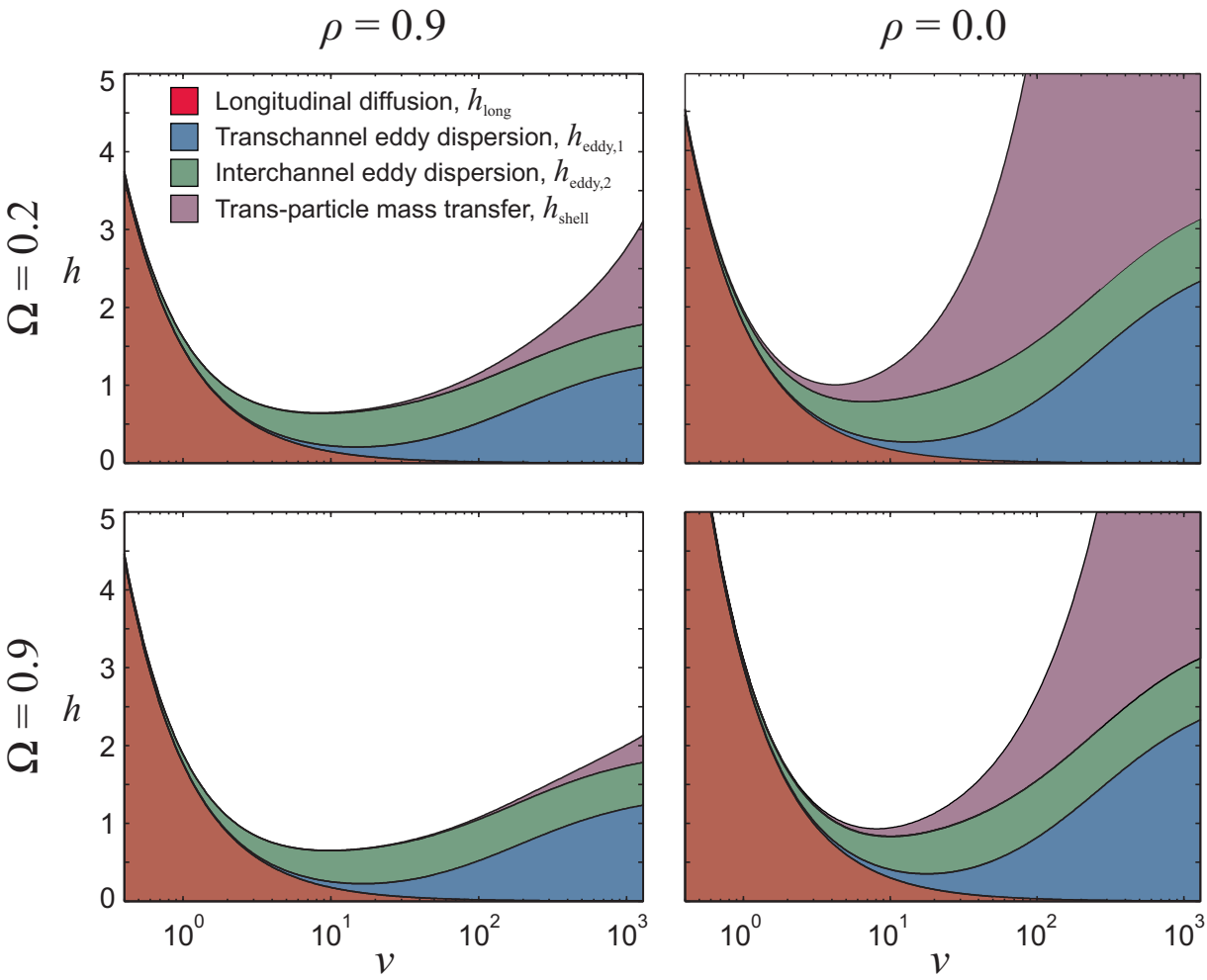

Figure 4.11: Individual contributions from the reduced plate height terms h_{long}, $h_{\mathrm{eddy},1}$, $h_{\mathrm{eddy},2}$, and h_{shell} (cf. Eq. (4.64)) to the total reduced plate height h as a function of the reduced velocity ν for two shell diffusivities Ω and core-to-particle diameter ratios ρ.

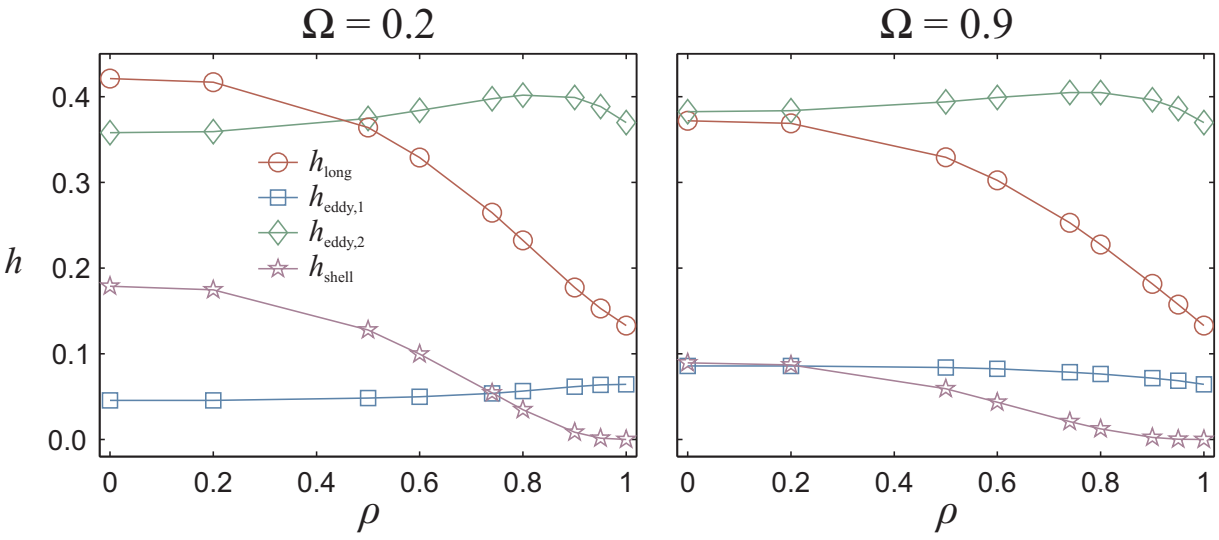

Figure 4.12: Individual contributions from the reduced plate height terms h_{long}, $h_{\mathrm{eddy},1}$, $h_{\mathrm{eddy},2}$, and h_{shell} (cf. Eq. (4.64) to the total reduced plate height h at the optimal reduced velocity ν_{opt} as a function of the core-to-particle diameter ratio ρ for $\Omega = 0.2$ and 0.9.

increase of $h_{\mathrm{eddy},1}$. At large values of ν (not analyzed in this work), $h_{\mathrm{eddy},1}$ is expected to achieve an asymptotic value, cf. Eq. (4.59).

Short-range interchannel dispersion appears due to velocity biases taking place over distances larger than a particle diameter. Characteristic distances were extracted in Section 4.5.3: The parameters $\alpha_2 = 1.37$ and $\gamma_2 = 2.0$ determine, respectively, the width and length of the interchannel layer cell in the Giddings theory. At large value of ν, the dominant mechanism for the velocity equilibration over these distances is advection, which allows tracers to visit different interparticle channels characterized by different local flow velocity. Though local flow velocity and its bias between two channels in the laminar flow regime scales linearly with ν, the advective transport rate is also proportional to ν. As a result, $h_{\mathrm{eddy},2}$ achieves asymptotic behavior (constant width of the green-colored areas in Figure 4.11) at much lower ν than $h_{\mathrm{eddy},1}$.[63,67,158] The advective mechanism of velocity equilibration over short-range interchannel distances is almost unaffected by the parameters of the porous shells, which explains why $h_{\mathrm{eddy},2}$ hardly depends on ρ and Ω.

The contribution of h_{shell} (violet-colored areas in Figure 4.11) to the total reduced plate height h becomes remarkable only at reduced velocities ν >100 and ν >5 for core–shell ($\rho = 0.9$) and completely porous particles ($\rho = 0.0$), respectively. This confirms the conclusions obtained from a comparative plate height analysis for columns packed with core–shell and fully porous particles.[269] Though the magnitude of the h_{shell} term increases with ν, it is not dominant around the minimum of the reduced plate height curves. The influence of Ω (0.2 vs. 0.9) on h_{shell} (Figure 4.11) is less pronounced than the influence of ρ (0.0 vs. 0.9). It indicates that the contribution from the trans-particle mass transfer resistance is mainly determined by the shell thickness rather than the shell diffusion coefficient.

Finally, we analyzed the contributions of h_{long}, $h_{\mathrm{eddy},1}$, $h_{\mathrm{eddy},2}$, and h_{shell} to the total reduced plate height at the optimal fluid velocities corresponding to the minima of h, as determined from our simulations. The results of this analysis are presented in Figure 4.12, where we use the same color-coding as in Figure 4.11 to designate the contributions from the different plate height terms. For both Ω-values (0.2 and 0.9) the contribution of the h_{long} term (red color in Figure 4.12) decreases with ρ, while there is little difference in the two curves for the different Ω-values, demonstrating that use of particles with thinner porous shells allows to reduce h significantly at the optimal mobile phase velocity ν_{opt}. The same behavior in dependence of Ω and ρ is observed for h_{shell} (violet). However, the magnitude of this contribution to the total reduced plate height at ν_{opt} is several times less than h_{long}. At the same time, the values of h_{shell} for ρ <0.5 and $\Omega = 0.9$ are half of those with $\Omega = 0.2$. This can be explained by lower trans-particle mass-transfer resistance due to faster diffusion according to Figure 4.10. Transchannel and short-range interchannel eddy dispersion contributions (blue and green colors in Figure 4.12) are almost independent from Ω and ρ. However, the $h_{\mathrm{eddy},2}$ contribution to the total reduced plate height is always several times larger than $h_{\mathrm{eddy},1}$. For $\rho > 0.5$ and both values of Ω, the short-range interchannel eddy dispersion becomes dominant and at $\rho = 1.0$ (i.e., for nonporous particles) the $h_{\mathrm{eddy},2}$ term exceeds the sum of the other three terms (h_{long}, $h_{\mathrm{eddy},1}$, and h_{shell}).

To summarize, the data in Figure 4.12 allow to conclude that a reduction of the total reduced plate height at the optimal reduced velocity ν_{opt} in packings of core–shell particles compared to fully porous particles arises due to decreased contributions from the longitudinal effective diffusivity and trans-particle mass transfer resistance (red and violet colors). While the former contribution is almost insensitive to a change of the effective analyte diffusivity in the porous shells, the latter at least reveals a noticeable dependence on Ω. At the same time, both transchannel and short-range interchannel eddy dispersion contributions to h at ν_{opt} are almost independent from the parameters of the porous shells, Ω and ρ.

4.6 Summary and conclusions

We proposed a numerical three-dimensional model to simulate advective–diffusive mass transport in random packings of core–shell particles. A packing-generation algorithm was adopted to prepare isotropic and macroscopically homogeneous beds with external porosity of 0.4. The flow velocity field in the interparticle void space of the packings was calculated using the LBM approach. Mass transport of 3×10^5 small, inert tracers in the interparticle void space (due to advection and diffusion) and in the porous shells of the particles (due to only diffusion) was modeled by a RWPT technique. The structure of the particles' porous shells was characterized by two parameters, the solid core-to-particle diameter ratio ($\rho = d_{\mathrm{core}}/d_{\mathrm{p}}$) and the effective diffusion coefficient of the tracers in the shells normalized by their diffusion coefficient in the bulk solution ($\Omega = D_{\mathrm{shell}}/D_{\mathrm{m}}$).

The developed simulation framework was used to determine the reduced plate height h as a function of the reduced velocity ν ($0.5 < \nu 1000$) for different values of ρ and Ω. Simulated h–ν

curves were then fitted by the reduced plate height equation, Eq. (4.18), involving three independent terms due to longitudinal diffusion (h_{long}), eddy dispersion (h_{eddy}), and trans-particle mass transfer resistance (h_{shell}). In turn, h_{eddy} in the bulk packings was assumed to be composed of two terms describing eddy dispersion at the transchannel and short-range interchannel length scales, respectively ($h_{\mathrm{eddy},1}$ and $h_{\mathrm{eddy},2}$). To perform a fitting procedure, the h_{long} term in Eq. (4.18) was analyzed by independent simulations of purely diffusive transport of tracer molecules in the interparticle void space and porous shells. The trans-particle mass-transfer resistance term (h_{shell}) was assumed to depend linearly on the reduced velocity, in line with the model of Kaczmarski and Guiochon,[261] which accounts for analyte retention in the porous shell of a single particle. In the systems we investigated in this work (nonadsorbing tracer), retention occurs only because of zero mobile-phase velocity in the particles' porous shells. We showed that Eq. (4.18) involving $h_{\mathrm{eddy},1}$ and $h_{\mathrm{eddy},2}$ terms from the original Giddings theory of coupled eddy dispersion does not describe adequately the h–ν curves for core–shell particles (cf. Figure 4.4). By contrast, Eq. (4.64) involving an extension of the original Giddings theory to core–shell particles, developed and presented in Section 4.4, fits the simulated h–ν curves that we obtained for $0 \leq \rho \leq 1$ and $\Omega = 0.2$ and 0.9 very well (Figure 4.6). In addition, our analysis indicates that the model of trans-particle mass transfer for a single core–shell particle[261] is applicable to particle-packings but requires introduction of a scaling factor, the value of which depends on Ω.

The presented approach allowed us to analyze the contributions associated with individual mass transfer mechanisms to the total reduced plate height Eq. (4.64) in packings of core–shell particles depending on porous shell characteristics. Particularly, simulations confirmed that the enhanced efficiency of columns packed with core–shell particles compared to fully porous particles comes from a reduced contribution of h_{eddy} in the plate height equation (Figure 4.8).[51,59] Specifically, a reduction of eddy dispersion is observed mainly on the transchannel scale (Figure 4.11). A thinner porous shell and higher shell diffusivity result in a faster velocity equilibration between tracers located in the interparticle channels and particle shells, leading to a reduction of the $h_{\mathrm{eddy},1}$ term. Eddy dispersion at the short-range interchannel scale ($h_{\mathrm{eddy},2}$) is much less affected by the porous shell properties, because advection (the dominating mass-transfer mechanism on this scale for ν >10) occurs only in the interparticle void space and is not affected by the shells. The h_{shell} contribution to the total reduced plate height increases with ν and depends strongly on Ω and ρ (Figure 4.11). However, for ν close to the optimal velocity ν_{opt} the contribution of this term is not dominant (Figures 4.11 and 4.11). This confirms the conclusions of Gritti and Guiochon[59] that in a velocity range typical for chromatographic separations (ν <20) the trans-particle mass-transfer resistance is usually small, whether the column is packed with core–shell or with fully porous particles.

Thus, the presented simulation approach coupled with the proposed extensions of Giddings eddy dispersion model and the model of trans-particle mass transfer of Kaczmarski and Guiochon[261] allows to perform a very detailed analysis of the contributions from individual mass-transport mechanisms to the total plate height in packings of core–shell particles. The proposed approach can be extended to investigate individual contributions to the total plate

height in real chromatographic columns (particulate packings, silica and polymer monoliths), using information on the actual bed morphology or even on particle and monolith mesopore space characteristics, obtained from three-dimensional physical reconstruction by confocal laser scanning microscopy[214,304] or electron tomography.[305,306]

Acknowledgement

This work was supported by the Deutsche Forschungsgemeinschaft DFG (Bonn, Germany) under grant TA 268/5-1. Computational resources on IBM iDataPlex and IBM BlueGene/Q systems were provided by RZG (Rechenzentrum Garching, Germany) and FZJ (Forschungszentrum Jülich, Germany). We are grateful to the John von Neumann Institute for Computing (NIC) and the Jülich Supercomputing Center (JSC) for allocation of a special CPU-time grant (NIC project number: 8214, JSC project ID: HMR10). We thank Dr. Fabrice Gritti (Department of Chemistry, University of Tennessee, Knoxville, TN) for fruitful discussions.

[214] S. Bruns et al. *Anal. Chem.*, 84, pp. 4496–503, 2012.
[304] K. Hormann and U. Tallarek. *J. Chromatogr. A*, 1312, pp. 26–36, 2013.
[305] T. Müllner et al. *Mater. Today*, 17, pp. 404–411, 2014.
[306] D. Stoeckel et al. *Langmuir*, 30, pp. 9022–7, 2014.

Conclusion

In this thesis we conducted a computational investigation of flow and mass transport problems in disordered and ordered porous materials. These materials are commonly found in liquid chromatography and heterogeneous catalysis with fixed particulate or monolithic beds. In order to conduct these simulations, a framework based on the lattice-Boltzmann and random-walk particle tracking methods was developed and extended. The parallelization of these methods for supercomputers allowed us to perform simulations of fluid flow and mass transport on an unprecedented scale, ranging from pore level up to the scale of a column. As a result, the transient and asymptotic behavior of macroscopic transport parameters was recovered for different types of materials and the behavior of these parameters was further analyzed and quantified.

In each chapter of this thesis we address a well-defined topic related to diffusion, flow, and hydrodynamic dispersion in ordered and disordered (mostly particulate) materials. A short description of each chapter is presented below.

- In Chapter 1 we investigated the influence of the particle (sphere) size distribution (PSD) on mass diffusion, hydraulic permeability, and hydrodynamic dispersion by a case study of two particular PSDs derived from industrial samples of real packing materials. The PSDs were obtained from commercial core–shell (narrow PSD) and fully-porous particles (wide PSD). With a variation of the bed porosity ε (interstitial void volume fraction) of generated sets of packings, from closely packed to loosely packed beds ($0.36 \leq \varepsilon \leq 0.46$), we demonstrate that the influence of the PSD on the permeability, effective diffusion, and hydrodynamic dispersion is marginal in comparison to the influence of the packing porosity. Importantly, this result implies that on the contrary to popular claims, the exceptionally high chromatographic performance of core–shell particles cannot be attributed to their narrow PSD.
- In Chapter 2 we analyzed the impact of the macroscopic packing confinement (column format) on the *longitudinal* hydrodynamic dispersion in random packings of spheres and microfabricated pillar arrays (ordered structure). Particularly, we compared hydrodynamic dispersion in unconfined (infinite), partially confined, and fully confined structures and showed that the confinement can increase the minimum plate height up to ten times. For the confined packings of spheres we demonstrate that the conduit cross-sectional shape is correlated with the porosity oscillations in the wall region, which in turn influence hydrodynamic dispersion by the oscillations in the local fluid velocity. Overall, our simulations show

that the circular conduit cross-section has a superior separation performance compared with the other shapes. Moreover, we compared hydrodynamic dispersion coefficients for confined particulate beds of different degree of heterogeneity with the ordered pillar arrays and we show that (i) pillar arrays outperform particulate beds for the range of reduced velocities $\nu \leq 100$ (small analytes), but perform worse in the range of high reduced velocities due to diffusion-limitations in the lateral equilibration in a material with ordered microstructure; (ii) a reduction of the degree of heterogeneity can improve the separation performance of particulate columns almost twofold.

- Chapter 3 is dedicated to the analysis of transverse dispersion – a mechanism that controls the magnitude of the longitudinal dispersion coefficient. More precisely, we analyzed the transient and asymptotic behavior of transverse hydrodynamic dispersion in three types of chromatographic systems: (i) particulate beds, (ii) a physically reconstructed silica monolith, and (iii) microfabricated pillar arrays. We compared the transverse hydrodynamic dispersion in these structures and pointed out a fundamentally different behavior of transverse dispersion coefficients in ordered and disordered structures (pillar arrays vs. particulate beds and monoliths). Overall, our findings extend the understanding of the longitudinal dispersion behavior covered in Chapter 2.
- Chapters 1–3 deal with materials consisting of nonporous (impermeable) structural elements (individual pillars, spheres in a packing, monolith skeleton), i.e., the investigation was limited to the hydrodynamics in the interstitial macropores of the chromatographic beds (excluding the mesopores inside the stationary phase). In Chapter 4 we extended our simulation framework to investigate mass transport in beds of spherical particles with a porous shell that is accessible for the diffusion of the analyte. Subsequently, we identified the individual contributions to the overall plate height (i.e., longitudinal diffusion, eddy dispersion, and trans-particle mass transfer) and analyzed them separately. Guided by the simulation results, we extended the coupled theory of eddy dispersion developed by Giddings to account for retention caused by stagnant zones of analyte entrained in the shells of the particles. Finally, we compared the results of simulations with the theory of Kaczmarski and Guiochon and confirmed that the theory is applicable up to a constant factor.

Computer simulations are the core method of investigations in this work. This method allowed us to analyze the behavior of the transport parameters in different porous materials and to solve the forward problem – the transition from the local geometrical and physical parameters of the system to its macroscopic transport parameters. Strikingly, the same numerical toolbox can now be applied to solve the inverse problem, i.e., find the geometrical and physical parameters beneficial for faster and more efficient chromatographic separations or more efficient mixing and thus enhanced reaction rates in catalytic reactors.

Overall, the current study focuses on systems that are commonly found in chemistry. However, due to the generality of the mathematical description of mass transport and fluid flow, it is possible to take it one step further and apply the same numerical toolbox to study the properties of materials implicated in other science fields, such as geology and biology.

Bibliography

[1] A. B. KARA, P. A. ROCHFORD, and H. E. HURLBURT "An optimal definition for ocean mixed layer depth" in: *Journal of Geophysical Research* 105.C7 (2000), p. 16803 DOI: 10.1029/2000JC900072 (see p. 1)

[2] M. J. R. FASHAM, H. W. DUCKLOW, and S. M. MCKELVIE "A nitrogen-based model of plankton dynamics in the oceanic mixed layer" in: *Journal of Geophysical Research* 48.3 (1990), pp. 591–639 DOI: 10.1357/002224090784984678 (see p. 1)

[3] W. MUNK and C. WUNSCH "Abyssal recipes II: energetics of tidal and wind mixing" in: *Deep Sea Research Part I: Oceanographic Research Papers* 45.12 (1998), pp. 1977–2010 DOI: 10.1016/S0967-0637(98)00070-3 (see p. 1)

[4] C. WOESE "The universal ancestor" in: *Proceedings of the National Academy of Sciences of the United States of America* 95.12 (1998), pp. 6854–6859 DOI: 10.1073/pnas.95.12.6854 (see p. 1)

[5] N. GALTIER, N. TOURASSE, and M. GOUY "A nonhyperthermophilic common ancestor to extant life forms" in: *Science* 283.5399 (1999), pp. 220–221 DOI: 10.1126/science.283.5399.220 (see p. 1)

[6] D. L. THEOBALD "A formal test of the theory of universal common ancestry" in: *Nature* 465.7295 (2010), pp. 219–22 DOI: 10.1038/nature09014 (see p. 1)

[7] L. D. LANDAU and E. M. LIFSCHITZ *Fluid mechanics* 2nd ed. Butterworth–Heinemann, 2007 (see pp. 1, 83)

[8] J. BEAR *Dynamics of fluids in porous media* Dover Publications, 1988 (see p. 1)

[9] H. HE, M. ZHONG, D. KONKOLEWICZ, K. YACATTO, T. RAPPOLD, G. SUGAR, N. E. DAVID, J. GELB, N. KOTWAL, A. MERKLE, and K. MATYJASZEWSKI "Three-dimensionally ordered macroporous polymeric materials by colloidal crystal templating for reversible CO2 capture" in: *Advanced Functional Materials* 23.37 (2013), pp. 4720–4728 DOI: 10.1002/adfm.201300401 (see p. 2)

[10] P. YANG, A. H. RIZVI, B. MESSER, B. F. CHMELKA, G. M. WHITESIDES, and G. D. STUCKY "Patterning porous oxides within microchannel networks" in: *Advanced Materials* 13.6 (2001), pp. 427–431 DOI: 10.1002/1521-4095(200103)13:6<427::AID-ADMA427>3.0.CO;2-C (see p. 2)

[11] J. H. CUSHMAN *The Physics of Fluids in Hierarchical Porous Media: Angstroms to Miles* Springer Netherlands, 1997 (see p. 2)

[12] D. HLUSHKOU and U. TALLAREK "Transition from creeping via viscous-inertial to turbulent flow in fixed beds" in: *Journal of Chromatography A* 1126 (2006), pp. 70–85 DOI: 10.1016/j.chroma.2006.06.011 (see pp. 2, 83, 86, 88)

[13] I. FATT "The network model of porous media. 1. Capillary pressure characteristics" in: *Transactions of the American institute of mining and metallurgical engineers* 207.7 (1956), 144–159 (see p. 2)

[14] I. FATT "The network model of porous media. 2. Dynamic properties of a single size tube network" in: *Transactions of the American institute of mining and metallurgical engineers* 207.7 (1956), 160–163 (see p. 2)

[15] I. FATT "The network model of porous media. 1. Dynamic properties of networks with tube radius distribution" in: *Transactions of the American institute of mining and metallurgical engineers* 207.7 (1956), 164–181 (see p. 2)

[16] G. TAYLOR "Dispersion of soluble matter in solvent flowing slowly through a tube" in: *Philosophical Transactions of the Royal Society A: Mathematical, Physical & Engineering Sciences* 219 (1953), pp. 186–203 DOI: 10.1098/rspa.1953.0139 (see pp. 2, 42, 47, 63, 121)

[17] R. ARIS "On the dispersion of a solute in a fluid flowing through a tube" in: *Proceedings of the Royal Society A: Mathematical, Physical and Engineering Sciences* 235.1200 (1956), pp. 67–77 DOI: 10.1098/rspa.1956.0065 (see pp. 2, 121)

[18] P. M. ADLER and H. BRENNER "Transport processes in spatially periodic capillary networks. 1. Geometrical description and linear flow hydrodynamics" in: *Physicochemical Hydrodynamics* 5.3-4 (1984), pp. 245–268 (see p. 2)

[19] P. M. ADLER and H. BRENNER "Transport processes in spatially periodic capillary networks. 2. Taylor dispersion with mixing vertices" in: *Physicochemical Hydrodynamics* 5.3-4 (1984), pp. 269–285 (see p. 2)

[20] M. J. BLUNT "Flow in porous media — pore-network models and multiphase flow" in: *Current Opinion in Colloid & Interface Science* 6.3 (2001), pp. 197–207 DOI: 10.1016/S1359-0294(01)00084-X (see p. 2)

[21] H. DONG and M. BLUNT "Pore-network extraction from micro-computerized-tomography images" in: *Physical Review E* 80.3 (2009), p. 036307 DOI: 10.1103/PhysRevE.80.036307 (see p. 2)

[22] J. H. CUSHMAN, L. S. BENNETHUM, and B. X. HU "A primer on upscaling tools for porous media" in: *Advances in Water Resources* 25.8-12 (2002), pp. 1043–1067 DOI: 10.1016/S0309-1708(02)00047-7 (see p. 3)

[23] H. BRENNER "Dispersion resulting from flow through spatially periodic porous media" in: *Philosophical Transactions of the Royal Society A: Mathematical, Physical & Engineering Sciences* 297 (1980), pp. 81–133 DOI: 10.1098/rsta.1980.0205 (see pp. 3, 33, 57, 60, 97)

[24] M. QUINTARD and S. WHITAKER "Transport in ordered and disordered porous media: Volume-averaged equations, closure problems, and comparison with experiment" in: *Chemical Engineering Science* 48 (1993), pp. 2537–2564 DOI: 10.1016/0009-2509(93)80266-S (see p. 3)

[25] L. W. GELHAR and C. L. AXNESS "Three-dimensional stochastic analysis of macrodispersion in aquifers" in: *Water Resources Research* 19.1 (1983), pp. 161–180 DOI: 10.1029/WR019i001p00161 (see p. 3)

[26] P. M. ADLER *Porous Media: Geometry and Transports* Butterworth-Heinemann Series in Chemical Engineering, 1992 (see p. 3)

[27] D. A. EDWARDS, M. SHAPIRO, H. BRENNER, and M. SHAPIRA "Dispersion of inert solutes in spatially periodic, two-dimensional model porous media" in: *Transport in Porous Media* 6.4 (1991), pp. 337–358 DOI: 10.1007/BF00136346 (see pp. 3, 57, 99)

[28] J. SALLES, J.-F. THOVERT, R. DELANNAY, L. PREVORS, J.-L. AURIAULT, and P. M. ADLER "Taylor dispersion in porous media. Determination of the dispersion tensor" in: *Physics of Fluids A: Fluid Dynamics* 5 (1993), pp. 2348–2376 DOI: 10.1063/1.858751 (see pp. 3, 57, 99)

[29] V. MOURZENKO, J.-F. THOVERT, O. VIZIKA, and P. M. ADLER "Geometrical and transport properties of random packings of polydisperse spheres" in: *Physical Review E* 77 (2008), p. 066306 DOI: 10.1103/PhysRevE.77.066306 (see p. 3)

[30] GRIER D. A. *When Computers Were Human* 2nd ed. Princeton University Press, 2007 (see p. 3)

[31] J. VON NEUMANN and H. H. GOLDSTINE "Numerical inverting of matrices of high order" in: *Bulletin of the American Mathematical Society* 53.11 (1947), pp. 1021–1099 DOI: 10.1090/S0002-9904-1947-08909-6 (see p. 3)

[32] P. L. BHATNAGAR, E. P. GROSS, and M. KROOK "A model for collision processes in gases. I. Small amplitude processes in charged and neutral one-component systems" in: *Physical Review* 94.3 (1954), pp. 511–525 DOI: 10.1103/PhysRev.94.511 (see pp. 4, 39, 82)

[33] C. BARDOS, F. GOLSE, and D. LEVERMORE "Fluid dynamic limits of kinetic equations. I. Formal derivations" in: *Journal of Statistical Physics* 63.1-2 (1991), pp. 323–344 DOI: 10.1007/BF01026608 (see p. 4)

[34] F. GOLSE and L. SAINT-RAYMOND "The incompressible Navier–Stokes limit of the Boltzmann equation for hard cutoff potentials" in: *Journal de Mathématiques Pures et Appliquées* 91.5 (2009), pp. 508–552 DOI: 10.1016/j.matpur.2009.01.013 (see p. 4)

[35] C. W. GARDINER *Handbook of stochastic methods: for physics, chemistry and the natural sciences* 2nd ed. Springer-Verlag, 1996 (see p. 5)

[36] P. SALAMON, D. FERNÀNDEZ-GARCIA, and J. J. GÓMEZ-HERNÁNDEZ "A review and numerical assessment of the random walk particle tracking method" in: *Journal of Contaminant Hydrology* 87 (2006), pp. 277–305 DOI: 10.1016/j.jconhyd.2006.05.005 (see pp. 5, 85)

[37] F. DELAY, P. ACKERER, and C. DANQUIGNY "Simulating solute transport in porous or fractured formations using random walk particle tracking: A review" in: *Vadose Zone Journal* 4 (2005), pp. 360–379 DOI: 10.2136/vzj2004.0125 (see pp. 5, 85, 116)

[38] A.D. DAUS, E.O. FRIND, and E.A. SUDICKY "Comparative error analysis in finite element formulations of the advection-dispersion equation" in: *Advances in Water Resources* 8.2 (1985), pp. 86–95 DOI: 10.1016/0309-1708(85)90005-3 (see p. 5)

[39] G. LIU, C. ZHENG, and S. M. GORELICK "Limits of applicability of the advection-dispersion model in aquifers containing connected high-conductivity channels" in: *Water Resources Research* 40.8 (2004), W08308 DOI: 10.1029/2003WR002735 (see p. 5)

[40] M. N. GUDDATI and B. YUE "Modified integration rules for reducing dispersion error in finite element methods" in: *Computer Methods in Applied Mechanics and Engineering* 193.3-5 (2004), pp. 275–287 DOI: 10.1016/j.cma.2003.09.010 (see p. 5)

[41] P. E. KLOEDEN and E. PLATEN *Numerical solution of stochastic differential equations* Springer-Verlag, 1995 (see p. 5)

[42] S. KHIREVICH, A. DANEYKO, and U. TALLAREK "Simulation of fluid flow and mass transport at extreme scale" in: *Jülich Blue Gene/P Extreme Scaling Workshop 2010* ed. by B. MOHR and W. FRINGS Forschungszentrum Jülich, Jülich Supercomputing Centre, 2010 (see pp. 5, 81)

[43] S. KHIREVICH "High-Performance Computing of Flow, Diffusion, and Hydrodynamic Dispersion in Random Sphere Packings" PhD thesis Germany: Philipps-Universität Marburg, 2010 (see pp. 5, 25, 34, 38, 41, 42, 45, 55, 81, 84, 86, 115, 116, 121)

[44] B. D. KANDHAI "Large scale lattice-Boltzmann simulations: computational methods and applications" PhD thesis The Netherlands: University of Amsterdam, 1999 (see p. 6)

[45] D. KANDHAI, A. KOPONEN, A. G. HOEKSTRA, M. KATAJA, J. TIMONEN, and P. M. A. SLOOT "Implementation aspects of 3D lattice-BGK: boundaries, accuracy, and a new fast relaxation method" in: *Journal of Computational Physics* 150 (1999), pp. 482–501 DOI: 10.1006/jcph.1999.6191 (see p. 6)

[46] D. KANDHAI, D. J.-E. VIDAL, A. G. HOEKSTRA, H. HOEFSLOOT, P. IEDEMA, and P. M.A. SLOOT "Lattice-Boltzmann and finite element simulations of fluid flow in a SMRX Static Mixer Reactor" in: *International Journal for Numerical Methods in Fluids* 31.6 (1999), pp. 1019–1033 DOI: 10.1002/(SICI)1097-0363(19991130)31:6<1019::AID-FLD915>3.0.CO;2-I (see pp. 6, 81)

[47] D. KANDHAI, D. HLUSHKOU, A. G. HOEKSTRA, P. M. A. SLOOT, H. VAN AS, and U. TALLAREK "Influence of stagnant zones on transient and asymptotic dispersion in macroscopically homogeneous porous media" in: *Physical Review Letters* 88 (2002), p. 234501 DOI: 10.1103/PhysRevLett.88.234501 (see pp. 6, 16, 32, 43, 81)

[48] J. R. MAZZEO, U. D. NEUE, M. KELE, and R. S. PLUMB "Advancing LC Performance with Smaller Particles and Higher Pressure" in: *Analytical Chemistry* 77.23 (2005), 460 A–467 A DOI: 10.1021/ac053516f (see pp. 8, 51, 75)

[49] K. D. PATEL, A. D. JERKOVICH, J. C. LINK, and J. W. JORGENSON "In-depth characterization of slurry packed capillary columns with 1.0-μm nonporous particles using reversed-phase isocratic ultrahigh-pressure liquid chromatography" in: *Analytical Chemistry* 76 (2004), pp. 5777–5786 DOI: 10.1021/ac049756x (see pp. 8, 29, 31, 48, 58, 75)

[50] J. J. KIRKLAND, T. J. LANGLOIS, and J. J. DESTEFANO "Fused core particles for HPLC columns" in: *American Laboratory* 39.8 (2007), pp. 18–21 (see pp. 8, 75, 111)

[51] G. GUIOCHON and F. GRITTI "Shell particles, trials, tribulations and triumphs" in: *Journal of Chromatography A* 1218.15 (2011), pp. 1915–38 DOI: 10.1016/j.chroma.2011.01.080 (see pp. 8, 17, 51, 75, 76, 111, 113, 138, 149)

[52] A. CAVAZZINI, F. GRITTI, K. KACZMARSKI, N. MARCHETTI, and G. GUIOCHON "Mass-transfer kinetics in a shell packing material for chromatography" in: *Analytical chemistry* 79.15 (2007), pp. 5972–9 DOI: 10.1021/ac070571a (see pp. 8, 76)

[53] J. O. OMAMOGHO, J. P. HANRAHAN, J. TOBIN, and J. D GLENNON "Structural variation of solid core and thickness of porous shell of 1.7 μm core-shell silica particles on chromatographic performance: narrow bore columns" in: *Journal of Chromatography A* 1218.15 (2011), pp. 1942–53 DOI: 10.1016/j.chroma.2010.11.067 (see pp. 8, 76)

[54] J. WILL THOMPSON, R. A. LIEBERMAN, and J. W JORGENSON "Hydrodynamic chromatography for the size classification of micron and sub-micron sized packing materials" in: *Journal of Chromatography A* 1216.45 (2009), pp. 7732–8 DOI: 10.1016/j.chroma.2009.08.088 (see pp. 8, 76)

[55] J. S. BAKER, J. C. VINCI, A. D. MOORE, and L. A COLÓN "Physical characterization and evaluation of HPLC columns packed with superficially porous particles" in: *Journal of Separation Science* 33.17-18 (2010), pp. 2547–57 DOI: 10.1002/jssc.201000251 (see p. 8)

[56] D. Cabooter, A. Fanigliulo, G. Bellazzi, B. Allieri, A. Rottigni, and G. Desmet "Relationship between the particle size distribution of commercial fully porous and superficially porous high-performance liquid chromatography column packings and their chromatographic performance" in: *Journal of Chromatography A* 1217.45 (2010), pp. 7074–81 DOI: 10.1016/j.chroma.2010.09.008 (see pp. 8, 9)

[57] F. Gritti, I. Leonardis, J. Abia, and G. Guiochon "Physical properties and structure of fine core-shell particles used as packing materials for chromatography Relationships between particle characteristics and column performance" in: *Journal of Chromatography A* 1217.24 (2010), pp. 3819–43 DOI: 10.1016/j.chroma.2010.04.026 (see pp. 8, 9, 20, 43, 51)

[58] J. O. Omamogho and J. D Glennon "Comparison between the efficiencies of sub-2 μm C18 particles packed in narrow bore columns" in: *Analytical chemistry* 83.5 (2011), pp. 1547–56 DOI: 10.1021/ac102139a (see p. 8)

[59] F. Gritti and G. Guiochon "Mass transfer resistance in narrow-bore columns packed with 1.7 μm particles in very high pressure liquid chromatography" in: *Journal of Chromatography A* 1217.31 (2010), pp. 5069–5083 DOI: 10.1016/j.chroma.2010.05.059 (see pp. 9, 112, 113, 138, 140, 149)

[60] E. Oláh, S. Fekete, J. Fekete, and K. Ganzler "Comparative study of new shell-type, sub-2 micron fully porous and monolith stationary phases, focusing on mass-transfer resistance" in: *Journal of Chromatography A* 1217.23 (2010), pp. 3642–53 DOI: 10.1016/j.chroma.2010.03.052 (see p. 9)

[61] X. Garcia, L. T. Akanji, M. J. Blunt, S. K. Matthai, and J. P. Latham "Numerical study of the effects of particle shape and polydispersity on permeability" in: *Physical Review E* 80 (2009), p. 021304 DOI: 10.1103/PhysRevE.80.021304 (see p. 9)

[62] R. S. Maier, M. R. Schure, J. P. Gage, and J. D. Seymour "Sensitivity of pore-scale dispersion to the construction of random bead packs" in: *Water Resources Research* 44 (2008), W06S03 DOI: 10.1029/2006WR005577 (see pp. 9, 32, 81, 93)

[63] S. Khirevich, A. Daneyko, A. Höltzel, A. Seidel-Morgenstern, and U. Tallarek "Statistical analysis of packed beds, the origin of short-range disorder, and its impact on eddy dispersion" in: *Journal of Chromatography A* 1217 (2010), pp. 4713–4722 DOI: 10.1016/j.chroma.2010.05.019 (see pp. 9, 18, 20, 21, 31, 32, 34, 43, 45, 50–52, 55, 77, 81, 93, 113, 115, 124, 133, 147)

[64] B. G. Yew, J. Ureta, R. A. Shalliker, E. C. Drumm, and G. Guiochon "Mechanics of column beds: II. Modeling of coupled stress–strain-flow behavior" in: *AIChE Journal* 49 (2003), pp. 642–664 DOI: 10.1002/aic.690490310 (see pp. 9, 22, 29, 31, 56, 71)

[65] C. Song, P. Wang, and H. A. Makse "A phase diagram for jammed matter" in: *Nature* 453.7195 (2008), pp. 629–632 DOI: 10.1038/nature06981 (see p. 9)

[66] J. C. Giddings *Dynamics of Chromatography: principles and theory* Marcel Dekker, 1965 (see pp. 9, 16, 18, 20, 28, 31, 40, 46, 49–52, 54, 63, 69, 70, 89, 109, 112, 123–126, 129, 131, 142, 143)

[67] S. Khirevich, A. Höltzel, A. Seidel-Morgenstern, and U. Tallarek "Time and length scales of eddy dispersion in chromatographic beds" in: *Analytical Chemistry* 81.16 (2009), pp. 7057–7066 DOI: 10.1021/ac901187d (see pp. 9, 12, 18, 28, 31–33, 45, 46, 49–52, 70, 74, 81, 86, 89, 113, 147)

[68] A. W. BOWMAN and A. AZZALINI *Applied Smoothing Techniques for Data Analysis: The Kernel Approach with S-Plus Illustrations* Oxford University Press, 1997 (see pp. 10, 77)

[69] J. E. GENTLE *Random Number Generation and Monte Carlo Methods* 2nd ed. Springer, 2003 (see pp. 10, 77)

[70] S. KHIREVICH, A. HÖLTZEL, D. HLUSHKOU, and U. TALLAREK "Impact of conduit geometry and bed porosity on flow and dispersion in noncylindrical sphere packings" in: *Analytical Chemistry* 79 (2007), pp. 9340–9349 DOI: 10.1021/ac071428k (see pp. 11, 30, 32, 33, 46, 54, 81)

[71] S. KHIREVICH, A. HÖLTZEL, S. EHLERT, A. SEIDEL-MORGENSTERN, and U. TALLAREK "Large-scale simulation of flow and transport in reconstructed HPLC-microchip packings" in: *Analytical Chemistry* 81.12 (2009), pp. 4937–4945 DOI: 10.1021/ac900631d (see pp. 11, 30, 32, 43, 54, 81, 84)

[72] R. S. MAIER, D. M. KROLL, R. S. BERNARD, S. E. HOWINGTON, J. F. PETERS, and H. T. DAVIS "Pore-scale simulation of dispersion" in: *Physics of Fluids* 12 (2000), pp. 2065–2079 DOI: 10.1063/1.870452 (see pp. 11, 13, 32, 34, 40, 42, 45, 115, 121)

[73] S. KHIREVICH, A. HÖLTZEL, and U. TALLAREK "Transient and asymptotic dispersion in confined sphere packings with cylindrical and non-cylindrical conduit geometries" in: *Philosophical Transactions of the Royal Society A: Mathematical, Physical & Engineering Sciences* 369.1945 (2011), pp. 2485–93 DOI: 10.1098/rsta.2011.0027 (see pp. 11, 32, 43, 46, 54, 81)

[74] P. M. ADLER, M. ZUZOVSKY, and H. BRENNER "Spatially periodic suspensions of convex particles in linear shear flows. II. Rheology" in: *International Journal of Multiphase Flow* 11 (1985), pp. 387–417 DOI: 10.1016/0301-9322(85)90064-3 (see pp. 11, 40)

[75] M. A. GALLIVAN, D. R. NOBLE, J. G. GEORGIADIS, and R. O. BUCKIUS "An evaluation of the bounce-back boundary condition for lattice Boltzmann simulations" in: *International Journal for Numerical Methods in Fluids* 25 (1997), pp. 249–263 DOI: 10.1002/(SICI)1097-0363(19970815)25:3<249::AID-FLD546>3.0.CO;2-7 (see pp. 11, 40, 83, 116)

[76] C. PAN, L.-S. LUO, and C. T. MILLER "An evaluation of lattice Boltzmann schemes for porous medium flow simulation" in: *Computers & Fluids* 35 (2006), pp. 898–909 DOI: 10.1016/j.compfluid.2005.03.008 (see pp. 11, 40, 83)

[77] M. R. SCHURE, R. S. MAIER, D. M. KROLL, and H. T. DAVIS "Simulation of packed-bed chromatography utilizing high-resolution flow fields: Comparison with models" in: *Analytical Chemistry* 74 (2002), pp. 6006–6016 DOI: 10.1021/ac0204101 (see pp. 11, 32, 40, 45, 81, 84, 114)

[78] J. A. RUDNICK and G. D. GASPARI *Elements of the random walk: an introduction for advanced students and researchers* Cambridge University Press, 2004 (see pp. 11, 41, 85, 116)

[79] P. SZYMCZAK and A. J. C. LADD "Boundary conditions for stochastic solutions of the convection–diffusion equation" in: *Physical Review E* 68 (2003), p. 036704 DOI: 10.1103/PhysRevE.68.036704 (see pp. 12, 41, 85, 123)

[80] W. GROPP and A. LUSK E. SKJELLUM *Using MPI: Portable Parallel Programming with the Message-Passing Interface* 2nd ed. MIT Press, 1999 (see pp. 12, 42, 85)

[81] D. KANDHAI, U. TALLAREK, D. HLUSHKOU, A. G. HOEKSTRA, P. M. A. SLOOT, and H. VAN AS "Numerical simulation and measurement of liquid hold-up in biporous media containing discrete stagnant zones" in: *Philosophical Transactions of the Royal Society A: Mathematical, Physical & Engineering Sciences* 360 (2002), pp. 521–534 DOI: 10.1098/rsta.2001.0952 (see pp. 13, 34, 42, 84)

[82] F. A. L. DULLIEN *Porous media: fluid transport and pore structure* 2nd ed. Academic Press, 1992 (see pp. 13, 14)

[83] P. C. CARMAN *Flow of Gases Through Porous Media* Academic Press, 1956 (see pp. 13, 14)

[84] H. L. WEISSBERG "Effective diffusion coefficient in porous media" in: *Journal of Applied Physics* 34 (1963), pp. 2636–2639 DOI: 10.1063/1.1729783 (see p. 16)

[85] E. MAURET and M. RENAUD "Transport phenomena in multi-particle systems — I. Limits of applicability of capillary model in high voidage beds-application to fixed beds of fibers and fluidized beds of spheres" in: *Chemical Engineering Science* 52 (1997), pp. 1807–1817 DOI: 10.1016/S0009-2509(96)00499-X (see p. 16)

[86] M. BARRANDE, R. BOUCHET, and R. DENOYEL "Tortuosity of porous particles" in: *Analytical Chemistry* 79 (2007), pp. 9115–9121 DOI: 10.1021/ac071377r (see p. 16)

[87] F. GRITTI, I. LEONARDIS, D. SHOCK, P. STEVENSON, A. SHALLIKER, and G. GUIOCHON "Performance of columns packed with the new shell particles, Kinetex-C18" in: *Journal of Chromatography A* 1217.10 (2010), pp. 1589–603 DOI: 10.1016/j.chroma.2009.12.079 (see pp. 16, 65, 111, 115)

[88] R. F. PROBSTEIN *Physicochemical hydrodynamics* Wiley, 1994 (see p. 16)

[89] D. L. KOCH and J. F. BRADY "Dispersion in fixed beds" in: *Journal of Fluid Mechanics* 154 (1985), pp. 399–427 DOI: 10.1017/S0022112085001598 (see pp. 16, 91)

[90] S. G. WEBER and P. W. CARR "High Performance Liquid Chromatography" in: ed. by P. R. BROWN and R. A. HARTWICK John Wiley & Sons, 1989 chap. 1 (see pp. 16, 65, 69, 108)

[91] M. SAHIMI *Flow and transport in porous media and fractured rock: From classical methods to modern approaches* Wiley-VCH, 1995 (see pp. 16, 31, 89, 91)

[92] U. D. NEUE *HPLC columns: theory, technology, and practice* Wiley-VCH, 1997 (see p. 17)

[93] G. GUIOCHON, A. FELINGER, A. M. KATTI, and D. G. SHIRAZI *Fundamentals of Preparative and Nonlinear Chromatography* Elsevier, 2006 (see p. 17)

[94] D. CABOOTER, J. BILLEN, H. TERRYN, F. LYNEN, P. SANDRA, and G. DESMET "Detailed characterisation of the flow resistance of commercial sub-2 μm reversed-phase columns" in: *Journal of Chromatography A* 1178 (2008), pp. 108–117 DOI: 10.1016/j.chroma.2007.11.086 (see p. 17)

[95] F. GRITTI and G. GUIOCHON "Non-invasive measurement of eddy diffusion in very efficient liquid chromatography columns packed with sub-3 μm shell particles" in: *Chemical Engineering Science* 65.23 (2010), pp. 6327–6340 DOI: 10.1016/j.ces.2010.09.021 (see pp. 20, 43, 51, 71)

[96] S. BRUNS and U. TALLAREK "Physical reconstruction of packed beds and their morphological analysis: core-shell packings as an example" in: *Journal of Chromatography A* 1218.14 (2011), pp. 1849–60 DOI: 10.1016/j.chroma.2011.02.013 (see pp. 22, 29, 31, 43, 56, 71)

[97] R. S. MAIER, D. M. KROLL, R. S. BERNARD, S. E. HOWINGTON, J. F. PETERS, and H. T. DAVIS "Hydrodynamic dispersion in confined packed beds" in: *Physics of Fluids* 15 (2003), pp. 3795–3815 DOI: 10.1063/1.1624836 (see pp. 28, 31, 32, 46, 47, 52, 70, 81, 89, 113)

[98] J. M. P. Q. DELGADO "A critical review of dispersion in packed beds" in: *Heat and Mass Transfer* 42 (2006), pp. 279–310 DOI: 10.1007/s00231-005-0019-0 (see pp. 28, 31, 49, 69, 74)

[99] M. GIESE, K. ROTTSCHÄFER, and D. VORTMEYER "Measured and modeled superficial flow profiles in packed beds with liquid flow" in: *AIChE Journal* 44.2 (1998), pp. 484–490 DOI: 10.1002/aic.690440225 (see pp. 28, 31)

[100] A. J. SEDERMAN, P. ALEXANDER, and L. F. GLADDEN "Structure of packed beds probed by Magnetic Resonance Imaging" in: *Powder Technology* 117 (2001), pp. 255–269 DOI: 10.1016/S0032-5910(00)00374-0 (see pp. 28, 31)

[101] A. DE KLERK "Voidage variation in packed beds at small column to particle diameter ratio" in: *AIChE Journal* 49 (2003), pp. 2022–2029 DOI: 10.1002/aic.690490812 (see pp. 28, 31, 71)

[102] J. THEUERKAUF, P. WITT, and D. SCHWESIG "Analysis of particle porosity distribution in fixed beds using the discrete element method" in: *Powder Technology* 165 (2006), pp. 92–99 DOI: 10.1016/j.powtec.2006.03.022 (see pp. 28, 31)

[103] G. E. MUELLER "Radial porosity in packed beds of spheres" in: *Powder Technology* 203.3 (2010), pp. 626–633 DOI: 10.1016/j.powtec.2010.07.007 (see pp. 28, 31)

[104] G. GUIOCHON, E. DRUMM, and D. CHERRAK "Evidence of a wall friction effect in the consolidation of beds of packing materials in chromatographic columns" in: *Journal of Chromatography A* 835 (1999), pp. 41–58 DOI: 10.1016/S0021-9673(98)01068-1 (see pp. 29, 31, 71)

[105] R. A. SHALLIKER, B. S. BROYLES, and G. GUIOCHON "Physical evidence of two wall effects in liquid chromatography" in: *Journal of Chromatography A* 888 (2000), pp. 1–12 DOI: 10.1016/S0021-9673(00)00517-3 (see pp. 29, 31, 71)

[106] R. A. SHALLIKER, V. WONG, B. S. BROYLES, and G. GUIOCHON "Visualization of bed compression in an axial compression liquid chromatography column" in: *Journal of Chromatography A* 977 (2002), pp. 213–223 DOI: 10.1016/S0021-9673(02)01273-6 (see pp. 29, 31, 71)

[107] J. H. KNOX and J. F. PARCHER "Effect of the column to particle diameter ratio on the dispersion of unsorbed solutes in chromatography" in: *Analytical Chemistry* 41 (1969), pp. 1599–1606 DOI: 10.1021/ac60281a009 (see pp. 29, 31)

[108] W. LI, D. PYO, Y. WAN, E. IBAÑEZ, A. MALIK, and M. L. LEE "Low aspect ratio packed capillary columns in supercritical fluid chromatography" in: *Journal of Microcolumn Separations* 8.4 (1996), pp. 259–268 DOI: 10.1002/(SICI)1520-667X(1996)8:4<259::AID-MCS3>3.0.CO;2-0 (see pp. 29, 31, 58)

[109] R. T. KENNEDY and J. W. JORGENSON "Preparation and evaluation of packed capillary liquid chromatography columns with inner diameters from 20 to 50 μm" in: *Analytical Chemistry* 61 (1989), pp. 1128–1135 DOI: 10.1021/ac00185a016 (see pp. 29, 31, 48, 58)

[110] S. HSIEH and J. W. JORGENSON "Preparation and evaluation of slurry-packed liquid chromatography microcolumns with inner diameters from 12 to 33 μm" in: *Analytical Chemistry* 68 (1996), pp. 1212–1217 DOI: 10.1021/ac950682m (see pp. 29, 31, 48, 58)

[111] P. S. DITTRICH and A. MANZ "Lab-on-a-chip: microfluidics in drug discovery" in: *Nature Reviews Drug Discovery* 5 (2006), pp. 210–218 DOI: 10.1038/nrd1985 (see p. 29)

[112] D. JANASEK, J. FRANZKE, and A. MANZ "Scaling and the design of miniaturized chemical-analysis systems" in: *Nature* 442.7101 (2006), pp. 374–80 DOI: 10.1038/nature05059 (see p. 29)

[113] A. RÍOS, A. ESCARPA, M. C. GONZÁLEZ, and A. G. CREVILLÉN "Challenges of analytical microsystems" in: *TrAC Trends in Analytical Chemistry* 25.5 (2006), pp. 467–479 DOI: 10.1016/j.trac.2005.11.012 (see p. 29)

[114] G. P. ROZING "Trends in HPLC column formats — microbore, nanobore and smaller" in: *LC-GC Europe* 16 (2003), pp. 14–19 (see pp. 29, 48)

[115] J. Hernández-Borges, Z. Aturki, A. Rocco, and S. Fanali "Recent applications in nanoliquid chromatography" in: *Journal of Separation Science* 30 (2007), pp. 1589–1610 DOI: 10.1002/jssc.200700061 (see pp. 29, 48)

[116] J. M. Saz and M. L. Marina "Application of micro- and nano-HPLC to the determination and characterization of bioactive and biomarker peptides" in: *Journal of Separation Science* 31 (2008), pp. 446–458 DOI: 10.1002/jssc.200700589 (see pp. 29, 48)

[117] D. Tao, L. Zhang, Y. Shan, Z. Liang, and Y. Zhang "Recent advances in micro-scale and nano-scale high-performance liquid-phase chromatography for proteome research" in: *Analytical and Bioanalytical Chemistry* 399.1 (2011), pp. 229–41 DOI: 10.1007/s00216-010-3946-7 (see pp. 29, 48)

[118] K. Faure "Liquid chromatography on chip" in: *Electrophoresis* 31.15 (2010), pp. 2499–511 DOI: 10.1002/elps.201000051 (see pp. 29, 30, 48)

[119] S. Jung, S. Ehlert, J.-A. Mora, K. Kraiczek, M. Dittmann, G. P. Rozing, and U. Tallarek "Packing density, permeability, and separation efficiency of packed microchips at different particle-aspect ratios" in: *Journal of Chromatography A* 1216 (2009), pp. 264–273 DOI: 10.1016/j.chroma.2008.11.073 (see pp. 29, 30, 71)

[120] S. Ehlert, T. Rösler, and U. Tallarek "Packing density of slurry-packed capillaries at low aspect ratios" in: *Journal of Separation Science* 31 (2008), pp. 1719–1728 DOI: 10.1002/jssc.200800018 (see p. 29)

[121] I. M. Lazar, P. Trisiripisal, and H. A. Sarvaiya "Microfluidic liquid chromatography system for proteomic applications and biomarker screening" in: *Analytical Chemistry* 78 (2006), pp. 5513–5524 DOI: 10.1021/ac060434y (see p. 30)

[122] K. W. Ro, J. Liu, and D. R. Knapp "Plastic microchip liquid chromatography-matrix-assisted laser desorption/ionization mass spectrometry using monolithic columns" in: *Journal of Chromatography A* 1111 (2006), pp. 40–47 DOI: 10.1016/j.chroma.2006.01.105 (see p. 30)

[123] D. S. Reichmuth, T. J. Shepodd, and B. J. Kirby "Microchip HPLC of peptides and proteins" in: *Analytical Chemistry* 77 (2005), pp. 2997–3000 DOI: 10.1021/ac048358r (see p. 30)

[124] Y. Yang, C. Li, J. Kameoka, K. H. Lee, and H. G. Craighead "A polymeric microchip with integrated tips and *in situ* polymerized monolith for electrospray mass spectrometry" in: *Lab on a Chip* 5 (2005), pp. 869–876 DOI: 10.1039/b503025k (see p. 30)

[125] A. Bhattacharyya and C. M. Klapperich "Thermoplastic microfluidic device for on-chip purification of nucleic acids for disposable diagnostics" in: *Analytical Chemistry* 78 (2006), pp. 788–792 DOI: 10.1021/ac051449j (see p. 30)

[126] J. Liu, C.-F. Chen, C.-W. Tsao, C.-C. Chang, C.-C. Chu, and D. L. DeVoe "Polymer microchips integrating solid-phase extraction and high-performance liquid chromatography using reversed-phase polymethacrylate monoliths" in: *Analytical Chemistry* 81 (2009), pp. 2545–2554 DOI: 10.1021/ac802359e (see p. 30)

[127] S. Jung, A. Höltzel, S. Ehlert, J.-A. Mora, K. Kraiczek, M. Dittmann, G. P. Rozing, and U. Tallarek "Impact of conduit geometry on the performance of typical particulate microchip packings" in: *Analytical Chemistry* 81 (2009), pp. 10193–10200 DOI: 10.1021/ac902069x (see pp. 30, 50)

[128] H. Yin, K. Killeen, R. Brennen, D. Sobek, M. Werlich, and T. van de Goor "Microfluidic chip for peptide analysis with an integrated HPLC column, sample enrichment column, and nano-

electrospray tip" in: *Analytical Chemistry* 77 (2005), pp. 527–533 DOI: 10.1021/ac049068d (see p. 30)

[129] A. ISHIDA, T. YOSHIKAWA, M. NATSUME, and T. KAMIDATE "Reversed-phase liquid chromatography on a microchip with sample injector and monolithic silica column" in: *Journal of Chromatography A* 1132 (2006), pp. 90–98 DOI: 10.1016/j.chroma.2006.07.025 (see p. 30)

[130] C.-Y. SHIH, Y. CHEN, J. XIE, Q. HE, and Y.-C. TAI "On-chip temperature gradient interaction chromatography" in: *Journal of Chromatography A* 1111 (2006), pp. 272–278 DOI: 10.1016/j.chroma.2005.08.075 (see p. 30)

[131] J. LIU, K.-W. RO, R. NAYAK, and D. R. KNAPP "Monolithic column plastic microfluidic device for peptide analysis using electrospray from a channel opening on the edge of the device" in: *International Journal of Mass Spectrometry* 259 (2007), pp. 65–72 DOI: 10.1016/j.ijms.2006.08.017 (see p. 30)

[132] J. F. BOROWSKY, B. C. GIORDANO, Q. LU, A. TERRAY, and G. E. COLLINS "Electroosmotic flow-based pump for liquid chromatography on a planar microchip" in: *Analytical Chemistry* 80 (2008), pp. 8287–8292 DOI: 10.1021/ac801497r (see p. 30)

[133] M. T. KOESDJOJO, C. R. KOCH, and V. T. REMCHO "Technique for microfabrication of polymeric-based microchips from an SU-8 master with temperature-assisted vaporized organic solvent bonding" in: *Analytical Chemistry* 81 (2009), pp. 1652–1659 DOI: 10.1021/ac802450u (see p. 30)

[134] S. EHLERT, K. KRAICZEK, J.-A. MORA, M. DITTMANN, G. P. ROZING, and U. TALLAREK "Separation efficiency of particle-packed HPLC microchips" in: *Analytical Chemistry* 80 (2008), pp. 5945–5950 DOI: 10.1021/ac800576v (see pp. 30, 71)

[135] S. KHIREVICH, A. HÖLTZEL, D. HLUSHKOU, A. SEIDEL-MORGENSTERN, and U. TALLAREK "Structure–transport analysis for particulate packings in trapezoidal microchip separation channels" in: *Lab on a Chip* 8 (2008), pp. 1801–1808 DOI: 10.1039/b810688f (see pp. 30, 32, 46, 54, 81)

[136] D. S. PETERSON "Solid supports for micro analytical systems" in: *Lab on a Chip* 5 (2005), pp. 132–139 DOI: 10.1039/b405311g (see p. 30)

[137] M. DE PRA, W. TH. KOK, and P. J. SCHOENMAKERS "Topographic structures and chromatographic supports in microfluidic separation devices" in: *Journal of Chromatography A* 1184 (2008), pp. 560–572 DOI: 10.1016/j.chroma.2007.09.086 (see p. 30)

[138] K. W. RO, R. NAYAK, and D. R. KNAPP "Monolithic media in microfluidic devices for proteomics" in: *Electrophoresis* 27 (2006), pp. 3547–3558 DOI: 10.1002/elps.200600058 (see p. 30)

[139] D. A. MAIR, E. GEIGER, A. P. PISANO, J. M. J. FRÉCHET, and F. SVEC "Injection molded microfluidic chips featuring integrated interconnects" in: *Lab on a Chip* 6 (2006), pp. 1346–1354 DOI: 10.1039/b605911b (see p. 30)

[140] P. A. LEVKIN, S. EELTINK, T. R. STRATTON, R. BRENNEN, K. ROBOTTI, H. YIN, K. KILLEEN, F. SVEC, and J. M. J. FRÉCHET "Monolithic porous polymer stationary phases in polyimide chips for the fast high-performance liquid chromatography separation of proteins and peptides" in: *Journal of Chromatography A* 1200 (2008), pp. 55–61 DOI: 10.1016/j.chroma.2008.03.025 (see p. 30)

[141] M. VÁZQUEZ and B. PAULL "Review on recent and advanced applications of monoliths and related porous polymer gels in micro-fluidic devices" in: *Analytica Chimica Acta* 668.2 (2010), pp. 100–13 DOI: 10.1016/j.aca.2010.04.033 (see p. 30)

[142] I. NISCHANG, O. BRUEGGEMANN, and F. SVEC "Advances in the preparation of porous polymer monoliths in capillaries and microfluidic chips with focus on morphological aspects" in: *Analytical*

and Bioanalytical Chemistry 397.3 (2010), pp. 953–60 DOI: 10.1007/s00216-010-3550-x (see p. 30)

[143] W. De Malsche, H. Eghbali, D. Clicq, J. Vangelooven, H. Gardeniers, and G. Desmet "Pressure-driven reverse-phase liquid chromatography separations in ordered nonporous pillar array columns" in: *Analytical Chemistry* 79 (2007), pp. 5915–5926 DOI: 10.1021/ac070352p (see pp. 30, 35, 45, 57, 58)

[144] F. Detobel, S. De Bruyne, J. Vangelooven, W. De Malsche, T. Aerts, H. Terryn, H. Gardeniers, S. Eeltink, and G. Desmet "Fabrication and chromatographic performance of porous-shell pillar-array columns" in: *Analytical chemistry* 82.17 (2010), pp. 7208–17 DOI: 10.1021/ac100971a (see pp. 30, 35, 57)

[145] L. C. Taylor, N. V. Lavrik, and M. J. Sepaniak "High-aspect-ratio, silicon oxide-enclosed pillar structures in microfluidic liquid chromatography" in: *Analytical chemistry* 82.22 (2010), pp. 9549–56 DOI: 10.1021/ac1023342 (see pp. 30, 35, 57, 72)

[146] G. Guiochon "The limits of the separation power of unidimensional column liquid chromatography" in: *Journal of Chromatography A* 1126 (2006), pp. 6–49 DOI: 10.1016/j.chroma.2006.07.032 (see pp. 31, 52, 63, 69)

[147] E. Vandre, R. S. Maier, D. M. Kroll, A. McCormick, and H. T. Davis "Diameter-dependent dispersion in cylindrical bead packs" in: *AIChE Journal* 54.8 (2008), pp. 2024–2028 DOI: 10.1002/aic.11529 (see p. 31)

[148] F. Gritti and G. Guiochon "Impact of retention on trans-column velocity biases in packed columns" in: *AIChE Journal* 56.6 (2010), pp. 1495–1509 DOI: 10.1002/aic.12074 (see pp. 31, 52, 70, 92)

[149] B. Manz, L. F. Gladden, and P. B. Warren "Flow and dispersion in porous media: Lattice-Boltzmann and NMR studies" in: *AIChE Journal* 45 (1999), pp. 1845–1854 DOI: 10.1002/aic.690450902 (see pp. 32, 81)

[150] M. D. Mantle, A. J. Sederman, and L. F. Gladden "Single- and two-phase flow in fixed-bed reactors: MRI flow visualisation and lattice-Boltzmann simulations" in: *Chemical Engineering Science* 56 (2001), pp. 523–529 DOI: 10.1016/S0009-2509(00)00256-6 (see pp. 32, 81)

[151] R. S. Maier, D. M. Kroll, R. S. Bernard, S. E. Howington, J. F. Peters, and H. T. Davis "Enhanced dispersion in cylindrical packed beds" in: *Philosophical Transactions of the Royal Society A: Mathematical, Physical & Engineering Sciences* 360 (2002), pp. 497–506 DOI: 10.1098/rsta.2001.0951 (see pp. 32, 46, 47, 52, 81)

[152] M. R. Schure, R. S. Maier, D. M. Kroll, and H. T. Davis "Simulation of ordered packed beds in chromatography" in: *Journal of Chromatography A* 1031 (2004), pp. 79–86 DOI: 10.1016/j.chroma.2003.12.030 (see pp. 32, 60, 63, 81, 93, 99, 113)

[153] D. Hlushkou, A. Seidel-Morgenstern, and U. Tallarek "Numerical analysis of electroosmotic flow in dense regular and random arrays of impermeable, nonconducting spheres" in: *Langmuir* 21 (2005), pp. 6097–6112 DOI: 10.1021/la050239z (see pp. 32, 43, 81)

[154] M. R. Schure and R. S. Maier "How does column packing microstructure affect column efficiency in liquid chromatography?" in: *Journal of Chromatography A* 1126 (2006), pp. 58–69 DOI: 10.1016/j.chroma.2006.05.066 (see pp. 32, 81, 93, 113)

[155] R. S. Maier, D. M. Kroll, and H. T. Davis "Diameter-dependent dispersion in packed cylinders" in: *AIChE Journal* 53 (2007), pp. 527–530 DOI: 10.1002/aic.11083 (see pp. 32, 46, 47, 52)

[156] H. BAI, J. THEUERKAUF, P. A. GILLIS, and P. M. WITT "A Coupled DEM and CFD Simulation of Flow Field and Pressure Drop in Fixed Bed Reactor with Randomly Packed Catalyst Particles" in: *Industrial & Engineering Chemistry Research* 48.8 (2009), pp. 4060–4074 DOI: 10.1021/ie801548h (see p. 32)

[157] R. S. MAIER and R. S. BERNARD "Lattice-Boltzmann accuracy in pore-scale flow simulation" in: *Journal of Computational Physics* 229 (2010), pp. 233–255 DOI: 10.1016/j.jcp.2009.09.013 (see p. 32)

[158] A. DANEYKO, A. HÖLTZEL, S. KHIREVICH, and U. TALLAREK "Influence of the particle size distribution on hydraulic permeability and eddy dispersion in bulk packings" in: *Analytical chemistry* 83.10 (2011), pp. 3903–10 DOI: 10.1021/ac200424p (see pp. 32, 43, 45, 50–52, 75, 76, 78, 81, 84, 93, 113, 116, 124, 133, 147)

[159] S. KHIREVICH, A. HÖLTZEL, A. DANEYKO, A. SEIDEL-MORGENSTERN, and U. TALLAREK "Structure-transport correlation for the diffusive tortuosity of bulk, monodisperse, random sphere packings" in: *Journal of Chromatography A* 1218.37 (2011), pp. 6489–97 DOI: 10.1016/j.chroma.2011.07.066 (see pp. 32, 34, 43, 50, 55, 60, 77, 81, 89, 91)

[160] H. BRENNER and P. M. ADLER "Dispersion Resulting from Flow through Spatially Periodic Porous Media II. Surface and Intraparticle Transport" in: *Philosophical Transactions of the Royal Society A: Mathematical, Physical & Engineering Sciences* 307.1498 (1982), pp. 149–200 DOI: 10.1098/rsta.1982.0108 (see pp. 33, 57, 60, 97)

[161] D. L. KOCH, R. G. COX, H. BRENNER, and J. F. BRADY "The effect of order on dispersion in porous media" in: *Journal of Fluid Mechanics* 200 (1989), pp. 173–188 DOI: 10.1017/S0022112089000613 (see pp. 33, 57, 60, 61, 63, 97)

[162] R. BENZI, S. SUCCI, and M. VERGASSOLA "The lattice Boltzmann equation: theory and applications" in: *Physics Reports* 222 (1992), pp. 145–197 DOI: 10.1016/0370-1573(92)90090-M (see pp. 38, 81, 82)

[163] S. CHEN and G. D. DOOLEN "Lattice Boltzmann method for fluid flows" in: *Annual Review of Fluid Mechanics* 30 (1998), pp. 329–364 DOI: 10.1146/annurev.fluid.30.1.329 (see pp. 38, 81–83)

[164] S. SUCCI *The lattice Boltzmann equation for fluid dynamics and beyond* Oxford University Press, 2001 (see pp. 38, 81–83)

[165] UBERTINI S., BELLA G., ORSZAG S. A., and SUCCI S. *Lectures on Lattice Boltzmann Methods for Complex Fluid Flows* Science4 Press, 2009 (see pp. 38, 81, 82)

[166] S. CHAPMAN and T. G. COWLING *The mathematical theory of non-uniform gases* 3rd ed. Cambridge University Press, 1990 (see pp. 38, 40, 83)

[167] U. FRISCH, B. HASSLACHER, and Y. POMEAU "Lattice-gas automata for the Navier–Stokes equation" in: *Physical Review Letters* 56 (1986), pp. 1505–1508 DOI: 10.1103/PhysRevLett.56.1505 (see p. 39)

[168] G. R. MCNAMARA and G. ZANETTI "Use of the Boltzmann equation to simulate lattice-gas automata" in: *Physical Review Letters* 61 (1988), pp. 2332–2335 DOI: 10.1103/PhysRevLett.61.2332 (see p. 39)

[169] ROTHMAN D. H. and ZALESKI S. *Lattice-Gas Cellular Automata* Cambrige Unversity Press, 1997 (see pp. 39, 82, 83)

[170] Y. H. QIAN, D. D'HUMIÈRES, and P. LALLEMAND "Lattice BGK models for Navier–Stokes equation" in: *EPL* 17 (1992), pp. 479–484 DOI: 10.1209/0295-5075/17/6/001 (see pp. 39, 82, 116)

[171] X. HE and L.-S. LUO "Lattice Boltzmann Model for the Incompressible Navier–Stokes Equation" in: *Journal of Statistical Physics* 88.3/4 (1997), pp. 927–944 DOI: 10.1023/B:JOSS.0000015179.12689.e4 (see pp. 40, 83)

[172] M. ZUZOVSKY "Spatially periodic suspensions of convex particles in linear shear flows. III. Dilute arrays of spheres suspended in Newtonian fluids" in: *Physics of Fluids* 26.7 (1983), p. 1714 DOI: 10.1063/1.864370 (see p. 40)

[173] D. A. EDWARDS, M. SHAPIRO, P. BAR-YOSEPH, and M. SHAPIRA "The influence of Reynolds number upon the apparent permeability of spatially periodic arrays of cylinders" in: *Physics of Fluids A: Fluid Dynamics* 2.1 (1990), pp. 45–55 DOI: 10.1063/1.857691 (see p. 40)

[174] R. ARIS "On the dispersion of a solute by diffusion, convection and exchange between phases" in: *Philosophical Transactions of the Royal Society A: Mathematical, Physical & Engineering Sciences* 252 (1959), pp. 538–550 DOI: 10.1098/rspa.1959.0171 (see pp. 42, 47, 63)

[175] D. HLUSHKOU, D. KANDHAI, and U. TALLAREK "Coupled lattice-Boltzmann and finite-difference simulation of electroosmosis in microfluidic channels" in: *International Journal for Numerical Methods in Fluids* 46.5 (2004), pp. 507–532 DOI: 10.1002/fld.765 (see p. 43)

[176] D. HLUSHKOU, V. APANASOVICH, A. SEIDEL-MORGENSTERN, and U. TALLAREK "Numerical simulation of electrokinetic microfluidics in colloidal systems" in: *Chemical Engineering Communications* 193.7 (2006), pp. 826–839 DOI: 10.1080/00986440500267295 (see p. 43)

[177] D. HLUSHKOU "Numerical Simulation of Flow and Mass Transport in (Electro)Chromatographic Systems" PhD thesis Magdeburg, Germany: Institute of Chemical and Process Engineering, Otto-von-Guericke-Universität, 2003 (see p. 43)

[178] F. GRITTI and G. GUIOCHON "Mass transfer kinetics, band broadening and column efficiency" in: *Journal of Chromatography A* 1221 (2012), pp. 2–40 DOI: 10.1016/j.chroma.2011.04.058 (see pp. 43, 50, 51, 92, 112, 115)

[179] S. BRUNS, T. MÜLLNER, M. KOLLMANN, J. SCHACHTNER, A. HÖLTZEL, and U. TALLAREK "Confocal laser scanning microscopy method for quantitative characterization of silica monolith morphology" in: *Analytical chemistry* 82.15 (2010), pp. 6569–75 DOI: 10.1021/ac100909t (see pp. 43, 75)

[180] S. BRUNS, T. HARA, B. M. SMARSLY, and U. TALLAREK "Morphological analysis of physically reconstructed capillary hybrid silica monoliths and correlation with separation efficiency" in: *Journal of Chromatography A* 1218.31 (2011), pp. 5187–94 DOI: 10.1016/j.chroma.2011.05.090 (see pp. 43, 72)

[181] D. HLUSHKOU, S. BRUNS, and U. TALLAREK "High-performance computing of flow and transport in physically reconstructed silica monoliths" in: *Journal of Chromatography A* 1217.23 (2010), pp. 3674–3682 DOI: 10.1016/j.chroma.2010.04.004 (see pp. 44, 75, 79, 81, 83, 84, 121)

[182] D. HLUSHKOU, S. BRUNS, A. HÖLTZEL, and U. TALLAREK "From pore scale to column scale dispersion in capillary silica monoliths" in: *Analytical chemistry* 82.17 (2010), pp. 7150–9 DOI: 10.1021/ac101393b (see pp. 44, 72, 74, 79, 81, 84, 86, 93, 95, 107, 109, 114)

[183] D. HLUSHKOU, S. BRUNS, A. SEIDEL-MORGENSTERN, and U. TALLAREK "Morphology-transport relationships for silica monoliths: From physical reconstruction to pore-scale simulations" in: *Journal of Separation Science* 34.16-17 (2011), pp. 2026–37 DOI: 10.1002/jssc.201100158 (see pp. 44, 75, 79, 81, 84, 93, 95, 96, 114)

[184] H. EGHBALI, V. VERDOOLD, L. VANKEERBERGHEN, H. GARDENIERS, and G. DESMET "Experimental investigation of the band broadening arising from short-range interchannel heterogeneities in chromatographic beds under the condition of identical external porosity" in: *Analytical Chemistry* 81 (2009), pp. 705–715 DOI: 10.1021/ac802124p (see pp. 44, 45, 123)

[185] H. EGHBALI, W. DE MALSCHE, J. DE SMET, J. BILLEN, M. DE PRA, W. TH. KOK, P. J. SCHOENMAKERS, H. GARDENIERS, and G. DESMET "Experimental investigation of the band broadening originating from the top and bottom walls in micromachined nonporous pillar array columns" in: *Journal of Separation Science* 30 (2007), pp. 2605–2613 DOI: 10.1002/jssc.200700203 (see p. 45)

[186] P. MAGNICO and M. MARTIN "Dispersion in the interstitial space of packed columns" in: *Journal of Chromatography A* 517 (1990), pp. 31–49 DOI: 10.1016/S0021-9673(01)95708-5 (see pp. 49, 133)

[187] J. H. KNOX "Band dispersion in chromatography — a universal expression for the contribution from the mobile zone" in: *Journal of Chromatography A* 960 (2002), pp. 7–18 DOI: 10.1016/S0021-9673(02)00240-6 (see p. 49)

[188] J. C. GIDDINGS "'Eddy' diffusion in chromatography" in: *Nature* 184 (1959), pp. 357–358 DOI: 10.1038/184357a0 (see pp. 50, 130, 131)

[189] J. E. MACNAIR, K. C. LEWIS, and J. W. JORGENSON "Ultrahigh-Pressure Reversed-Phase Liquid Chromatography in Packed Capillary Columns" in: *Analytical Chemistry* 69.6 (1997), pp. 983–989 DOI: 10.1021/ac961094r (see p. 51)

[190] J. E. MACNAIR, K. D. PATEL, and J. W. JORGENSON "Ultrahigh-pressure reversed-phase capillary liquid chromatography: Isocratic and gradient elution using columns packed with 1.0-μm particles" in: *Analytical Chemistry* 71.3 (1999), pp. 700–708 DOI: 10.1021/ac9807013 (see p. 51)

[191] S. FEKETE, K. GANZLER, and J. FEKETE "Facts and myths about columns packed with sub-3 μm and sub-2 μm particles" in: *Journal of Pharmaceutical and Biomedical Analysis* 51.1 (2010), pp. 56–64 DOI: 10.1016/j.jpba.2009.08.003 (see p. 51)

[192] E. HAMDAN, J. MILTHORPE, and J. LAI "An extended macroscopic model for solute dispersion in confined porous media" in: *Chemical Engineering Journal* 137 (2008), pp. 614–635 DOI: 10.1016/j.cej.2007.05.031 (see p. 52)

[193] F. GRITTI and G. GUIOCHON "Relationship between trans-column eddy diffusion and retention in liquid chromatography: theory and experimental evidence" in: *Journal of Chromatography A* 1217.41 (2010), pp. 6350–65 DOI: 10.1016/j.chroma.2010.07.029 (see pp. 52, 70, 92)

[194] F. GRITTI and G. GUIOCHON "Mass transfer kinetic mechanism in monolithic columns and application to the characterization of new research monolithic samples with different average pore sizes" in: *Journal of Chromatography A* 1216.23 (2009), pp. 4752–67 DOI: 10.1016/j.chroma.2009.04.034 (see p. 52)

[195] U. TALLAREK, E. BAYER, and G. GUIOCHON "Study of dispersion in packed chromatographic columns by pulsed field gradient nuclear magnetic resonance" in: *Journal of the American Chemical Society* 120 (1998), pp. 1494–1505 DOI: 10.1021/ja9726623 (see p. 55)

[196] K. M. USHER, C. R. SIMMONS, and J. G. DORSEY "Modeling chromatographic dispersion: A comparison of popular equations" in: *Journal of Chromatography A* 1200 (2008), pp. 122–128 DOI: 10.1016/j.chroma.2008.05.073 (see p. 55)

[197] A. Okabe *Spatial tessellations: concepts and applications of Voronoi diagrams* 2nd ed. John Wiley & Sons, 2000 (see p. 55)

[198] D. A. Edwards, M. Shapiro, and H. Brenner "Dispersion and reaction in two-dimensional model porous media" in: *Physics of Fluids A: Fluid Dynamics* 5.4 (1993), p. 837 DOI: 10.1063/1.858631 (see p. 57)

[199] H. P. A. Souto and C. Moyne "Dispersion in two-dimensional periodic porous media. Part II. Dispersion tensor" in: *Physics of Fluids* 9 (1997), pp. 2253–2263 DOI: 10.1063/1.869347 (see pp. 57, 99, 103)

[200] D. Buyuktas and W. W. Wallender "Dispersion in spatially periodic porous media" in: *Heat and Mass Transfer* 40 (2004), pp. 261–270 DOI: 10.1007/s00231-003-0441-0 (see pp. 57, 99)

[201] P. Gzil, N. Vervoort, G. V. Baron, and G. Desmet "Advantages of perfectly ordered 2-D porous pillar arrays over packed bed columns for LC separations: a theoretical analysis" in: *Analytical chemistry* 75.22 (2003), pp. 6244–50 DOI: 10.1021/ac034345m (see pp. 57, 58, 63)

[202] N. Vervoort, J. Billen, P. Gzil, G. V. Baron, and G. Desmet "Importance and reduction of the sidewall-induced band-broadening effect in pressure-driven microfabricated columns" in: *Analytical chemistry* 76.15 (2004), pp. 4501–7 DOI: 10.1021/ac049930h (see p. 57)

[203] J. De Smet, P. Gzil, G. V. Baron, and G. Desmet "On the 3-dimensional effects in etched chips for high performance liquid chromatography-separations" in: *Journal of Chromatography A* 1154 (2007), pp. 189–197 DOI: 10.1016/j.chroma.2007.03.076 (see p. 57)

[204] M. De Pra, W. Th. Kok, J. G. E. Gardeniers, G. Desmet, S. Eeltink, J. W. van Nieuwkasteele, and P. J. Schoenmakers "Experimental study on band dispersion in channels structured with micropillars" in: *Analytical Chemistry* 78 (2006), pp. 6519–6525 DOI: 10.1021/ac060915h (see p. 58)

[205] J. Eijkel "Chip-based HPLC: the quest for the perfect column" in: *Lab on a chip* 7.7 (2007), pp. 815–7 DOI: 10.1039/b707464f (see p. 58)

[206] G. Stegeman, J. C. Kraak, and H. Poppe "Dispersion in packed-column hydrodynamic chromatography" in: *Journal of Chromatography A* 634.2 (1993), pp. 149–159 DOI: 10.1016/0021-9673(93)83001-9 (see p. 58)

[207] N. Wu, Y. Liu, and M. L Lee "Sub-2 μm porous and nonporous particles for fast separation in reversed-phase high performance liquid chromatography" in: *Journal of Chromatography A* 1131.1-2 (2006), pp. 142–50 DOI: 10.1016/j.chroma.2006.07.042 (see p. 58)

[208] S. Torquato *Random heterogeneous materials: microstructure and macroscopic properties* Springer, 2002 (see p. 60)

[209] D. J. Gunn and C. Pryce "Dispersion in packed beds" in: *Transactions of the Institution of Chemical Engineers* 47 (1969), T341 (see p. 60)

[210] K. Miyabe "Evaluation of Chromatographic performance of various packing materials having different structural characteristics as stationary phase for fast high performance liquid chromatography by new moment equations" in: *Journal of Chromatography A* 1183.1-2 (2008), pp. 49–64 DOI: 10.1016/j.chroma.2007.12.064 (see p. 70)

[211] F. Gritti and G. Guiochon "Importance of sample intraparticle diffusivity in investigations of the mass transfer mechanism in liquid chromatography" in: *AIChE Journal* 57.2 (2011), pp. 346–358 DOI: 10.1002/aic.12280 (see p. 70)

[212] F. GRITTI and G. GUIOCHON "Kinetic investigation of the relationship between the efficiency of columns and their diameter" in: *Journal of Chromatography A* 1218.12 (2011), pp. 1592–602 DOI: 10.1016/j.chroma.2010.12.023 (see p. 71)

[213] G. E. MUELLER "Numerically packing spheres in cylinders" in: *Powder Technology* 159 (2005), pp. 105–110 DOI: 10.1016/j.powtec.2005.06.002 (see p. 71)

[214] S. BRUNS, J. P. GRINIAS, L. E. BLUE, J. W. JORGENSON, and U. TALLAREK "Morphology and separation efficiency of low-aspect-ratio capillary ultrahigh pressure liquid chromatography columns" in: *Analytical chemistry* 84.10 (2012), pp. 4496–503 DOI: 10.1021/ac300326k (see pp. 71, 150)

[215] G. GUIOCHON "Monolithic columns in high-performance liquid chromatography" in: *Journal of Chromatography A* 1168.1-2 (2007), 101–68; discussion 100 DOI: 10.1016/j.chroma.2007.05.090 (see p. 71)

[216] K. S. MRIZIQ, J. A. ABIA, Y. LEE, and G. GUIOCHON "Structural radial heterogeneity of a silica-based wide-bore monolithic column" in: *Journal of Chromatography A* 1193.1-2 (2008), pp. 97–103 DOI: 10.1016/j.chroma.2008.04.004 (see p. 71)

[217] J. A. ABIA, K. S. MRIZIQ, and G. A GUIOCHON "Radial heterogeneity of some analytical columns used in high-performance liquid chromatography" in: *Journal of Chromatography A* 1216.15 (2009), pp. 3185–91 DOI: 10.1016/j.chroma.2009.02.034 (see p. 71)

[218] K. KANAMORI, H. YONEZAWA, K. NAKANISHI, K. HIRAO, and H. JINNAI "Structural formation of hybrid siloxane-based polymer monolith in confined spaces" in: *Journal of Separation Science* 27.10-11 (2004), pp. 874–886 DOI: 10.1002/jssc.200401816 (see p. 72)

[219] M. MOTOKAWA, M. OHIRA, H. MINAKUCHI, K. NAKANISHI, and N. TANAKA "Performance of octadecylsilylated monolithic silica capillary columns of 530 μm inner diameter in HPLC" in: *Journal of Separation Science* 29.16 (2006), pp. 2471–2477 DOI: 10.1002/jssc.200600335 (see p. 72)

[220] R. ROUX, M. ABI JAOUDÉ, and C DEMESMAY "Improvement of Chromatographic performances of in-situ synthesized hybrid C8 silica monoliths by reduction of structural radial heterogeneities" in: *Journal of Chromatography A* 1216.18 (2009), pp. 3857–63 DOI: 10.1016/j.chroma.2009.02.070 (see p. 72)

[221] T. HARA, S. MAKINO, Y. WATANABE, T. IKEGAMI, K. CABRERA, B. SMARSLY, and N. TANAKA "The performance of hybrid monolithic silica capillary columns prepared by changing feed ratios of tetramethoxysilane and methyltrimethoxysilane" in: *Journal of Chromatography A* 1217.1 (2010), pp. 89–98 DOI: 10.1016/j.chroma.2009.11.019 (see p. 72)

[222] K. HORMANN, T. MÜLLNER, S. BRUNS, A. HÖLTZEL, and U. TALLAREK "Morphology and separation efficiency of a new generation of analytical silica monoliths" in: *Journal of Chromatography A* 1222 (2012), pp. 46–58 DOI: 10.1016/j.chroma.2011.12.008 (see p. 72)

[223] F. GRITTI and G. GUIOCHON "Measurement of the eddy dispersion term in chromatographic columns: III. Application to new prototypes of 4.6 mm I.D. monolithic columns" in: *Journal of Chromatography A* 1225 (2012), pp. 79–90 DOI: 10.1016/j.chroma.2011.12.055 (see p. 72)

[224] F. GRITTI and G. GUIOCHON "Measurement of the eddy dispersion term in chromatographic columns. II. Application to new prototypes of 2.3 and 3.2 mm I.D. monolithic silica columns" in: *Journal of Chromatography A* 1227 (2012), pp. 82–95 DOI: 10.1016/j.chroma.2011.12.065 (see p. 72)

[225] A. DANEYKO, S. KHIREVICH, A. HÖLTZEL, A. SEIDEL-MORGENSTERN, and U. TALLAREK "From random sphere packings to regular pillar arrays: effect of the macroscopic confinement on hy-

drodynamic dispersion" in: *Journal of Chromatography A* 1218.45 (2011), pp. 8231–48 DOI: 10.1016/j.chroma.2011.09.039 (see pp. 72, 80, 81, 86, 97, 103, 108, 109, 113, 116, 121)

[226] J. OP DE BEECK, W. DE MALSCHE, D. S. TEZCAN, P. DE MOOR, and G. DESMET "Impact of the limitations of state-of-the-art micro-fabrication processes on the performance of pillar array columns for liquid chromatography" in: *Journal of Chromatography A* 1239 (2012), pp. 35–48 DOI: 10.1016/j.chroma.2012.03.054 (see pp. 74, 107)

[227] N. WU, J. A. LIPPERT, and M. L LEE "Practical aspects of ultrahigh pressure capillary liquid chromatography" in: *Journal of Chromatography A* 911.1 (2001), pp. 1–12 DOI: 10.1016/S0021-9673(00)01188-2 (see p. 76)

[228] J. A. ANSPACH, T. D. MALONEY, R. W. BRICE, and L. A COLÓN "Injection valve for ultrahigh-pressure liquid chromatography" in: *Analytical chemistry* 77.22 (2005), pp. 7489–94 DOI: 10.1021/ac051213f (see p. 76)

[229] J. W. JORGENSON "Capillary liquid chromatography at ultrahigh pressures" in: *Annual Review of Analytical Chemistry* 3 (2010), pp. 129–150 DOI: 10.1146/annurev.anchem.1.031207.113014 (see p. 76)

[230] A. FELINGER "Diffusion time in core-shell packing materials" in: *Journal of Chromatography A* 1218.15 (2011), pp. 1939–41 DOI: 10.1016/j.chroma.2010.10.025 (see p. 76)

[231] F. GRITTI, J. OMAMOGHO, and G. GUIOCHON "Kinetic investigation of narrow-bore columns packed with prototype sub-2 μm superficially porous particles with various shell thickness" in: *Journal of Chromatography A* 1218.40 (2011), pp. 7078–93 DOI: 10.1016/j.chroma.2011.07.037 (see p. 76)

[232] S. KHIREVICH, A. HÖLTZEL, and U. TALLAREK "Validation of pore-scale simulations of hydrodynamic dispersion in random sphere packings" in: 13.3 (2013), pp. 801–822 DOI: 10.4208/cicp.361011.260112s (see pp. 78, 81, 86, 115, 116, 121)

[233] F. GRITTI and G. GUIOCHON "Measurement of the eddy diffusion term in chromatographic columns. I. Application to the first generation of 4.6mm I.D. monolithic columns" in: *Journal of Chromatography A* 1218.31 (2011), pp. 5216–27 DOI: 10.1016/j.chroma.2011.05.101 (see p. 79)

[234] H. KOKU, R. S. MAIER, K. J. CZYMMEK, M. R. SCHURE, and A. M. LENHOFF "Modeling of flow in a polymeric chromatographic monolith" in: *Journal of Chromatography A* 1218.22 (2011), pp. 3466–75 DOI: 10.1016/j.chroma.2011.03.064 (see pp. 81, 93, 95, 114)

[235] H. KOKU, R. S. MAIER, M. R. SCHURE, and A. M. LENHOFF "Modeling of dispersion in a polymeric chromatographic monolith" in: *Journal of Chromatography A* 1237 (2012), pp. 55–63 DOI: 10.1016/j.chroma.2012.03.005 (see pp. 81, 114)

[236] L. LEBON, L. OGER, J. LEBLOND, J. P. HULIN, N. S. MARTYS, and L. M. SCHWARTZ "Pulsed gradient NMR measurements and numerical simulation of flow velocity distribution in sphere packings" in: *Physics of Fluids* 8.2 (1996), p. 293 DOI: 10.1063/1.868839 (see p. 88)

[237] R. S. MAIER, D. M. KROLL, Y. E. KUTSOVSKY, H. T. DAVIS, and R. S. BERNARD "Simulation of flow through bead packs using the lattice Boltzmann method" in: *Physics of Fluids* 10 (1998), pp. 60–74 DOI: 10.1063/1.869550 (see p. 88)

[238] M. L. JOHNS, A. J. SEDERMAN, A. S. BRAMLEY, L. F. GLADDEN, and P. ALEXANDER "Local transitions in flow phenomena through packed beds identified by MRI" in: *AIChE Journal* 46.11 (2000), pp. 2151–2161 DOI: 10.1002/aic.690461108 (see p. 88)

[239] Y. E. KUTSOVSKY, L. E. SCRIVEN, H. T. DAVIS, and B. E. HAMMER "NMR imaging of velocity profiles and velocity distributions in bead packs" in: *Physics of Fluids* 8.4 (1996), p. 863 DOI: 10.1063/1.868867 (see p. 88)

[240] M. RASHIDI, L. PEURRUNG, A. F. B. TOMPSON, and T. J. KULP "Experimental analysis of pore-scale flow and transport in porous media" in: *Advances in Water Resources* 19.3 (1996), pp. 163–180 DOI: 10.1016/0309-1708(95)00048-8 (see p. 88)

[241] J. GÖTZ, K. ZICK, C. HEINEN, and T. KÖNIG "Visualisation of flow processes in packed beds with NMR imaging: determination of the local porosity, velocity vector and local dispersion coefficients" in: *Chemical Engineering and Processing: Process Intensification* 41.7 (2002), pp. 611–629 DOI: 10.1016/S0255-2701(01)00185-4 (see p. 88)

[242] X. REN, S. STAPF, and B. BLÜMICH "NMR velocimetry of flow in model fixed-bed reactors of low aspect ratio" in: *AIChE Journal* 51.2 (2005), pp. 392–405 DOI: 10.1002/aic.10318 (see p. 88)

[243] N. W. HALPERN-MANNERS, J. L. PAULSEN, V. S. BAJAJ, and A. PINES "Remotely detected MRI velocimetry in microporous bead packs" in: *The Journal of Physical Chemistry A* 115.16 (2011), pp. 4023–30 DOI: 10.1021/jp109728j (see p. 88)

[244] J. M. P. Q. DELGADO "Longitudinal and Transverse Dispersion in Porous Media" in: *Chemical Engineering Research and Design* 85.9 (2007), pp. 1245–1252 DOI: 10.1205/cherd07017 (see pp. 89, 91)

[245] J. H. KNOX, G. R. LAIRD, and P. A. RAVEN "Interaction of radial and axial dispersion in liquid chromatography in relation to the "infinite diameter effect" in: *Journal of Chromatography A* 122 (1976), pp. 129–145 DOI: 10.1016/S0021-9673(00)82240-2 (see p. 92)

[246] C. H. EON "Comparison of broadening patterns in regular and radially compressed large-diameter columns" in: *Journal of Chromatography A* 149 (1978), pp. 29–42 DOI: 10.1016/S0021-9673(00)80977-2 (see p. 92)

[247] D. S. HORNE, J. H. KNOX, and L. MCLAREN "A Comparison of Mobile-Phase Peak Dispersion in Gas and Liquid Chromatography" in: *Separation Science* 1.5 (1966), pp. 531–554 DOI: 10.1080/01496396608049464 (see pp. 92, 131)

[248] N. W. HAN, J. BHAKTA, and R. G. CARBONELL "Longitudinal and lateral dispersion in packed beds: effect of column length and particle size distribution" in: *AIChE Journal* 31 (1985), pp. 277–288 DOI: 10.1002/aic.690310215 (see p. 93)

[249] J. R. F. GUEDES DE CARVALHO and J. M. P. Q. DELGADO "Lateral dispersion in liquid flow through packed beds at Pe < 1,400" in: *AIChE Journal* 46 (2000), pp. 1089–1095 DOI: 10.1002/aic.690460520 (see p. 93)

[250] F. GRITTI, T. FARKAS, J. HENG, and G. GUIOCHON "On the relationship between band broadening and the particle-size distribution of the packing material in liquid chromatography: theory and practice" in: *Journal of Chromatography A* 1218.45 (2011), pp. 8209–21 DOI: 10.1016/j.chroma.2011.09.034 (see p. 93)

[251] U. TALLAREK, F. C. LEINWEBER, and A. SEIDEL-MORGENSTERN "Fluid Dynamics in Monolithic Adsorbents: Phenomenological Approach to Equivalent Particle Dimensions" in: *Chemical Engineering & Technology* 25.12 (2002), pp. 1177–1181 DOI: 10.1002/1521-4125(20021210)25:12<1177::AID-CEAT1177>3.0.CO;2-V (see pp. 95, 107)

[252] W. GILLE, D. ENKE, and F. JANOWSKI "Stereological Macropore Analysis of a Controlled Pore Glass by use of Small-Angle Scattering" in: *Journal of Porous Materials* 8.3 (2001), pp. 179–191 DOI: 10.1023/A:1012223404017 (see p. 96)

[253] A. EIDSATH "Dispersion in pulsed systems — III Comparison between theory and experiments for packed beds" in: *Chemical Engineering Science* 38.11 (1983), pp. 1803–1816 DOI: 10.1016/0009-2509(83)85037-4 (see p. 99)

[254] M. QUINTARD and S. WHITAKER "Convection, dispersion, and interfacial transport of contaminants: Homogeneous porous media" in: *Advances in Water Resources* 17.4 (1994), pp. 221–239 DOI: 10.1016/0309-1708(94)90002-7 (see p. 99)

[255] M. L. PORTER, F. J. VALDÉS-PARADA, and B. D. WOOD "Comparison of theory and experiments for dispersion in homogeneous porous media" in: *Advances in Water Resources* 33.9 (2010), pp. 1043–1052 DOI: 10.1016/j.advwatres.2010.06.007 (see pp. 99, 103)

[256] M. J. E. GOLAY and J. G. ATWOOD "Early phases of the dispersion of a sample injected in poiseuille flow" in: *Journal of Chromatography A* 186 (1979), pp. 353–370 DOI: 10.1016/S0021-9673(00)95261-0 (see p. 99)

[257] U. TALLAREK, E. RAPP, T. SCHEENEN, E. BAYER, and H. VAN AS "Electroosmotic and Pressure-Driven Flow in Open and Packed Capillaries: Velocity Distributions and Fluid Dispersion" in: *Analytical Chemistry* 72.10 (2000), pp. 2292–2301 DOI: 10.1021/ac991303i (see p. 99)

[258] P. T. CALLAGHAN, S. L. CODD, and J. D. SEYMOUR "Spatial coherence phenomena arising from translational spin motion in gradient spin echo experiments" in: *Concepts in Magnetic Resonance* 11.4 (1999), pp. 181–202 DOI: 10.1002/(SICI)1099-0534(1999)11:4<181::AID-CMR1>3.0.CO;2-T (see p. 103)

[259] P. T. CALLAGHAN and S. L. CODD "Flow coherence in a bead pack observed using frequency domain modulated gradient nuclear magnetic resonance" in: *Physics of Fluids* 13 (2001), pp. 421–427 DOI: 10.1063/1.1336810 (see p. 103)

[260] S. STAPF, SONG-I HAN, C. HEINE, and B. BLÜMICH "Spatiotemporal correlations in transport processes determined by multiple pulsed field gradient experiments" in: *Concepts in Magnetic Resonance* 14.3 (2002), pp. 172–211 DOI: 10.1002/cmr.10021 (see p. 103)

[261] K. KACZMARSKI and G. GUIOCHON "Modeling of the mass-transfer kinetics in chromatographic columns packed with shell and pellicular particles" in: *Analytical chemistry* 79.12 (2007), pp. 4648–56 DOI: 10.1021/ac070209w (see pp. 111, 114, 143–145, 149)

[262] J. J. DESTEFANO, T. J. LANGLOIS, and J. J. KIRKLAND "Characteristics of superficially-porous silica particles for fast HPLC: some performance comparisons with sub-2 μm particles" in: *Journal of Chromatographic Science* 46.3 (2008), pp. 254–260 DOI: 10.1093/chromsci/46.3.254 (see p. 111)

[263] S. A. SCHUSTER, B. M. WAGNER, B. E. BOYES, and J. J. KIRKLAND "Wider pore superficially porous particles for peptide separations by HPLC" in: *Journal of Chromatographic Science* 48 (2010), pp. 566–571 DOI: 10.1093/chromsci/48.7.566 (see p. 111)

[264] F. GRITTI and G. GUIOCHON "Perspectives on the evolution of the column efficiency in liquid chromatography" in: *Analytical Chemistry* 85.6 (2013), pp. 3017–35 DOI: 10.1021/ac3033307 (see p. 111)

[265] S. FEKETE and D. GUILLARME "Kinetic evaluation of new generation of column packed with 1.3 μm core-shell particles" in: *Journal of Chromatography A* 1308 (2013), pp. 104–13 DOI: 10.1016/j.chroma.2013.08.008 (see p. 111)

[266] F. GRITTI and G. GUIOCHON "Rapid development of core-shell column technology: accurate measurements of the intrinsic column efficiency of narrow-bore columns packed with 4.6 down to 1.3 μm superficially porous particles" in: *Journal of Chromatography A* 1333 (2014), pp. 60–9 DOI: 10.1016/j.chroma.2014.01.061 (see p. 111)

[267] F. GRITTI and G. GUIOCHON "Possible resolution gain in enantioseparations afforded by core-shell particle technology" in: *Journal of Chromatography A* 1348 (2014), pp. 87–96 DOI: 10.1016/j.chroma.2014.04.041 (see p. 111)

[268] R. HAYES, A. AHMED, T. EDGE, and H. ZHANG "Core-shell particles: preparation, fundamentals and applications in high performance liquid chromatography" in: *Journal of Chromatography A* 1357 (2014), pp. 36–52 DOI: 10.1016/j.chroma.2014.05.010 (see p. 111)

[269] F. GRITTI and G. GUIOCHON "Quantification of individual mass transfer phenomena in liquid chromatography for further improvement of column efficiency" in: *LC GC North America* 32.12 (2014), pp. 928–940 (see pp. 111, 147)

[270] N. LAMBERT, I. KISS, and A. FELINGER "Mass-transfer properties of insulin on core-shell and fully porous stationary phases" in: *Journal of Chromatography A* 1366 (2014), pp. 84–91 DOI: 10.1016/j.chroma.2014.09.025 (see p. 111)

[271] J. C. HEATON and D. V. MCCALLEY "Comparison of the kinetic performance and retentivity of sub-2 μm core-shell, hybrid and conventional bare silica phases in hydrophilic interaction chromatography" in: *Journal of Chromatography A* 1371 (2014), pp. 106–116 DOI: 10.1016/j.chroma.2014.10.013 (see p. 111)

[272] S. FEKETE, D. GUILLARME, and M. W. DONG "Superficially porous particles: perspectives, practices, and trends" in: *LC GC North America* 32.6 (2014), p. 420 (see p. 111)

[273] L. E. BLUE and J. W. JORGENSON "1.1 μm Superficially porous particles for liquid chromatography: Part II: Column packing and chromatographic performance" in: *Journal of Chromatography A* 1380 (2015), pp. 71–80 DOI: 10.1016/j.chroma.2014.12.055 (see p. 111)

[274] H. DONG and J. D. BRENNAN "Tailoring the properties of sub-3 μm silica core-shell particles prepared by a multilayer-by-multilayer process" in: *Journal of Colloid and Interface Science* 437 (2015), pp. 50–7 DOI: 10.1016/j.jcis.2014.09.033 (see p. 111)

[275] P. JANDERA, T. HÁJEK, and M. STAŇKOVÁ "Monolithic and core-shell columns in comprehensive two-dimensional HPLC: a review" in: *Analytical and Bioanalytical Chemistry* 407.1 (2015), pp. 139–51 DOI: 10.1007/s00216-014-8147-3 (see p. 111)

[276] R. W. BRICE, X. ZHANG, and L. A. COLÓN "Fused-core, sub-2 μm packings, and monolithic HPLC columns: a comparative evaluation" in: *Journal of Separation Science* 32.15-16 (2009), pp. 2723–31 DOI: 10.1002/jssc.200900091 (see p. 111)

[277] F. GRITTI and G. GUIOCHON "Comparison of heat friction effects in narrow-bore columns packed with core–shell and totally porous particles" in: *Chemical Engineering Science* 65.23 (2010), pp. 6310–6319 DOI: 10.1016/j.ces.2010.09.019 (see p. 111)

[278] J. J. VAN DEEMTER, F. J. ZUIDERWEG, and A. KLINKENBERG "Longitudinal diffusion and resistance to mass transfer as causes of nonideality in chromatography" in: *Chemical Engineering Science* 5 (1956), pp. 271–289 DOI: 10.1016/0009-2509(56)80003-1 (see p. 111)

[279] L. LAPIDUS and N. R. AMUNDSON "Mathematics of adsorption in beds VI. The effect of longitudinal diffusion in ion exchange and chromatographic columns" in: *The Journal of Physical Chemistry* (1952), pp. 984–988 DOI: 10.1021/j150500a014 (see p. 111)

[280] S. BRUNS, D. STOECKEL, B. M. SMARSLY, and U. TALLAREK "Influence of particle properties on the wall region in packed capillaries" in: *Journal of Chromatography A* 1268 (2012), pp. 53–63 DOI: 10.1016/j.chroma.2012.10.027 (see pp. 113, 140)

[281] A. DANEYKO, D. HLUSHKOU, S. KHIREVICH, and U. TALLAREK "From random sphere packings to regular pillar arrays: analysis of transverse dispersion" in: *Journal of Chromatography A* 1257 (2012), pp. 98–115 DOI: 10.1016/j.chroma.2012.08.024 (see p. 113)

[282] D. HLUSHKOU, K. HORMANN, A. HÖLTZEL, S. KHIREVICH, A. SEIDEL-MORGENSTERN, and U. TALLAREK "Comparison of first and second generation analytical silica monoliths by pore-scale simulations of eddy dispersion in the bulk region" in: *Journal of Chromatography A* 1303 (2013), pp. 28–38 DOI: 10.1016/j.chroma.2013.06.039 (see p. 114)

[283] D. HLUSHKOU, F. GRITTI, A. DANEYKO, G. GUIOCHON, and U. TALLAREK "How microscopic characteristics of the adsorption kinetics impact macroscale transport in chromatographic beds" in: *The Journal of Physical Chemistry C* 117.44 (2013), pp. 22974–22985 DOI: 10.1021/jp408362u (see p. 114)

[284] D. HLUSHKOU, F. GRITTI, G. GUIOCHON, A. SEIDEL-MORGENSTERN, and U. TALLAREK "Effect of adsorption on solute dispersion: A microscopic stochastic approach" in: *Analytical Chemistry* 86.9 (2014), pp. 4463–4470 DOI: 10.1021/ac500309p (see p. 114)

[285] F. GRITTI, K. HORVATH, and G. GUIOCHON "How changing the particle structure can speed up protein mass transfer kinetics in liquid chromatography" in: *Journal of Chromatography A* 1263.9 (2012), pp. 84–98 DOI: 10.1016/j.chroma.2012.09.030 (see p. 115)

[286] P. SALAMON, D. FERNÀNDEZ-GARCIA, and J. J. GÓMEZ-HERNÁNDEZ "Modeling tracer transport at the MADE site: The importance of heterogeneity" in: *Water Resources Research* 43 (2007), W08404 DOI: 10.1029/2006WR005522 (see p. 116)

[287] H. HOTEIT, R. MOSE, A. YOUNES, F. LEHMANN, and PH ACKERER "Three-dimensional modeling of mass transfer in porous media using the mixed hybrid finite elements and the random-walk methods" in: *Mathematical Geology* 34.4 (2002), pp. 435–456 DOI: 10.1023/A:1015083111971 (see pp. 117, 119)

[288] D. LIM "Numerical study of nuclide migration in a nonuniform horizontal flow field of a high-level radioactive waste repository with multiple canisters" in: *Nuclear Technology* 156.2 (2006), pp. 222–245 (see p. 117)

[289] J. M. RAMIREZ, E. A. THOMANN, E. C. WAYMIRE, J. CHASTANET, and B. D. WOOD "A note on the theoretical foundations of particle tracking methods in heterogeneous porous media" in: *Water Resources Research* 44.1 (2008), pp. 1–5 DOI: 10.1029/2007WR005914 (see p. 119)

[290] M. BECHTOLD, J. VANDERBORGHT, O. IPPISCH, and H. VEREECKEN "Efficient random walk particle tracking algorithm for advective-dispersive transport in media with discontinuous dispersion coefficients and water contents" in: *Water Resources Research* 47.10 (2011), W10526 DOI: 10.1029/2010WR010267 (see pp. 119, 120)

[291] M.H. BLEES and J.C. LEYTE "The effective translational self-diffusion coefficient of small molecules in colloidal crystals of spherical particles" in: *Journal of Colloid and Interface Science* 166.1 (1994), pp. 118–127 DOI: 10.1006/jcis.1994.1278 (see pp. 122, 123)

[292] A. S. SANGANI and A. ACRIVOS "Slow flow through a periodic array of spheres" in: *International Journal of Multiphase Flow* 8 (1982), pp. 343–360 DOI: 10.1016/0301-9322(82)90047-7 (see p. 121)

[293] A. A. ZICK and G. M. HOMSY "Stokes flow through periodic arrays of spheres" in: *Journal of Fluid Mechanics* 115 (1982), pp. 13–26 DOI: 10.1017/S0022112082000627 (see p. 121)

[294] U. M. SCHEVEN, S. KHIREVICH, A. DANEYKO, and U. TALLAREK "Longitudinal and transverse dispersion in flow through random packings of spheres: A quantitative comparison of experiments, simulations, and models" in: *Physical Review E* 89.5 (2014), p. 053023 DOI: 10.1103/PhysRevE.89.053023 (see pp. 123, 133)

[295] J. C. GIDDINGS and R. A. ROBISON "Failure of the eddy diffusion concept of gas chromatography" in: *Analytical Chemistry* 34.8 (1962), pp. 885–890 DOI: 10.1021/ac60188a005 (see p. 130)

[296] J. C. GIDDINGS "Evidence on the nature of eddy diffusion in gas chromatography from inert (nonsorbing) column data" in: *Analytical Chemistry* 35.10 (1963), pp. 1338–1341 DOI: 10.1021/ac60203a036 (see p. 130)

[297] A. KLINKENBERG "Evidence on the nature of eddy diffusion in gas chromatography from inert (nonsorbing) column data" in: *Analytical Chemistry* 38.3 (1966), pp. 489–490 DOI: 10.1021/ac60235a028 (see p. 130)

[298] A. KLINKENBERG and F. SJENITZER "'Eddy' diffusion in chromatography" in: *Nature* 187.4742 (1960), p. 1023 DOI: 10.1038/1871023a0 (see p. 130)

[299] C. HORVATH and H.-J. LIN "Movement and band spreading of unsorbed solutes in liquid chromatography" in: *Journal of Chromatography A* 126 (1976), pp. 401–420 DOI: 10.1016/S0021-9673(01)84088-7 (see p. 131)

[300] A. L. BERDICHEVSKY and U. D. NEUE "Nature of the eddy dispersion in packed beds" in: *Journal of Chromatography A* 535 (1990), pp. 189–198 DOI: 10.1016/S0021-9673(01)88944-5 (see p. 131)

[301] P. D. SCHETTLER and J. C. GIDDINGS "Application of the Nonequilibrium Theory of Chromatography to a Variable Flow Correlation Model of Complex Flow and Coupling" in: *The Journal of Physical Chemistry* 357.1 (1966), pp. 2582–2589 DOI: 10.1021/j100842a021 (see p. 133)

[302] J. C. GIDDINGS and P. D. SCHETTLER "General nonequilibrium theory of chromatography with complex flow transport" in: *The Journal of Physical Chemistry* 78.8 (1969), pp. 2577–2582 DOI: 10.1021/j100842a020 (see p. 133)

[303] F. GRITTI and G. GUIOCHON "General HETP equation for the study of mass-transfer mechanisms in RPLC" in: *Analytical Chemistry* 78.15 (2006), pp. 5329–5347 DOI: 10.1021/ac060203r (see p. 143)

[304] K. HORMANN and U. TALLAREK "Analytical silica monoliths with submicron macropores: current limitations to a direct morphology-column efficiency scaling" in: *Journal of Chromatography A* 1312 (2013), pp. 26–36 DOI: 10.1016/j.chroma.2013.08.087 (see p. 150)

[305] T. MÜLLNER, A. ZANKEL, F. SVEC, and U. TALLAREK "Finite-size effects in the 3D reconstruction and morphological analysis of porous polymers" in: *Materials Today* 17.8 (2014), pp. 404–411 DOI: 10.1016/j.mattod.2014.07.003 (see p. 150)

[306] D. STOECKEL, C. KÜBEL, K. HORMANN, A. HÖLTZEL, B. M. SMARSLY, and U. TALLAREK "Morphological analysis of disordered macroporous-mesoporous solids based on physical reconstruction

by nanoscale tomography" in: *Langmuir* 30.30 (2014), pp. 9022–7 DOI: 10.1021/la502381m (see p. 150)